Titel der Arbeit:

Nonrenewal spiking in Neural and Calcium signaling

DISSERTATION

zur Erlangung des akademischen Grades

doctor rerum naturalium
(Doc. rer. nat.)
im Fach: *Physik*,
Spezialisierung: *Theoretische Physik*

eingereicht an der

Mathematisch-Naturwissenschaftlichen Fakultät
der Humboldt-Universität zu Berlin

von

M. Sc. Lukas RAMLOW

Präsidentin der Humboldt-Universität zu Berlin
Prof. Dr. Julia von Blumenthal

Dekanin der Mathematisch-Naturwissenschaftlichen Fakultät
Prof. Dr. Caren Tischendorf

Gutachter:

1. Prof. Dr. Benjamin Lindner
2. Prof. Dr. Martin Falcke
3. Prof. Dr. Igor Sokolov

Tag der mündlichen Prüfung: 21.12.2023

Selbständigkeitserklärung

Ich erkläre, dass ich die Dissertation selbständig und nur unter Verwendung der von mir gemäß § 7 Abs. 3 der Promotionsordnung der Mathematisch-Naturwissenschaftlichen Fakultät, veröffentlicht im Amtlichen Mitteilungsblatt der Humboldt-Universität zu Berlin Nr. 42/2018 am 11.07.2018 angegebenen Hilfsmittel angefertigt habe.

Unterschrift:

Datum: 25.09.2023

Zusammenfassung

Viele Zellen übertragen Informationen in Form von kurzen Pulsen, so genannten Spikes. Dazu gehören elektrisch erregbare Neuronen, die Spikes in ihrer Membranspannung erzeugen, sowie eine große Anzahl elektrisch nicht-erregbarer Zellen, die Spikes in der intrazellulären Kalziumkonzentration erzeugen. Obwohl die physikalischen Größen und die Zeitskalen der Signale unterschiedlich sind, gibt es einige grundlegende Eigenschaften der Spike-Erzeugung, die beide Systeme gemeinsam haben: Erstens stellt ein positiver Rückkopplungsmechanismus sicher, dass ein Spike zuverlässig ausgelöst wird, sobald die spikende Variable einen bestimmten Schwellenwert überschreitet. Zweitens sind die Zeitpunkte, zu denen der Schwellenwert überschritten wird, das Ergebnis eines Zufallsprozesses und stellen somit selbst einen Zufallsprozess dar. Drittens führt die wiederholte Auslösung eines Spikes zu einer zunehmenden Hemmung der Auslösung weiterer Spikes, ein Phänomen, das als Spike-Frequenz-Adaptation bekannt ist.

Trotz dieser Gemeinsamkeiten unterscheiden sich die Modellierungsansätze zum Teil erheblich. Insbesondere reduzierte phänomenologische Modelle, so genannte *integrate-and-fire* (IF) Modelle, sind in Computational Neuroscience weit verbreitet, wurden aber bisher zur Beschreibung der Erzeugung von Ca^{2+}-Spikes nicht verwendet. IF-Modelle beschreiben die Dynamik der Spikevariablen nur bis zu einem bestimmten Schwellenwert, ab dem ein Spike als ausgelöst gilt und die Spikevariable zurückgesetzt wird. Der stereotype Spike wird also nicht modelliert, sondern durch eine Fire-and-Reset-Regel ersetzt. Dies hat den Vorteil, dass die komplexe nichtlineare Dynamik, die dem Spike seine Form gibt, nicht berücksichtigt werden muss. Stattdessen konzentrieren sich IF-Modelle auf die oft viel einfachere Dynamik unterhalb der Schwelle und erzeugen eine Abfolge von stochastischen Spike-Zeiten, die mit dem Überschreiten der Schwelle verbunden sind. Sie stellen somit ein Verbindung zwischen stochastischen dynamischen Modellen einerseits und stochastischen Punktprozessen andererseits her.

Eine typische Vereinfachung in der theoretischen Behandlung von Punktprozessen ist die Annahme, dass die Interspike-Intervalle (ISI) statistisch unabhängig voneinander sind. Ein Punktprozess mit dieser Eigenschaft wird als Erneuerungsprozess bezeichnet und ist vollständig durch die ISI-Verteilung bestimmt. Experimentelle Untersuchungen (insbesondere an Neuronen) haben jedoch gezeigt, dass die Intervalle in der Regel nicht unabhängig voneinander, sondern miteinander korreliert sind. Solche Korrelationen sind auf Prozesse zurückzuführen, die sich im Vergleich zu einem typischen ISI langsam ändern. Dies schließt Prozesse ein, die die Anpassung der Feuerrate vermitteln. Es ist daher anzunehmen, dass auch die Intervalle zwischen Kalziumspikes korreliert sind. Die statistische Analyse von Modellen, die einen *nicht-erneuerbaren* Punktprozess erzeugen, ist Gegenstand dieser Doktorarbeit.

Im zweiten Kapitel befassen wir uns zunächst mit der nicht-erneuerbaren Spike-Erzeugung in neuronalen Systemen und konzentrieren uns auf die Berechnung des seriellen Korrelationskoeffizienten (SCC). Dieser Koeffizient wurde in der Vergangenheit für Neuronen mit Spike-Frequenz-Adaptation und für Neuronen unter dem Einfluss von zeitlich korreliertem Rauschen berechnet. Letzteres kann als Approximation eines korrelierten Eingangsstroms betrachtet werden, wie er durch synaptische Filterung oder Netzwerkprozesse entsteht. Der allgemeinste Fall, in dem diese beiden langsamen Prozesse interagieren, wurde bisher nicht theoretisch behandelt. Wir schließen diese Lücke und betrachten ein mehrdimensionales IF Modell mit Spike-Frequenz-Adaptation, das durch ein korreliertes Rauschen getrieben wird. Basierend auf der Phasenreduktion dieses allgemeinen Modells leiten wir eine analytische Formel für den SCC her. Es zeigt sich, dass die Wahl der unterschwelligen Dynamik des IF-Modells die Phasenantwortfunktion und den SCC bestimmt. Wir verifizieren die Theorie anhand des leaky- und generalized IF-Modells. Zusätzlich betrachten wir zwei Spezialfälle: Einen Fall, in dem der Adaptationsstrom und das korrelierte Rauschen von einer endlichen Population von Ionenkanälen stammen, und einen Fall, in dem das Rauschen in seinen statistischen Eigenschaften dem eines rekurrenten Netzwerks im asynchronen irregulären Zustand ähnelt. Wir zeigen, dass die Theorie, obwohl sie für schwach gestörte IF-Modelle entwickelt wurde, den SCC auch für stärkere Störungen qualitativ beschreibt und sogar auf detailliertere leitfähigkeitsbasierte Modelle anwendbar ist. Die entwickelte Theorie ist somit in der Lage, die Intervallkorrelationen eines breiten Spektrums biophysikalisch relevanter Situationen zu beschreiben.

Im dritten Kapitel befassen wir uns dann mit der nicht-erneuerbaren Erzeugung von Kalziumspikes in elektrisch nicht-erregbaren Zellen. Wir formulieren zunächst ein phänomenologisches IF-Modell, das die stochastische Kalziumfreisetzung aus dem endoplasmatischen Retikulum (ER) durch Kalziumkanalcluster und die langsame Entleerung des ER beschreibt. Letzteres ist für die Adaptation der Feuerrate verantwortlich. Der Kalziumstrom durch die Cluster wird durch eine Markov-Kette beschrieben und stellt einen komplizierten stochastischen Prozess dar, der die theoretische Behandlung des Modells erschwert. Experimentell ist jedoch bekannt, dass sich die Zeitskala der ISI nicht in der Kinetik der Cluster widerspiegelt. Dies motiviert eine Diffusionsnäherung, bei der der Kalziumstrom durch ein Gaußsches weißes Rauschen mit Kalziumabhängigem Mittelwert und Rauschintensität ersetzt wird. Für beide Statistiken leiten wir exakte analytische Ausdrücke her. Wir untersuchen das Modell zunächst in einer reduzierten Variante, in der wir annehmen, dass sich die Kalziumkonzentration im ER nicht ändert. In diesem Fall ist das Modell eindimensional und erzeugt einen quasi-erneuerbaren Pulszug. Für diese Modellvariante erlaubt die Ersetzung des Kalziumstroms durch ein weißes Rauschen die Berechnung der Momente der ISI-Verteilung auf der Basis der Fokker-Planck-Gleichung (FPG). Die experimentell beobachtete Transiente, während der sich die Feuerrate langsam anpasst, kann jedoch nur durch das vollständige Modell beschrieben werden, das die Entleerung des ER berücksichtigt. Die theoretische Behandlung dieses zweidimensionalen Modells mit Hilfe der FPG ist wesentlich komplizierter. Für die ISI-Statistiken erster Ordnung, wie den Mittelwert und den Koeffizienten der Variation, leiten wir approximative Ausdrücke her. Zur Beschreibung der Transienten führen wir die Anzahl der transienten Intervalle (Länge der Transienten) und die kumulative Refraktärzeit (Stärke der Adapation) ein und leiten Näherungen für diese beiden Statistiken ab. Wir untersuchen, wie diese transienten ISI-Statistiken mit den ISI-Korrelationen im stationären Zustand zusammenhängen und verifizieren die Ergebnisse mittels experimentellen Daten. Dabei zeigt sich, dass stärkere Anpassungen der Intervalle tendenziell mit stärkeren Korrelationen und längere Transienten tendenziell mit schwächeren Korrelationen einhergehen. Diese Trends werden bis zu einem gewissen Grad von den experimentellen Daten verifiziert, obwohl gleichzeitig häufig positive Korrelationen beobachtet werden, die durch unser Modell nicht erklärt werden können.

In dieser Arbeit erweitern wir existierende Theorien zur Beschreibung von nicht-erneuerbaren Punktprozessen in Computational Neuroscience, um die biophysikalisch plausibelste Situation zu berücksichtigen, in der zwei korrelationsinduzierende Prozesse interagieren, um Intervallkorrelationen zu bilden. Darüber hinaus verwenden wir die Klasse der IF-Modelle, um die Erzeugung von Ca^{2+} Spikes zu beschreiben. Dies erweist sich als sehr aufschlussreich. Das vorgeschlagene Modell ist in der Lage, experimentelle Sequenzen von Spike-Zeiten hinsichtlich ihrer statistischen Eigenschaften sowohl im transienten als auch im stationären Zustand quantitativ zu reproduzieren. Darüber hinaus kann das Modell analytisch behandelt werden und erlaubt uns, etablierte Methoden der Computational Neuroscience auf das Gebiet der mathematischen Zellbiologie zu übertragen. Dies ermöglicht die Berechnung einer Vielzahl von Spike-Statistiken, entweder exakt mittels der FPG im Fall des reduzierten Modells oder näherungsweise mit einem selbstkonsistenten Ansatz für das vollständige Modell. Dies trägt dazu bei, die relevanten Prozesse, die an der Erzeugung von Ca^{2+}-Spikes beteiligt sind, besser zu verstehen.

Abstract

Many cells transmit information by short pulses, so-called spikes. These include electrically excitable neurons, which generate spikes in their membrane voltage, and various electrically non-excitable cells, which generate spikes in the intracellular calcium (Ca^{2+}) concentration. Although the physical quantities and the time scales of the signals are different, some principles of spike generation are shared by both systems: First, a positive feedback mechanism ensures that a spike is reliably initiated once the spiking variable exceeds a certain threshold. Second, the times the threshold is crossed result from a random process and thus form a random process as well. Third, the emission of each spike increasingly inhibits the generation of further spikes, a phenomenon known as spike-frequency adaptation.

Despite these similarities, some of the modeling approaches differ significantly. Specifically, reduced phenomenological models, so-called *integrate-and-fire* (IF) models, are widely used in computational neuroscience but have not yet been adopted to describe the generation of Ca^{2+} spikes. IF models describe the dynamics of the spiking variable only up to a certain threshold, at which point a spike is said to be fired and the spiking variable is reset. Thus, the stereotypical spike is not modeled but replaced by a fire-and-reset rule. This has the advantage that the complex nonlinear dynamics that give the spike its shape do not need to be considered. Instead, IF models focus on the often much simpler subthreshold dynamics and generate a sequence of stochastic spike times associated with the crossings of the threshold. Therefore, they provide a link between dynamic models on the one hand and stochastic point processes on the other.

A typical simplification in the theoretical treatment of point processes is the assumption that the interspike intervals (ISI) are statistically independent. A point process with this property is called a renewal process and is completely determined by the ISI distribution. However, experimental studies (especially on neurons) have shown that the intervals are usually correlated rather than independent. Such correlations are due to processes that change slowly compared to a typical ISI. This includes processes that mediate spike-frequency adaptation. It is, therefore, reasonable to assume that the intervals between Ca^{2+} spikes are also correlated. The statistical analysis of models that produce a *nonrenewable* point process is the subject of this dissertation.

In the second chapter, we study nonrenewal spike generation in neural systems and focus on calculating the serial correlation coefficient (SCC). This coefficient has been calculated in the past for neurons with spike-frequency adaptation and for neurons driven by a temporally correlated noise. The latter can be regarded as an approximation of a correlated input current, as it may result from synaptic filtering or network processes. The most general case, in which these two slow processes interact, has not been treated theoretically so far. We fill this gap and consider a multidimensional IF model with spike-frequency adaptation driven by a correlated noise. Based on the phase reduction of this general model, we derive an analytical formula for the SCC. It is shown that the choice of the subthreshold dynamics of the IF model determines the phase response curve and the SCC. We verify the theory using the leaky and generalized IF models. In addition, we consider two special cases: A case in which the adaptation current and the correlated noise originate from a finite population of ion channels and a case in which the noise resembles in its statistical properties that of a recurrent network in the asynchronous irregular state. Although developed for weakly perturbed IF models, we show that the theory qualitatively describes the SCC for stronger perturbations and is even applicable to more detailed conductance-based models. Thus, the developed theory can describe interval correlations in various biophysically relevant situations.

In the third chapter, we study the nonrenewal generation of Ca^{2+} spikes in electrically non-excitable cells. We first formulate a phenomenological IF model that accounts for the stochastic release of Ca^{2+} from the endoplasmic reticulum (ER) by Ca^{2+} channel clusters and the slow depletion of the ER. The latter mediates spike-frequency adaptation in this system. The Ca^{2+} current through the clusters is described by a Markov chain and forms a complicated stochastic process that does not readily permit the theoretical treatment of the model. However, experimentally, it is known that the time scale of the ISIs is not reflected in the kinetics of the clusters. This motivates a diffusion approximation in which the Ca^{2+} current is replaced by a Gaussian white noise with a Ca^{2+}-dependent mean and noise intensity. We derive exact analytical expressions for these two statistics. We first examine the model in a reduced version, assuming that the ER's Ca^{2+} concentration does not change. In this case, the model is one-dimensional and generates a quasi-renewable spike train. For this model variant, the replacement of the Ca^{2+} current by a white noise allows us to calculate the moments of the ISI distribution based on the Fokker-Planck equation (FPE). However, the experimentally observed transient, during which the spike frequency slowly adapts, can only be described by the full model that accounts for the ER depletion. The theoretical treatment of this two-dimensional model using the FPE is much more complicated. We derive approximate expressions for the first-order ISI statistics, such as the mean and the coefficient of variation. To describe the transients, we introduce the number of transient intervals (length of transients) and the cumulative refractory period (strength of adaptation) and derive approximations for these two statistics. We study how these transient ISI statistics are related to the stationary ISI correlations and test the results using experimental data. We find that stronger adaptation of the intervals tends to be associated with stronger correlations and that longer transients tend to be associated with weaker correlations. These trends are verified to some extent by the experimental data, although positive correlations that our model cannot explain are also observed.

In this thesis, we extend the existing theory on nonrenewable spike generation in computational neuroscience to account for the biophysically most plausible situation where two correlation-inducing processes interact to shape interval correlations. We also propose to apply the class of IF models to describe the generation of Ca^{2+} spikes. This turns out to be very fruitful. The proposed model is able to quantitatively reproduce experimental sequences of spike times in terms of their statistical properties in both the transient and stationary states. Moreover, the model is analytically tractable and allows us to transfer established methods from computational neuroscience to the field of mathematical cell biology. This enables us to calculate various spiking statistics, either exactly using FPE in the case of the reduced model, or approximately using a self-consistent approach for the full model. This may help to shed light on the relevant processes involved in the generation of Ca^{2+} spikes.

Contents

Chapter 1

Introduction

The ability to perceive and respond to information from the environment is an essential part of life. This applies not only to humans, who can perceive their environment with their senses, but also to the smallest unit of life, the cell, which can perceive a variety of chemical messengers with the help of special receptors. Fascinatingly, different signaling systems encode information in a similar way, namely in the form of sequences of short pulses as shown in Fig. 1.1. The present work deals with the generation of these pulses in neuronal and calcium (Ca^{2+}) signaling.

The elementary processing units of the nervous system are the nerve cells or neurons. Neurons differ from other cells in that they are electrically excitable, i.e., they can generate short electrical pulses, so-called action potentials or spikes (cf. Fig. 1.1 left panel). These spikes vary little in shape each time they are fired and have a typical duration of about 1 ms to 2 ms [9]. In contrast, the time between two spikes can vary greatly depending on the type of neuron, ranging from milliseconds in P-units to tens of milliseconds in fast-spiking interneurons to hundreds of milliseconds in pyramidal cells [10–12]. Spikes are considered the biophysical basis of information processing and transmission in the nervous system. For example, neurons in the sensory periphery translate all information or stimuli that we perceive from the environment with our senses into sequences of spikes - so-called spike trains. These information-bearing spike sequences are then transmitted to the brain, where they are further processed by neurons in the central nervous system. In the brain, neurons are highly interconnected; a typical neuron in the cortex is connected to more than 10,000 other neurons via so-called synapses [13]. Thus, the output spike train of one neuron is part of the input spike train of another neuron and can itself be interpreted as a stimulus. The properties of a stimulus that lead to a response by a subsequent neuron become more complex and abstract as the level of processing increases. Nevertheless, the notion that all information is ultimately encoded in the spike trains of the brain is a central paradigm of neuroscience [14]. To understand how spike sequences are processed in the brain, one must first understand the elementary processing units of the brain, the neurons.

A single neuron is itself a complex system that can be divided into three functionally distinct parts: the dendrite, the soma, and the axon. The dendrite is a highly ramified structure that receives synaptic input and transmits it to the soma. The soma, in turn, integrates the synaptic input and triggers a spike when a certain threshold is exceeded. The spike is then transmitted via the axon to the dendrite of other neurons. The basis for the generation of the spike is a non-equilibrium that is maintained by the neuron. Like any other cell, a neuron is surrounded by a cell membrane. Within this membrane, various small ion channels and pumps create a continuous flow of ions and maintain a difference in the concentration of various ions between the interior and exterior of the neuron. This results in an electrical potential difference along the cell membrane called the membrane potential or voltage. Even in the resting state (without stimulation), neurons have a membrane potential of about -70 mV [9, 15]. This non-equilibrium state allows the neuron to generate spikes upon stimulation via a nonlinear dependence of the ion currents through the channels on the membrane potential. In particular, depolarization of the membrane above a certain threshold leads to the activation of voltage-gated sodium channels, resulting in a sodium influx, which further depolarizes the membrane, and so on. This strong positive feedback mechanism is responsible for the upstroke of the famous action potential [16]. However, spike generation is not a deterministic but a stochastic process. One reason for this is that the channel proteins are in thermal contact with their environment and are subject to constant random collisions with the surrounding molecules. This leads to stochastic opening and closing of the ion channels, which in turn leads to stochastic ion currents and to fluctuations in the membrane potential [17]. As a result, when a neuron is repeatedly driven by the same stimulus, the

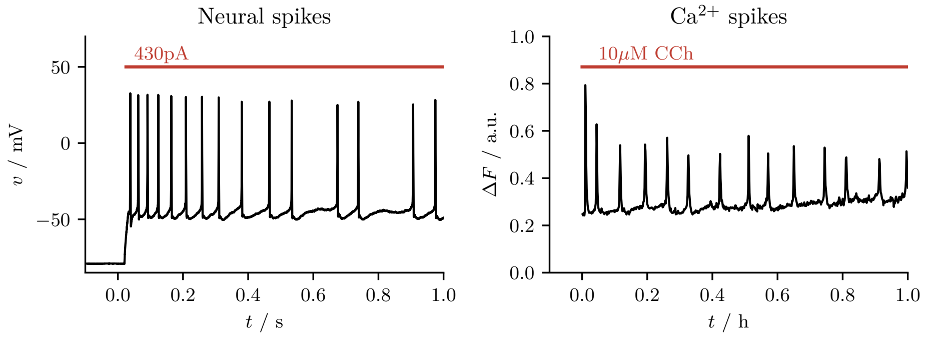

FIGURE 1.1: Comparison between neural and Ca^{2+} spiking. Left panel shows neural spiking observed in layer 6a neurons of the primary visual cortex of mice (Rorb-IRES2-Cre) exposed to the onset of a constant current stimulation at 430 pA (red line). Allen Brain Atlas, celltypes.brain-map.org/experiment/electrophysiology/490612150. Right panel shows Ca^{2+} spikes observed in HEK cells stimulated with 10 µmol dm^{-3} carbamylcholine (CCh) (red line). Changes in free cytosolic Ca^{2+} concentration are measured indirectly by changes in the Ca^{2+} indicator Fura-2 fluorescence ratio ΔF. Data were measured as described in [7, 8] and provided by M. Falcke.

spike times vary. Another ubiquitous feature of neuronal spike generation is the decrease in firing rate after an initial increase in response to the onset of a constant stimulus [18]. This phenomenon is known as spike frequency adaptation and is mediated by slow negative feedback mechanisms. In summary, the dynamics of a single neuron are highly complex, influenced by stochasticity, fast positive feedback mechanisms, and slow negative feedback mechanisms.

A completely different process is the signal transduction via Ca^{2+}-dependent pathways, which are mainly used by electrically nonexcitable cells. In many cells, the binding of an extracellular messenger triggers a biochemical cascade that ultimately leads to a short, repeated increase in the intracellular Ca^{2+} concentration (cf. Fig. 1.1 right panel). This triggers the cellular response, for example, by binding Ca^{2+} to the regulatory protein calmodulin (CaM). Although CaM itself is not enzymatically active, it is responsible for activating hundreds of other proteins that possess CaM recruitment sites [19]. Cellular responses regulated by the intracellular Ca^{2+} concentration include processes as diverse as muscle contraction and relaxation, synaptic neurotransmitter secretion, gene transcription, fertilization, and apoptosis [20–27]. Interestingly, Ca^{2+} signals also often take the form of short, pulse-like increases in the intracellular Ca^{2+} concentration so-called Ca^{2+} oscillations or spikes, which regulate various cellular functions through stimulus-dependent patterns [24, 28]. Even though the generated spike patterns are enormously versatile [23], the spikes typically last a few seconds, and the interspike intervals are on the order of minutes [8, 27]. Like neurons, cells that use Ca^{2+} as a second messenger invest much of their energy to maintain a non-equilibrium situation through various ion pumps. In this case, primarily ATPase pumps that relentlessly push Ca^{2+} against a gradient from the cytosol either into the endoplasmic reticulum (ER) or out of the cell. This results in an extraordinarily low Ca^{2+} concentration in the cytosol of about 100 nM and up to 20,000 times lower than the Ca^{2+} concentration in the ER and extracellular medium [19, 29]. This extreme Ca^{2+} gradient allows the cell to respond rapidly to an extracellular stimulus with an increase in the intracellular Ca^{2+} concentration either by an influx of Ca^{2+} from the extracellular medium via voltage-gated Ca^{2+} channels or by a release of Ca^{2+} from the ER via so-called inositol 1,4,5-trisphosphate (IP_3) channels. In this thesis, we focus on Ca^{2+} release from the ER. However, the rapid increase in intracellular Ca^{2+} during a spike from approximately 100 nM to 1 mM is not only due to the strong gradient but also due to a nonlinear positive feedback mechanism. Contrary to what the name suggests, IP_3 channels are not only regulated by IP_3 but also by intracellular Ca^{2+} itself. Therefore, an increase in the intracellular Ca^{2+} concentration leads to an increased Ca^{2+} release from the ER. This mechanism is called Ca^{2+}-induced Ca^{2+} release (CICR) and ensures the reliable initiation of a Ca^{2+} spike once the intracellular Ca^{2+} concentration exceeds a certain threshold. As for neural spike generation, the generation of Ca^{2+} spikes is a stochastic process because the opening and closing of IP_3 channels occurs in thermal contact with the environment. This leads to a stochastic release of Ca^{2+} from the ER and to fluctuations in intracellular Ca^{2+} concentration. Moreover, slow negative feedback mechanisms, such as the slow depletion of the ER over several spikes, give rise to an adaptation of the firing rate or equivalently a prolongation of the interspike intervals when spikes are repeatedly fired [30–32]. Thus, the generation of Ca^{2+} spikes is also a complex process affected by stochasticity as well as positive and negative feedback mechanisms on different time scales.

Despite the different physical quantities in which neural and Ca^{2+} spikes are observed and the different time scales on which they occur, the generation of neural and Ca^{2+} spikes follows similar principles [2]. First, the spike generation is a stochastic process, and so is the sequence of spike times [7, 33]. This is partly due to the probabilistic opening and closing of the ion channels. In the context of neural spiking, we will see that other, potentially stronger sources of noise also contribute to the stochasticity [34]. Second, a strong positive feedback mechanism reliably initiates the spikes once a certain threshold is exceeded. In both cases, this positive feedback is mediated by ion channels whose opening contributes to the generation of the spike and whose opening probability depends positively on the spiking quantity [35, 36]. Third, each spike progressively inhibits the formation of further spikes until a stationary state is reached. Stochastic spiking and adaptation are thus two essential features of both neural and Ca^{2+} signaling and result in a sequence of spike times with a rich statistical structure. Therefore, describing spike generation using models that account for the fluctuations and incorporate slow feedback mechanisms is essential for a comprehensive understanding of neural activity and Ca^{2+} spiking.

In the context of neural signaling, the reliable initiation of a stereotypical spike has led to the realization that the spike time rather than the spike shape carries the information. This perspective is reflected in the mathematical models used to describe neural activity and in the statistical analysis of the spike train as a stochastic point process [37]. In particular, it is reflected in the formulation of phenomenological integrate-and-fire (IF) models [38, 39], that describe the spiking variable only up to a certain threshold and replace the stereotypical spike with a fire-and-reset rule. These models have the advantage that the complex nonlinear dynamics that shape the spike do not have to be taken into account. Instead, other dynamic aspects can be considered, e.g., those that mediate the adaptation of the firing rate [40, 41]. Despite their simplistic approach, IF models can reproduce the spike times of real neurons to an astonishing degree [42–44]. In the context of Ca^{2+} signaling, such a modeling approach has not yet been adopted. This is surprising given the strong similarities in the spike generation and the great success of the IF model in computational neuroscience. Developing a phenomenological model to describe the formation of Ca^{2+} spikes is one part of this thesis.

A common simplification in the study of spike formation is the assumption that there is no significant memory beyond the last spike time. This implies that the intervals between spikes are statistically independent. A point process with statistically independent intervals is called a *renewal* process [45]. Although this assumption is convenient from a mathematical point of view, it is often not satisfied. We have already noted that in both neural and Ca^{2+} signaling, the spike sequence in response to the onset of a constant stimulus often exhibits an initial transient during which the firing rate gradually decreases and, conversely, the intervals between spikes gradually increase. Such transients are usually associated with slow processes that affect the generation of spikes over multiple spike times. As a result, even long after the initial transient, when the spiking statistics no longer depend on the absolute time elapsed since the stimulation, such processes can cause the interspike intervals to be correlated rather than independent. A point process with correlated intervals is called a *nonrenewal* process [46].

This thesis is concerned with the mathematical modeling and statistical analyses of nonrenewal spiking in neural and Ca^{2+} signaling. In the following sections we will first introduce a number of stochastic processes that are useful in this regard.

1.1 Markov chain

We have argued that the gating (opening and closing) of ion channels, which is ultimately responsible for the formation of neural and Ca^{2+} spikes, is a stochastic process because it occurs in thermal contact with the surrounding molecules in the intracellular medium [47]. In its simplest form, a mathematical model describing an ion channel should distinguish between at least two states (open or closed) and describe the stochastic transition between them. Often the structure of an ion channel is more complicated, for example because the channel has a tetrameric structure and consists of four subunits, all of which must bind a particular molecule or ligand for the channel to open [48]. Thus, a more detailed model that distinguishes for each of these subunits whether the ligand is bound or not would have to distinguish up to 2^4 different states for the entire ion channel. What the simple and more detailed descriptions of a channel have in common is that a number of *discrete* states are distinguished, and the transition between them occurs at random times.

A model class that combines both these aspects and is often used to describe the activity of ion channels are so-called continuous time Markov chains (CTMCs). A CTMC $y(t)$ is a special Markov process with a discrete state space S and continuous time t. CTMCs possess the Markov property, i.e., the future state of the process depends only on the current state. In more mathematical terms, the conditional probability of finding the state $s_i \in S$ at time t_i given the full history of the process

$$p(y(t_i) = s_i | y(t_{i-1}) = s_{i-1}; \ldots ; y(t_1) = s_1) = p(y(t_i) = s_i | y(t_{i-1}) = s_{i-1}) \tag{1.1.1}$$

is uniquely determined by the *transition* probability $p(y(t_i) = s_i | y(t_{i-1}) = s_{i-1})$ for all times $t_1 < \cdots < t_{i-1} < t_i$ and all states $s_1, \ldots, s_i$ [49, 50]. The defining quantities of a such a Markov chain are the transition rates q_{ij}, which, when multiplied by a short time interval Δt, provide the transition probability from one state s_i to another state s_j. The transition rates form the elements of the transition rate matrix

$$Q = \begin{pmatrix} q_{11} & q_{12} & \cdots & q_{1n} \\ q_{21} & q_{22} & & \\ \vdots & & \ddots & \\ q_{n1} & & & q_{nn} \end{pmatrix} \tag{1.1.2}$$

sometimes abbreviated by $Q = (q_{ij})$. The diagonal elements are chosen so that $q_{jj} = -\sum_{i \neq j} q_{ij}$ and the columns of Q sum to zero. This reflects that there are no sources or sinks of probability for such models and implies that the transition rate matrix does not have full rank. Thus, every statistical measure formally determined by inverting Q requires an additional condition. For example, the probability of finding the state s_i at time t is denoted by $p(i, t)$ and governed by the master equation

$$\dot{\boldsymbol{p}} = Q \cdot \boldsymbol{p} \tag{1.1.3}$$

with the probability vector

$$\boldsymbol{p}(t) = \begin{pmatrix} p(1,t) & p(2,t) & \ldots \end{pmatrix}^T . \tag{1.1.4}$$

For $\boldsymbol{p}(t)$ to be uniquely determined, the additional normalization condition $\sum_i p(i, t) = 1$ is required.

As a simple example of a Markov chain let us consider a two-state system that obeys the following reaction scheme:

$$\text{open} \underset{\alpha}{\overset{\beta}{\rightleftharpoons}} \text{close}. \tag{1.1.5}$$

The transition from the open to the closed state occurs at the closing rate β, and the reverse transition occurs at the opening rate α. This system can be regarded as a minimal model of an ion channel. In most biophysical cases, the rates are not constant but depend on other variables, such as the voltage or ligand concentration, which is an important feature of many ion channels [15]. However, as an introductory example, we will simply consider a model with constant rates. A realization $y(t)$ of the two-state system - also known as a dichotomous noise [51] - is shown in Fig. 1.2. The transition rate matrix corresponding to the schematic representation (Eq. 1.1.5) is given by

$$Q = \begin{pmatrix} -\beta & \alpha \\ \beta & -\alpha \end{pmatrix} \tag{1.1.6}$$

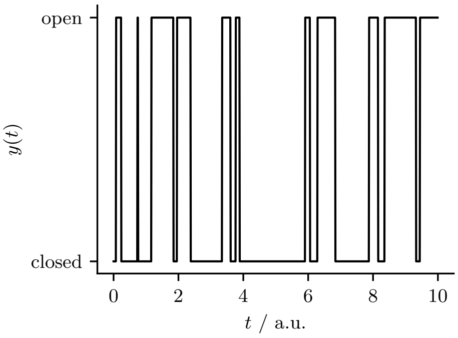

FIGURE 1.2: Example of a time series of a two-state Markov chain $y(t)$.

and allows the calculation of statistics of interest using the master equation. The arguably most commonly computed statistics are the stationary probabilities

$$p_0(\text{open}) = \frac{\alpha}{\alpha + \beta}, \tag{1.1.7}$$

$$p_0(\text{close}) = \frac{\beta}{\alpha + \beta}, \tag{1.1.8}$$

which signify the fraction of time the model spends in the open and closed states, respectively. These statistics can be calculate using the *stationary* master equation

$$0 = Q \cdot \boldsymbol{p_0} \tag{1.1.9}$$

together with the normalization $p_0(\text{open}) + p_0(\text{close}) = 1$ where $\boldsymbol{p_0} = (p_0(\text{open}), p_0(\text{close}))^T$ is the stationary probability vector.

In terms of spike generation, it is usually not the activity or ionic current through a single channel that is of interest but rather the current through a larger but finite population of channels. In the following section, we show that for a population of ion channels, the fraction of open channels can often be described mathematically conveniently by random processes with a continuous state space.

1.2 Langevin equation

Probably the first systematic observation of random motion was made by Robert Brown in 1827. He observed that small pollen particles, when suspended in water, moved in a jerky and irregular manner - a process we now call Brownian motion [52, 53]. For almost a century, the mystery of Brownian motion remained unsolved until Einstein published an explanation in 1905 [54] . He showed that the random motion of the pollen could be explained by very frequent collisions with the even smaller molecules of the liquid in which the pollen were suspended.

Some time after Einstein, Paul Langevin presented a new approach in 1908, which he famously claimed was "infinitely more simple" [55]. He formulated an equation similar to Newton's equation of motion, but with an additional random force or noise. If the inertia term is neglected, the result is a differential equation known as a Langevin equation

$$\dot{x} = f(x) + \sqrt{2D(x)}\xi(t), \tag{1.2.1}$$

where $\xi(t)$ is a (continuous) Gaussian random process with $\langle \xi(t) \rangle = 0$ and $\langle \xi(t)\xi(t') \rangle = \delta(t - t')$, $f(x)$ is the drift function, and $D(x)$ is the noise intensity. The process $\xi(t)$ is also known as a *Gaussian white noise*, where the term "white" refers to the fact that the power spectrum (see below) of the process is flat and all frequencies are equally represented - similar to how white light can be thought of as the superposition of light of different colors or wavelengths. The description of the random processes by a Gaussian white noise is based on the assumption that the fluctuations are fast compared to any other time scale in the system. In this case, the fluctuations are approximately uncorrelated in time. Langevin's equation was the first example of a *stochastic* differential equation, i.e. a differential equation with a random term $\xi(t)$.

Let us return to the two-state channel model that we have considered in the previous section to understand how a Langevin equation can be motivated. We have already noted that in terms of the spike generation, it is usually the current through a large but finite population of channels that is of interest. Although the relative fluctuations of the ionic current through a population of channels are smaller than the fluctuations of the current through a single channel, they remain finite for a finite population. These fluctuations are referred to as channel noise [17] and can be approximated by a Langevin equation if a sufficiently large number of channels is considered. Since Langevin equations describe diffusion processes, this procedure is often referred to as a diffusion approximation. Here, we follow the derivation by Lindner [56]. Let us consider the number of open channels $n_{\text{open}}(t)$ at time t in a population of N two-state channels. Since we are considering a two-state system, the number of closed channels need not be considered separately, but is given by $n_{\text{close}}(t) = N - n_{\text{open}}(t)$. Therefore, we simply denote the number of open channels by $n(t)$. The goal is to derive a simplified description of the dynamics of $n(t)$. To this end, we consider the change of the number of open channels

$$\delta n(t) = n(t + \Delta t) - n(t) \tag{1.2.2}$$

over a time window Δt. If this time window is sufficiently small, the probability of a single channel closing during Δt is given by $\beta \Delta t \ll 1$, and the probability of a single channel opening is given by $\alpha \Delta t \ll 1$. For a population of independent channels, the number of channels closing in a small time window Δt follows a Poisson distribution with mean $n(t)\beta\Delta t$ and variance $n(t)\beta\Delta t$. The same applies to the number of opening channels with mean $(N - n(t))\alpha\Delta t$ and variance $(N - n(t))\alpha\Delta t$. Together, these two mean values give the expected change in the number of open channels in a small time window

$$\langle \delta n(t) \rangle = (N - n(t))\alpha\Delta t - n(t)\beta\Delta t, \tag{1.2.3}$$

as well as the variance

$$\left\langle \Delta(\delta n(t))^2 \right\rangle = (N - n(t))\alpha\Delta t + n(t)\beta\Delta t. \tag{1.2.4}$$

If the population is sufficiently large, i.e. for large N, the distribution of the number of transitions in the time window Δt will be Gaussian distributed according to the central limit theorem [57]. The Gaussian distribution is fully determined by the mean and variance and the change over a small time window can be approximated by

$$\delta n(t) = \langle \delta n(t) \rangle + \sqrt{\langle \Delta \delta n(t)^2 \rangle}\, \nu_t, \tag{1.2.5}$$

where ν_t are independent Gaussian distributed random numbers with zero mean and unit variance. Note that since ν_t is a continuous random variable, so is $\delta n(t)$. Inserting Eq. 1.2.2, 1.2.3, and 1.2.4 into Eq. 1.2.5 and dividing by Δt yields the difference equation

$$\frac{n(t + \Delta t) - n(t)}{\Delta t} = \alpha(N - n(t)) - \beta n(t) + \sqrt{\frac{\alpha(N - n(t)) + \beta n(t)}{\Delta t}}\, \nu_t, \tag{1.2.6}$$

that can be thought of as a discretization of the stochastic differential equation

$$\dot{n} = \alpha(N - n) - \beta n + \sqrt{\alpha(N - n) + \beta n}\, \xi(t), \tag{1.2.7}$$

where $\xi(t) = \lim_{\Delta t \to 0} \nu_t / \sqrt{\Delta t}$ is the Gaussian white noise we have introduced above. Sometimes it is more convenient to consider the fraction of open channels denoted $x(t) = n(t)/N$ in which case Eq. 1.2.7 becomes

$$\dot{x} = \alpha(1 - x) - \beta x + \sqrt{\frac{\alpha(1 - x) + \beta x}{N}}\, \xi(t), \tag{1.2.8}$$

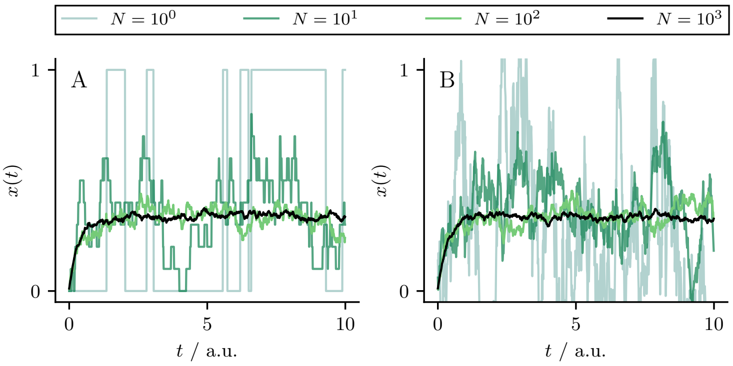

FIGURE 1.3: Fraction of open channels $x(t)$ in a population of n two-state channel models with $x(0) = 0$. Panels A and B show the fraction of open channels obtained from stochastic simulations of a population of two-state Markov models or from stochastic simulations of the Langevin approximation according to Eq. 1.2.8. The approximation becomes more accurate as the number of channels n increases.

with the drift function $f(x) = \alpha(1-x) - \beta x$ and noise intensity $D(x) = (\alpha(1-x) + \beta x)/(2N)$[1]. From this equation it is easy to see that, as we mentioned earlier, the relative fluctuations decrease with the number of channels N. In Fig. 1.3, we compare the fraction of open channels $x(t)$ obtained from simulations of a population of two-state channel models (panel A) with the approximation given by Eq. 1.2.8 (panel B). As the number of channels N increases, the approximation by a diffusion process becomes more accurate. This means that the superposition of many discrete random processes can be well described by a continuous random process.

Eq. 1.2.7 and 1.2.8 are Langevin equations. Such equations are mathematically convenient because the fact that the white noise is delta-correlated implies that the driven process, here $n(t)$ or $x(t)$, is a Markov process. At the same time, the delta correlation of the process $\xi(t)$ also implies that its variance is infinite. In other words, $\xi(t)$ fluctuates infinitely fast between plus and minus infinity. Therefore, a Langevin equation must always be interpreted as an idealized or coarse description because no biophysical process changes infinitely fast. Nevertheless, a description by a Langevin equation is useful because it allows one to use the powerful arsenal of the theory of Markov processes [59, 60]. For example the rather general Langevin equation 1.2.1 possess the corresponding Fokker-Planck equation (FPE) [61]

$$\frac{\partial}{\partial t}P(x,t) = \frac{\partial}{\partial x}\left[-f(x) + \frac{\partial}{\partial x}D(x)\right]P(x,t), \tag{1.2.9}$$

describing the evolution of the probability density $P(x,t)$. Note that the variable x has a different meaning in the Langevin and Fokker-Planck equations. In the Langevin equation, $x(t)$ is a realization of a stochastic process. In the FPE, x is a state variable and $P(x,t)dx$ is the probability that a realization at time t takes a value in the interval $[x, x+dx]$.

Stochastic differential equations, or Langevin equations, are of course not limited to describing the motion of a Brownian particle or the fraction of open channels, but can be applied to a wide range of diffusion processes. The general assumption underlying the formulation of a Langevin equation is that there exists a time window Δt small enough that the mean change can be linearized and large enough that the fluctuations are the result of a large number of independent random events. The fluctuations can then be described by a Gaussian random number according to the central limit theorem. This includes the change of the membrane potential in neurons or the change of intracellular Ca^{2+} concentration [33, 62–64]. In these two cases, stochastic differential equations are often considered, which in turn generate a sequence of stochastic spike times. This leads us to the third and last stochastic process introduced here.

---

[1] A Langevin equation with a noise intensity that depends on the variable driven by the white noise requires an interpretation [58]. For simplicity, we interpret the Langevin equation here in terms of Itô and note that the so-called Itô-Stratonovich dilemma will be discussed in more detail in Chap. 3.

1.3 Stochastic point process

Many cells generate an ordered sequence of random spike times:

$$\dots t_{i-1}, t_i, t_{i+1}, \dots \tag{1.3.1}$$

These spike times form a point process, which is a collection of points randomly distributed over some space. In our case, this is a collection of random spike times distributed over the time axis. The simplest point process - associating points with spike times - is the homogeneous Poisson process that is characterized by two features:

1. The probability to find a spike time t_i in a small time bin $[t, t+\Delta t]$ is independent of the time t; there is no trend in the data.
2. The probability to find a spike time t_i in a small time bin $[t, t+\Delta t]$ is independent of previous spike times t_{i-1}; there is no dependence between spike times.

The first assumption defines a *stationary* point process; the second assumption defines a point process with statistically *independent* spike times [46, 65]. The collection of spike times is closely related to the spike train

$$z(t) = \sum_i \delta(t - t_i), \tag{1.3.2}$$

a sequence of delta functions $\delta(\cdot)$ at the spike times as well as the spike count

$$N(T) = \int_0^T z(t), \tag{1.3.3}$$

the number of spikes in a time window T (where we have used T to indicate that this window is generally not small).

Here, we introduce a number of selected statistics that characterize the stochastic spike times and specifically focus on a *stationary* point process, i.e., a process that does not depend on absolute time. The first important statistic is the stationary firing rate r_0 that is the probability of finding a spike time in an infinitesimally small interval Δt

$$r_0 = \lim_{\Delta t \to 0} \frac{\mathrm{Prob}(t < t_i < t + \Delta t)}{\Delta t} = p_{\mathrm{spike}}(t). \tag{1.3.4}$$

This rate can be obtained as a temporal average of the spike train

$$\langle z(t) \rangle = \lim_{T\to\infty} \frac{1}{T} \int_0^T \sum_i \delta(t - t_i) = \lim_{T\to\infty} \frac{N(T)}{T} = r_0. \tag{1.3.5}$$

For $T \to \infty$, the fluctuations of the spike count $N(T)$ vanish, and division by the time bin T gives the stationary rate r_0. For a Poisson process, where the probability of finding a spike in a small time window is independent of previous spike times, the firing rate is the only relevant statistic. This is because the joint probability of finding a spike at t and another spike at $t+\tau$ simply factorizes into the marginal distributions of finding a spike at t and finding a spike at $t+\tau$, i. e. $p(t, t+\tau) = p_{\mathrm{spike}}(t) p_{\mathrm{spike}}(t+\tau) = r_0^2$. Consequently, the Poisson process is completely determined by the firing rate.

We can ease the assumption that spike times are independent and describe the dependence between spike times by the spike-train auto correlation function[2]

$$C_{zz}(\tau) = \langle z(t+\tau) z(t) \rangle - \langle z(t+\tau) \rangle \langle z(t) \rangle, \tag{1.3.6}$$

where the first term on the r.h.s. is the joint probability of finding a spike at time t and a spike at $t+\tau$. For a point process, this probability can also be written as $\langle z(t+\tau) z(t) \rangle = r_0 \delta(\tau) + m(\tau)$ [46], where the delta function at $\tau = 0$ reflects that there was a spike at $t+0$. The function $m(\tau)$

---

[2] The Poisson process also has a correlation function $C_{zz}(\tau) = r_0 \delta(\tau)$, but the probability of finding another spike at some time $\tau > 0$ is always given by the stationary firing rate.

is the probability of finding *another* spike at $t+\tau$. The second term on the r.h.s. of Eq. 1.3.6 gives the probability of finding a spike at t times the probability of finding a spike at $t+\tau$. Due to the stationarity of the considered process, this is the squared probability of finding a spike at any time, $\langle z(t+\tau)\rangle\langle z(t)\rangle = r_0^2$.

If the spike train has oscillatory components, for example, if spikes occur regularly, it may be convenient to analyze the spike train in the frequency domain. To this end, one defines the (one-sided) Fourier transform of the spike train

$$\tilde{z}_T(\omega) = \int_0^T dt\, z(t) e^{i\omega t}. \tag{1.3.7}$$

Note that because $z(t)$ is a sum of delta functions, the integral turns into a sum of complex numbers $\tilde{z}_T(\omega) = \sum_i \exp(i\omega t_i)$. Using Eq. 1.3.7, we can define the spike-train power spectrum

$$S(\omega) = \lim_{T\to\infty} \frac{\langle |\tilde{z}_T(\omega)|^2\rangle}{T}, \tag{1.3.8}$$

a second-order statistics[3] that, by the Wiener-Khinchin theorem [57], is related to the correlation function

$$S(\omega) = \int_{-\infty}^{\infty} d\tau\, C(\tau) e^{i\omega t}. \tag{1.3.9}$$

The two aforementioned statistics are based on the spike train. There are also statistics based on the spike count, most prominently the Fano factor

$$F(T) = \frac{\langle (N(T) - \langle N(T)\rangle)^2\rangle}{\langle N(T)\rangle} = \frac{\langle \Delta N(T)^2\rangle}{\langle N(T)\rangle}, \tag{1.3.10}$$

that compares the variance of the spike count to its mean as a function of the time window T. For small time windows $T\to 0$, finding a spike is essentially a Poisson process. In this case we find $\langle N(T)\rangle = r_0 T$ and $\langle N(T)^2\rangle = r_0 T$. Accordingly, the Fano factor starts at $F(T=0) = 1$ and decreases linearly for small T [66]´

$$\lim_{T\to 0} F(T) \approx \frac{r_0 T - (r_0 T)^2}{r_0 T} = 1 - r_0 T. \tag{1.3.11}$$

In the opposite limit of large time windows, the Fano factor can be interpreted as the diffusion coefficient of the spike count. This is so because the mean grows linearly in time $\langle N(T)\rangle = r_0 T$ so that in the limit $T\to\infty$, we obtain the mean square displacement of the spike count per unit time:

$$\lim_{T\to\infty} F(T) = \lim_{T\to\infty} \frac{\langle \Delta N(T)^2\rangle}{r_0 T} = \frac{2D_N}{r_0}. \tag{1.3.12}$$

The additional factor 2 comes from the fact that the diffusion coefficient is defined as $D_x = \lim_{t\to\infty}\langle \Delta x^2\rangle/2t$ [67]. Using the Kubo relation [68], we can relate the noise intensity of the spike count to the auto-correlation function of the spike train $D_N = \int_0^\infty d\tau\, C_{zz}(\tau)$, and thus the asymptotic Fano factor to the low-frequency limit of the power spectrum

$$r_0 \lim_{T\to\infty} F(T) = 2D_N = 2\int_0^\infty d\tau\, C_{zz}(\tau) = \lim_{\omega\to 0} S(\omega). \tag{1.3.13}$$

For the last equality, we have used that the correlation function is symmetric $C_{zz}(\tau) = C_{zz}(-\tau)$.

Besides the spike times t_i, the *interspike interval* (ISI)

$$T_i = t_{i+1} - t_i, \tag{1.3.14}$$

the times between two adjacent spikes, are often of interest. The indices are chosen so that the time between the first and the second spike corresponds to the first interval. Since we have assumed

---

[3] The numerator $\langle |\tilde{z}_T(\omega)|^2\rangle = \int_0^T\int_0^T dt_1 dt_2\, z(t_1)z(t_2)e^{i\omega(t_1-t_2)}$ contains the spike train at different times.

that spike times do not depend on absolute time, their differences do not depend on absolute time either. The sequence of ISIs

$$\dots, T_{i-1}, T_i, T_{i+1}, \dots \tag{1.3.15}$$

is a stationary sequence, and all intervals obey the same probability density function:

$$\lim_{\Delta t \to 0} \frac{\text{Prob}(T < T_i < T + \Delta t)}{\Delta t} = p_{\text{ISI}}(T). \tag{1.3.16}$$

We have defined a Poisson process by the statistical independence of the spike times. Similarly, a *renewal* point process can be defined by the statistical independence of the interspike intervals [45]. However, the assumption of statistical independence of interspike intervals is a much weaker constraint. For a renewal process, the joint probability for any number of intervals satisfies

$$p(T_i, T_j, T_k, \dots) = p_{\text{ISI}}(T_i) p_{\text{ISI}}(T_j) p_{\text{ISI}}(T_k) \dots . \tag{1.3.17}$$

In other words, the ISIs are independent and identically distributed and thus fully characterized by the marginal distribution or ISI density $p_{\text{ISI}}(T)$ (where we have omitted the i because all intervals are statistically identical). The moments of the ISIs are given by

$$\langle T^n \rangle = \int_0^\infty dT \, T^n p_{\text{ISI}}(T). \tag{1.3.18}$$

The mean $\langle T \rangle$ and the variance $\langle \Delta T^2 \rangle = \langle (T - \langle T \rangle)^2 \rangle$ can be used to determine the coefficient of variation (CV)

$$C_V(T) = \frac{\sqrt{\langle \Delta T^2 \rangle}}{\langle T \rangle}, \tag{1.3.19}$$

a dimensionless measure that compares the standard deviation to the mean of the ISI. The CV is informative about the irregularity of the underlying point process. If we associate regularity with how reliably the next spike time can be predicted based on the current spike time, then the most regular point process one can think of is given by the spike times generated by a deterministic oscillator. In this case, a spike time t_i allows all other spike times to be derived. The ISIs are delta distributed $p_{\text{ISI}}(T) = \delta(T - \langle T \rangle)$, their variance vanishes, and we obtain a CV that is zero. In that sense, the most irregular point process is given by the Poisson process. In this case, all spike times are statistically independent. The ISIs are exponentially distributed $p_{\text{ISI}}(T) = r_0 \exp(-r_0 T)$, mean and standard deviation are both given by $\langle T \rangle = \sqrt{\langle \Delta T^2 \rangle} = 1/r_0$ and the CV is equal to 1 [46].

In the renewal case, the ISI density and the spike-train power spectrum have a strikingly simple relation. To see this, we define the n-th order interval $T^{(n)} = t_{i+n} - t_i = \sum_{k=0}^{n-1} T_{i+k}$ and denote the probability density of the n-th order interval by $p_n(T)$. This allows us to express the function $m(\tau)$ that appears in the spike-train auto correlation function in terms of interval statistics as follows

$$m(\tau) = \sum_{n=1}^{\infty} p_n(\tau), \quad \tau > 0. \tag{1.3.20}$$

This is because $m(\tau)$ is the probability of finding *any* spike at time $t + \tau$ and $p_n(T)$ is the probability of finding the n-th spike after the reference spike at time τ. Put differently, summing the probabilities of finding the first, second, third, ...spike at time τ gives exactly the probability of finding *any* spike at time τ. Substituting Eq. 1.3.20 into Eq. 1.3.9, taking the Fourier transform, and evaluating the resulting sum [45, 69], yields

$$S_{\text{renew}}(\omega) = r_0 \frac{1 - |\tilde{p}_{\text{ISI}}(\omega)|^2}{|1 - \tilde{p}_{\text{ISI}}(\omega)|^2}. \tag{1.3.21}$$

where $\tilde{p}_{\mathrm{ISI}}(\omega)$ is the Fourier transform of the ISI density. The power spectrum also has two interesting limits that allow us to read off simple statistics of the spike train and interspike interval directly. First, in the high-frequency limit, the power spectrum saturates at the firing rate

$$\lim_{\omega\to\infty} S(\omega) = r_0, \tag{1.3.22}$$

a result that can be explained, for example, using the Wiener-Khinkchin theorem (Eq. 1.3.9), because at high frequencies the integral over positive and negative values of τ exactly cancels, except for the delta function $r_0\delta(\tau)$, which gives the firing rate. The low-frequency limit of the power spectrum is given by

$$\lim_{\omega\to 0} S_{\mathrm{renew}}(\omega) = r_0 C_V^2(T), \tag{1.3.23}$$

which can be derived from Eq. 1.3.21 by expanding the Fourier transform of the ISI density up to the second order and using $\partial_\omega^n \tilde{p}(\omega = 0) = i^n \langle T^n \rangle$.

So far, we have discussed *first-order* statistics derived from the ISI density $p_{\mathrm{ISI}}(T)$ because we have considered a renewal point process where the ISIs are statistically independent. For a nonrenewal process, the ISIs are no longer statistically independent, and we have to take into account *higher-order* statistics, generally the n-interval joint probability density

$$p(\underbrace{T_i, T_j, T_k, \ldots}_{n}). \tag{1.3.24}$$

In this thesis, we pursue a more modest goal and are mainly interested in *second-order* statistics associated with the density

$$p(T_i, T_{i+k}), \tag{1.3.25}$$

that characterizes the dependence of two intervals on each other. Note that we are still dealing with a stationary process, which means that the density does not explicitly depend on i but only on the lag between the two intervals k (similar to the fact that the spike-train auto-correlation function Eq. 1.3.6 does only depend on the time difference τ). From Eq. 1.3.25, one can derive the second-order moment

$$\langle T_i T_{i+k} \rangle = \int_0^\infty \int_0^\infty dT_{i+k} dT_i\, T_{i+k}, T_i p(T_i, T_{i+k}), \tag{1.3.26}$$

and the so-called covariance

$$\langle \Delta T_i \Delta T_{i+k} \rangle = \langle (T_i - \langle T \rangle)(T_{i+k} - \langle T \rangle) \rangle, \tag{1.3.27}$$

a measure that indicates whether two intervals, on average, deviate similarly from the mean. Usually, one considers a linear, dimensionless version of the covariance, the so-called serial correlation coefficient (SCC) [46]

$$\rho_k = \frac{\langle \Delta T_i \Delta T_{i+k} \rangle}{\langle \Delta T^2 \rangle}, \tag{1.3.28}$$

that compares the covariance to the variance and ranges between $-1 < \rho_k < 1$. The SCC is a linear measure in the sense that the conditional mean $\langle \Delta T_{i+k} | \Delta T_i \rangle \approx \rho_k \Delta T_i$ [4] is assumed to depend linearly on ΔT_i. What exactly can we learn from the SCC? To answer this question, we consider - without loss of generality - two adjacent intervals T_i, T_{i+1} and their respective deviations from the mean ΔT_i, ΔT_{i+1}. If, on average, these two intervals deviate similarly from the mean, i.e., if both intervals are on average longer (or shorter) than the mean, then the signs of the two deviations agree, and the SCC is positive ($\rho_1 > 0$). In this case, the intervals are said to be correlated. In the opposite case, if a long interval is usually followed by a short interval (or vice versa), then the signs of the deviations differ, and the SCC is negative ($\rho_1 < 0$). In this case, the intervals are said to be anticorrelated. Finally, if the SCC vanishes ($\rho_1 = 0$), the intervals are said to be uncorrelated.

---

[4] The notation $\langle x|y \rangle = \int dx\, x p(x|y)$ refers to the conditional mean of x given y, where $p(x|y) = p(x,y)/p(y)$ is the conditional probability.

The SCC is certainly an interesting statistic on its own. It describes the linear dependence between two intervals, only present if the spike-generating process is sufficiently complex. Apart from this, the SCC is also reflected in other statistics, such as the low-frequency limit of the power spectrum [56]

$$\lim_{\omega \to 0} S(\omega) = r_0 C_V^2(T)(1 + 2\sum_{k=1}^{\infty} \rho_k). \tag{1.3.29}$$

This is important because the power spectrum of the spontaneous (no stimulus) spike train serves as a background spectrum if additional stimuli are applied. A reduction due to negative ISI correlations can thus improve the signal-to-noise ratio for slow signals [70, 71]. According to Eq. 1.3.13, the asymptotic Fano factor is also affected by the sum of the SCCs

$$\lim_{T \to \infty} F(T) = C_V^2(T)(1 + 2\sum_{k} \rho_k). \tag{1.3.30}$$

This measure indicates how broadly the spike count is distributed and can improve the detection of a weak signal by influencing how confidently a shift in the mean of this distribution can be attributed to an actual stimulus [72, 73].

1.4 Organization of the thesis

So far, we have introduced a number of stochastic processes that are important in describing spike generation. We have seen that ion channel activity, which regulates the ion currents responsible for spike formation, is typically described by Markov chains with a discrete state space. Conversely, the dynamics of the spiking variable, be it the membrane potential or the intracellular Ca^{2+}, often results from the activity of a large number of (different) ion channels and forms a continuous random process that can be described by a Langevin equation. Finally, the sequence of spike times itself can be understood as a stochastic point process.

In Chap. 2, we are concerned with nonrenewal spike generation in neural signaling. In particular, we are interested in a situation where two slow processes interact and influence spike generation. To study this situation, we consider a multidimensional integrate-and-fire model endowed with a self-inhibitory adaptation current and subject to a temporally correlated noise. The dependence between intervals can be measured by the serial correlation coefficient introduced in the following section. To compute the SCC in this case, we generalize the weak-noise theory of Schwalger and Lindner [74] to account for both correlation-inducing processes. We will show that the interval correlations observed in this situation are given by a weighted sum of the correlation coefficients that would be obtained by considering only one correlation-inducing process at a time. Although the theory is limited to mean-driven neuron models, it allows us to predict the correlation coefficient in various interesting situations, such as when the subthreshold dynamics of the membrane potential is a simple integration process or a more complex oscillatory process. Furthermore, different exponentially correlated noise processes can be considered. This includes cases where the noise and the adaptation originate from a common source or where the noise is generated by a recurrent network in the asynchronous irregular state. Finally, we show that although the theory is developed for the integrate-and-fire framework, we can predict the SCC for the conductance-based Traub-Miles model with a slow M-type current.

In Chap. 3, we are concerned with nonrenewal spike generation in Ca^{2+} signaling. In this case, the spiking variable is not the membrane potential but the (free) intracellular or cytosolic Ca^{2+} concentration. Another difference from spike generation in neurons is that Ca^{2+} does not enter the cell from the extracellular medium, but is released from an intracellular store, the endoplasmic reticulum. Neuronal and Ca^{2+} spiking are similar in that the generation of spikes is a random process that involves a strong positive feedback, and the length of intervals between spikes increases systematically during an initial transient. To capture Ca^{2+} spike generation, we formulate a two-component model that describes the stochastic gating of the Ca^{2+}-releasing channels in the ER membrane by a Markov model and the dynamics of the Ca^{2+} concentration in the cytosol and ER by an integrate-and-fire model. For this model, interspike interval statistics are difficult to calculate because the Ca^{2+} current through the corresponding channels is a complicated stochastic process. However, based on the observed timescale separation, this Ca^{2+} current can be substituted by a Gaussian white noise, for which we show that the Ca^{2+}-dependent mean and the Ca^{2+}-dependent noise intensity can be calculated analytically. This allows the formulation of a Langevin equation and the calculation of the interspike intervals statistics through the Fokker-Planck equation. We then turn to the influence of the Ca^{2+} concentration in the ER on spike formation. Since some of the Ca^{2+} released from the ER during the spike is lost to the extracellular medium and the ER is slowly replenished, we follow the idea that cumulative depletion of the ER is responsible for the observed transient. We investigate the effect of such a slow variable on the spike generation and, among others, derive expressions for the length of the transient and for the strength of the adaptation of the interspike intervals. We relate these transient statistics to the observed interval correlations discussed in detail in Chap. 2 and test whether the correlations predicted by the model are confirmed in the experiment.

Chapter 2

Nonrenewal spiking in neural signaling

2.1 Introduction

Neurons are electrically excitable cells and the elementary processing units of the brain. They are interconnected to one another and communicated through short electric pulses, so-called action potentials or spikes. A neuron can roughly be divided into three functionally different parts. The dendrite that accumulates the arriving input from other neurons, the cell body or soma that performs a nonlinear operation on the input and initiates the action potentials, and the axon that transmits the action potential to the dendrites of other neurons. The junction between two neurons is called the synapse. The most common type of synapse is the chemical synapse, which is not directly connected, but transmits the action potential from the pre- to the postsynaptic neuron by releasing neurotransmitters into the synaptic cleft. At the postsynaptic site, these transmitters bind to specific receptors, causing an influx of positively or negatively charged ions from the extracellular medium into the postsynaptic cell and an excitatory or inhibitory postsynaptic potential, respectively. A typical neuron in the cortex connects to more than 10.000 other neurons [13]. A Purkinje cell in the cerebellum may even receive up to 150.000 synaptic contacts [14].

To understand how the brain processes information, one must first understand the elementary processing unit. The neuron itself is a complex system that sums or integrates incoming spikes until a certain threshold is reached, and in turn, another spike is fired. The stereotyped spike is formed by the interaction of multiple nonlinear voltage-dependent ion currents: Neurons, like other cells, are surrounded by a plasma membrane (PM) that separates the inside of the cell from the extracellular medium. Ion pumps maintain concentration gradients of different ions and establish an electrical potential across the PM of about $-70\,\mathrm{mV}$ [9, 15]. When the neuron is stimulated, and the membrane potential is depolarized above a certain threshold, a positive feedback mechanism mediated by sodium (Na^+) channels initiates the spike and raises the membrane well above the firing threshold. After the spike, the neuron is first repolarized by the efflux of potassium (K^+), and then the concentration gradient is restored by Na^+-K^+ pumps.

Hodgkin and Huxley [16] were the first to measure these currents and describe the dynamics of the membrane potential in terms of differential equations. Models that follow the approach of Hodgkin and Huxley and capture the spike generation in terms of ion channels with voltage-dependent conductance are called *conductance-based* models [9, 13, 37]. These models provide a detailed biophysical description but are high-dimensional, nonlinear, and thus difficult to treat analytically. Moreover, and contrary to Hodgkin and Huxley's description, generating an action potential is a stochastic process [33, 34]. There are several reasons for this. One is the probabilistic gating of ion channels. This leads to a stochastic ion current in a finite population of channels (channel noise). A second reason is that transmitting action potentials across the synapse is unreliable. Even if the transmission was reliable, the sheer number of arriving excitatory and inhibitory inputs in a recurrent network constitutes a quasi-random input current (network noise). All these processes lead to fluctuation in the membrane potential, and a comprehensive understanding of neural activity must account for these fluctuations by formulating stochastic models.

Integrate-and-fire models [38, 39] are particularly useful in this regard, as they are often analytically tractable even in the stochastic case and allow insights into the interaction of noise, signal, and nonlinear neural dynamics. These models take advantage of the fact that the stereotypical action potential cannot contribute to the transmission of information. Therefore, it is not necessary to model the complex processes that shape the action potential. Instead, the membrane potential is reset whenever it exceeds a certain threshold, and a spike is said to be fired. Despite their simplistic approach, such models can reproduce the spike times of real neurons surprisingly well [42–44].

A common simplification in the study of neural activity lies in the assumption that ISIs are statistically independent [33, 62]. This implies that the fluctuations are assumed to be fast (uncorrelated) and that no other slow processes affect the spike generation. Renewal models are well understood [45] and allow for a far-reaching theory of recurrent networks [75, 76]. In a stochastic IF model, such a renewal spike train is generated when the noise is uncorrelated, and all variables are reset after each spike (the state of the model is "renewed"). This simplification is not specific to IF models; the Hodgkin-Huxley model driven by Gaussian white noise also generates a quasi-renewal process [3]. However, interval correlations are often observed experimentally [72, 73, 77–84]. The SCC introduced in Eq. 1.3.28 provides a measure to quantify such correlations. The causes of interval correlations are manifold. Positive correlations can be caused by slow channel gating [85, 86], synaptic filtering [87, 88], or slow network processes [89–91]. In these cases, the fluctuations in the membrane potential are no longer fast but temporally correlated. A prominent mechanism exhibited by many neurons and associated with negative interval correlations is the fatigue of a neuron after repeated firing. This phenomenon is known as spike-frequency adaptation and is manifested by a gradual decrease in the firing rate after an initial increase in response to the onset of a constant stimulus. Adaptation currents include Ca^{2+}-gated K^{+} currents, M-type currents, and the slow recovery of Na^{+} channels [18]. Such correlations play an important role in transmitting slow signals or detecting weak signals as they are reflected in the low-frequency limit of the power spectrum (Eq. 1.3.29) and the asymptotic Fano factor (Eq. 1.3.30).

While the effects of a correlated noise [66, 92–95] and a slow adaptation current [40, 74, 96, 97] on the ISI correlations have been studied separately, a more general theory that predicts the SCC in the presence of both these processes is lacking. In this chapter, we extend the theory developed by Schwalger and Lindner [74], which allows us to describe interval correlations in weakly perturbed mean-driven neuron models with a spike-triggered adaptation current, to account for an additional correlated noise process [1]. To the best of our knowledge, we provide the first theoretical study of interval correlations in the presence of multiple correlation-inducing processes. We address the question of what patterns of interval correlations can be expected in this case and how they relate not only to the adaptation and correlated noise but also to the internal dynamics of the neural system. Since the theory assumes that the neuron is mean-driven and weakly perturbed, it mainly applies to neurons in the sensory periphery.

This chapter is organized as follows: In Sec. 2.2, we introduce a number of neuron models. We start with conductance-based models, which are a prime example of an excitable system. We then turn to more phenomenological IF models, which are the working models of this chapter. We have already pointed out that despite their phenomenological approach, such models have been shown to mimic the response of cortical neurons with remarkable accuracy [42–44]. At the same time, IF models remain analytically tractable, even when spike generation is a nonrenewal process [40, 66, 74, 92–97]. However, even within the IF framework, this case is analytically challenging. Therefore, in Sec. 2.3, we introduce the phase reduction method, which projects a higher-dimensional limit cycle oscillator onto a one-dimensional phase variable. This reduced phase description allows to calculate the SCC for various integrate-and-fire models as long as the phase response curve (PRC) is analytically accessible. We show that this is generally the case for linear models and that some general statements can still be made about nonlinear models as long as they are one-dimensional. In Sec. 2.4, we calculate the SCC for a stochastic multidimensional IF model with a spike-triggered adaptation current and a correlated noise using the phase response curve. As an instructive example of the method, in Sec. 2.4.1, we first calculate the SCC for a multidimensional IF model driven by correlated and uncorrelated noise sources, but without a spike-triggered adaptation. In this case, the SCC can be related to the correlation functions or power spectra of the two noise sources. The derivation of the SCC for the full model is presented in Sec. 2.4.2. We then discuss the patterns of interval correlations in a number of special cases. We start with the leaky and generalized IF models with spike-triggered adaptation and correlated noise in Sec. 2.4.3 and Sec. 2.4.4. These two models have qualitatively different PRCs, resulting in different response characteristics. In Sec. 2.4.5, we then consider a scenario in which we assume that both the correlated noise and the adaptation arise from a finite population of slow ion channels and ask how the correlation coefficient depends on the common timescale of the two processes. In Sec. 2.4.6, we consider a noise process with reduced power at low frequencies, as it can result from a recurrent neural network. In this case, the noise itself can lead to negative interval correlations. We then test the range of validity of the theory in Sec. 2.4.7. It turns out that even if the SCC cannot be described quantitatively, the qualitative behavior is still captured by the theory. Finally, in Sec. 2.4.8, we show that the theory captures the SCC well even for the conductance-based Traub-Miles model with a slow M-type current.

2.2 Modeling neural dynamics

In this section, we give a brief overview of the modeling approaches to describe neural dynamics. First, we present a selection of point-neuron models. These models neglect the spatial extent of the neuron. We start with conductance-based models, which include the classical Hodgkin-Huxley model. We then consider the class of integrate-and-fire models, which are phenomenological in their description but not completely disconnected from conductance-based models. IF models have the advantage of being analytically tractable, even in the stochastic case. The description becomes more complicated when processes are considered that contribute to the generation of neuronal spikes being a nonrenewal process. The mathematical formulation of such processes eventually leads to the model for which we calculate the serial correlation coefficient in Sec. 2.4.

2.2.1 Conductance-based models

Biophysically, the generation of an action potential is the result of different ion currents that permeate the cell membrane through ion channels. In 1952 Hodgkin and Huxley [16] were the first to successfully measure these currents in the giant axon of the squid and to formulate a system of ordinary differential equations that capture the generation of an action potential.

The Hodgkin-Huxley (HH) model describes the dynamics of the membrane potential/voltage during an action potential by three ion currents [9, 13, 37]

$$C_m \dot{V} = -\underbrace{g_{\mathrm{L}}(V - E_{\mathrm{L}})}_{I_{\mathrm{L}}} - \underbrace{g_{\mathrm{Na}} m^3 h (V - E_{\mathrm{Na}})}_{I_{\mathrm{Na}}} - \underbrace{g_{\mathrm{K}} n^4 (V - E_{\mathrm{K}})}_{I_{\mathrm{K}}} + I(t), \tag{2.2.1}$$

namely a leak, sodium, and potassium current I_{L}, I_{Na}, and I_{K}, respectively. We also consider an arbitrary input current $I(t)$, which can represent different stimuli or the input received by a neuron in a recurrent neural network. The leak, sodium, and potassium currents are determined by a reversal potential E_{x} and a maximum conductance g_{x}. In addition, the sodium and potassium currents depend on the so-called gating variables n, m, and h that are themselves dynamical variables, governed by

$$\tau_x(V)\dot{x} = -x + x_\infty(V), \quad x = n, m, h. \tag{2.2.2}$$

In other words, for a clamped voltage, the gating variables approach their steady-state value $x_\infty(V)$ exponentially with a time constant $\tau_x(V)$. The voltage dependence of the steady state values and time constants is illustrated in Fig. 2.1. The stationary values are bound between zero and one. This is because the gating variables are associated with the fraction of open channels. To see this we reformulate Eq. 2.2.2 as follows

$$\dot{x} = \alpha_x(V)(1 - x) - \beta_x(V)x, \quad x = n, m, h, \tag{2.2.3}$$

where we have used $\tau_x(V) = 1/(\alpha_x(V) + \beta_x(V))$ and $x_\infty(V) = \alpha_x(V)/(\alpha_x(V) + \beta_x(V))$. Eq. 2.2.3 can be interpreted as the thermodynamic limit of a large number of two-state systems as described in Sec. 1.2 with (voltage-dependent) transition rates $\alpha_x(V)$ and $\beta_x(V)$

$$\text{open} \underset{\alpha_x(V)}{\overset{\beta_x(V)}{\rightleftharpoons}} \text{close}, \tag{2.2.4}$$

where the variable x represents the fraction of the two-state systems in one specific state (the fraction in the other state is given by $1 - x$). Consequently, n, m, and h cannot fall below zero nor exceed one. In Eq. 2.2.1, the ion currents do not depend linearly on the gating variables and

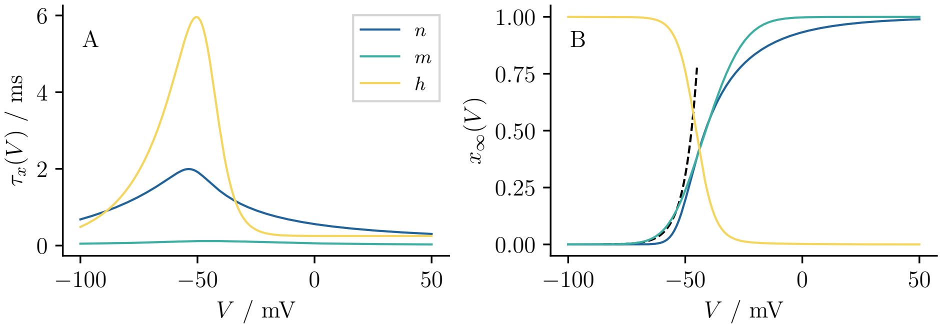

FIGURE 2.1: Panel A and B show the time constants $\tau_x(V)$ and steady-state values $x_\infty(V)$ for the three gating variables n, m, and h as functions of the voltage V, respectively. The dashed line shows an approximation of $m_\infty(V)$ near the resting potential $V_0 \approx -65\,\text{mV}$ by an exponential function $\Delta_T \exp[(v - \hat{v}_T)\Delta T]$. Parameters are according to Table 2.1.

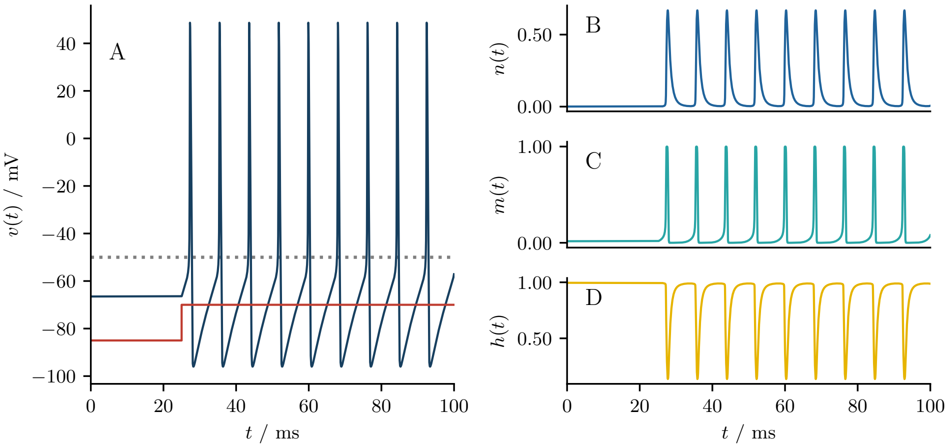

FIGURE 2.2: Panel A shows the voltage trajectory $v(t)$ (blue line) in response to a constant current stimulation $I(t) = 5\,\text{pA}$ applied at 25 ms (red line). Before applying the current, the voltage at rest is about $V_0 \approx -65\,\text{mV}$. After applying the current, the model repeatedly fires an action potential, i.e., the voltage rapidly rises and falls. Panel B, C, and D show the trajectory of the three gating variables $n(t)$, $m(t)$, and $h(t)$, respectively. Parameters are according to Table 2.1.

thus cannot be readily interpreted as the fraction of channels in the open state. For example, the potassium current $I_\text{K} = g_\text{K} n^4 (V - E_\text{K})$ depends on n^4. Instead, the interpretation is usually that the potassium channel has four identical but independent subunits that must all be in one (of two) conformational state for the entire channel to open. The gating variable n is then interpreted as the probability of a single subunit being in the desired state so that for four independent subunits, the probability is n^4. For the sodium current $I_\text{Na} = g_\text{Na} m^3 h (V - E_\text{Na})$ the interpretation is similar, again the channel state is determined by four independent but non-identical subunits, three of which are described by the gating variable m and one by the gating variable h. In addition, the two gating variables behave differently; while m increases, h decreases with voltage V. The result is a low sodium current at both small and large voltages and only significantly different from zero at intermediate voltage values - an important feature in the generation of action potentials.

The dynamics of the full system governed by Eq. 2.2.1 with parameters according to Table 2.1 as suggested by Traub and Miles [98] (also known as the Traub-Miles model) in response to a constant current $I(t) = 5\,\text{pA}$ stimulation applied at 25 ms are shown in Fig. 2.2. Before the stimulation, the membrane potential and gating variables rest at a stable fixed point. When the stimulation is applied, the fixed point loses its stability, and a stable limit cycle emerges. While the full four-dimensional phase space cannot be displayed, it is evident that the system possesses a period solution characterized by a repeated sharp rise and fall of the voltage that constitutes the

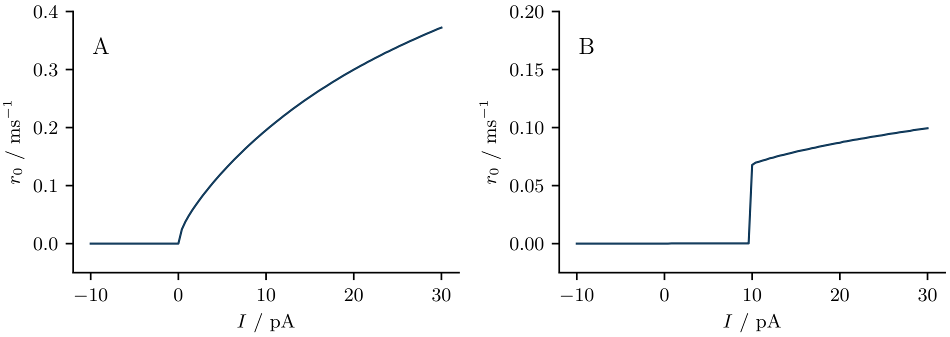

FIGURE 2.3: The firing rate r_0 in response to a constant current stimulation I (f-I curve) for two different sets of parameters according to Table 2.1 (A) and Table 2.2 (B). In panel A, the f-I curve is a continuous function of the input current so that the Traub-Miles model is of class I. In panel B, the f-I curve is a discontinuous function, i.e., the classical Hodgkin-Huxley model is of class II.

spike. An important related measure is the spike time t_i, which can be defined as the time at which a certain voltage threshold is exceeded, for example $-50\,\mathrm{mV}$ (dotted line in Fig. 2.2A). This allows us to define the firing rate r_0, either by the average number of spikes per unit time or, in this case, simply by the inverse of the time between two adjacent spikes $r_0 = 1/(t_{i+1} - t_i)$. Since we are dealing with a deterministic model, the time between two spikes (after any transition) is always given by the period T^* of the limit cycle.

The firing rate r_0 as a function of a constant input current I is referred to as the f-I curve (where f stands for the firing *frequency*). Generally, below some critical input current - the rheobase - no spikes are observed, and the firing rate is zero. This corresponds to the existence of a stable fixed point for the dynamical system. At the rheobase a bifurcation occurs. For currents above the rheobase, a limit cycle emerges, spikes are periodically emitted, and the firing rate attains a finite value. Interestingly, depending on the choice of parameters for the conductance-based model, the f-I curve at the rheobase can be continuous as in Fig. 2.3A or discontinuous as in Fig. 2.3B. Neuron models with a continuous f-I curve are called class I [99]. A continuous spike onset can occur through a saddle-node on the limit cycle bifurcation, in which case the model is also referred to as Type I. This is because a trajectory on the limit cycle can be arbitrarily slow in the vicinity of the ghost of the fixed point (depending on how far we are from the bifurcation). The result is an arbitrarily long period of the limit cycle and an arbitrarily low firing rate. Neurons with a discontinuous f-I curve are called class II and require a spike onset via a Hopf bifurcation or similar, where the oscillatory behavior is already present before the bifurcation takes place, but the amplitude of the oscillation needs to build up. If the spike onset occurs via a Hopf bifurcation or similar, the model is also called Type II. We will see in Sec. 2.3 that the distinction between Type I and Type II neurons, based on the bifurcation, is relevant for the response characteristics of a neuron model.

So far, we have applied a constant current to the Traub-Miles model, resulting in a periodic solution with an always identical spike shape. This is not surprising since the r.h.s. of Eq. 2.2.1 did not change. Of course, it is well known that the stereotypical shape of the action potential is not due to the constant input current but is a property of neuronal spiking. To illustrate this, we prepare the Traub-Miles model at its resting state and apply three current pulses with varying amplitude (in three different simulations), as shown in Fig. 2.4A. The first stimulation is subcritical and does not trigger a spike; the next two are supercritical and trigger two identical spikes. Such a behavior is a well-known feature of an *excitable system*, where a sufficiently strong stimulation pushes the system out of the resting state over a quasi-separatrix, leading to a large detour in the phase space (the spike) before the system returns to the resting state [100]. Additionally, before the model has fully returned to its resting state, it is often insensitive to a second stimulation. This is illustrated in Fig. 2.4B. Again, we prepare the Traub-Miles model in the resting state and apply a supercritical current stimulation that triggers a spike. We then apply the same stimulation again and observe that the second response depends on the time elapsed since the first stimulation. For the black line in Fig. 2.4B, only 10 ms elapsed between the end of the first and the beginning of

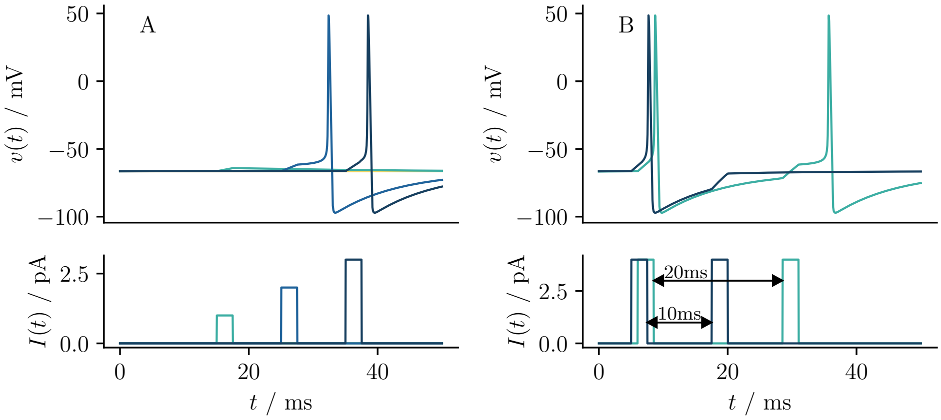

FIGURE 2.4: Panel A shows the response of the Traub-Miles model to three different short current pulses with increasing amplitude. The first pulse (cyan) is subcritical and does not trigger a spike. The other two pulses (blue and black) are supercritical and do trigger a stereotypical spike. Panel B shows the response of the Traub-Miles model to two supercritical current pulses, the second occurring 10 ms and 20 ms, respectively, after the end of the first. In the first case, no second spike is triggered because the model is in a refractory state. If the second pulse is applied later, a spike can be triggered again.

TABLE 2.1: **Simulation parameters for the Traub-Miles model [98, 101]**

Parameter	Value	Parameter	Value
g_{Na} [nS]	100	$a_h(V)$	$0.128\exp\left(-\frac{V+50}{18}\right)$
g_{L} [nS]	0.1	$a_m(V)$	$0.32\frac{V+54}{1-\exp\left(-\frac{V+54}{4}\right)}$
g_{K} [nS]	80	$a_n(V)$	$0.032\frac{V+52}{1-\exp\left(-\frac{V+52}{5}\right)}$
E_{Na} [mV]	50	$b_h(V)$	$\frac{4}{1+\exp\left(-\frac{V+27}{5}\right)}$
E_{L} [mV]	-67	$b_m(V)$	$0.28\frac{V+27}{\exp\left(\frac{V+27}{5}\right)-1}$
E_{K} [mV]	-100	$b_n(V)$	$0.5\exp\left(-\frac{V+57}{40}\right)$

the second stimulation. No second spike is observed. This changes if the period between the two stimulations is increased to 20 ms as for the cyan line in Fig. 2.4B, in which case we do observe a second spike. Hence, we see two core features of an excitable system. First, it produces a stereotypical response to a supercritical stimulation - the action potential has a stereotypical shape - and second, it possesses a certain refractory period during which no second response can be triggered - two action potentials do not overlap. We will return to these two properties to motivate reduced phenomenological neuron models.

2.2.2 Neural noise

A feature of neural spiking we have neglected completely so far is its strong random component. This becomes apparent when a neuron is repeatedly driven by the same time-dependent stimulus [102, 103], but also when a neuron is subject to a constant stimulation that does not vary in time [104]. In both cases, the neural response is subject to a large trial-to-trial variability that cannot be attributed to the stimulus. Another indication of neural noise is the so-called spontaneous activity, i.e., the firing of a spike in the absence of any stimulus [105]. Both neural variability and spontaneous activity indicate the presence of noise in the neural system.

The most prominent sources of neural variability are thermal, channel, and synaptic noise [34], which contribute to different extents depending on the context. Arguably the smallest noise

TABLE 2.2: **Simulation parameters for the Hodgkin-Huxley model [16]**

Parameter	Value	Parameter	Value
g_{Na} [nS]	120	$a_h(V)$	$0.07\exp(-0.05V)$
g_{L} [nS]	0.3	$a_m(V)$	$\frac{0.1(V-25)}{1-\exp(-0.1(V-25))}$
g_{K} [nS]	36	$a_n(V)$	$\frac{0.01(V-10)}{1-\exp(-0.1(V-10))}$
E_{Na} [mV]	115	$b_h(V)$	$\frac{1}{1+\exp(-0.1(V-30))}$
E_{L} [mV]	10.6	$b_m(V)$	$4\exp(-0.1V)$
E_{K} [mV]	-12	$b_n(V)$	$0.125\exp(-0.0125V)$

source is thermal noise, which is due to the random motion of molecules and leads to small fluctuations in the membrane potential. While these fluctuations do not directly play a significant role in the dynamics of the membrane potential, thermal noise also leads to the random opening and closing of individual ion channels and thus indirectly influences the voltage dynamics. The resulting fluctuations in the membrane potential are referred to as channel noise, and their relative amplitude decreases as the population of ion channels increases but remains finite as long as the population is finite. This is the main source of cell-intrinsic noise and is particularly important in peripheral neurons [17]. The situation is different when we consider neurons in a recurrent neural network, which are subject to a large number of excitatory and inhibitory synaptic inputs. For example, a pyramidal cell in the neocortex can receive between 5000 and 60.000 synapses from the same or different cortical regions [106]. In this case, the main source of noise is not cell-intrinsic but stems from the synaptic bombardment [107], which appears random due to the sheer number of inputs. Moreover, the transmission of spikes across synapses is itself an unreliable process, subject to fluctuations due to the stochastic release of neurotransmitters [108].

Regardless of the dominant noise source, generating an action potential is a stochastic process, and neither the spontaneous activity nor the response to a signal can be understood without taking these fluctuations into account. Therefore, studying neural dynamics in terms of stochastic models is essential.

2.2.3 Stochastic leaky integrate-and-fire model

We have seen that conductance-based models can describe the generation and capture the shape of the action potential. While these models paint a biophysically detailed picture, they have the disadvantage of being high-dimensional, nonlinear, and thus difficult to treat analytically. These problems become even more severe when stochastic versions of these models are considered. A common simplification in the description of neural spike generation is based on the realization that a spike often i) has a stereotypical shape and ii) is reliably emitted when the voltage exceeds a certain threshold. It is therefore concluded that i) the timing of the spike is more important than its shape, and ii) it is sufficient to consider the dynamics up to the threshold that led to the specific spike time. This motivates the integrate-and-fire model, where the voltage dynamics is considered only up to a certain threshold, and the spike is replaced by a fire-and-reset rule [38, 39].

The motivation presented here somewhat distorts the historical facts because already 45 years before Hodgkin and Huxley presented their famous model, it was Lapicque who formulated the first integrate-and-fire model in 1907 [109, 110]; he modeled a neuron by a parallel circuit consisting of a capacitor and a resistor and postulated that whenever the capacitor was sufficiently charged, a spike would be emitted and the capacitor would be discharged. This corresponds to what is now known as the leaky integrate-and-fire (LIF) model, where the voltage across the capacitor represents the membrane potential, and the additional resistance gives rise to a leak current. However, this is not the only way to "derive" the LIF model. We can also return to Eq. 2.2.1 and assume that below the firing threshold, the membrane is passive, i.e., the dynamics of the gating variables are independent of the voltage V. Under this assumption, the dynamics

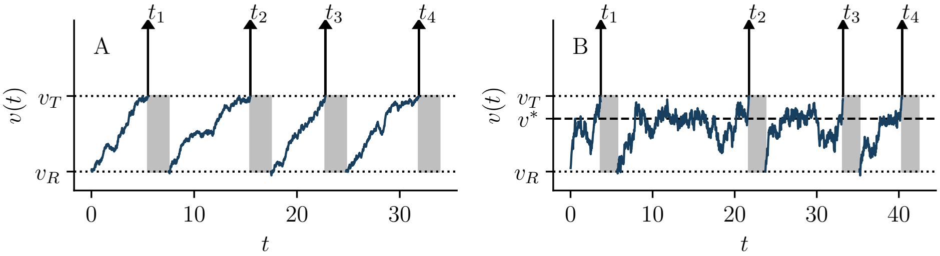

FIGURE 2.5: Illustration of a stochastic leaky integrate-and-fire model Eq. 2.2.6. The voltage is initiated at its reset value v_R (lower dotted line) and increases towards the threshold v_T (upper dotted line). Upon hitting the threshold (upper dotted line), i.e., if $v(t) > v_T$, a spike is emitted at time $t_i = t$. This is followed by a refractory period (gray area), after which the voltage-like variable is reset to v_R. In panel A, the model is mean-driven. In panel B, the model is excitable with fixed point v^* between reset and threshold (dashed line). Parameters: $v_R = 0$, $v_T = 1$, $\tau_{\text{ref}} = 2$, A: $\mu = 0.2$, $\gamma = 0.1$, $D = 0.05$, B: $\mu = 0.7$, $\gamma = 1.0$, $D = 0.3$

can be simplified as follows

$$C_m \dot{V} = -g_0(V - E_0) + I(t), \tag{2.2.5}$$

where g_0 is an effective conductance and E_0 is the resting potential. Let us further assume that the current $I(t) = I_0 + \sqrt{2\hat{D}}\xi_v(t)$ consists of a deterministic mean I_0 and a stochastic part that can be approximated by a Gaussian white noise $\xi_v(t)$ with intensity $\hat{D}$ and autocorrelation function $\langle \xi_v(t)\xi_v(t')\rangle = \delta(t - t')$. We will return to the exact meaning of this approximation in the third chapter of this thesis. For now, let us take it for granted and think of $I(t)$ as the current resulting from synaptic bombardment or the stochastic opening and closing of a population of ion channels. In both cases, given a sufficiently large number of arriving postsynaptic potentials or transitions of channel states, the current $I(t)$ over a small time bin will be the sum of small stochastic currents and, according to the central limit theorem, will be Gaussian distributed. If the stochastic part of $I(t)$ additionally changes fast compared to the dynamics of the membrane potential, it can be approximated by a white (delta correlated) noise, $\langle \xi_v(t)\xi_v(t')\rangle = \delta(t - t')$. Endowing Eq. 2.2.5 with an additional fire-and-reset rule and rescaling the variables and parameters leads to the (stochastic) LIF model in the form we will use throughout this thesis:

$$\begin{aligned} &\dot{v} = -\gamma v + \mu + \sqrt{2D}\xi_v(t), \\ &\text{if } v(t) = v_T \to t_i = t,\ v(t + \tau_{\text{ref}}) = v_R. \end{aligned} \tag{2.2.6}$$

Here $v = V - E_0$ is the shifted voltage with resting potential at $v = 0$, $\gamma = g_0/C_m$ is the inverse membrane time constant $\tau_m = 1/\gamma$, $\mu = I_0/C_m$ is a constant input current relative to the membrane capacitance, $D = \hat{D}/C_m^2$ is the rescaled noise intensity and τ_{ref} is the refractory period that can be associated with the duration of the spike. We stress again that this model consists of two independent parts, first the subthreshold dynamics, here determined by the parameters μ, γ, and D, and secondly, the fire-and-reset rule, i.e., whenever the voltage v exceeds the threshold v_T a delta spike $\delta(t - t_i)$ is said to be fired at the spike time t_i and the voltage is reset to v_R after some refractory period τ_{ref}. The sum of all the delta spikes defines the *spike train* $z(t) = \sum_i \delta(t - t_i)$, which is the most important output of an IF model. For example, an ensemble average of the spike trains provides the instantaneous firing rate $r(t) = \langle z(t)\rangle$. Stochastic integrate-and-fire models have been studied extensively in the computational neuroscience literature [33, 62, 111–113] and the noise is in general not limited to be Gaussian distributed or delta correlated [95, 114, 115].

In Fig. 2.5A and B, we show an exemplary realization of Eq. 2.2.6. In both cases, the voltage starts at the reset value $v(0) = v_R$ and increases over time. At the spike time $t = t_1$, the voltage crosses the threshold for the first time, and a delta spike is fired (indicated by an arrow). After a certain refractory period (gray area), the voltage is reset to v_R, and the cycle starts anew until a second spike is emitted at spike time t_2, and the voltage is reset again, and so on. The difference between Fig. 2.5A and B concerns the existence of a fixed point v^* between reset and threshold for the corresponding deterministic system (obtained by setting $D = 0$ in Eq. 2.2.6). Recall that at the fixed point, the voltage of the deterministic system does not change $\dot{v}(v^*) = -\gamma v^* + \mu = 0$, which implies $v^* = \mu/\gamma$. In Fig. 2.5A, these two parameters are chosen so that the fixed point lies beyond the firing threshold $v^* > v_T$, and the model reaches the threshold and fires periodically even in the absence of noise. This is referred to as the *mean-driven* regime, which is usually associated with a rather regular spike emission. In contrast, in Fig. 2.5B, the fixed point is below the firing threshold $v^* < v_T$ (but above the reset value), so no spiking would be observed for the deterministic system. However, for the stochastic system, the voltage will occasionally exceed the threshold due to the fluctuation of the voltage. This is referred to as the fluctuation-driven or *excitable* regime and is associated with a more irregular spike emission. It should be noted that even in the excitable regime, spikes can occur periodically if the difference between the threshold and fixed point $\Delta v = v_T - v^*$ and the noise intensity D are chosen just right, an effect known as coherence resonance [100, 116].

2.2.4 Integrator and resonator models

So far, we have introduced the LIF model - a linear, one-dimensional model that generates a renewal point process. However, IF models are neither limited to being linear [113, 117–119] nor one-dimensional [120–122] and can be formulated more generally as follows:

$$\begin{aligned} \dot{v} &= f_0(v, \mathbf{w}) + \mu + \sqrt{2D}\xi_v(t), \\ \dot{w}_j &= f_j(v, \mathbf{w}), \\ &\text{if } v(t) = v_T \to t_i = t,\, v(t) = v_R,\, \mathbf{w}(t) = \mathbf{w}_R. \end{aligned} \tag{2.2.7}$$

Here, $\mathbf{w}$ are auxiliary variables that are also reset upon spiking, and $f_0(v, \mathbf{w})$ and $f_j(v, \mathbf{w})$ are the generalized drift functions for the voltage and auxiliary variables, respectively. (Note that we have set the refractory period to zero, $\tau_{\text{ref}} = 0$, and will continue to do so from here on.) Because all variables are reset at spikes, and the noise is uncorrelated, such a model will always generate a renewal point process. Here, we introduce two well-known IF models, one that is one-dimensional but nonlinear and another that is two-dimensional but again linear. Specifically, we are interested in the firing rate response of these models and the distinction between class I and class II neuron models based on the f-I curve. We will see that one-dimensional IF models are always class I and that only the introduction of a second variable leads to an IF model that can mimic the firing rate response of a class II neuron. Since this distinction is only meaningful in the deterministic limit, we will, for now, return to the case where $D = 0$.

First, let us briefly recall the LIF model with the linear drift function

$$f_0(v) = -\gamma v, \tag{2.2.8}$$

shown in Fig. 2.6A$_1$. The model is in the excitable regime if the function $f_0(v) + \mu$ has a zero (cyan line) and, thus, a fixed point (black dot) below the firing threshold. In the mean-driven regime, the drift decreases with increasing voltage but has no zero below the threshold (blue line). The transition between these two regimes occurs when the fixed point $v^* = \mu/\gamma$ is pushed above the threshold by increasing the input μ. This results in a continuous f-I curve (see Fig. 2.6A$_2$) because depending on μ, the dynamics can become arbitrarily slow, and the firing rate arbitrarily small.

Going beyond the LIF model, we introduce the exponential integrate-and-fire (EIF) model with the drift

$$f_0(v) = -\gamma v + \Delta_T \exp[(v - \hat{v}_T)/\Delta_T]. \tag{2.2.9}$$

The first term on the r.h.s. again describes the leak and can give rise to a stable fixed point, as for the cyan in Fig. 2.6. The second term is an (increasing) exponential nonlinearity with a quasi-threshold $\hat{v}_T$, and parameter Δ_T that determines how sharp and steep the exponential function is. Due to the exponential nonlinearity, the voltage will rise at some point, resulting in a second (unstable) fixed point if the drift has crossed zero before. This allows the model to operate again in the mean-driven and excitable regime. The transition between the two regimes occurs via a saddle-node-on-limit-cycle bifurcation, making the EIF model a true Type I model. The result is

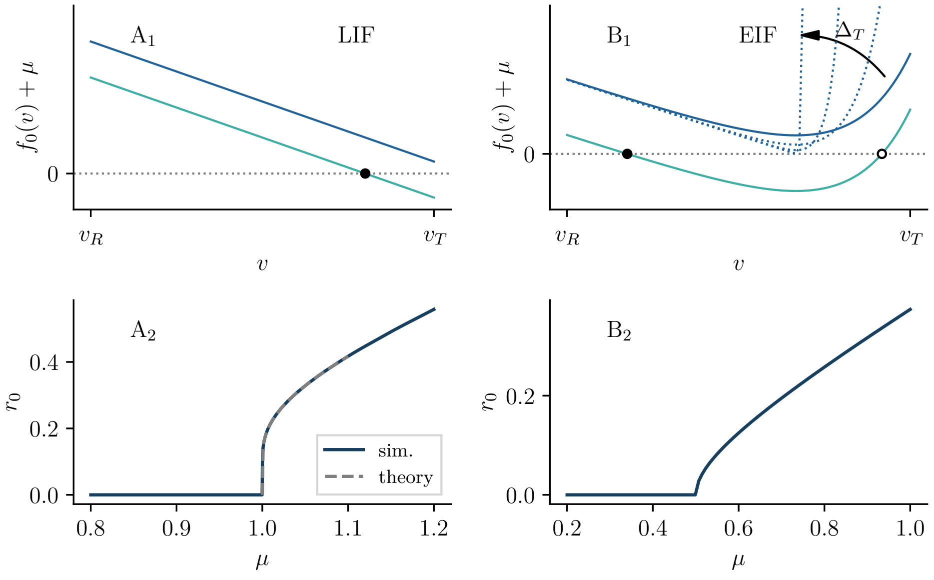

FIGURE 2.6: Panel A$_1$ and B$_1$ show the deterministic drift $f_0(v)+\mu$ for the LIF and EIF models, respectively. If the drift has no zero between reset v_R and threshold v_T (blue line), the model is in the mean-driven regime; if the drift function has a zero (cyan line), the model is in the excitable regime. A black dot or circle indicates the zero depending on whether the corresponding fixed point of the model is stable or unstable. Panel A$_2$ and B$_2$ show the f-I curves for the two models in the deterministic limit ($D=0$), which are continuous in both cases.

again a continuous f-I curve, for the same reason as discussed for the LIF model. Thus, both are class I models. In fact, any one-dimensional IF model is of class I because the fixed point or its ghost cannot be bypassed, so the drift near the bifurcation must always be close to zero. We noted that in the limit $\Delta_T \to 0$, the EIF model is equivalent to the LIF model with firing threshold at $\hat{v}_T$ as demonstrated in Fig. 2.6B$_1$ where the arrow indicates decreasing values of Δ_T.

The EIF model is particularly interesting because it connects the phenomenological LIF model and the biophysically detailed Hodgkin-Huxley model in two ways. A detailed description of both is beyond the scope of this section. We will only briefly sketch the motivations here. First, the drift function can be estimated experimentally using dynamical I-V curves [42, 123]. This is done by returning to Eq. 2.2.5, replacing the linear leak term with an unknown nonlinearity $f(V)$, and rearranging the terms to obtain $f(V(t)) = I(t) - C_m\dot{V}(t)$. Then a time-dependent current $I(t)$ is injected, and the change in the voltage $\dot{V}$ is measured. Suppose the capacitance is known (a problem addressed in [42]). In that case, this allows one to plot $f(V)$, a function that is very well approximated by the combination of a linear and an exponential term for cortical pyramidal cells. Second, as shown by Gerstner et al. [9] in Sec. 5.2. the EIF model can be motivated based on an approximation of the Hodgkin-Huxley model where the exponential term is related to the sodium current. To this end, one considers Eq. 2.2.1 and replaces the gating variables h and n by their values at the resting potential h_{rest} and n_{rest}, and additionally assume that m is in equilibrium with the voltage, so that can be substituted by its steady-state value $m_0(V)$ (shown in Fig. 2.1A). This allows one to approximate Eq. 2.2.1 near the resting potential by

$$C_m\dot{V} \approx -g_{\text{eff}}(V-E_{\text{eff}}) - g_{\text{NA}}m_0(V)^3h(V_{\text{rest}}-E_{\text{Na}}) + I \tag{2.2.10}$$

with $g_{\text{eff}} = g_K n_{\text{rest}}^4 + g_L$ and $E_{\text{eff}} = (g_K n_{\text{rest}}^4 E_K + g_L E_l)/(g_K n_{\text{rest}}^4 + g_L)$ that form the effective leak term. The nonlinearity comes from $m_0(V)$, which near the resting potential is well approximated by $\Delta_T \exp[(v-\hat{v}_T)/\Delta_T]$, as demonstrated in Fig. 2.1A by the dashed line. This shows that although IF models are phenomenological, they can be biophysically motivated to some extent. It also shows that even the simple LIF model provides a biophysically plausible description of the subthreshold voltage dynamics if the positive feedback is strong enough (a limit corresponding to $\Delta T \to 0$ for the EIF model).

To realize the firing-rate response of a class II neuron model in the IF framework, we need

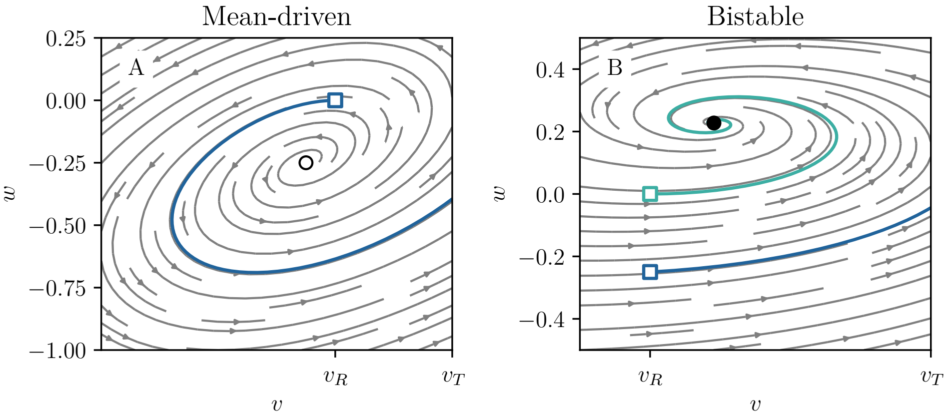

FIGURE 2.7: Panel A and B show the phase-space of the GIF model with an unstable and a stable fixed point, respectively. In panel A, the model exhibits a (globally) unstable fixed point (black circle), and every trajectory reaches the threshold irrespective of the reset value (except for the fixed point). The model is in the mean-driven regime. The blue line indicates a specific trajectory with reset values $v_R = 0, w_R = 0$ (blue square). In panel B the model exhibits a stable fixed point (black dot), and whether a trajectory reaches the threshold depends on the reset values. A trajectory (cyan line) with reset value $v_R = 0, w_R = 0$ (cyan square) does not reach the threshold, while a trajectory (blue line) with reset value $v_R = 0, w_R = -1/4$ (blue square) does.

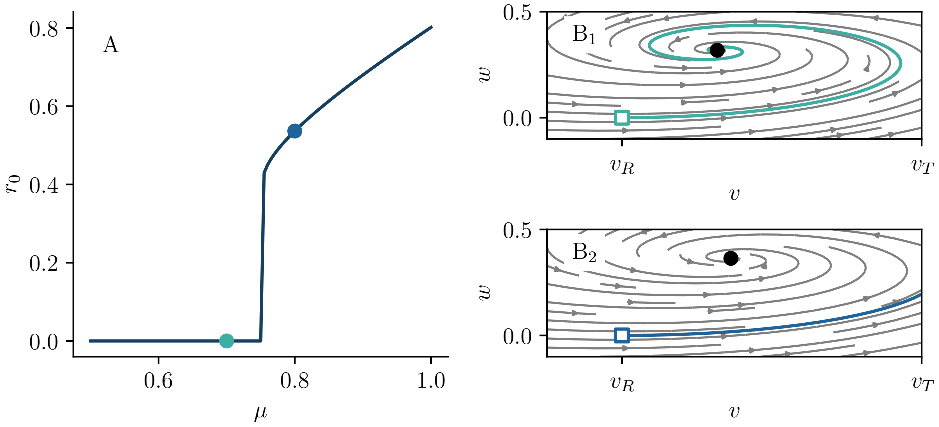

FIGURE 2.8: Panel A shows the f-I curve of the GIF model. Panel B_1 and B_2 show the phase-space with a stable fixed point (black dot) and a trajectory initiated at $v_R = 0, w_R = 0$ for two different values of μ indicated in panel A. For the GIF model, the fixed point is not on the limit cycle, which leads to a discontinuous f-I curve.

to consider so-called resonate-and-fire models, which have a second variable [120–122]. This is so because a discontinuous f-I curve implies a spike-onset via a Hopf-bifurcation (or similar), requiring at least two-dimensional phase space. The particular model we consider here will be referred to as the generalized integrate-and-fire (GIF) model with one auxiliary variable w and the linear drift functions:

$$\begin{aligned} f_0(v,w) &= -\gamma v - \beta w, \\ f_1(v,w) &= (v-w)/\tau_w. \end{aligned} \tag{2.2.11}$$

In Fig. 2.7A and B, we show the phase space of the GIF model together with the unstable (black circle in A) or stable (black dot in B) fixed point. The blue and cyan lines show exemplary trajectories initialized at the reset point marked by a square. As for the one-dimensional model, we can distinguish two firing regimes based on the existence or stability of the fixed point. First, the mean-driven regime, which can be realized by choosing the parameters such that the fixed point becomes unstable. Since for the two-dimensional GIF model, the firing threshold is not a point but a line, the outward spiraling trajectory will certainly hit this threshold line and trigger a spike as shown in Fig. 2.7A. Unlike the one-dimensional models for the GIF model, the existence of a stable fixed point does not imply that the system is excitable. Instead, whether the system approaches a fixed point or fires periodically depends on the choice of the reset values. This is illustrated in Fig. 2.7B, where a trajectory initiated at $v = 0$, $w = 0$ (cyan line) approaches the fixed point, while a trajectory initiated at $v = 0$, $w = -1/4$ (blue line) reaches the threshold. In this case, the GIF model is bistable. If the model is prepared in the bistable regime with reset values so that the fixed point is approached, increasing the input current can indeed lead to a discontinuous f-I curve, as demonstrated in Fig. 2.8. To this end, we have chosen the same parameters as for the cyan line Fig. 2.7B but increased μ. This moves the fixed point, located at $v^* = w^* = \mu/(\gamma + \beta)$, closer to the threshold line but does not change its stability (assuming complex eigenvalues the real part is given by $(\gamma + \tau_w^{-1})/2$). In Fig. 2.8B$_1$, we see a trajectory that barely misses the threshold line and does not trigger a spike. In Fig. 2.8B$_2$, we have increased μ somewhat so that the trajectory crosses the threshold and causes a periodic spike emission. The two values of μ are indicated in Fig. 2.8A by the respective color of the trajectory. Crucially, the moment the input current μ is increased sufficiently to trigger a spike, this leads to a firing rate that is not at all close to zero. This is so because here, the fixed point is not *on* the limit cycle, so the drift is not necessarily close to zero in the vicinity of the bifurcation. The GIF model can thus mimic a class II neuron model.

2.2.5 Nonrenewal spike generation

The models we have presented so far generate a renewal spike train. However, as we pointed out in the introduction, there is growing experimental evidence that ISIs are not independent but correlated over a few intervals [72, 73, 77–84]. Computational studies have identified two main processes that can cause interval correlations

1. slow self-inhibitory currents [40, 74, 81, 82],
2. temporally correlated input noise [66, 82, 92, 95].

In the following, we briefly discuss the biophysical basis of these two processes and their integration into the integrate-and-fire framework. The effect of these processes on the stationary statistics of the spike train, in particular the serial correlation coefficient, is also described.

Spike-frequency adaptation

One prominent mechanism by which ISIs can be correlated is the presence of a negative feedback current. Such a current often leads to the widespread phenomenon of spike-frequency adaptation, which refers to the observation that when stimulated by a constant current, almost all types of neurons exhibit an initial high firing rate that gradually decreases as more and more spikes are emitted, similar to what is illustrated in Fig. 2.9C. This phenomenon results from the self-inhibitory feedback current, which effectively slows down the neuron's dynamics and reduces its ability to fire additional spikes. According to Benda and Herz [18], the three main types of adaptation currents are

1. M-Type current - slow potassium current caused by voltage-gated high-threshold potassium channels [124],
2. mAHP-type current - slow potassium current mediated by calcium-dependent potassium channels [125],
3. Slow recovery from inactivation of the fast sodium channel [126],

and can be described by a single adaptation variable governed by

$$\tau_a(V)\dot{a} = -a + a_\infty(V) \tag{2.2.12}$$

(except for the mAHP-type current, where the dependence is not on the voltage but on calcium), very similar to what we have seen for the gating variables of a conductance-based model. How exactly this adaptation variable affects the voltage dynamics depends on the specific current. However, in general, a takes on the role of an additional gating variable that affects one of the three ion currents mentioned in Sec. 2.2.1.

In the IF framework, Treves [127] was the first to consider an LIF model endowed with a *spike-triggered* adaptation variable that is instantaneously increased whenever a spike is emitted. A somewhat similar adaptive LIF model is given by [74]:

$$\begin{aligned} \dot{v} &= -\gamma v + \mu - a + \sqrt{2D}\xi_v(t), \\ \tau_a \dot{a} &= -a + \tau_a \Delta \sum \delta(t - t_i), \\ &\text{if } v(t) = v_T \to t_i = t,\, v(t) = v_R. \end{aligned} \tag{2.2.13}$$

Except for the fact that Treves has considered i) a recurrent neural network and ii) an adaptation variable a that takes on the role of a gating variable and is thus multiplied by the difference between the voltage and the respective reversal potential, which is more similar to a conductance-based formalism. In Eq. 2.2.13, the adaptation variable resembles a current. To relate to Eq. 2.2.12, this spike-triggered adaptation corresponds to a situation where the time constant $\tau_a(V)$ is independent of the voltage, and the steady-state value $a_\infty(V)$ changes significantly only during the action potential. In the IF framework, the action potential is reduced to a point in time, and the effect of the voltage-dependent steady-state value $a_\infty(V)$ during the spike is described by the delta function. Thus, in the absence of a spike, the adaptation variable decays exponentially to zero with the time constant τ_a. At a spike time, the delta function takes effect, and the adaptation variable is immediately increased by Δ. The behavior of the adaptive LIF model (Eq. 2.2.13) in response to the onset of constant current $\mu = 5$ at $t = 5$ is illustrated in Fig. 2.9. Once stimulated, the model begins to fire spikes (black vertical lines in Fig. 2.9A). At the same time, the adaptation $a(t)$ builds up and inhibits the model's ability to emit further spikes (Fig. 2.9B). Specifically, the adaptation builds up until the exponential decay between two spikes and the increase during a spiking balance on average. As a result, we observe a firing rate that gradually decreases and saturates at some finite value (Fig. 2.9C). Note that unlike the trajectories $v(t)$ and $a(t)$, the calculation of the instantaneous firing rate $r(t)$ involves an ensemble average: to compute $r(t)$, we consider a large ensemble of adaptive LIF models subjected to the constant current stimulus described above and estimate the firing rate by the fraction of realizations that cross the firing threshold in a short time bin $[t, t + \Delta t]$ divided by Δt. This procedure is closely related to the definition of the (stationary) firing rate as the probability of finding a spike in the short time bin Δt according to Eq. 1.3.4.

As we have seen, spike-frequency adaptation is primarily a transient phenomenon. However, a slow adaptation variable also affects the spiking statistics in the stationary state by correlating ISIs. This has to do with the fact that $a(t)$ is not reset with each spike and thus can keep memory of previous ISIs. Many theoretical studies have addressed the question of how exactly a spike-triggered adaptation correlates the intervals and have concluded that in most cases, such a self-inhibitory feedback leads to *negative* ISI correlations [18, 40, 73, 74]. This is demonstrated in Fig. 2.10. Recall that adjacent intervals are negatively correlated if a long/short interval T_i is usually followed by a short/long interval T_{i+1}. In Fig. 2.10A we show the joint probability density $p(T_i, T_{i+1})$ centered around the mean ISI $\Delta T_i = T_i - \langle T \rangle$. Even with the naked eye, it can be seen that an interval T_i shorter than the mean ($\Delta T_{i+1} < 0$) usually leads to a subsequent interval T_{i+1} longer than the mean ($\Delta T_i > 0$) and vice versa. The red line in Fig. 2.10B shows a linear function with slope ρ_1 that can be interpreted as a linear approximation of the expected value of ΔT_{i+1} as a function of ΔT_i. The deviation between this line and what one would visually identify as the best linear fit result from the nonlinear dependence between the two interval deviations. That the relationship *must* be nonlinear is best illustrated by the fact that for large positive values $\Delta T_i > \langle T \rangle$ we cannot expect to find corresponding large negative values $\Delta T_{i+1} < \langle T \rangle$, as it would be predicted by the linear measure, simply because intervals must always be larger than zero. In Fig. 2.10B, we show the deviation of the joint probability density from the marginal distribution $p(T_i, T_{i+1})$ - $p_{\text{ISI}}(T)^2$ again centered around the mean ISI. Recall that in the renewal case, the joint probability factorizes $p(T_i, T_{i+1}) = p_{\text{ISI}}(T)^2$, so that Fig. 2.10B illustrates the increase or decrease in the probability to find a certain interval T_{i+1} given T_i, due to the spike train being nonrenewal.

How does a spike-triggered adaptation lead to negative interval correlations? First, for an LIF model, an inhibitory current always delays the next spike time. Consider an LIF model that is initiated at v_R and some value $a(t_i^+) = \hat{a}$, such that the expected value of the ISI T_i is the mean

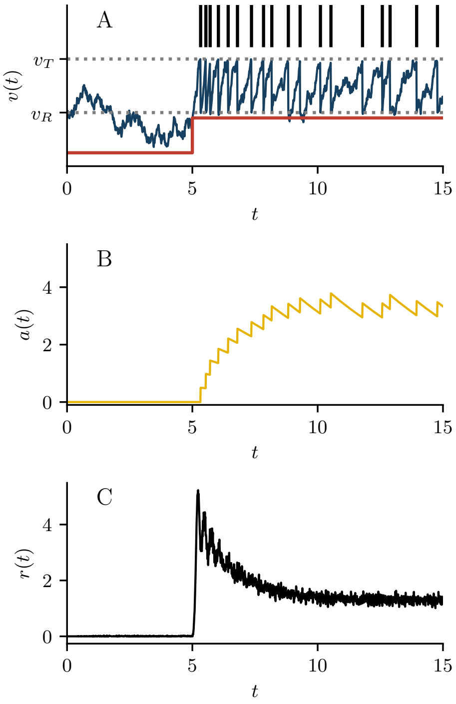

FIGURE 2.9: Spike-frequency adaptation in an adaptive LIF model in response to a constant current stimulation $\mu = 5$ applied at $t = 5$. Panel A, B, and C show the voltage $v(t)$, adaptation variable $a(t)$, and instantaneous firing rate $r(t)$ in response to the current stimulation, respectively. Spike times are indicated in A by black lines. Before the current is applied, practically no spikes are observed. The voltage fluctuates around its resting value, and the adaptation variable is at rest $a = 0$. Upon stimulation, the model begins to spike with a high firing rate that gradually decreases due to an increase in the adaptation variable. Parameters: $\mu = 5, \gamma = 1, \tau_a = 5, \Delta = 0.5, D = 0.1$

ISI $\langle T\rangle$. The plus t_i^+ indicates that the time should be taken immediately after the spike. This is important because at the spike time t_i, the value $a(t_i)$ is ambiguous depending on whether the delta kick was applied ($a(t_i^+)$) or not ($a(t_i^-)$). The actual ISI T_i will generally not coincide with the mean ISI. However, if it did, the adaptation variable at the beginning of the next interval would again be $a(t_{i+1}^+) = \hat{a}$ and the expected value of T_{i+1} would again be the mean ISI. Now consider a case where the ISI T_i is shorter than the mean $\Delta T_i < 0$. The initial conditions for the second interval T_{i+1} are v_R and some value of the adaptation variable $a(t_{i+1}^+) > \hat{a}$. This is so because the decay between two spikes is proportional to the length of the ISI and is thus reduced. Since the adaptation has an inhibitory effect on the voltage dynamics, the expected value for the next interval T_{i+1} will be longer than the mean $\langle \Delta T_{i+1} | \Delta T_i < 0\rangle > 0$. A similar argument can be made for an interval T_i longer than the mean. In both cases, we find that the expected value of ΔT_{i+1} is negatively correlated with ΔT_i, and the SCC is negative, $\rho_1 < 0$. Note that this explanation is based on the fact that an inhibitory current always delays the next spike time. We will see that this is not always the case for more complicated neuron models such as the GIF model.

A negative-feedback current is an important mechanism leading to interval correlation; however, it is certainly not the only one. In the following, we discuss a second mechanism by which ISIs can be correlated, namely if the noise itself is temporally correlated.

Correlated noise - The Ornstein-Uhlenbeck process

We have discussed three different sources of noise in the neuronal system that lead to fluctuations in the membrane potential and have described them by a white (uncorrelated) Gaussian noise. Such a description is reasonable if the fluctuations are fast compared to any other timescale in the system. Additionally, a white noise is convenient mathematically. For example, we have seen that an IF model (without adaptation) driven by such noise generates a renewal point process.

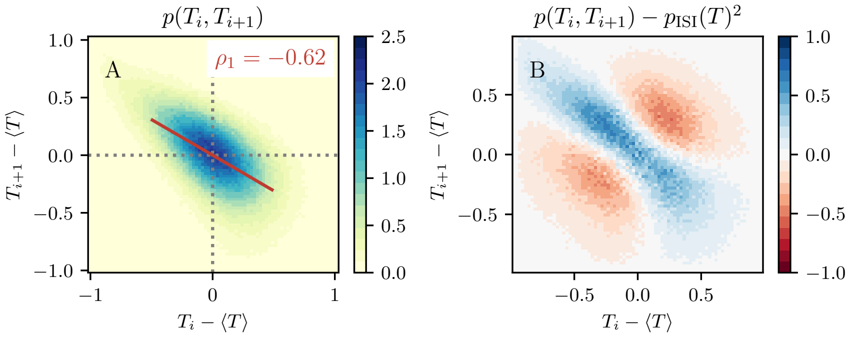

FIGURE 2.10: Interval correlations in an adaptive LIF model. Panel A shows the joint probability of adjacent intervals centered around the mean ISI. The red line indicates a linear approximation $\langle T_{i+1}|T_i\rangle \approx \rho_1 T_i$ with slope according to the SCC. Panel B shows the derivation of the joint probability from the marginal distribution. Parameters: $\mu = 20$, $\gamma = 1$, $\tau_a = 2$, $\Delta = 10$, $D = 1$

However, for a process to be truly delta-correlated, i.e., completely uncorrelated to itself when viewed at two different points in time that can be arbitrarily close to each other, the process must change infinitely fast. No biophysical process can have this property.

For example, channel noise arises from stochastic changes in the conformational state of ion channels. If one observes the state of a channel at a time t, the probability of finding the same state at a later time t' depends on the difference between the two times because the state of the ion channel does not change infinitely fast. This leads to a finite correlation time of the channel state. While in most cases, the change of the channel state is fast compared to the change of the voltage, this is not always the case. Ion channels that mediate spike-frequency adaptation may, for instance, change slowly. Similarly, synaptic noise may have a relevant timescale that cannot be neglected due to synaptic filtering. A presynaptic potential triggers the release of neurotransmitters into the synaptic cleft and leads to the activation of transmitter- or ligand-gated ion channels. Again, the kinetics of the ion channel determines the timescale of the postsynaptic potential, which is typically of the order of milliseconds, the same order of magnitude as the membrane time constant. A second mechanism, called short-term synaptic plasticity, which refers to an increase or decrease in synaptic response upon repeated transmission of a presynaptic potential, can affect synaptic dynamics on an even longer timescale, typically a few hundred milliseconds [128–130]. In all of the above cases, the noise affecting the voltage is correlated.

A simple stochastic process with a finite correlation time and exponential autocorrelation function is the Ornstein-Uhlenbeck (OU) process defined by [57, 60]

$$\tau_\eta \dot{\eta} = -\eta + \sqrt{2\sigma^2 \tau_\eta} \xi_\eta(t). \tag{2.2.14}$$

The random variable $\eta(t)$ is a low-pass filtered or colored noise that can be regarded as a Markovian embedding of a white noise $\xi_\eta(t)$. Just like the white noise $\xi_\eta(t)$, the colored noise $\eta(t)$ is (in the stationary case) Gaussian distributed according to $p(\eta) = \exp(-\eta^2/(2\sigma^2))/\sqrt{2\pi\sigma^2}$ with some variance σ^2. More importantly, the OU process is temporally correlated with the correlation function

$$\langle \eta(t)\eta(t')\rangle = C_{\eta\eta}(t-t') = \sigma^2 e^{-(|t-t'|)/\tau_\eta} \tag{2.2.15}$$

and correlation time τ_η[1]. We consider the LIF model again:

$$\begin{aligned} \dot{v} &= -\gamma v + \mu + \eta + \sqrt{2D}\xi_v(t), \\ \tau_\eta \dot{\eta} &= -\eta + \sqrt{2\sigma^2 \tau_\eta}\xi_\eta(t), \\ &\text{if } v(t) = v_T \rightarrow t_i = t,\ v(t) = v_R, \end{aligned} \tag{2.2.16}$$

---

[1] The correlation time is commonly defined by $\tau_x = \int_0^\infty d\tau\, C_{xx}(\tau)/\sigma_x^2$.

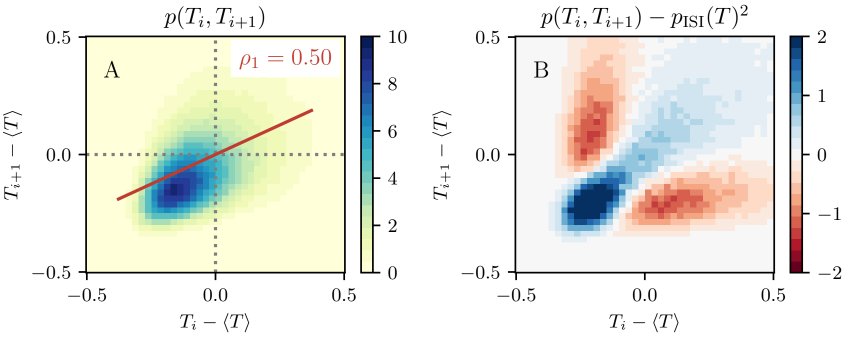

FIGURE 2.11: Interval correlations in an LIF model with correlated noise. Panel A shows the joint probability of adjacent intervals centered around the mean ISI. The red line indicates a linear approximation $\langle T_{i+1}|T_i\rangle \approx \rho_1 T_i$ with slope according to the SCC. Panel B shows the derivation of the joint probability from the marginal distribution. Parameters: $\mu = 2$, $\gamma = 0.5$, $\tau_\eta = 10$, $\sigma = 0.5$, $D = 0.05$

where the voltage dynamics is driven by both a colored noise $\eta(t)$ and a white noise $\xi_v(t)$, which can be considered to originate from a population of slow and fast ion channels, respectively. Due to the finite correlation time of the OU process, the ISIs are no longer independent as the noise changes slowly and thus affects several consecutive ISIs in a similar way. This is illustrated in Fig. 2.11 where strong positive interval correlations are observed.

Besides the OU process with an exponential correlation function, we note that a higher-dimensional Markovian embedding allows the realization of any correlation functions that can be approximated by a sum of exponential functions and damped harmonic oscillations [95]. This includes negatively correlated green noise with reduced power at low frequencies [131] or harmonic noise where most spectral power falls in a preferred frequency band [115]. In this thesis, however, we focus on exponentially correlated noise.

Spike-frequency adaptation and correlated noise

The model we consider in this chapter is a multidimensional IF model with a spike-triggered adaptation variable and a correlated noise:

$$\begin{aligned} \dot{v} &= f_0(v, \mathbf{w}) + \mu - a + \eta + \sqrt{2D}\xi_v(t), \\ \dot{w}_j &= f_j(v, \mathbf{w}), \\ \tau_a \dot{a} &= -a + \Delta \sum \delta(t - t_i), \\ \tau_\eta \dot{\eta} &= -\eta + \sqrt{2\sigma^2 \tau_\eta} \xi_\eta(t), \\ &\text{if } v(t) = v_T \rightarrow t_i = t,\, v(t) = v_R,\, \mathbf{w}(t) = \mathbf{w}_R. \end{aligned} \tag{2.2.17}$$

This is an extension of the model studied by Schwalger and Lindner [74] and can have much more complicated interval correlations. This is demonstrated in Fig. 2.12. At first glance, spiking seems to be renewal because $\rho_1 = 0$. However, this is not the case as $\rho_2 \neq 0$ does not vanish. The joint probability of the intervals T_i and T_{i+2} is shown in Fig. 2.12B and displays a weak negative correlation. While the SCC has been calculated in the past for an IF model with adaptation [74] or an IF model driven by colored noise [95], no theory has yet been developed to determine how the interaction of these two processes affects the correlations between intervals. In this chapter, we fill this gap and determine in the SCC for an IF model according to Eq. 2.2.17.

2.3 Phase reduction

As we have seen in the previous section, biophysically detailed conductance-based models are often high-dimensional and, as a consequence, difficult to treat analytically. The introduction of

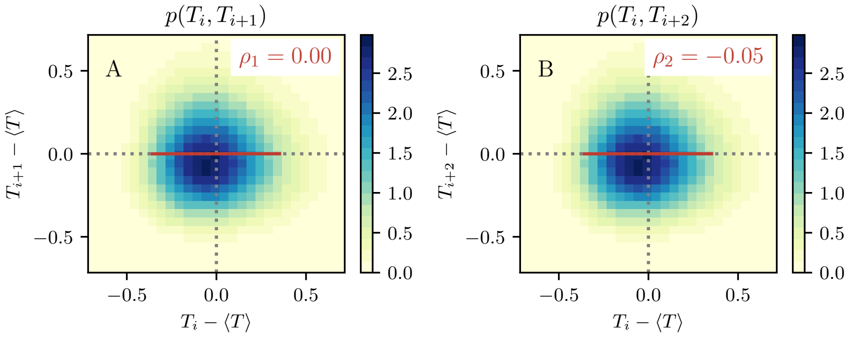

FIGURE 2.12: Interval correlations in an adaptive LIF model with correlated noise. Panels A and B show the joint probability of the two intervals T_i and T_{i+k} for $k = 1$ and $k = 2$, respectively. The red lines indicate a linear approximation $\langle T_{i+k} | T_i \rangle \approx \rho_k T_i$ with slope according to the SCC. Due to the interplay between adaptation and correlated noise, adjacent intervals are virtually uncorrelated ($\rho_1 \approx 0$), while more distant intervals are weakly correlated ($\rho_2 \neq 0$). Parameters: $\mu = 4$, $\gamma = 1$, $\tau_a = 2$, $\Delta = 2$, $\tau_\eta = 1.5$, $\sigma = \sqrt{0.15}$, $D = 0.01$

phenomenological integrate-and-fire models reduces this difficulty but does not completely eliminate it. The development of methods to reduce high-dimensional models by exploiting certain system properties is therefore desirable.

One such method explained in this section, which allows for the reduction of multidimensional systems that possess a limit cycle, is known as phase reduction [132]. In this framework, the dynamics on the limit cycle is described by a one-dimensional periodic phase variable that grows uniformly with time - and is thus very similar to time itself. Phase reduction techniques have proven extremely useful in computational neuroscience (see, for example [133–135]). This is so because it is reasonable to consider a sufficiently strongly stimulated neuron as an oscillator, but also because of the close relation between phase and spike time. The key to the success of this method lies not in the one-to-one mapping of the limit cycle to a phase variable but in the extension of the notion of a phase to the entire basin of attraction of the limit cycle. We will show that this extension gives rise to so-called isochrones, sets of constant phases, which can be used to quantify how a perturbation in the phase space of the original system affects the reduced phase variable. Typically, one considers the perturbation to be small and calculates the linear response of the phase variable using the corresponding linear response function, in this context called the phase-response curve. A somewhat different approach defines the PRC directly by the shift of the next spike time in response to a small perturbation of the voltage variable of a neuron [136]. This is a bit imprecise because it assumes a perturbation in a certain direction but has to do with the fact that the stimulation of a neuron often takes the form of a current or voltage stimulation. In either case, we will see that the PRC, whether defined by the linear response of the phase variable or by the shift of the next spike time, can be computed by a system of linear differential equations that is solvable for many IF models. In addition, we will distinguish two quantitatively different types of PRCs, which are closely related to the bifurcation by which the spike onset occurs and thus to the classification into Type I and Type II neurons. In Sec. 2.4, we will then see how the PRC can be used to calculate response characteristics, specifically the serial correlation coefficient.

2.3.1 Phase and Isochrones

Here, we recall the notions of phase and isochrone for a multidimensional oscillatory system [132]. Consider an n-dimensional differential equation

$$\frac{d\mathbf{x}}{dt} = F(\mathbf{x}), \tag{2.3.1}$$

where $F(\mathbf{x})$ is some function so that Eq. 2.3.1 possesses a T^*-periodic stable limit cylce denoted Γ. To make a relation to the models we have discussed above, we can, for instance, think of a (deterministic) IF model that fires periodically at $t_i = iT^*$ so that the period T^* is associated with the (deterministic) ISI. Recall that a limit cycle is said to be stable if we can define a basin of attraction $\mathcal{M}$ so that every trajectory $\mathbf{x}(t;\mathbf{x}_0)$ of the system with an initial condition in that basin of attraction $\mathbf{x}_0 \in \mathcal{M}$ eventually approaches the limit cycle [137]. Since Γ is a line in the n-dimensional phase space, it can be parameterized by a one-dimensional variable. To emphasize the periodic nature of this variable, it is often referred to as a phase φ, which can take values between 0 and 2π. Equivalently, one can choose a phase-like variable τ that is T^*-periodic as the limit cycle itself. We opt for the second variant and choose τ to parametrize the limit cycle. This choice, however, is only a matter of normalization and of no particular importance.

Strictly speaking, the phase is defined by a function $\theta(\mathbf{x}) : \mathbb{R}^n \to \mathbb{R}$ that assigns a number τ to each point on the limit cycle $\mathbf{x} \in \Gamma$

$$\theta(\mathbf{x}) = \tau, \tag{2.3.2}$$

with the additional condition that $\tau(t)$ grows uniformly in time as $\mathbf{x}(t)$ moves along the limit cycle, i.e. $\dot{\tau}(t) = 1$. At this point, one might ask what advantage there is in mapping a one-dimensional set of points (the limit cycle) to another one-dimensional set of points (the phase) that differ only in that the latter grows linearly with time. The answer lies in extending the definition of the phase from the limit cycle to the entire basin of attraction.

To this end, consider a point $\mathbf{y}_0 \in \mathcal{M}$ *off* the limit cycle and let $\mathbf{x}(t;\mathbf{y}_0)$ be the trajectory or solution to Eq. 2.3.1 with the initial condition $\mathbf{y}_0$. This trajectory eventually converges to the stable limit cycle as $t \to \infty$. Additionally consider a second point *on* the limit cycle $\mathbf{x}_0 \in \Gamma$ with trajectory $\mathbf{x}(t;\mathbf{x}_0)$. This second trajectory starts and stays on the limit cycle, so its phase is always well-defined. We can now assign a phase to the point $\mathbf{y}_0$ based on the asymptotic behavior of the corresponding trajectory. In particular, the two points $\mathbf{y}_0 \notin \Gamma$ (off the limit cycle) and $\mathbf{x}_0 \in \Gamma$ (on the limit cycle) are said to have the same asymptotic phase $\theta(\mathbf{y}_0) = \theta(\mathbf{x}_0)$ if they become indistinguishable for $t \to \infty$:

$$||\mathbf{x}_0 - \mathbf{y}_0||_\tau := \lim_{t\to\infty} ||\mathbf{x}(t;\mathbf{x}_0) - \mathbf{x}(t;\mathbf{y}_0)|| = 0. \tag{2.3.3}$$

A consequence of the extension of the notion of a phase from the limit cycle to the basin of attraction is that there are now several points $\mathbf{x}$ which have the same phase τ. In fact, for an n-dimensional system, there is a whole hyperplane ($n-1$-dimensional subspace) with an identical phase. Such a hyperplane of constant phase is called an isochrone [138] denoted $\ell(\tau)$ and is defined as the set of all points $\mathbf{y}$ off the limit cycle that have the same asymptotic phase as $\mathbf{x}$ on the limit cycle:

$$\ell(\tau) = \{\mathbf{y} \in \mathcal{M} | \, ||\mathbf{x} - \mathbf{y}||_\tau = 0, \theta(\mathbf{x}) = \tau\}. \tag{2.3.4}$$

It should be noted that the phase can also be extended to the basin of attraction by means of the so-called return-time phase. Briefly, one defines a hyperplane $\ell_{RT}(\tau)$ so that for every point $\mathbf{y} \in \ell_{RT}(\tau)$ the return-time from $\mathbf{y}$ to $\ell_{RT}(\tau)$ agrees with the period T^*. Finding such a hyperplane with constant return time is numerically challenging, even for the adaptive LIF model [3]. However, for deterministic systems, both phase definitions are identical [132].

In Fig. 2.13, we show the phase τ, calculated according to the asymptotic definition, for the deterministic adaptive LIF model (Eq. 2.2.13 with $D = 0$):

$$\begin{aligned} \dot{v} &= -\gamma v + \mu - a, \\ \tau_a \dot{a} &= -a + \Delta \textstyle\sum_i \delta(t - t_i), \\ \text{if } v(t) &= v_T \to t_i = t, \, v(t) = v_R. \end{aligned} \tag{2.3.5}$$

We distinguish two cases, one where the parameters are chosen so that after the reset, the velocity $-\gamma v + \mu - a > 0$ is positive (Fig. 2.13A) and one where the velocity is negative $-\gamma v + \mu - a < 0$ (Fig. 2.13B). Following Schwalger and Lindner [74], the first case is referred to as *weak* adaptation, while the second case is referred to as *strong* adaptation. In both cases, the parameters can be chosen so that the system has a limit cycle shown by the red lines. To compute the phase by means of Eq. 2.3.3, we first parameterize the limit cycle by $\tau \in [0, T^*]$ so that $\dot{\tau} = 1$. This defines the phase of a point on the limit cycle only up to a constant, i.e., we are free to choose which point is said to have phase zero. For IF models, the choice is rather natural since it is suggestive to define the reset point (marked by a red square) as the beginning of the limit cycle to have the

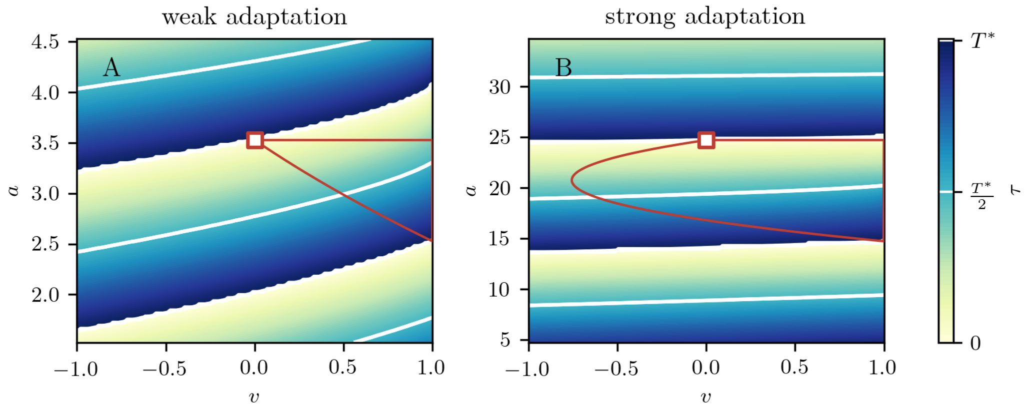

FIGURE 2.13: Asymptotic phase of an adaptive LIF model. Panels A and B show the asymptotic phase $\tau \in [0, T^*]$ for the deterministic adaptive LIF model with a weak and a strong adaptation, respectively. The limit cycle is shown by a red line, with the reset point marked by a red square. Specific isochrones with $\tau = nT^*/4$ with $n = 1, 2, \dots$ are shown by white lines. Parameters A$_1$: $\gamma = 1$, $\mu = 5$, $\tau_a = 2$, $\Delta = 2$; A$_2$: $\gamma = 1$, $\mu = 20$, $\tau_a = 2$, $\Delta = 20$.

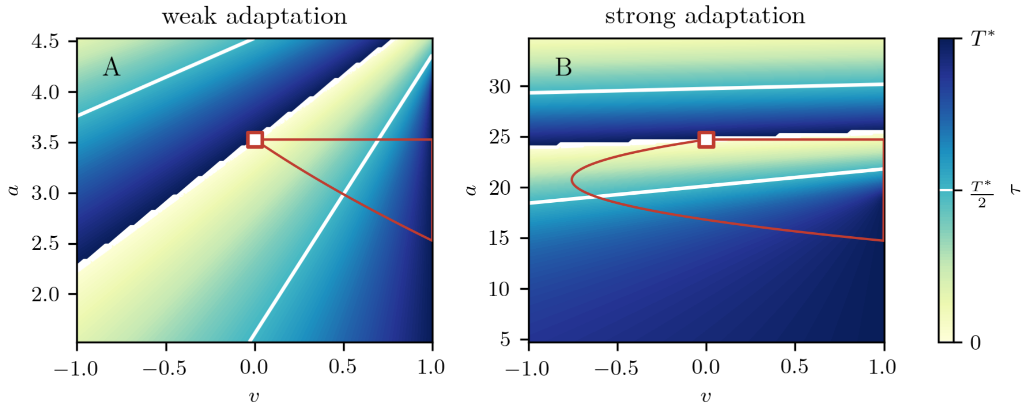

FIGURE 2.14: Spike-time phase for an adaptive LIF model. Panels A and B show the spike-time phase $\tau \in [0, T^*]$ for the deterministic adaptive LIF model with a weak and a strong adaptation, respectively. The limit cycle is shown by a red line, with the reset point indicated by a red square. White lines show specific isochrones. Parameters as in Fig. 2.13.

phase $\tau = 0$. For every other point off the limit cycle, the associated phase is calculated as follows: We chose a point $\mathbf{y}_0$ and let it evolve forward in time until $t = T^*$. The new point $\mathbf{y}_1 = \mathbf{x}(T^*; \mathbf{y}_0)$ is still on the same isochrone (think of the return-time phase) but closer to the limit cycle. This procedure is repeated multiples times, i.e., we observe the trajectory stroboscopically whenever t is a multiple of the period T^*, i.e., whenever $t = nT^*$ for $n \in \mathbb{N}$. The sequence of points $\mathbf{y}_n = \mathbf{x}(nT^*; \mathbf{y}_0)$ will eventually converge to some point on the limit cycle $\mathbf{x}_\Gamma$ for which the phase is known. Finally, we assign the same phase to the points $\mathbf{y}_n$, and in particular $\mathbf{y}_0$. Note that this implies that isochrones are not necessarily connected but can have multiple branches because a point far from the limit cycle can have the same phase as a point on the limit cycle, as shown in Fig. 2.13A and Fig. 2.13B. This, however, is not unique to IF models but simply because we can take any point in the phase space, calculate the trajectory backward in time for one period and find a new point that is farther from the limit cycle but has the same phase. Nothing guarantees that the contour lines of the phase landscape are connected.

We have seen how the phase function $\theta(\mathbf{x})$ can be calculated numerically. Finding an analytical expression for this function is, in general, much more complicated. However, to study phenomena in *weakly* perturbed oscillators, it is often sufficient to know the phase function in the proximity of the limit cycle [139]. In other words, a linear approximation of $\theta(\mathbf{x})$ evaluated on the limit cycle is sufficient. It turns out that this approximation is precisely what is known as the infinitesimal phase response curve (iPRC) that is introduced below and can be determined by a system of linear differential equations [135].

2.3.2 Phase response curve

To define the iPRC, we consider again Eq. 2.3.1. However, this time, the system moves along the limit cycle and is subject to an infinitesimally small perturbation, specifically a delta kick with amplitude $|\boldsymbol{\varepsilon}|$ applied at some phase τ:

$$\frac{d\mathbf{x}}{dt} = F(\mathbf{x}) + \boldsymbol{\varepsilon}\delta(t-\tau). \tag{2.3.6}$$

Because the system is periodic and moves along the limit cycle, we are only interested in times $t \in [0, T^*]$. For clarity, we can think again of an IF model in which case t can be thought of the time since the last spike, which in the deterministic case is naturally bound between 0 and T^*.

This perturbation will kick the system to a new phase $\tau'(\boldsymbol{\varepsilon}, \tau)$ that depends on the amplitude and direction of the perturbation but also on the phase τ at which the system was perturbed. Neurons, for example, are usually relatively insensitive to a perturbation when they have just spiked [140]. The difference between these two phases is given by

$$\Delta(\boldsymbol{\varepsilon}, \tau) = \tau'(\boldsymbol{\varepsilon}, \tau) - \tau \tag{2.3.7}$$

and can be related to the phase function $\theta(\mathbf{x})$. To this end consider a point $\mathbf{x}_\Gamma$ on the limit cycle with phase $\theta(\mathbf{x}_\Gamma) = \tau$ and a general perturbation $\boldsymbol{\varepsilon}$. The phase after the perturbation can be approximated by

$$\tau'(\boldsymbol{\varepsilon}, \tau) = \theta(\mathbf{x}_\Gamma(\tau) + \boldsymbol{\varepsilon}) \approx \tau + \nabla_{\mathbf{x}}\theta(\mathbf{x})|_{\mathbf{x}_\Gamma(\tau)} \cdot \boldsymbol{\varepsilon}, \tag{2.3.8}$$

where we have expanded the new phase up to the first order in $\boldsymbol{\varepsilon}$ because the perturbation is considered to be infinitesimal. We find that the phase shift is related to the gradient of the phase function

$$\Delta(\boldsymbol{\varepsilon}, \tau) = \nabla_{\mathbf{x}}\theta(\mathbf{x})|_{\mathbf{x}_\Gamma(\tau)} \cdot \boldsymbol{\varepsilon} \tag{2.3.9}$$

evaluated on the limit cycle. The vector-valued function

$$\mathbf{Z}(\tau) = \nabla_{\mathbf{x}}\theta(\mathbf{x})|_{\mathbf{x}_\Gamma(\tau)} \tag{2.3.10}$$

is referred to as the iPRC because it characterizes the response of the phase with respect to an infinitesimally small perturbation from the limit cycle in an arbitrary direction.

2.3.3 Adjoint Method

We have seen that the iPRC can be defined as the gradient of the phase function evaluated on the limit cycle, Eq. 2.3.10. This allows for an intuitive understanding of the iPRC as a linearization of the phase function corresponding to a linearization of the isochrone around the limit cycle, as pointed out by Wilson and Ermentrout [141]. Furthermore, this definition is very useful because although $\theta(\mathbf{x})$ is difficult to determine, its gradient is the solution to a linear differential equation, the so-called adjoint equation [142]

$$\frac{d\mathbf{Z}(\tau)}{d\tau} + A^T(\tau)\mathbf{Z}(\tau) = 0, \tag{2.3.11}$$

where $A(\tau) = \nabla_{\mathbf{x}}F(\mathbf{x})|_{\mathbf{x}_\Gamma(\tau)}$ is the Jacobian matrix of Eq. 2.3.1 evaluated on the limit cycle Γ, and A^T denotes its transposed $[A]_{ij} = [A^T]_{ji}$. Eq. 2.3.11 does not uniquely define the iPRC but additionally requires a normalization condition [135]

$$\mathbf{Z}(\tau) \cdot \frac{d\mathbf{x}_\Gamma(\tau)}{d\tau} = 1, \tag{2.3.12}$$

that is obtained by differentiating $\theta(\mathbf{x}_\Gamma(\tau)) = \tau$ with respect to τ and thus reflects the fact that the phase increases uniformly on the limit cycle. For smooth systems with a limit cycle, the remaining boundary conditions are periodic [143]:

$$\mathbf{Z}(\tau) = \mathbf{Z}(\tau + T^*). \tag{2.3.13}$$

It should be noted that for nonsmooth oscillators, specifically those who suffer a jump (or reset), the PRC can be discontinuous [144].

2.3.4 Direct Method

Usually, if one measures the iPRC in neural systems, either experimentally or numerically, one does so by considering a T^*-periodic system that has fired a spike at $t_i = 0$ and measures the time of the *next* spike $t_{i+1} = t_i + T(\varepsilon, \tau)$ in response to a perturbation to the voltage variable as a function of the phase at which the perturbation was applied [136]. The resulting interspike interval $T(\varepsilon, \tau)$ will, in general, not agree with the period of the system T^* and the deviation between the two

$$\delta T(\varepsilon, \tau) = T(\varepsilon, \tau) - T^*, \tag{2.3.14}$$

is used to define the iPRC by

$$Z_v(\tau) = -\lim_{\epsilon \to 0} \frac{\delta T(\varepsilon, \tau)}{\epsilon}. \tag{2.3.15}$$

Here the sign has been chosen so that the iPRC is positive ($Z_v > 0$) if a positive kick ($\epsilon > 0$) leads to an early spike time ($\delta T < 0$). Note that the perturbation we have considered here is a scalar function, as it is only applied to the voltage variable. We thus obtain a likewise scalar iPRC $Z_v(\tau)$ that corresponds to a certain component of the previously discussed vector-valued iPRC $\mathbf{Z}(\tau)$. Moreover, the iPRC defined in this way is based on a slightly different phase definition since it measures the shift of the *next* spike time, whereas previously, we considered the shift of the *asymptotic* spike time. In Fig. 2.14, we show this phase for the adaptive LIF model as we did for the asymptotic phase in Fig. 2.13. Note that the two definitions are not identical for an adaptive IF model, where a variable is not reset on a spike. Two trajectories starting at two different points in phase space that have the *next* spike in synchrony will therefore have the subsequent spikes in asynchrony. This includes the asymptotic spike time. Consequently, two points in phase space with the same spike time phase will have different asymptotic phases. This is true for every point in the phase space except for those on the limit cycle, where the two phase definitions are identical. This is because points on the limit cycle that have their next threshold crossing in synchrony also have every subsequent threshold crossing in synchrony (we are essentially considering the same point). We will see that this difference is reflected in the boundary condition of the iPRC.

First, however, we should make a connection between the two definitions of the iPRC, on the one hand, by means of the gradient of the phase function, and on the other hand, by means of the shift of the next spike time. To this end, it is vital to realize that $T^* - \tau'(\varepsilon, \tau)$ is exactly the time until the next spike. This is true as long as the phase is defined with respect to the shift of the next spike time. In this case the difference $\Delta(\varepsilon, \tau)$ is therefore related to the (negative) spike-time deviation:

$$\Delta(\varepsilon, \tau) = \tau'(\varepsilon, \tau) - \tau = T^* - T(\varepsilon, \tau) = -\delta T(\varepsilon, \tau). \tag{2.3.16}$$

Thus, the phase difference due to a small perturbation $\Delta(\varepsilon, \tau)$ and the spike-time deviation $\delta T(\varepsilon, \tau)$ are identical except for the sign. If we compare Eq. 2.3.15 with Eq. 2.3.9 and 2.3.10, assuming that the vector-valued perturbation therein is applied to a certain variable, which can be interpreted as the voltage, we see that $Z_v(\tau)$ is indeed the corresponding component of the vector-valued gradient

$$Z_v(\tau) = \lim_{\varepsilon \to 0} \frac{\nabla_{\mathbf{x}} \theta(\mathbf{x})|_{\mathbf{x}_\Gamma} \cdot \boldsymbol{\varepsilon}_v}{\varepsilon} = \nabla_{\mathbf{x}} \theta(\mathbf{x})|_{\mathbf{x}_\Gamma} \cdot \mathbf{e}_v, \tag{2.3.17}$$

where $\boldsymbol{\varepsilon}_v = \varepsilon \cdot \mathbf{e}_v$ is the perturbation applied to the voltage and $\mathbf{e}_v$ is the unit vector in the direction of the voltage.

The definition of the iPRC in terms of the deviation of the next spike time is instructive and numerically straightforward to implement. Furthermore, in some special cases, it even allows the PRC to be calculated analytically (for finite and infinite perturbations), as we will show now.

Example: Calculation of the iPRC for the LIF model by the direct method

As an instructive example, the definition of the iPRC according to Eq. 2.3.15 is illustrated in Fig. 2.15A using a simple LIF model that is subjected to a perturbation to the voltage with amplitude ϵ at phase τ:

$$\begin{aligned} \dot{v} &= \mu - \gamma v + \epsilon\delta(t-\tau), \\ \text{if } v(t) &= v_T \to t_i = t,\, v(t) = v_R. \end{aligned} \tag{2.3.18}$$

As usual, we assume the model has fired a spike at $t_i = 0$, and the voltage is initiated at $v(t_i) = v_R = 0$. In Fig. 2.15A, we distinguish two cases for the following interval. First, a case where the model is unperturbed ($\varepsilon = 0$), thus crossing the threshold and firing a second spike at $t_i + T^*$ (blue line). Second, a case where the model is perturbed, i.e., the voltage increases by the value ε at time τ and crosses the threshold at t_{i+1} (cyan line). The difference between the two intervals (T^* and T_i), or equivalently the spike times ($t_i + T^*$ and t_{i+1}), defines the deviation δT_i (red dotted line). In Fig. 2.15B, the relative deviation $\delta T_i/\varepsilon$, which in turn defines the PRC, is shown as a function of the phase τ at which the perturbation was applied for three different amplitudes ε. The relative deviation for the specific value $\varepsilon = 0.2$ that was used in Fig. 2.15A is shown by the cyan line in Fig. 2.15B. For finite perturbations, two parts of the PRC can be distinguished. Initially, the PRC increases monotonically because the time by which the spike is advanced δT is exactly the time it would have taken the system to get from $v(\tau)$ to $v(\tau) + \varepsilon$. For the LIF model, $v(\tau)$ slows down as the model progresses on the limit cycle, so the effect of a perturbation with a given amplitude increases the later the perturbation is applied. However, this is only true up to a phase τ^* where the PRC has a kink. This phase corresponds to the point where the perturbation is large enough to push the voltage directly above the threshold, i.e., $\varepsilon > v_T - v(\tau^*)$. This is because, after τ^*, the time the next spike can be advanced becomes smaller the closer one gets to the deterministic spike time. As a trivial example, consider a perturbation applied at $t_i + T^*$, which obviously cannot advance the spike time, so that $\delta T_i(\varepsilon, \tau = T^*) = 0$. The time τ^* for which the $\varepsilon > v_T - v(\tau^*)$ is satisfied increases as ε decreases (see yellow and blue lines). The iPRC is shown by a dotted line in Fig. 2.15A and is obtained for an infinitesimally small perturbation amplitude $\varepsilon \to 0$.

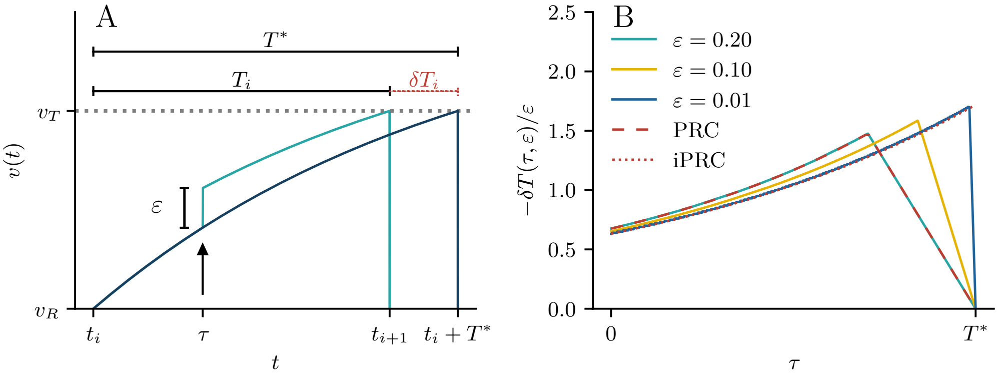

FIGURE 2.15: Panel A illustrates how a perturbation to the voltage affects the next spike time. Two integrate-and-fire models are initialized at $v(t_i) = v_R$. The voltage of the first model evolves unperturbed (blue line) and reaches the threshold after the deterministic period T^*. The voltage of the second model is shifted by $\varepsilon = 0.2$ at the time $t_i + \tau$ (cyan line) and reaches the threshold at an earlier time $t_{i+1} < t_i + T^*$. The difference between the two spike times is denoted δT_i and indicated by a dotted red line. Panel B shows the PRC $Z_v(\tau, \epsilon) = -\delta T_i(\tau, \varepsilon)/\varepsilon$ as a function of the phase τ at which the perturbation is applied for different values of ε. The cyan line corresponds to the value used in A and is compared to the theoretical prediction according to Eq. 2.3.23 (dashed line). For $\epsilon \to 0$, the PRC approaches the iPRC given by Eq. 2.3.24 (dotted line). Parameters $\gamma = 1$, $\mu = 1/(1-\exp(-1)) \approx 1.58$.

For the LIF model, the PRC (for finite perturbations) can be calculated analytically using Eq. 2.3.15. To this end we first calculate the deterministic period T^* ($\epsilon = 0$):

$$T^* = \int_0^{v_T} dv \, \frac{1}{\mu - \gamma v} = \gamma^{-1} \ln\left(\frac{\mu}{\mu - \gamma v_T}\right). \tag{2.3.19}$$

To calculate the perturbed interval, we split the integral in Eq. 2.3.19 into two parts, before and after the perturbation was applied at $v^* = v(\tau)$. Put differently, the time $T(\varepsilon, \tau)$ is composed of two times, namely the time it takes the model to get from $v_R = 0$ to v^* and from $v^* + \varepsilon$ to v_T:

$$T(\varepsilon, \tau) = \int_0^{v^*} dv \, \frac{1}{\mu - \gamma v} + \int_{v^*+\varepsilon}^{v_T} dv \, \frac{1}{\mu - \gamma v} \Theta(v_T - v). \tag{2.3.20}$$

The Heaviside function $\Theta(v)$ takes into account that a perturbation of v beyond the firing threshold yields the same spike time as a perturbation exactly to the threshold (as we have argued previously). We can rearrange the equations to identify the deviation of the spike time:

$$T(\varepsilon, \tau) = \int_0^{v_T} dv \, \frac{1}{\mu - \gamma v} - \int_{v^*}^{v^*+\varepsilon} \frac{1}{\mu - \gamma v} \Theta(v_T - v) = T^* + \delta T(\varepsilon, \tau). \tag{2.3.21}$$

The calculation of $\delta T(\varepsilon, \tau)$ requires the knowledge of v^* which is given by

$$\int_0^{\tau} dt = \int_0^{v^*} dv \, \frac{1}{\mu - \gamma v} \implies v^* = \frac{\mu}{\gamma}(1 - e^{-\gamma \tau}). \tag{2.3.22}$$

Finally, we have all the pieces together to solve for the deviation of the interval using Eq. 2.3.21 and Eq. 2.3.22:

$$\delta T(\varepsilon, \tau) = -\int_{v^*}^{v^*+\varepsilon} dv \, \frac{1}{\mu - \gamma v} \Theta(v_T - v) \quad = \begin{cases} -\gamma^{-1} \ln\left(1 - \varepsilon \frac{\gamma}{\mu} e^{\gamma \tau}\right), & \text{if } v^* + \varepsilon < v_T, \\ T^* - \tau, & \text{if } v^* + \varepsilon > v_T. \end{cases} \tag{2.3.23}$$

The second case corresponds to the situation where $v^* + \varepsilon$ lies beyond the threshold and can be understood as follows: If the model crosses the threshold due to the perturbation at time τ, then $t_{i+1} = \tau$ is the spike time and the deviation from the unperturbed interval is simply given by $T^* - \tau$. In Fig. 2.15B, the PRC according to Eq. 2.3.23 for $\varepsilon = 0.2$ is shown by a dashed line and shows excellent agreement with the cyan line obtained from numerical simulations. To obtain the iPRC $Z_v(\tau)$ according to Eq. 2.3.15, we expand $\delta T(\varepsilon, \tau)$ up to the first order (higher order terms vanish as $\varepsilon \to 0$):

$$Z_v(\tau) = -\lim_{\varepsilon \to 0} \frac{\delta T(0, \tau) + \varepsilon \delta T'(0, \tau)}{\varepsilon} = \frac{1}{\mu} e^{\gamma \tau}, \tag{2.3.24}$$

which is shown by a dashed line in Fig. 2.15B.

The direct method presented here allows for an intuitive understanding of the PRC and iPRC and their relation to the response of the spike timing to a certain perturbation. The disadvantage of this method is that it is difficult to utilize when dealing with systems that are more complicated than the LIF model, for example, for multidimensional IF models. In the following, we calculate the iPRC for a number of prominent IF models using the adjoint method. Because we will not return to the case of a finite perturbation, we will also refer to the iPRC simply as the PRC for ease of notation.

2.3.5 Phase response curves for integrate-and-fire neuron models

In the following, we show how to calculate the PRC using the adjoint method first for one-dimensional IF models and then for the LIF and GIF models in both cases with a spike-triggered adaptation current. These two models will be used frequently for illustrative purposes in Sec. 2.4. We note that these PRCs have already been calculated by Schwalger and Lindner [74] and are shown here for completeness.

We have already emphasized that the PRC obtained by the direct method Eq. 2.3.15 is not fully equivalent to the PRC defined by the adjoint method Eq. 2.3.11, 2.3.12, and 2.3.13. To emphasize this again, according to Eq. 2.3.15, two points have the same phase if they fire their next spike in synchrony. This is somewhat different from the definition of phase according to Eq. 2.3.3, where two points have the same phase if they become asymptotically indistinguishable, which only guarantees that they fire asymptotically synchronously. The former definition corresponds to the so-called "first-order PRC", which is often measured experimentally [136]. In this case, the adjoint method remains valid, except that the periodic boundary condition is replaced by

$$Z_{w_1}(T^*) = \cdots = Z_{w_N}(T^*) = Z_a(T^*) = 0. \tag{2.3.25}$$

This means that the PRC vanishes at the firing threshold for every variable except for the voltage. Schwalger and Lindner [74] have given a nice intuitive reasoning for these boundary conditions: If the isochrones are defined as sets that lead to the same spike time, then the threshold hyperplane is a special isochrone with phase $\tau = T^*$ (cf. Fig. 2.14). Close to the threshold (and limit cycle), the isochrones will thus be parallel to the threshold and perturbations in any direction but the voltage will not change the phase. Note that if we use Eq. 2.3.25 to evaluate the normalization Eq. 2.3.12 at $\tau = T^*$ we find

$$\dot{v}_\Gamma(T^*) Z_v(T^*) = 1. \tag{2.3.26}$$

In other words, the PRC with respect to the voltage evaluated at the threshold is given by the inverse velocity of the voltage $Z_v(T^*) = \dot{v}_\Gamma(T^*)^{-1}$. Specifically, this implies $Z_v(T^*) > 0$ because, in the mean-driven regime, the threshold is crossed even in the absence of fluctuations, so the velocity of the voltage must be positive at the threshold $\dot{v}_\Gamma(T^*) > 0$.

To calculate the PRC by means of the adjoint equation $\dot{\mathbf{Z}}(\tau) = -A^T(\tau)\mathbf{Z}(\tau)$ we first have to determine the (transposed) Jacobian matrix

$$A^T(\tau) = \left. \begin{pmatrix} \partial_v f_0 & \partial_v f_1 & \dots & \partial_v f_N & 0 \\ \partial_{w_1} f_0 & \partial_{w_1} f_1 & \dots & \partial_{w_1} f_N & 0 \\ \vdots & \vdots & \ddots & \vdots & \vdots \\ \partial_{w_N} f_0 & \partial_{w_N} f_1 & \dots & \partial_{w_N} f_N & 0 \\ -1 & \dots & \dots & 0 & -\tau_a^{-1} \end{pmatrix} \right|_{\mathbf{x}(\tau)=\mathbf{x}_\Gamma(\tau)} \tag{2.3.27}$$

evaluated on the limit cycle $\mathbf{x}_\Gamma(t)$. Because we consider a spike-triggered adaptation, the dynamics of $a(t)$ depend only on the spike times t_i but neither on v nor any of the auxiliary variables w_j. Consequently, the last column of $A^T(t)$ simplifies significantly (here, we would usually find the derivation of the dynamics of a with respect to v and w_j).

One-dimensional integrate-and-fire models

Solving the adjoint equation requires to specify the functions $f_0(v, \mathbf{w})$ and $f_j(v, \mathbf{w})$. However, some general statements can be derived for one-dimensional integrate-and-fire models with a spike-triggered adaptation. For these models, the (transposed) Jacobian matrix reduces to

$$A^T_{1\mathrm{D}}(\tau) = \left. \begin{pmatrix} \partial_v f_0 & 0 \\ -1 & -\tau_a^{-1} \end{pmatrix} \right|_{\mathbf{x}(t)=\mathbf{x}_\Gamma(\tau)} \tag{2.3.28}$$

and the PRC with respect to a perturbation to the voltage is the solution to the linear differential equation $\dot{Z}_v = f_0'(v_\Gamma(\tau))Z_v$ that can formally be solved [74]:

$$Z_v(\tau) = Z_v(T^*) \exp\left[\int_\tau^{T^*} dt'\, f_0'(v_\Gamma(t'))\right]. \tag{2.3.29}$$

Since the model is mean-driven, we can conclude that $Z_v(T^*) = \dot{v}_0(T^*)^{-1} > 0$ because the velocity $\dot{v}_\Gamma(t) = f_0(v_\Gamma(t)) + \mu - a_0(t)$ is always positive, especially at the phase T^*, i.e., at the threshold where the inverse velocity and thus the PRC is given by

$$Z_v(T^*) = \frac{1}{f_0(v_T) + \mu - a^* + \Delta/\tau_a}, \tag{2.3.30}$$

where a^* refers to the value of $a_0(t)$ right after the reset[2]. For one-dimensional IF models (with a spike-triggered adaptation variable), the PRC is thus strictly positive, a property generally associated with Type I neuron models [145]. This can also be understood intuitively because the voltage is a monotonically increasing function of time for any mean-driven, one-dimensional model. A positive kick to the voltage brings the model closer to the threshold and reduces the time until the next spike; there is simply no way how a positive kick of the voltage could cause a delay in the next spike. Such a delay would require some kind of detour in phase space that is only possible in higher dimensions.

We can also make a general statement about the PRC with respect to the adaptation variable $Z_a(\tau)$ governed by

$$\dot{Z}_a(\tau) = Z_v(\tau) + Z_a(\tau)/\tau_a. \tag{2.3.31}$$

The formal solution to this equation reads

$$Z_a(\tau) = e^{\tau/\tau_a}\left(Z_a(\tau_0) + \int_{\tau_0}^{t} Z_v(t')e^{-t'/\tau_a}\right), \tag{2.3.32}$$

where τ_0 is a reference phase, similar to an initial condition, at which $Z_a(\tau_0)$ is specified. Because the PRC in any direction but the membrane potential vanishes at the threshold hyperplane, it is convenient to choose $\tau_0 = T^*$ so that $Z_a(T^*) = 0$ which yields

$$Z_a(\tau) = -e^{\tau/\tau_a}\int_{t}^{T^*} dt' Z_v(t')e^{-t'/\tau_a}. \tag{2.3.33}$$

In contrast to $Z_v(t)$, this function is strictly negative, i.e., a positive kick to the adaptation variable delays the next spike. This is also reasonable since the adaptation current has an inhibitory effect on the voltage dynamics.

Linear integrate-and-fire models

Let us now turn to linear IF models for which we can often find exact expressions for the PRCs by means of the adjoint method. This is so because, in this case, the Jacobian matrix only contains constants, and its evaluation on the limit cycle becomes redundant. Moreover, for linear models, the PRCs $Z_v(\tau)$ and $Z_{w_j}(\tau)$ are independent of the adaptation variable (except for the normalization) because their governing equations do not depend on $Z_a(\tau)$ (Eq. 2.3.27). For this reason, we refer to the adaptive LIF model as a one-dimensional model since the spike-triggered adaptation does not add any qualitatively new behavior with respect to the PRC. In Fig. 2.16, we compare the PRCs for the adaptive LIF and GIF models either calculated numerically by the direct method (colored area) or analytically by the adjoint method (black lines).

First, we consider the LIF model with the leak term $f_0(v) = -\gamma v$. The PRCs are determined by

$$\frac{d}{d\tau}\begin{pmatrix} Z_v \\ Z_a \end{pmatrix} = A^T_{\text{aLIF}}\begin{pmatrix} Z_v \\ Z_a \end{pmatrix}, \quad \text{with} \quad A^T_{\text{aLIF}} = \begin{pmatrix} -\gamma & 0 \\ -1 & -\tau_a^{-1} \end{pmatrix}, \tag{2.3.34}$$

---

[2] The last term in the denominator $a(T^*) = a^* - \Delta/\tau_a$ requires some explanation. On the limit cycle, the decay of $a(t)$ over one period balances exactly its increase by Δ/τ_a upon reaching the threshold. This means that if $a_0(\tau = 0) = a^*$ is defined as the value of the adaptation variable at the beginning of an interval, then it follows that the value of the adaptation variable upon hitting the threshold but right before it is increased is given by $a_0(\tau = T^*) = a^* - \Delta/\tau_a$.

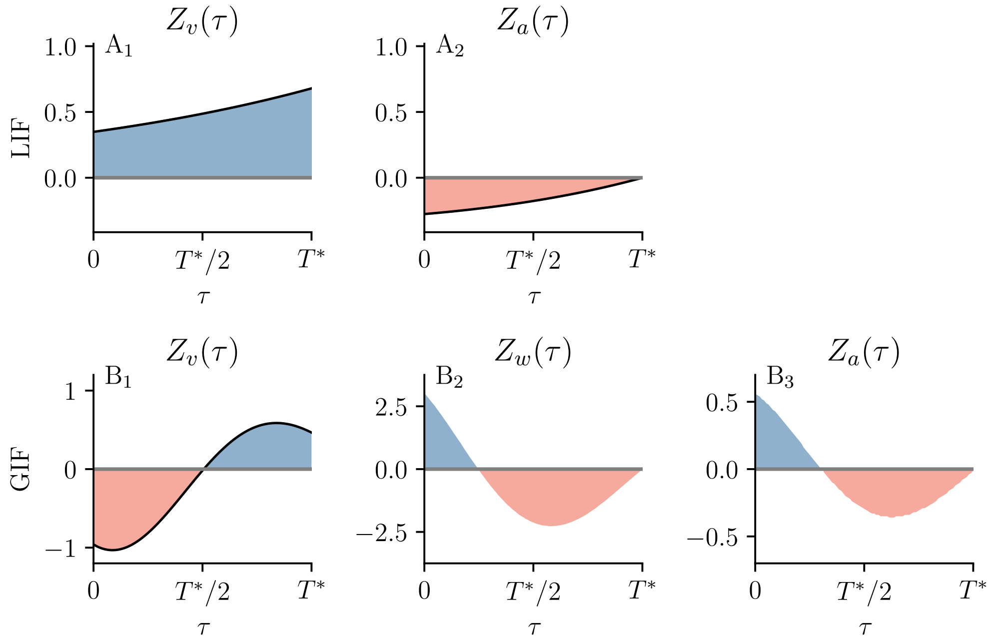

FIGURE 2.16: Panel A shows the two PRCs for the adaptive LIF model. The PRC of the voltage Z_v is strictly positive, while the PRC for the adaptation variable Z_a is strictly negative, as expected for a one-dimensional model. Panel B shows the three PRCs for the adaptive GIF model. Since the GIF model is two-dimensional, the PRC Z_v can become partially negative, as shown in B_1. Similarly, the PRC of the auxiliary variable Z_w and the PRC of the adaptation variable Z_a can be partially positive, although both variables enter the dynamics of the voltage with a negative sign. Theoretical predictions (black line) are compared to numerical calculations of the spike time deviation (filled curves). Parameters A: $\gamma = 1$, $\mu = 5$, $\tau_a = 2$, $\Delta = 2$; B: $\gamma = -1$, $\mu = -1$, $\tau_w = 2$, $\beta = 5$, $\tau_a = 1$, $\Delta = 0.1$.

and the usual normalization and boundary conditions. This system of linear differential equations is solved by:

$$Z_v(\tau) = \frac{e^{\gamma(\tau - T^*)}}{\dot{v}(T^*)} = \frac{e^{\gamma(\tau-T^*)}}{\mu - \gamma v_T - a^* + \Delta/\tau}, \tag{2.3.35}$$

$$Z_a(\tau) = \frac{e^{(\tau-T^*)/\tau_a} - e^{\gamma(\tau-T^*)}}{(\gamma - \tau_a^{-1})(\mu - \gamma v_T - a^* + \Delta/\tau)}, \tag{2.3.36}$$

and shown by a black line in Fig. 2.16A_1 and A_2. We can compare this result in the limit of a vanishing adaptation ($\Delta = 0$) to the PRC $Z_v(\tau) = \mu^{-1}e^{\gamma\tau}$ that has been calculated by the direct method in Sec. 2.3.4. For a vanishing adaptation, the velocity at the threshold and the period are given by $\dot{v}(T^*) = \mu - \gamma$ and $T^* = \gamma^{-1}\log(\mu/(\mu - \gamma v_T))$, respectively. The second equation can rearranged to obtain $\exp(-\gamma T^*) = (\mu - \gamma v_T)/\mu$. Substituting both in Eq. 2.3.35 yields

$$\lim_{a^* \to 0} Z_v(\tau) = \frac{e^{\gamma t}e^{-\gamma T^*}}{\mu - \gamma v_T} = \frac{e^{\gamma\tau}}{\mu}, \tag{2.3.37}$$

which agrees with the PRC calculated previously.

Secondly, we consider the two-dimensional GIF model with $f_0(v, w) = -\gamma v - \beta w$ and $f_1(v, w) = (v - w)/\tau_w$. The Jacobian matrix is given by

$$\frac{d}{d\tau}\begin{pmatrix} Z_v \\ Z_w \\ Z_a \end{pmatrix} = A^T_{\text{aGIF}} \begin{pmatrix} Z_v \\ Z_w \\ Z_a \end{pmatrix}, \quad \text{with} \quad A^T_{\text{aGIF}} = \begin{pmatrix} -\gamma & \tau_w^{-1} & 0 \\ -\beta & -\tau_w^{-1} & 0 \\ -1 & 0 & -\tau_a^{-1} \end{pmatrix}. \tag{2.3.38}$$

The solution to Eq. 2.3.38 was given by Schwalger and Lindner [74] and reads

$$Z_v(\tau) = \frac{e^{\frac{\nu}{2}(\tau - T^*)}\left[\cos(\Omega(\tau - T^*)) - \frac{1-\gamma\tau_w}{2\tau_w\Omega}\sin(\Omega(\tau - T^*))\right]}{\mu - \gamma v_t - \beta w_0(T^*) - a^* + \Delta/\tau_a} \tag{2.3.39}$$

with $\nu = \gamma + \tau_w^{-1}$ and $\Omega = \sqrt{\frac{\gamma+\beta}{\tau_w} - \frac{\nu^2}{4}}$ and is again shown by a black line in Fig. 2.16B$_1$. The PRC $Z_v(\tau)$ of the two-dimensional GIF model can thus be qualitatively different from the PRC of any one-dimensional model because it can be partially negative. This means that a positive kick to the voltage, even though it brings the model closer to the firing threshold, can delay the next spike time. The mechanism is illustrated in Fig. 2.17 using (for illustration purposes) a GIF model without adaptation. We first calculate the limit cycle (red line) corresponding to the trajectory $v(t), w(t)$ with the initial condition $v(0) = 0, w(0) = 0$ (red square) and compare it with a second trajectory (blue line) with the initial condition $v(0) = \varepsilon, w(0) = 0$ (blue square) corresponding to a perturbation of the system at phase $\tau = 0$. As a result of the initial perturbation, the blue trajectory makes a large detour in the phase space, which leads to a delay of the next spike (compared to the red trajectory). In general, the detour alone is insufficient to conclude that the next spike is delayed, but we also need to consider the velocity. For example, if we choose the initial condition so that the trajectory moves very close to the unstable fixed point (shown as a black circle in Fig. 2.17), the dynamics of v and w will become very slow, and it is conceivable that this will lead to a strong delay of the next spike, even though the trajectory is "shorter".

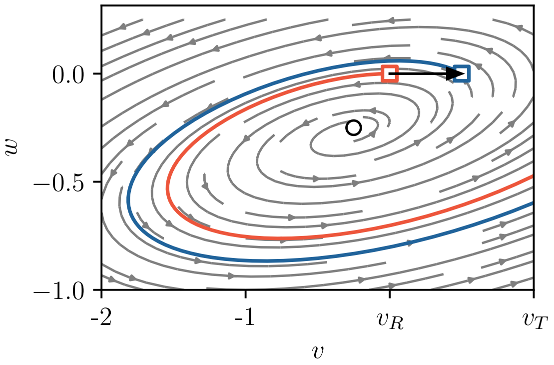

FIGURE 2.17: Illustration of the spike time delay due to a positive voltage perturbation at the beginning of the firing cycle in a (non-adaptive) GIF model. The red line indicates the limit cycle and corresponds to a trajectory of the GIF model with initial condition $v(0) = v_R, w(0) = w_R$ (red square). For the blue trajectory, the GIF model suffers an immediate (positive) perturbation so that the model is effectively initiated at $v(0) = v_R + \varepsilon, w(0) = w_R$ (blue square). The resulting trajectory takes a long detour through the phase space and reaches the threshold later than the blue trajectory, corresponding to a delay in the spike time. Parameters: $\gamma = -1, \mu = -1, \tau_w = 5,$ $\beta = 2$.

2.4 Interspike-interval correlations for tonically firing neurons

In this section, we return to the most general case and study a stochastic multidimensional IF neuron model endowed with a spike-triggered adaptation $a(t)$ and subject to both a correlated noise $\eta(t)$ and uncorrelated noise $\xi_v(t)$ as introduced in Eq. 2.2.17:

$$\begin{aligned} \dot{v} &= f_0(v, \mathbf{w}) + \mu - a + \eta + \sqrt{2D}\xi_v(t), \\ \dot{w}_j &= f_j(v, \mathbf{w}), \\ \tau_a \dot{a} &= -a + \Delta \sum \delta(t - t_i), \\ \tau_\eta \dot{\eta} &= -\eta + \sqrt{2\sigma^2 \tau_\eta}\xi_\eta(t), \\ &\text{if } v(t) = v_T \to t_i = t,\ v(t) = v_R,\ \mathbf{w}(t) = \mathbf{w}_R. \end{aligned} \tag{2.4.1}$$

We emphasize again that this model is an extension of the model studied by Schwalger and Lindner [74]. To calculate the SCC ρ_k using the PRC, we assume the system has a limit cycle solution in the deterministic limit ($D = 0, \sigma = 0$). As we have pointed out in Sec. 2.2, such a model generates a *nonrenewal* spike train, i.e., the intervals between successive spike times are not statistically independent but correlated. Specifically, in Eq. 2.4.1, the correlation between adjacent intervals T_i, T_{i+1} and generally between any two intervals T_i, T_{i+k} with $k > 0$ are due to the adaption current $a(t)$ on the one hand and the correlated noise $\eta(t)$ on the other hand. This is so because these two variables are not reset when a spike is fired and thus can carry information from one interspike interval to another.

In Sec. 1.3, we have explained that for a renewal point process, the ISI is fully characterized by its probability distribution $p_{\text{ISI}}(T)$. In contrast, for a nonrenewal point process, each ISI depends on the entire history of the intervals, and the joint probability distribution $p(T_i, T_{i+k})$ does not factorize into the marginal distributions. In Eq. 1.3.28, we introduced a measure that quantifies *linear* correlations between intervals, namely the SCC, which is repeated here for convenience:

$$\rho_k = \frac{\langle \Delta T_i \Delta T_{i+k} \rangle}{\langle \Delta T^2 \rangle}. \tag{2.4.2}$$

We recall that the SCC is a dimensionless measure that compares the covariance (numerator) to the variance (denominator) of the ISI and thus ranges between $-1 < \rho_k < 1$. This measure is positive if two intervals T_i, T_{i+k} deviate on average similarly from the mean, i.e., if both are longer (or shorter) than the mean. In this case, the intervals are said to be correlated. Conversely, if a long interval is usually followed by a short interval (or vice versa), the SCC is negative ($\rho_1 < 0$). In this case, the intervals are said to be anti-correlated. The goal of this chapter is to determine the SCC ρ_k for a multidimensional IF model with spike-triggered adaptation *and* correlated noise (Eq. 2.4.1).

Following Schwalger and Lindner [74], we perform a systematic first-order approximation of the ISI with respect to a perturbation from the limit cycle. In other words, we expand the intervals around their deterministic period

$$T_i \approx T^* + \delta T_i, \tag{2.4.3}$$

where $\delta T_i \propto \varepsilon^1$ and ε is an abstract parameter corresponding to the amplitude of the perturbation. Furthermore, we assume that the mean ISI is affected by the perturbation only in the second order of its amplitude so that (up to the first order) the mean and the deterministic interval agree

$$\langle T \rangle \approx T^*. \tag{2.4.4}$$

This allows to approximate deviations from the mean interval ΔT_i by the first-order deviation from the deterministic interval δT_i, and in turn to approximate the SCC as follows

$$\rho_k \approx \frac{\langle \delta T_i \delta T_{i+k} \rangle}{\langle \delta T^2 \rangle}. \tag{2.4.5}$$

Deviations from the deterministic limit cycle are exactly what the PRC quantifies. In fact, in Sec. 2.3.4, we have extensively discussed the definition of the PRC in terms of the spike-time deviation in response to a small voltage perturbation (repeated here for convenience):

$$Z_v(\tau) = -\lim_{\varepsilon \to 0} \frac{\delta T(\varepsilon, \tau)}{\varepsilon}. \tag{2.4.6}$$

Strictly speaking, this definition relied on a perturbation of the form $\epsilon\delta(t - \tau)$ applied to the voltage variable at a specific phase τ of the firing cycle. More generally, the linear response of the spike-time deviation to an arbitrary perturbation is given by the integral over the (vector-valued) response function

$$\delta T_i = -\int_0^{T^*} d\tau \, \mathbf{Z}(\tau) \mathbf{u}_i(\tau), \tag{2.4.7}$$

where $\mathbf{u}_i(\tau) = \mathbf{u}(t_i + \tau)$ is the perturbation, i.e. the deviation from the limit cycle, during the

i-th interval. In Fig. 2.18, we present a sketch illustrating how a voltage perturbation $u_i(\tau)$ (left panel) can be translated into a perturbation of the phase variable $Z_v(\tau)u_i(\tau)$ using of a phase-dependent weighting factor given by the PRC (middle panel), which is integrated over the entire interval T^* to obtain the deviation of the spike time δT_i (right panel). In order to determine the SCC according to Eq. 2.4.5 and 2.4.7, we have to identify the perturbation from the limit cycle over two different intervals $u_i(\tau)$ and $u_{i+k}(\tau)$, weight them by the PRC $Z(\tau)$, calculate the integral of the weighted perturbation, build products and finally form the average. This is demonstrated below by an instructive example where the perturbation from the limit cycle can be read directly from the dynamical equations.

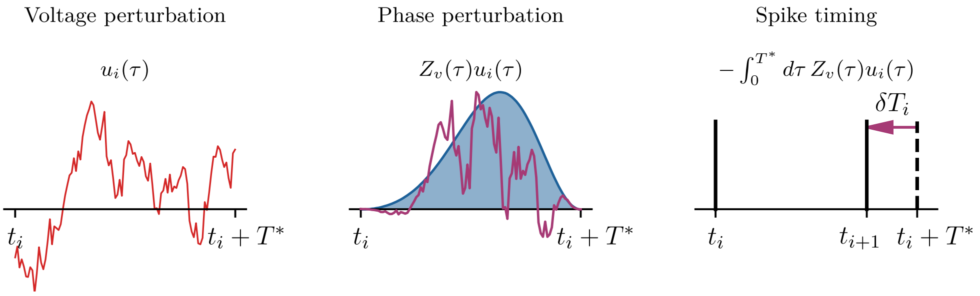

FIGURE 2.18: The left panel shows a continuous voltage perturbation $u_i(\tau)$ (red line) that affects a neuron model moving along the limit cycle. The perturbation of the voltage corresponds perturbation of the phase, as illustrated in the middle panel. The voltage perturbation is weighted by the PRC (blue curve) to obtain the phase perturbation (purple line) given by the product $Z_v(\tau)u_i(\tau)$. The integral of the phase perturbation gives the phase shift after time T^*. Due to the scaling of the phase $\tau \in [0, T^*]$, this phase shift equals the spike time deviation δT_i (purple arrow) shown in the right panel.

2.4.1 Correlation coefficient for integrate-and-fire models with correlated noise

Here, we calculate the SCC for a non-adaptive stochastic IF model that is subject to a correlated as well as uncorrelated noise:

$$\begin{aligned}
\dot{v} &= f_0(v, \mathbf{w}) + \mu + \eta + \sqrt{2D}\xi_v(t), \\
\dot{w}_j &= f_j(v, \mathbf{w}), \\
\tau_\eta \dot{\eta} &= -\eta + \sqrt{2\tau_\eta \sigma^2}\xi_\eta(t), \\
&\text{if } v(t) = v_T \to t_i = t,\ v(t) = v_R,\ \mathbf{w}(t) = \mathbf{w}_R.
\end{aligned} \tag{2.4.8}$$

A similar case was studied by Schwalger, Droste, and Lindner [95], except that they considered a more general correlated noise $\eta(t)$ with an arbitrary correlation function but no additional white noise. We will see that neither of these differences is particularly important for the derivation.

In Eq. 2.4.8, correlations between any two intervals are caused by the correlated noise $\eta(t)$. This is so because the voltage $v(t)$ and auxiliary variables $w_j(t)$ are reset whenever a spike is fired, and the Gaussian white noise $\xi_v(t)$ is uncorrelated per definition. None of these variables can transfer information from one ISI to another. Under the assumptions given in Sec. 2.3, in particular, that the model is mean-driven and the mean ISI $\langle T_i \rangle$ is well approximated by the deterministic ISI T^*, we can determine the deviations δT_i using the PRC $Z_v(\tau)$:

$$\delta T_i = -\int_0^{T^*} d\tau\, Z_v(\tau) u_i(\tau). \tag{2.4.9}$$

Here, $u_i(\tau)$ is the voltage perturbation over the i-th interval given by

$$u_i(\tau) = \eta(t_i + \tau) + \sqrt{2D}\xi_v(t_i + \tau). \tag{2.4.10}$$

This perturbation is obtained by comparing the governing equation of v in the stochastic (Eq. 2.4.8) and the deterministic case (Eq. 2.4.8 with $D = 0$ and $\sigma = 0$). Thus, the deterministic system is perturbed by two independent processes: the OU process $\eta(t)$ and the Gaussian white noise $\xi_v(t)$. Substituting this expression into Eq. 2.4.9 allows to calculate the deviation of the i-th interval T_i from the deterministic period T^*:

$$\delta T_i = -\int_0^{T^*} d\tau\, Z_v(\tau)\left[\eta(t_i+\tau) - \sqrt{2D}\xi_v(t_i+\tau)\right]. \tag{2.4.11}$$

The two occurring integrals are Gaussian random numbers:

$$H_i = \int_0^{T^*} d\tau\, Z(\tau)\eta(t_i+\tau), \tag{2.4.12}$$

$$\Xi_i = \int_0^{T^*} d\tau\, Z(\tau)\sqrt{2D}\xi_v(t_i+\tau), \tag{2.4.13}$$

which are independent because they arise from two different noise sources, ξ_η and ξ_v. The indices have been chosen so that H_i and Ξ_i are associated with the i-th interval. The covariance between two ISIs is given by

$$\begin{aligned}\langle \delta T_i \delta T_{i+k}\rangle =& \langle H_i H_{i+k} + \Xi_i \Xi_{i+k}\rangle \\ =& \int_0^{T^*}\int_0^{T^*} d\tau_1 d\tau_2\, Z(\tau_1)Z(\tau_2)\times \\ &\times \left[C_{\eta\eta}(t_{i+k}-t_i+\tau_2-\tau_1) + 2DC_{\xi\xi}(t_{i+k}-t_i+\tau_2-\tau_1)\right],\end{aligned} \tag{2.4.14}$$

where mixed terms $\langle H_i \Xi_j\rangle$ vanish because the random numbers are independent. The difference between the spike times in the argument of the correlation function can be simplified as follows

$$C(t_{i+k}-t_i+\tau_2-\tau_1) \approx C(kT^*+\tau_2-\tau_1), \tag{2.4.15}$$

because terms in the argument of the correlation function that are of the first order of the perturbation amplitude affect the covariance only in higher order. To make this argument more precise, we neglect the white noise for a moment so that the IF model is perturbed only by the OU process. In this case, the OU process's standard deviation σ equals the amplitude of the perturbation. The correlation function $C_{\eta\eta}(\tau) = \sigma^2 \exp(-|\tau|/\tau_\eta)$ itself is already of order σ^2 (here the leading order), considering additional first-order perturbations in the argument of the correlation function affects the covariance of the ISI at least in third order σ^3. Thus, the covariance can be expressed in leading order by

$$\langle \delta T_i \delta T_{i+k}\rangle = \int_0^{T^*}\int_0^{T^*} d\tau_1 d\tau_2\, Z(\tau_1)Z(\tau_2)\left[C_{\eta\eta}(kT^*+\tau_2-\tau_1) + 2DC_{\xi\xi}(kT^*+\tau_2-\tau_1)\right], \tag{2.4.16}$$

with $C_{\eta\eta}(t) = \sigma^2\exp(-|t|/\tau_\eta)$ and $C_{\xi\xi}(t) = \delta(t)$. In the following, we will keep the general expression $C_{\eta\eta}(t)$ because the results do not only apply to the specific correlation function of the OU process. Since the Gaussian white noise is delta correlated, it contributes to the variance ($k = 0$) but not to the covariance ($k \neq 0$) - an uncorrelated noise does not directly introduce correlations between intervals. It is, therefore, convenient to distinguish two cases. One in which the time windows over which the integrals are formed overlap ($k = 0$), and one in which they do not ($k > 0$):

$$\langle \delta T_i \delta T_{i+k}\rangle \approx \begin{cases} \int_0^{T^*}\int_0^{T^*} d\tau_1 d\tau_2\, Z(\tau_1)Z(\tau_2)\left[C_{\eta\eta}(\tau_2-\tau_1) + 2D\delta(\tau_2-\tau_1)\right], & k=0, \\ \int_0^{T^*}\int_0^{T^*} d\tau_1 d\tau_2\, Z(\tau_1)Z(\tau_2)\left[C_{\eta\eta}(kT^*+\tau_2-\tau_1)\right], & k>0. \end{cases} \tag{2.4.17}$$

The ratio of these two cases determines the SCC:

$$\rho_k = \frac{\int_0^{T^*}\int_0^{T^*} d\tau_1 d\tau_2\, Z(\tau_1)Z(\tau_2)\left[C_{\eta\eta}(kT^*+\tau_2-\tau_1)\right]}{\int_0^{T^*}\int_0^{T^*} d\tau_1 d\tau_2\, Z(\tau_1)Z(\tau_2)\left[C_{\eta\eta}(\tau_2-\tau_1)+2D\delta(\tau_2-\tau_1)\right]}. \tag{2.4.18}$$

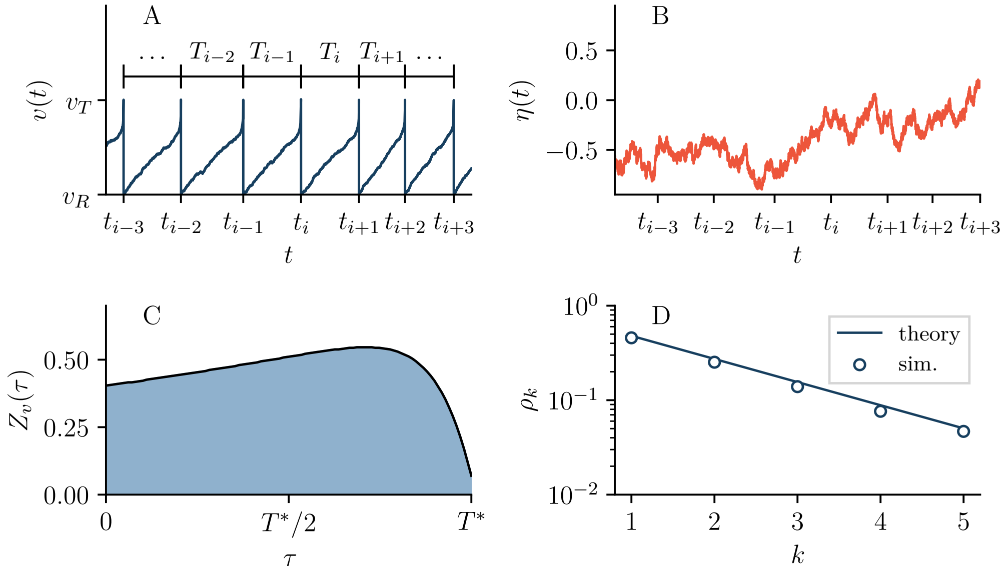

FIGURE 2.19: Serial correlations in a stochastic EIF model with correlated noise. Panel A shows a voltage trajectory $v(t)$ together with the spike times t_i and corresponding ISIs T_i. Panel B shows a trajectory of the slow varying noise $\eta(t)$ that is correlated over multiple spike times and affects adjacent ISIs similarly. Panel C shows the PRC of the EIF model. Panel D shows the SCC obtained from stochastic simulations (circle) and according to Eq. 2.4.18 (line). The exponential decay of ρ_k with k stems from the exponential correlation function of η. Parameters: $v_T = 2$, $\gamma = 1$, $\mu = 3$, $\Delta_T = 0.1$, $\sigma^2 = 0.1$, $\tau_\eta = 1$, $D = 0.01$, $T^* \approx 0.56$.

In Fig. 2.19, we use an EIF model ($f_0(v) = \mu - \gamma v + \Delta_T \exp[(v - \hat{v}_T)/\Delta_T]$) subject to an OU noise and calculate the SCC according to Eq. 2.4.18. As we have pointed in Sec. 2.2.4 out, the EIF model is of special interest because its nonlinearity can be attributed to the positive feedback mediated by the Na$^+$ current. In Fig. 2.19A we show $v(t)$ over multiple spike times $\dots, t_{i-1}, t_i, t_{i+1}, \dots$ together with the corresponding ISIs $\dots, T_{i-1}, T_i, T_{i+1}, \dots$. The trajectory of the perturbation, here the OU process $\eta(t)$ is shown in Fig. 2.19B. For the EIF model, the PRC has to be determined numerically and is shown in Fig. 2.19C. Because it is strictly positive, as for any one-dimensional model, a positive perturbation to the voltage always advances the phase and results in a shortened interval (and vice versa). The resulting SCC

$$\rho_k = \rho_1 e^{-(k-1)T^*/\tau_\eta}, \tag{2.4.19}$$

is an exponential function of the lag k (Fig. 2.19D) just like the correlation function of the OU process. This is so because in the case of the OU process the dependence of the correlation function $C_{\eta\eta}(kT^* + \tau_2 - \tau_1) = \sigma^2 \exp(-|kT^* + \tau_2 - \tau_1|/\tau_\eta)$ on k can be removed from the absolute value $|kT^* + \tau_2 - \tau_1| = (k-1)T^* + |T^* + \tau_2 - \tau_1|$ and from the integral because $\tau_1, \tau_2 \in [0, T^*]$.

As we have mentioned above, a similar result (specifically for the case $D = 0$) has already been derived by Schwalger, Droste, and Lindner [95], who chose to express the result in the Fourier domain

$$\rho_k = \frac{\int_{-\infty}^{\infty} df\, |\tilde{Z}(f)|^2 S_{\eta\eta}(f) e^{i2\pi f k T^*}}{\int_{-\infty}^{\infty} df\, |\tilde{Z}(f)|^2 \left[S_{\eta\eta}(f) + 2D\right]}, \tag{2.4.20}$$

using the finite Fourier transform $\tilde{Z}(f) = \int_0^{T^*} d\tau\, Z(\tau) \exp(i2\pi f \tau)/T^*$ and the Wiener–Khinchin theorem $C(\tau) = \int_{-\infty}^{\infty} df\, S(f) \exp(i2\pi f \tau)$. Eq. 2.4.18 and Eq. 2.4.20 are equivalent, but depending on the context, it may be more convenient to use one or the other.

The derived expression relates the SCC to i) the PRC of a deterministic integrate-and-fire model and ii) the correlation function of the noise. Based on the derivation presented, one might wonder to what extent the particular model affects the expression of the SCC beyond the PRC.

In other words, could any model be used as long as the PRC is accessible? This is not the case because the fact that all variables are reset upon firing of an action potential is essential to derive the perturbation (Eq. 2.4.10) in the first place. For example, suppose another variable is directly or indirectly affected by the noise and is not reset when the threshold is reached. In that case, its initial value at the beginning of each interval generally does not agree with the deterministic value and also contributes to the perturbation. This can lead to significant interval correlations even if the model is driven by a white noise [74, 146]. We will consider this scenario below.

2.4.2 Correlation coefficient for adaptive integrate-and-fire models with correlated noise

Let us now return to the full model (Eq. 2.4.1) repeated here for convenience:

$$\begin{aligned} \dot{v} &= f_0(v, \mathbf{w}) + \mu - a + \eta + \sqrt{2D}\xi_v(t), \\ \dot{w}_j &= f_j(v, \mathbf{w}), \\ \tau_a \dot{a} &= -a + \Delta \sum \delta(t - t_i), \\ \tau_\eta \dot{\eta} &= -\eta + \sqrt{2\tau_\eta \sigma^2}\xi_\eta(t), \\ &\text{if } v(t) = v_T \to t_i = t,\, v(t) = v_R,\, \mathbf{w}(t) = \mathbf{w}_R. \end{aligned} \tag{2.4.21}$$

In contrast to Eq. 2.4.8, this model is additionally subject to a slow adaptation current $a(t)$, which is not reset when a spike is fired, but is increased by Δ/τ_a.

In order to familiarize ourselves with the interplay of adaptation and correlated noise, we consider the EIF model again. The time course of the voltage $v(t)$, the adaptation $a(t)$, and the correlated noise $\eta(t)$ are shown in Fig. 2.20A. As before, the colored noise perturbs the voltage directly and would by itself generate positive ISI correlations. However, the (correlated and uncorrelated) noise also causes an indirect perturbation via the adaptation variable. That the adaptation variable at the beginning of the ISIs does not always take the value corresponding to the deterministic limit is illustrated in Fig. 2.20B where we show the deterministic limit cycle (red line) together with a noisy trajectory (blue line). The initial conditions (over an ISI) $a_i := a(t_i^+)$ taken right after the reset do, in general, not agree with the deterministic value a^*. We briefly recall why this is the case: In the deterministic limit, the IF model moves along the limit cycle, and the adaptation decays exponentially $a(t) = a^* \exp(-t/\tau_a)$ between spikes (t is measured relative to the last spike time t_i). When a spike is fired, the adaptation is immediately increased by Δ/τ_a. In this limit, decrease and increase are always balanced. In the stochastic case, the ISIs will generally not coincide with the deterministic period T^*. Consequently, the adaptation variable decreases more when $T_i > T^*$ or less when $T_i < T^*$. Since the increment Δ/τ_a is fixed, the peak adaptation values a_i deviate from the limit cycle depending on the deviation of the ISI from the deterministic period. How such a spike-triggered adaption shapes the SCC ρ_k for stochastic IF models driven solely by a white noise was studied extensively by Schwalger and Lindner [74] and we will return to this special case in the limit $\tau_\eta \to 0$ for our model. Here the case is more complicated since the correlated noise that caused the deviation say a shortening, of the ISI T_i compared to T^* will generally also contribute to a shortening of the next interval T_{i+1}. At the same time, the adaptation has the opposite effect; a shortened interval T_i results in a lengthened interval T_{i+1} on average. Which of these two effects determines the correlation between the intervals T_i and T_{i+1} depends on various parameters, including white noise intensity. For the specific set of parameters considered in Fig. 2.20, we observe that adjacent intervals ($k = 1$) are effectively uncorrelated, while intervals further apart ($k > 1$) are negatively correlated (circles in Fig. 2.20D). Still, the theory derived in the following is capable to explain these patterns.

Perturbation from the limit cycle

To calculate the SCC, we must first formulate the perturbation $\mathbf{u}_i(\tau)$ from the limit cycle. As we have just argued, the noise indirectly affects the adaptation variable, so the perturbation is not readily obtained. Instead, the perturbation can be perceived in two ways that ultimately paint the same picture.

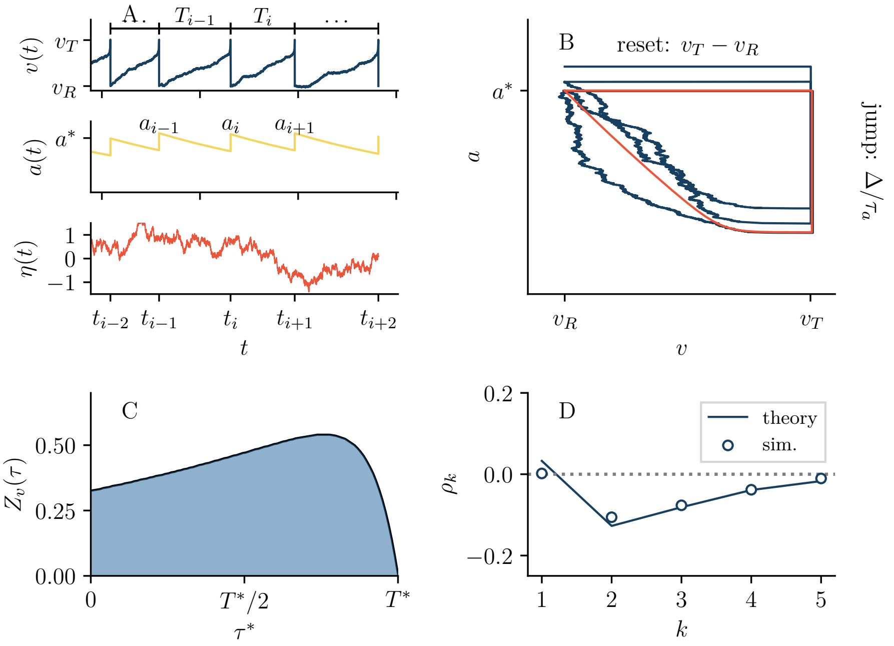

FIGURE 2.20: Serial correlations in a stochastic adaptive EIF model with correlated noise. Panels A show trajectories of the voltage $v(t)$, adaptation variable $a(t)$, and correlated noise $\eta(t)$ together with the spike times t_i and ISIs T_i. Panel B shows trajectories in the v-a plane together with the deterministic limit cycle (red line). Right after a spike, the value of the voltage is always given by v_R due to the reset, while the value of the adaptation variable can vary. Panel C shows the PRC of the adaptive EIF model. Panel D depicts the SCC obtained from stochastic simulations (circle) and according to Eq. 2.4.47 (line). The SCC is close to zero at lag $k = 1$, negative at $k = 2$, and returns to zero at higher lags. Parameters: $v_T = 2$, $\gamma = 1$, $\mu = 5$, $\Delta_T = 0.1$, $\tau_a = 2$, $\Delta = 2\,\sigma^2 = 0.5$, $\tau_\eta = 0.5$, $D = 0.035$, $T^* \approx 0.75$.

As a first approach, we can calculate both the PRC for the voltage $Z_v(\tau)$ *and* for the adaptation variable $Z_a(\tau)$ and find the corresponding perturbations of the voltage $u_i^v(\tau)$ and adaptation $u_i^a(\tau)$. Treated this way, the perturbation of the voltage can be read again from the dynamic equations:

$$u_i^v(\tau) = \eta(t_i + \tau) + \sqrt{2D}\xi_v(t_i + \tau). \tag{2.4.22}$$

The perturbation to the adaptation, in turn, is given by the deviation of the initial condition $a(t_i) = a_i$ from the deterministic value a^*. This can be described by a delta kick with amplitude $\delta a_i = a_i - a^*$ applied to the adaptation at phase $\tau = 0$ so that $u_i^a(\tau)$ is given by

$$u_i^a(\tau) = \delta a_i \delta(\tau). \tag{2.4.23}$$

Deviations from the deterministic interval can then be calculated by

$$\delta T_i = -\int_0^{T^*} d\tau \left(Z_v(\tau)[\eta(t_i + \tau) + \sqrt{2D}\xi_v(t_i + \tau)] + Z_a(\tau)\delta a_i \delta(\tau) \right). \tag{2.4.24}$$

As a second approach, we can treat the deviation of the adaptation variable from the limit cycle $\delta a(t)$ as a continuous perturbation to the voltage. This continuous perturbation can be calculated because between two spikes $a(t)$ is governed by a simple linear differential equation (Eq. 2.4.21):

$$\delta a_i(\tau) = a_i(\tau) - a_\Gamma(\tau) = a_i e^{-\tau/\tau_a} - a^* e^{-\tau/\tau_a} = \delta a_i e^{-\tau/\tau_a}. \tag{2.4.25}$$

Here, $a_i(\tau)$ is the actual trajectory of the adaptation over an ISI, $a_\Gamma(t)$ is the trajectory of the adaptation on the limit cycle, and $\delta a_i(\tau)$ is the time-dependent deviation of the adaptation from the limit cycle that affects the voltage. The perturbation to the voltage variable can thus be expressed as follows

$$u_i^v(\tau) = -\delta a_i e^{-\tau/\tau_a} + \eta(t_i+\tau) + \sqrt{2D}\xi_v(t_i+\tau), \tag{2.4.26}$$

and deviations of the intervals are given by

$$\delta T_i = -\int_0^{T^*} d\tau\, Z_v(\tau)[-\delta a_i e^{-\tau/\tau_a} + \eta(t_i+\tau) + \sqrt{2D}\xi_v(t_i+\tau)]. \tag{2.4.27}$$

Both approaches are fully equivalent, and it remains to be shown that Eq. 2.4.24 and Eq. 2.4.27 are identical. By comparison of these two equations, it becomes clear that we have to show that

$$\int_0^{T^*} Z_a(\tau)\delta a_i \delta(\tau) = -\int_0^{T^*} d\tau\, Z_v(\tau)\delta a_i e^{-\tau/\tau_a}. \tag{2.4.28}$$

In Eq. 2.3.33, we have seen that for a purely spike-triggered adaptation, where the dynamics of $a(t)$ do not depend on $v(t)$ explicitly, the PRC with respect to a can be expressed by the PRC with respect to v as follows:

$$Z_a(\tau) = -\int_\tau^{T^*} d\tau' Z_v(\tau') e^{(\tau-\tau')/\tau_a}. \tag{2.4.29}$$

If we insert this expression into Eq. 2.4.28 we obtain

$$\int_0^{T^*} Z_a(\tau)\delta a_i \delta(\tau) = Z_a(0)\delta a_i = -\int_0^{T^*} d\tau\, Z_v(\tau) e^{-\tau/\tau_a} \tag{2.4.30}$$

and find that Eq. 2.4.28 holds. In the following, we will use the voltage perturbation because it only requires the knowledge of the PRC $Z_v(\tau)$.

Derivation of the general correlation coefficient

We now proceed to calculate the SCC. As in Sec. 2.4.1, we can build the product of interval deviations and form the average to express the covariance

$$\begin{aligned}\langle \delta T_i \delta T_{i+k}\rangle = \int_0^{T^*}\int_0^{T^*} d\tau_1 d\tau_2\, Z(\tau_1)Z(\tau_2)\langle(-\delta a_i e^{-\tau_1/\tau_a} + \eta(t_i+\tau_1) + \sqrt{2D}\xi_v(t_i+\tau_1))\times \\ (-\delta a_{i+k} e^{-\tau_2/\tau_a} + \eta(t_{i+k}+\tau_2) + \sqrt{2D}\xi_v(t_{i+k}+\tau_2))\rangle,\end{aligned} \tag{2.4.31}$$

however, here we can not directly determine ρ_k because both the covariance $\langle \delta a_i \delta a_{i+k}\rangle$ and the cross-correlations $\langle \delta a_i H_{i+k}\rangle$, $\langle \delta a_i \Xi_{i+k}\rangle$ are unknown (the Gaussian random numbers H_{i+k} and Ξ_{i+k} have been defined in Eq. 2.4.12 and Eq. 2.4.13, respectively). To circumvent this problem, we pursue a similar strategy as done by Schwalger and Lindner [74] and derive a second relation for the interval deviations δT_i in terms of adjacent peak adaptation values a_i, a_{i+1}. This allows to express the covariance of the ISI $\langle \delta T_i \delta T_{i+k}\rangle$ by the covariance of the peak adaptation value $\langle \delta a_i \delta a_{i+k}\rangle$, and to establish a stochastic map by which the covariance $\langle \delta a_i \delta a_{i+k}\rangle$ can be traced back to the correlation functions of the noise sources $\langle H_i H_{i+k}\rangle$, $\langle \Xi_i \Xi_{i+k}\rangle$ (two terms appearing in Eq. 2.4.14).

We have already seen that the time course of the adaptation variable is deterministic over an ISI so that two adjacent peak adaptation values a_i and a_{i+1} are related by the length of the interval in between:

$$a_{i+1} = a_i e^{-T_i/\tau_a} + \Delta/\tau_a. \tag{2.4.32}$$

Following Schwalger and Lindner [74], this allows to relate deviation of the peak adaptation values $\delta a_i = a_i - a^*$ to deviation of the ISIs $\delta T_i = T_i - T^*$ by linearizing Eq. 2.4.32:

$$\begin{aligned}a^* + \delta a_{i+1} &= (a^* + \delta a_i)e^{-(T^*+\delta T_i)/\tau_a} + \Delta/\tau_a \\ &\approx (a^* + \delta a_i)e^{-T^*/\tau_a} - \delta T_i (a^*/\tau_a)e^{-T^*/\tau_a} + \Delta/\tau_a,\end{aligned} \tag{2.4.33}$$

where we have expanded the exponential function with respect to a small deviation of the interval $\exp(-\delta T_i/\tau_a) \approx 1 - \delta T_i/\tau_a$ and subsequently neglected second order terms, in particular $\delta a_i \delta T_i$. Rearranging terms and using $a^* = (\Delta/\tau_a)/(1-\exp(-T^*/\tau_a))$[3] yields the second expression for the spike time deviation:

$$\delta T_i = \frac{\tau_a}{a^*}\left(\delta a_i - e^{T^*/\tau_a}\delta a_{i+1}\right). \tag{2.4.34}$$

This allows us to express the SCC in terms of the covariance $\langle \delta a_i \delta a_{i+k}\rangle$ as follows

$$\rho_k = \frac{\langle \delta T_i \delta T_{i+k}\rangle}{\langle \delta T_i\rangle^2} = \frac{(1+\alpha^2)\langle \delta a_i \delta a_{i+k}\rangle - \alpha\langle \delta a_i \delta a_{i+k+1}\rangle - \alpha\langle \delta a_i \delta a_{i+k-1}\rangle}{(1+\alpha^2)\langle \delta a_i^2\rangle - 2\alpha\langle \delta a_i \delta a_{i+1}\rangle}. \tag{2.4.35}$$

Here, we have introduced $\alpha = \exp(-T^*/\tau_a)$ and used that the indices of the covariance (representing times) can be shifted simultaneously since the covariance is a stationary statistic and depends only on the difference of times. Finally, by combining Eq. 2.4.27 and 2.4.34, we establish a stochastic map that relates adjacent peak adaptation values:

$$\delta a_{i+1} = \alpha\nu\delta a_i + \frac{\alpha a^*}{\tau_a}(H_i + \Xi_i), \quad \text{with} \quad \nu = 1 - \frac{a^*}{\tau_a}\int_0^{T^*} d\tau\, Z(\tau)e^{-\tau/\tau_a}. \tag{2.4.36}$$

Again, H_i and Ξ_i are the Gaussian random numbers describing the linear response to the colored and white noise, respectively. In contrast, ν is a constant, reflecting that the dynamics of the adaptation variable over an ISI are deterministic. Eq. 2.4.36 can be applied iteratively to itself to find a relation between any two peak adaptation values

$$\begin{aligned}\delta a_{i+k} =& (\alpha\nu)\delta a_{i+k-1} + \frac{\alpha a^*}{\tau_a}(H_{i+k-1} + \Xi_{i+k-1})\\ =& (\alpha\nu)^2\delta a_{i+k-2} + \alpha\nu\frac{\alpha a^*}{\tau_a}(H_{i+k-2} + \Xi_{i+k-2}) + + \frac{\alpha a^*}{\tau_a}(H_{i+k-1} + \Xi_{i+k-1})\\ &\vdots\\ =& (\alpha\nu)^k\delta a_i + \frac{\alpha a^*}{\tau_a}\sum_{n=1}^{k}(\alpha\nu)^{k-n}(H_{i+n-1} + \Xi_{i+n-1}),\end{aligned} \tag{2.4.37}$$

which allows us to obtain the covariance by multiplying with δa_i and averaging:

$$\langle \delta a_i \delta a_{i+k}\rangle = (\alpha\nu)^k\langle \delta a_i^2\rangle + \frac{\alpha a^*}{\tau_a}\sum_{n=1}^{k}(\alpha\nu)^{k-n}(\langle \delta a_i H_{i+n-1}\rangle + \langle \delta a_i \Xi_{i+n-1}\rangle). \tag{2.4.38}$$

Since we have already established a relation between the covariance of the ISI and the covariance of the peak adaptation value, evaluating the sum in Eq. 2.4.38 allows us to determine the SCC.

To evaluate the sum, it is useful to realize that cross-correlations $\langle \delta a_i \Xi_{i+n-1}\rangle$ vanish because for $n \geq 1$ the random numbers Ξ_{i+n-1} contain the Gaussian white noise only *after* the spike time t_i and are therefore uncorrelated to the peak adaptation value δa_i *at* the spike time t_i. Cross-correlations between the peak adaptation value at time t_i and the colored noise at $t > t_i$ can be expressed in terms of the covariance at time t_i and the conditional mean of the OU process:

$$\langle \delta a_i H_{i+k}\rangle = \langle \delta a_i H_i\rangle e^{-kT^*/\tau_\eta} = \langle \delta a_i H_i\rangle \beta^k, \quad \text{if} \quad k \geq 1. \tag{2.4.39}$$

Here we used that $\langle H_{i+k}\rangle \approx \langle H_i\rangle \exp(-kT^*/\tau_\eta)$ and approximated $t_{i+k} - t_i \approx kT^*$ because we are only interested in the leading order of the cross-correlation (considering deviations δT_i would lead to higher order terms $\delta a_i H_i \delta T_i$). The covariance $\langle \delta a_i \delta a_{i+k}\rangle$ can therefore be simplified as

---

[3] In the deterministic limit Eq. 2.4.32 becomes $a^* = a^*\exp(-T^*/\tau_a) + \Delta/\tau_a$ and be rearranged to calculate the deterministic peak adaptation value $a^* = (\Delta/\tau_a)/(1-\exp(-T^*/\tau_a))$.

follows

$$\begin{aligned}\langle\delta a_i\delta a_{i+k}\rangle &= (\alpha\nu)^k\langle\delta a_i^2\rangle + \frac{\alpha a^*}{\tau_a}\sum_{n=1}^{k}(\alpha\nu)^{k-n}\beta^{n-1}\langle\delta a_i H_i\rangle \\ &= (\alpha\nu)^k\langle\delta a_i^2\rangle + \frac{\alpha a^*}{\tau_a}\left(\frac{(\alpha\nu)^k-\beta^k}{\alpha\nu-\beta}\right)\langle\delta a_i H_i\rangle.\end{aligned} \tag{2.4.40}$$

The evaluation of the sum relies on the fact that the conditional mean of the correlated noise that appears in Eq. 2.4.39 decays exponentially with time since only in this case the argument becomes a geometric sequence. This is a crucial step in the derivation of the SCC and restricts the theory to an exponentially correlated noise. To proceed, we use the stochastic map Eq. 2.4.36 to trace the variance and covariance back to the autocorrelation of the noise terms. An equation for the variance $\langle\delta a_i^2\rangle$ can be obtained by squaring the map Eq. 2.4.36 and averaging:

$$\begin{aligned}\langle\delta a_i^2\rangle &= (\alpha\nu)^2\langle\delta a_i^2\rangle + \frac{2\alpha^2\nu a^*}{\tau_a}\langle\delta a_i H_i\rangle + \left(\frac{\alpha a^*}{\tau_a}\right)^2(\langle H_i^2\rangle + \langle\Xi_i^2\rangle) \\ &= \frac{\alpha^2 a^*}{\tau_a^2(1-(\alpha\nu)^2)}\left(2\nu\tau_a\langle\delta a_i H_i\rangle + a^*(\langle H_i^2\rangle + \langle\Xi_i^2\rangle)\right).\end{aligned} \tag{2.4.41}$$

For the covariance $\langle\delta a_i H_i\rangle$ the map is multiplied by H_{i+1} and averaged

$$\begin{aligned}\langle\delta a_i H_i\rangle &= \alpha\nu\langle\delta a_i H_{i+1}\rangle + \frac{\alpha a^*}{\tau_a}\langle H_i H_{i+1}\rangle \\ &= \frac{\alpha a^*}{\tau_a(1-\alpha\nu\beta)}\langle H_i H_{i+1}\rangle,\end{aligned} \tag{2.4.42}$$

where we have used $\langle\delta a_i H_{i+1}\rangle = \beta\langle\delta a_i H_i\rangle$ and the fact that the term containing Ξ_i drops out because the noise terms are independent of each other. We are finally equipped to calculate the SCC because all terms have been traced back to either the variances $\langle H_i^2\rangle$ and $\langle\Xi_i^2\rangle$ or the covariance $\langle H_i H_{i+1}\rangle$.

Let us briefly conclude what we have derived so far. First, we have expressed the SCC ρ_k in terms of the covariance of the peak adaptation value $\langle\delta a_i\delta a_{i+k}\rangle$ (Eq. 2.4.35). Secondly, we have related this covariance to the variance $\langle\delta a_i^2\rangle$ and another covariance $\langle\delta a_i\delta H_i\rangle$ (Eq. 2.4.40). Finally, we have shown that these two terms are determined by the known variances $\langle H_i^2\rangle$ and $\langle\Xi_i^2\rangle$ as well as the known covariance $\langle H_i H_{i+1}\rangle$ (Eq. 2.4.41 and Eq. 2.4.42).

Still the combination of Eq. 2.4.35, 2.4.40, 2.4.41 and 2.4.42 is cumbersome in practice. Since the complete derivation of the variance and covariance step-by-step is too tedious, we highlight only a few steps that should be sufficient to make the calculation comprehensible. We start with the variance that is still relatively easy to determine:

$$\begin{aligned}\langle\delta T_i^2\rangle &= (1+\alpha^2)\langle\delta a_i^2\rangle - 2\alpha\langle\delta a_i\delta a_{i+1}\rangle \\ &= (1+\alpha^2)\langle\delta a_i^2\rangle - 2\alpha\nu\langle\delta a_i^2\rangle - \frac{a^*}{\tau_a}\alpha\langle\delta a_i H_i\rangle \\ &= (1-2\alpha\nu+\alpha^2)\langle\delta a_i^2\rangle - \frac{a^*}{\tau_a}\alpha\langle\delta a_i H_i\rangle.\end{aligned} \tag{2.4.43}$$

To get from the first to the second line, we used Eq. 2.4.40 for $k = 1$. Finding an expression in terms of $\langle\delta a_i^2\rangle$ and $\langle\delta a_i H_i\rangle$ is sufficient because the ratio between these two terms can be replaced by the correlation functions of the noise terms. The covariance is a bit more complicated

$$\langle\delta T_i\delta T_{i+k}\rangle = (1+\alpha^2)\langle\delta a_i\delta a_{i+k}\rangle - \alpha\langle\delta a_i\delta a_{i+k+1}\rangle - \alpha\langle\delta a_i\delta a_{i+k-1}\rangle \tag{2.4.44}$$

replacing the three covariances $\langle \delta a_i \delta a_{i+k} \rangle$ using Eq. 2.4.40 for $k-1$, k, and $k+1$ yields:

$$
\begin{aligned}
\langle \delta T_i \delta T_{i+k} \rangle &= ((1+\alpha^2)(\alpha\nu) - \alpha(\alpha\nu)^2 - \alpha)(\alpha\nu)^{k-1}\langle \delta a_i^2 \rangle \\
&+ \frac{a^*\alpha}{\tau_a}\left((1+\alpha^2)\frac{(\alpha\nu)^k - \beta^k}{\alpha\nu - \beta} - \alpha\frac{(\alpha\nu)^{k+1} - \beta^{k+1}}{\alpha\nu - \beta} - \alpha\frac{(\alpha\nu)^{k-1} - \beta^{k-1}}{\alpha\nu - \beta} \right) \langle \delta a_i H_i \rangle \\
&= -\alpha(1-\alpha^2\nu)(1-\nu)(\alpha\nu)^{k-1}\langle \delta a_i^2 \rangle \\
&- \frac{a^*}{\tau_a}\frac{\alpha}{\alpha\nu - \beta}\alpha(1-\alpha^2\nu)(1-\nu)(\alpha\nu)^{k-1}\langle \delta a_i H_i \rangle \\
&+ \frac{a^*}{\tau_a}\frac{\alpha}{\alpha\nu - \beta}(1-\alpha\beta)(\beta-\alpha)\beta^{k-1}\langle \delta a_i H_i \rangle .
\end{aligned}
\tag{2.4.45}
$$

The problem can be simplified somewhat by taking advantage of the SCC being a ratio of the covariance and variance. Therefore it is sufficient to determine the following term

$$
\frac{\tau_a}{\alpha a^*}\frac{\langle \delta a_i^2 \rangle}{\langle \delta a_i H_i \rangle} = \frac{2\alpha\nu}{1-(\alpha\nu)^2} + \frac{1-\alpha\nu\beta}{1-(\alpha\nu)^2}\frac{\langle H_i^2 \rangle + \langle \Xi_i^2 \rangle}{\langle H_i H_{i+1} \rangle},
\tag{2.4.46}
$$

that is obtained by combing Eq. 2.4.41 and Eq. 2.4.42. Finally, forming the ratio between Eq. 2.4.45 and Eq. 2.4.43 and substituting Eq. 2.4.46 in the resulting expression yields the SCC [1]:

$$
\rho_k = \left(\frac{A}{C}\right)\rho_{k,a} + \left(\frac{B}{C}\right)\rho_{k,\eta},
\tag{2.4.47}
$$

with the two specific correlation coefficients:

$$
\rho_{k,a} = \underbrace{-\frac{\alpha(1-\alpha^2\nu)}{1+\alpha^2-2\alpha^2\nu}(1-\nu)}_{\rho_{1,a}}(\alpha\nu)^{k-1},
\tag{2.4.48}
$$

and

$$
\rho_{k,\eta} = \underbrace{\frac{\int_0^{T^*}\int_0^{T^*} d\tau_1 d\tau_2\, Z(\tau_1)Z(\tau_2)\sigma^2 \exp(-|T^*+\tau_2-\tau_1|/\tau_\eta)}{\int_0^{T^*}\int_0^{T^*} d\tau_1 d\tau_2\, Z(\tau_1)Z(\tau_2)\left[\sigma^2\exp(-|\tau_2-\tau_1|/\tau_\eta) + 2D\delta(\tau_2-\tau_1)\right]}}_{\rho_{1,\eta}}\beta^{k-1},
\tag{2.4.49}
$$

and the coefficients

$$
A = 1 + \frac{(1+(\alpha\nu)^2 - 2\alpha\nu\beta)}{\alpha\nu-\beta}\rho_{1,\eta} - \alpha\nu\beta,
\tag{2.4.50a}
$$

$$
B = \frac{(1-(\alpha\nu)^2)(1-\alpha\beta)(\alpha-\beta)}{(1+\alpha^2-2\alpha^2\nu)(\alpha\nu-\beta)},
\tag{2.4.50b}
$$

$$
C = 1 + 2\rho_{1,a}\rho_{1,\eta} - \alpha\nu\beta,
\tag{2.4.50c}
$$

$$
\alpha = e^{-\frac{T^*}{\tau_a}}, \quad \beta = e^{-\frac{T^*}{\tau_\eta}}, \quad \nu = 1 - \frac{a^*}{\tau_a}\int_0^{T^*} d\tau\, Z(\tau)e^{-\tau/\tau_a}.
\tag{2.4.50d}
$$

The main result of this chapter, Eq. 2.4.47, implies that the SCC for a multidimensional stochastic adaptive IF model driven by an OU process is a sum of two geometric sequences. Moreover, these two sequences correspond to the SCCs $\rho_{k,a}$ and $\rho_{k,\eta}$ except for a prefactor that does not depend on k. Previous analytical studies have often considered one correlation-inducing process at a time, i.e., either an adaptive neuron model driven by white noise [85, 97] or a (non-adaptive) neuron model driven by correlated noise [66, 92, 95]. These studies find that the respective SCC is a single geometric sequence of the form $s_k = s_1 r^{k-1}$, $k \geq 1$. As a reminder, the absolute value $|s_k|$ of such a sequence decays exponentially with lag k, the sign at $k = 1$ (corresponding to the correlation coefficient for adjacent intervals) is determined by s_1, and the full sequence may alternate, depending on the sign of the base r. In summary, a single geometric sequence can realize four different patterns of interval correlations. In contrast, our result, i.e., the sum of two geometric sequences, can account for a much larger number of patterns of interval correlations. Such deviations from a single geometric series have indeed been observed experimentally [147]. Indirect evidence for negative short-term correlations combined with positive long-term correlations has been provided by [148, 149]. To this end, Lowen and Teich [148] determined the Fano $F(T)$ factor using the spike train of an auditory neuron and compared it to the Fano factor of the same spike train but with shuffled interspike intervals. They find that for large time windows T, the Fano factor of the shuffled spike train is reduced compared to the unshuffled case. According to Eq. 1.3.30, this implies that the sum over all SCCs is positive. Conversely, for intermediate times, the Fano factor of the shuffled spike train is increased compared to the unshuffled case. They conclude that for the first few lags k, the SCC is negative (short-term negative correlations), while the sum of all SCCs is positive (long-term positive correlations).

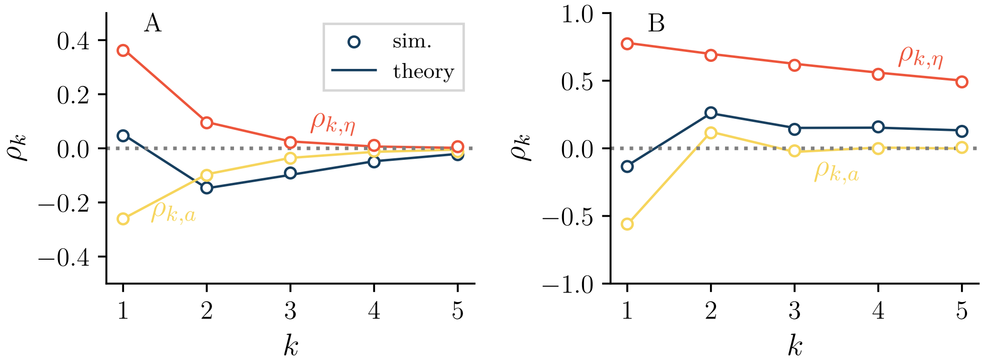

FIGURE 2.21: Serial correlations in a stochastic adaptive LIF model with correlated noise. Both panels show the general SCC ρ_k (blue circles and line) obtained by considering the full model as well as the two specific SCC $\rho_{k,\eta}$ (red circle and line; $\Delta = 0$), $\rho_{k,a}$ (yellow circle and line; $\sigma = 0$) obtained by considering one correlation inducing process at a time. Panel A and B differ in the base pattern exhibited by the specific SCC $\rho_{k,a}$ (exponential in A and oscillatory in B) and the number of intervals over which the specific SCC $\rho_{k,\eta}$ decays (small in A and large in B). In both cases, the general SCC cannot be described by a single exponential function but is small at $k = 1$, changes sign at $k = 2$ and slowly approaches zero for higher lags. Parameters $\gamma = 1$, $\sigma = 2 \cdot 10^{-2}$, $D = 1 \cdot 10^{-3}$; A: $\mu = 5$, $\tau_a = 2$, $\Delta = 2$, $\tau_\eta = 0.5$, $T^* \approx 0.66$; B: $\mu = 20$, $\tau_a = 1$, $\Delta = 10$, $\tau_\eta = 5$, $T^* \approx 0.55$.

To illustrate how the interplay of the two correlation-inducing processes shapes the SCC, we consider three versions of the LIF model, from which we obtain the two specific SCC $\rho_{k,a}$, $\rho_{k,\eta}$, as well as the general SCC ρ_k shown in Fig. 2.21. For the SCC $\rho_{k,\eta}$ (red line and circles), we use a LIF model without adaptation driven by a correlated noise (Eq. 2.2.16). In this case, the SCC can only decay exponentially because the base of the geometric sequence is given by β and obeys $0 < \beta < 1$. This is true regardless of the neuron model considered. Specifically for the LIF model with strictly positive PRC, the prefactor $\rho_{1,\eta}$ is also positive so that the exponential decay of $\rho_{k,\eta}$ shown in Fig. 2.21A and B is indeed the only pattern of interval correlations that can be realized. This may no longer be the case when we consider two-dimensional neuron models, for which we have already seen that the PRC can be partially negative. For the SCC $\rho_{k,a}$ (yellow line and circles) we consider an adaptive LIF model driven by uncorrelated noise (Eq. 2.2.13). In this case, a richer repertoire of interval correlations is possible since the base of the geometric sequence $\alpha\nu$ is not necessarily positive but obeys $-1 < \alpha\nu < 1$. Note that since $0 < \alpha < 1$, the sign is determined by ν. In addition, as we will show below, for models with strictly positive PRC, the prefactor $\rho_{1,a}$ is negative. Thus, two patterns of interval correlations can be realized for the LIF model: Either the SCC decays exponentially as shown in Fig. 2.21A or oscillatory as shown in Fig. 2.21B. In Sec. 2.4.3, we will discuss these two cases in more detail and explain how they relate to the strength of the adaptation.

In contrast to the two cases discussed so far, more complicated patterns can be observed for the general SCC ρ_k. For example, the pattern shown in Fig. 2.21A (blue line and circles) is characterized by a very small positive first correlation coefficient, whereas higher lags have pronounced negative correlations. This can be understood as follows: Consider a reference interval T_i shorter than the mean because the correlated noise $\eta(t)$ over this interval happened to be larger than zero, thus advancing the next spike time. As mentioned earlier, this leads to an increase in the adaptation, which, if considered individually, would delay the next spike time and thus prolong the following interval T_{i+1}. However, there is an opposite effect because the OU process is positively correlated with itself and tends to take positive values on average over the next interval T_{i+1} as well. If the parameters are chosen carefully, these two effects can be balanced so that correlations between adjacent intervals vanish. However, if we additionally assume that the timescale of the OU process is shorter than the timescale of the adaptation $\tau_\eta < \tau_a$, we can realize a situation where the adaptation still affects the third interval T_{i+2}, but the OU process does not because it becomes practically uncorrelated with its previous values (during the interval T_i). The adaptation will then prolong the interval T_{i+2} compared to the mean, and we find $\langle \Delta T_i \Delta T_{i+2} \rangle < 0$. This is exactly the case in Fig. 2.21A. In Fig. 2.21B, we show the inverse, where again the SCC ρ_1 is close to zero for the same reason we have just discussed, and the SCC at higher lags is dominated by the OU process because now $\tau_\eta > \tau_a$.

We have seen that completely new patterns of interval correlations become possible if we consider a neuron model with a spike-triggered adaptation that is additionally subject to a correlated noise. Still the possible patterns depend crucially on the PRC, in particular on whether the PRC is partially negative or not. Therefore, we discuss two distinct cases in Sec. 2.4.3 and Sec. 2.4.4: First, the LIF model with a strictly positive PRC, a case we have already begun to discuss here, and second, the GIF model with partially negative PRC.

2.4.3 Integrator models with adaptation and correlated noise

Here we study the SCC for a one-dimensional IF model, in the sense that no auxiliary variables are considered, and the drift in Eq. 2.4.21 reduces to $f_0(v, \mathbf{w}) = f(v)$. In Sec. 2.3.5, we have shown that for one-dimensional IF models, the PRC can be solved formally according to Eq. 2.3.29:

$$Z_v(\tau) = Z_v(T^*) \exp\left[\int_\tau^{T^*} dt\, f'(v_\Gamma(t))\right]. \tag{2.4.51}$$

Recall that the PRC evaluated at the phase $\tau = T^*$ is equivalent to the inverse velocity of the voltage of the deterministic system at the threshold $Z(T^*) = \dot{v}(T^*)^{-1} = (f(v_T) + \mu - a^* + \Delta/\tau_a)^{-1}$. This is an important insight because, for an oscillating system that fires spikes even in the absence of noise, this velocity must always be positive, which leads to the conclusion that the entire PRC $Z(\tau)$ is positive (the exponential term cannot be negative). One-dimensional systems thus resemble type I neuron models with positive PRC [145].

According to Eq. 2.4.48 the SCC $\rho_{k,a} = \rho_{1,a}(\alpha\nu)^{k-1}$ is a geometric sequence with the prefactor:

$$\rho_{1,a} = -\frac{\alpha(1-\alpha^2\nu)}{1+\alpha^2-2\alpha^2\nu}(1-\nu). \tag{2.4.52}$$

To show this, we first show that the fraction is positive regardless of the PRC. Using $0 < \alpha = \exp(-T^*/\tau_a) < 1$ and $|\alpha\nu| < 1$, it is immediately clear that the numerator $\alpha(1-\alpha(\alpha\nu))$ is positive. The same can be shown for the denominator, because $1 + \alpha^2 - 2\alpha^2\nu > \alpha^2\nu + \alpha^2 - 2\alpha^2\nu = \alpha(1 - \alpha\nu) > 0$. Thus, the sign of the prefactor is determined by the second term $(1-\nu)$. Eq. 2.4.50d reveals that this term can only be negative if the PRC is also negative. The second SCC $\rho_{k,\eta}$ decays exponentially with k and has a non-negative prefactor due to the positive PRC. In summary, in a Type I neuron model with a non-negative PRC, a spike-triggered adaptation elicits negative correlations between adjacent intervals ($\rho_1 < 0$) followed by an either monotonic or oscillatory decay with the lag. Conversely, a correlated noise leads to positive interval correlations with a characteristic number of correlated intervals determined by T^*/τ_η.

In Fig. 2.22, we study the general SCC ρ_k and distinguish two cases based on the sign of the parameter ν that determines the base pattern of the SCC $\rho_{k,a}$. These two cases are closely related to the shape of the limit cycle shown by a red line in Fig. 2.22A$_1$ and B$_1$. This is so because for one-dimensional models ν is related to the velocity $\dot{v}(\tau = 0)$ at the reset point [74]. To see this

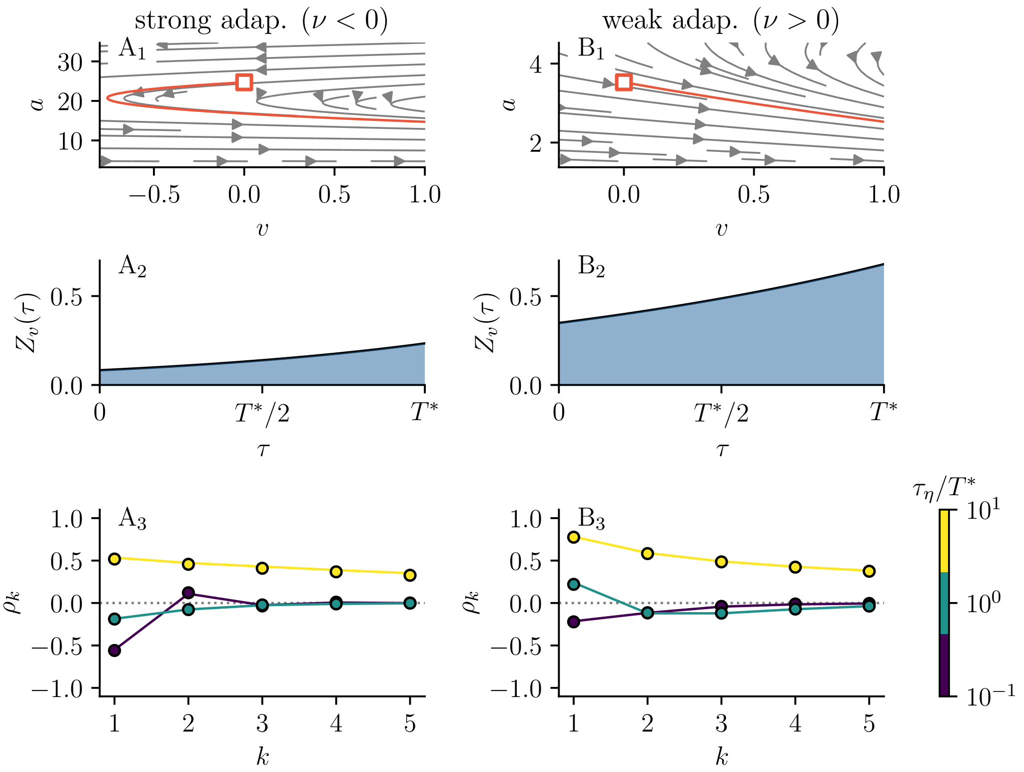

FIGURE 2.22: Patterns of interval correlations for the LIF model. Panels A$_1$ and B$_1$ show the deterministic limit cycle with the reset point marked by a red square. In A$_1$, the adaptation at the reset point is so strong that the drift at the reset point becomes negative, and the voltage initially takes negative values, implying $\nu < 0$. In B$_1$, the adaptation is weaker, and the drift at the reset point is positive. This implies $\nu > 0$. Panel A$_2$ and B$_2$ show the PRC $Z_v(\tau)$. Panel A$_3$ and B$_3$ show the SCC ρ_k for different correlation times τ_η. For small values of τ_η, the noise becomes essentially white, and the adaptation dominates the SCC. In this case, the pattern of the SCC ρ_k (purple circles and line) is oscillatory for $\nu < 0$ and exponential for $\nu > 0$. For large values of τ_η, the SCC is dominated by the correlated noise and becomes positive (yellow circles and line). Parameters A: $\gamma = 1$, $\mu = 20$, $\tau_a = 2$, $\Delta = 20$, $\sigma = 10^{-1}$, $D = 0$, $T^* \approx 1.0$; B: $\gamma = 1$, $\mu = 5$, $\tau_a = 2$, $\Delta = 2$, $\sigma = 10^{-1}$, $D = 0$, $T^* \approx 0.67$

consider Eq. 2.3.32 with the initial condition $t_0 = 0$ evaluated at $\tau = T^*$:

$$Z_a(T^*) = e^{T^*/\tau_a}\left(Z_a(0) + \int_0^{T^*} dt\, Z_v(t)e^{-t/\tau_a}\right). \tag{2.4.53}$$

Using $Z_a(T^*) = 0$ and substituting ν in Eq. 2.4.53 yields

$$\nu = 1 + \frac{a^*}{\tau_a} Z_a(0). \tag{2.4.54}$$

The PRC Z_a can be related to the PRC Z_v and, more importantly, to the velocity $\dot{v}(0)$ at the reset point using their normalization (Eq. 2.3.12) at $\tau = 0$:

$$\dot{v}(0)Z(0) + \dot{a}(0)Z_a(0) = 1. \tag{2.4.55}$$

The velocity of the adaptation is given by $\dot{a}(0) = -a^*/\tau_a$ so that we obtain

$$\nu = \dot{v}(0)Z(0). \tag{2.4.56}$$

As we have argued several times for the adaptive LIF model, the PRC is positive $Z_v(t) > 0$, so that $\nu < 1$ implies $\dot{v}(0) = \mu - \gamma v_R - a^* < 0$, and the limit cycle makes an initial detour toward negative values of the voltage variable (red line in Fig. 2.22A$_1$). The drift becomes positive only after $a(t_i + t) = a^* \exp(-t/\tau_a)$ has relaxed sufficiently. Following [74], we refer to this case as strong adaptation. In the second case ($\nu < 1$), the limit cycle makes no such detour because the drift remains positive $\dot{v} > 0$ even after resetting v and increasing a. We refer to this case as weak adaptation. In both cases, we have already seen in Sec. 2.3.2 that the PRC for the adaptive LIF model can be calculated analytically because the drift $f(v) = -\gamma v$ depends linearly on v, and consequently $f'(v_\Gamma) = -\gamma$ does not require knowledge of the time-dependent solution $v_\Gamma(t)$ on the limit cycle. The solution is given by Eq. 2.3.35

$$Z_v(\tau) = \frac{e^{\gamma(\tau - T^*)}}{\mu - \gamma v_T - a^* + \Delta/\tau} \tag{2.4.57}$$

and is shown in Fig. 2.22A$_2$ and B$_2$. In Fig. 2.22A$_3$ and B$_3$, we inspect how the general SCC depends on the correlation time τ_η given in terms of the deterministic period T^*. Note that we do not consider any additional white noise ($D = 0$), so the OU process is the only noise source and thus directly affects the ISIs, but thereby also causes the deviation of the peak adaptation value. It is, therefore, interesting to ask how the SCC depends on the timescale and whether, for example, the positive correlations caused by the noise are eventually outweighed by the negative correlations caused by the adaptation (or vice versa).

First of all, for $\tau_\eta \ll T^*$, the OU process becomes essentially white, and the correlations are caused solely by the adaptation. Consequently, the general SCC reduces to $\rho_{k,a}$. In the opposite limit, where the OU process is correlated over multiple periods $\tau_\eta \gg T^*$, the general SCC reduces to $\rho_{k,\eta}$ (if the absence of a white noise), implying that the OU process dominates the interval correlations. This is so because in this limit, $\eta(t)$ can be regarded as a constant modulation of the input current, causing multiple ISIs to deviate from the mean similarly. The adaptation can diminish this effect but cannot alter the common sign of these deviations. The pattern can become more complicated for intermediate correlation times $\tau_\eta = T^*$. In Fig. 2.22B$_3$, the SCC for $k = 1$ is determined by the correlated noise so that adjacent intervals are positively correlated, while for $k > 1$, the SCC is determined by the adaptation, and intervals become negatively correlated.

2.4.4 Resonator models with adaptation and correlated noise

Here we study the SCC for a two-dimensional IF model, the GIF model introduced in Sec. 2.2.4. For this model, the drifts of the voltage and auxiliary variable are given by $f_0(v, w) = -\gamma v - \beta_w w$ and $f_1(v, w) = (v - w)/\tau_w$. We note that the auxiliary variable w is also reset upon firing and thus does not introduce any interval correlations. Recall that for this linear model, the PRC can be calculated analytically as we have shown in Sec. 2.3.2 (Eq. 2.3.39):

$$Z_v(\tau) = \frac{e^{\frac{\nu}{2}(\tau - T^*)}\left[\cos(\Omega(\tau - T^*)) - \frac{1-\gamma\tau_w}{2\tau_w\Omega}\sin(\Omega(\tau - T^*))\right]}{\mu - \gamma v_T - \beta w_0(T^*) - a^* + \Delta/\tau_a}. \tag{2.4.58}$$

The decisive new feature of this PRC is that it can become partially negative, as in Type II neuron models. In other words, a positive kick to the voltage can delay the next spike time.

In Fig. 2.23, we show the PRC in three cases together with the SCC. Because the GIF model includes the LIF model as a limit case, we expect that the pattern discussed in Sec. 2.4.3 can also be realized by the GIF [4]. Indeed, the observed patterns shown in Fig. 2.23A and B for $\nu < 0$ and $\nu > 0$ can also be observed for the LIF model and have already been discussed. Quantitative details depend on the parameters thought. For example, in Fig. 2.23A$_2$, the SCC is still dominated by the adaptation even for $\tau_\eta \gg T^*$, which is probably related to the fact that τ_a is larger here. Qualitatively new interval correlations can be realized if the PRC is partially negative and ν becomes larger than one. In this case, intervals can be positively correlated even if the correlation time of the OU process is short ($\tau_\eta/T^* = 10^{-2}$). This is so because the inhibitory current caused by the adaptation can now have opposing effects on two adjacent intervals. Note that the dependence of the first correlation coefficient ρ_1 on τ_η is non-monotonic. It starts positive for very short correlation times $\tau_\eta/T^* = 10^{-2}$, decreases as the ratio reaches an intermediate value $\tau_\eta/T^* = 1$, and subsequently increases until adjacent intervals are positively correlated again for

---

[4] The GIF model reduces to the LIF model for $\tau_w \to 0$, in which case $v = w$ and the parameter $\gamma_{\mathrm{LIF}} = \gamma_{\mathrm{GIF}} + \beta$.

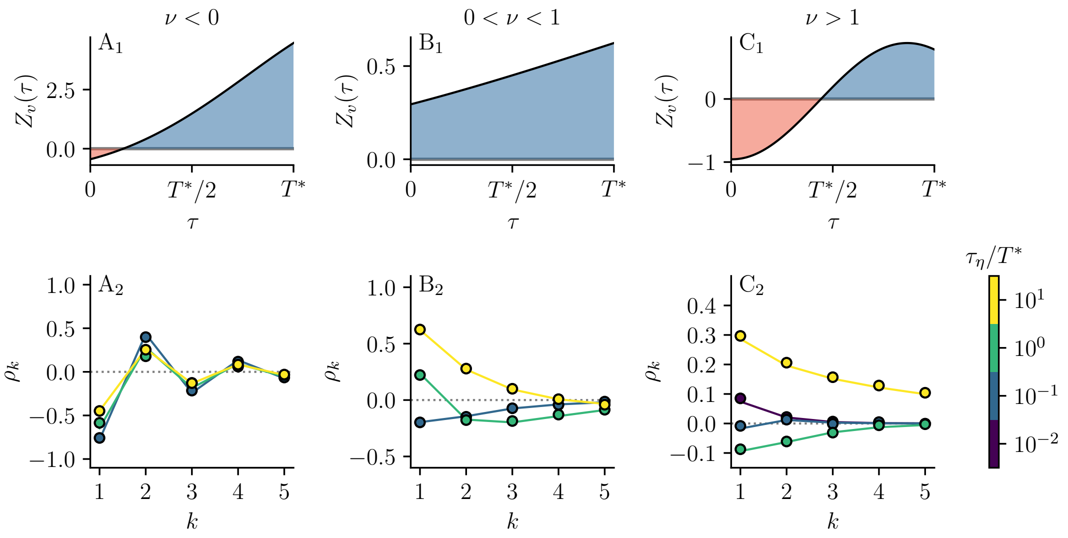

FIGURE 2.23: Pattern of interval correlations for the GIF model. Panel A$_1$, B$_1$, and C$_1$ show the PRC $Z_v(\tau)$. Panel A$_2$, B$_2$, and C$_2$ show the SCC ρ_k for different correlation times τ_η. The two cases $\nu < 0$ shown in panel A and $0 < \nu < 1$ shown in panel B are similar to those in Fig. 2.22. The case $\nu > 1$ shown in C is novel and implies a partially negative PRC that can give rise to a counterintuitive behavior of the SCC ρ_k. For small correlation times τ_η, the SCC is positive for all lags (purple circles and line). As the correlation time increases, the SCCs become negative (cyan circles and line) before they become positive again at large correlation times (yellow circles and line). Parameters A: $\gamma = 1$ $\mu = 10$, $\tau_w = 1.5$, $\beta = 3$, $\tau_a = 10$, $\Delta = 10$, $\sigma = 10^{-3}$, $D = 0$, $T^* \approx 1.24$; B: $\gamma = 1$ $\mu = 20$, $\tau_w = 1.5$, $\beta = 1.5$, $\tau_a = 10$, $\Delta = 10$, $\sigma = 10^{-3}$, $D = 0$, $T^* \approx 0.57$; C: $\gamma = -1$ $\mu = 1$, $\tau_w = 1.1$, $\beta = 5$, $\tau_a = 1$, $\Delta = 2.3$, $\sigma = 10^{-3}$, $D = 0$, $T^* \approx 1.91$

$\tau_\eta/T^* = 10^1$. This more complex dependence of ρ_1 on τ_η is shown in more detail in Fig. 2.24A and compared to a similar case for a non-adaptive GIF in Fig. 2.24B.

To understand the behavior of the SCC shown in Fig. 2.23C, we consider the effects of the adaptation and the correlated noise separately. (We have seen that the general SCC is a superposition of the two specific SCCs.) For the adaptation, we again consider a shortened reference interval $T_i < T^*$, which induces a positive deviation of the peak adaptation value $\delta a_i > 0$ and, in turn, an inhibitory current $-\delta a_i \exp(-\tau/\tau_a)$ acting over the interval T_{i+1}. If the adaptation timescale τ_a is chosen such that the inhibitory current acts mainly on the part of the ISI where the PRC is negative ($\tau_a \approx T^*/2$ in Fig. 2.23C), the interval T_{i+1} will also be shortened. A similar argument applies to an extended reference interval $T_i > T^*$, in which case $\delta a_i < 0$. In both cases, adjacent intervals deviate similarly from the mean and are positively correlated. Turning to the correlated noise, for short correlation times ($\tau_\eta/T^* = 10^{-2}$), the noise is essentially white and does not introduce any significant interval correlations. For longer correlation times, still smaller than the portion of the ISI for which the PRC is negative, values of $\eta(t)$ preserved beyond a spike time have an opposing effect on the interval before and after the spike, and the intervals become anti-correlated. Hence, as τ_η increases, the SCC initially decreases until the correlation time τ_η coincides with the portion of the ISI for which the PRC is negative. This time is highlighted by a vertical line in Fig. 2.24. Finally, if the correlation time is increased further, interval correlations become positive again. This is because for $\tau_\eta \gg T^*$ the particular shape of the PRC becomes irrelevant; the noise may advance or delay the next spike time depending on the particular phase τ of the firing cycle, but it does so in the same way for the following interval and so both intervals deviate similarly from the mean. In Fig. 2.24B, we demonstrate this minimization of the correlation coefficient in a GIF model without adaptation. The parameters have been chosen so that the PRCs in Fig. 2.23C and Fig. 2.24A approximately agree.

This shows that a low-pass filtered noise can cause negative interval correlation in a resonator model, which is another independent mechanism by which negative ISI correlations can be induced. Other known mechanisms include the combination of a spike-triggered adaptation and white noise [40, 73, 150], short-term depression and white noise [95], and high-pass filtered network noise from regularly firing neurons [95].

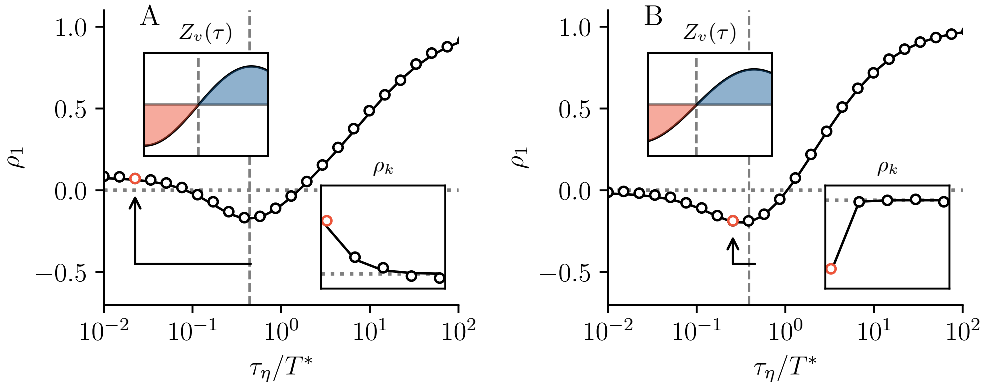

FIGURE 2.24: Serial correlation coefficient ρ_1 for the GIF model. Panel A shows the first SCC ρ_1 as a function of the correlation time τ_η for an adaptive GIF model with parameters as in Fig. 2.23C. Panel B shows the same statistics for a GIF model without adaptation and parameters chosen so that the PRCs (inset in A and B) qualitatively agree. Due to the partially negative PRC, the SCC ρ_1 initially decreases with increasing correlation time until the correlation time coincides with the fraction of the ISI for which the PRC is negative. This time is indicated by a dashed vertical line. Subsequently, the SCC increases and becomes positive. Parameters A: $\gamma = -1$ $\mu = 1$, $\tau_w = 1.1$, $\beta = 5$, $\tau_a = 1$, $\Delta = 2.3$, $\sigma = 10^{-4}$, $D = 0$, $T^* \approx 1.91$; B: $w_R = 1$, $\gamma = -1$ $\mu = 1$, $\tau_w = 1.1$, $\beta = 5$, $\tau_a = 0$, $\Delta = 0$, $\sigma = 10^{-3}$, $D = 0$, $T^* \approx 1.76$

2.4.5 Adaptation-channel noise

So far, we have considered scenarios where the adaptation and correlated noise are independent processes with independent time constants. However, we can regard these two processes also as an idealized description of an adaptation current through a finite population of stochastically opening and closing ion channels with voltage-dependent gating kinetics [85, 86]. The slowly varying Ca^{2+}-dependent K$^+$ current is just one example of such a spike-triggered adaptation current [40, 101, 127] and other candidates are known [18]. We recall that for a finite population, the summed current through all these channels is stochastic, which is commonly referred to as channel noise. These fluctuations become smaller the larger the population is but do not vanish for a finite number of channels. As shown by [85], the summed current can be split into a deterministic part, corresponding to the dynamics of the adaptation $a(t)$ in our model, and a stochastic part, corresponding to the OU process $\eta(t)$. We refer to the combination of these two currents $a(t) + \eta(t)$ as *adaptation-channel noise*. The additional white noise can be seen as the result of the stochastic opening and closing of ion channels with fast gating kinetics.

Due to the common origin of the deterministic adaptation and the correlated noise, the previously independent timescales are now equal and are denoted by $\tau_c := \tau_a = \tau_\eta$. This also implies that the parameters $\alpha = \exp(-T^*/\tau_a)$ and $\beta = \exp(-T^*/\tau_\eta)$ are identical, which has a profound effect on the general SCC (Eq. 2.4.47). The SCC ρ_k reduces to a single geometric sequence because the parameter B defined in Eq. 2.4.50 vanishes (note the term $\alpha - \beta$ in the numerator). Possible interval correlations thus include only the exponentially decaying or alternating patterns. However, it is not clear whether correlations between adjacent intervals are determined by the deterministic adaptation or by the correlated noise, i.e., whether ρ_1 will be positive or negative.

To answer this equation, we consider an LIF model with adaptation-channel noise and plot in Fig. 2.25 the correlation coefficient ρ_1 as a function of the common timescale τ_c for different white noise intensities D. Theoretical predictions according to Eq. 2.4.47 are shown as lines, while correlations measured from stochastic simulations are shown as circles. We first discuss the two limit cases $\Delta = 0$ and $\sigma = 0$, shown in red and yellow, respectively. For $\Delta = 0$ the deterministic part of the adaptation-channel noise vanishes ($a(t) = 0$) and the SCC reduces to

$$\lim_{\Delta \to 0} \rho_k = \rho_{k,\eta}. \tag{2.4.59}$$

This is so because $a^* = 0$ implies $\nu = 1$ and $\rho_{1,a} = 0$ (Eq. 2.4.48) and the prefactors become $B = 1 - \alpha\beta$ and $C = 1 - \alpha\beta$ so that $B/C = 1$. As pointed out in Sec. 2.4.1, in this case, the SCC is

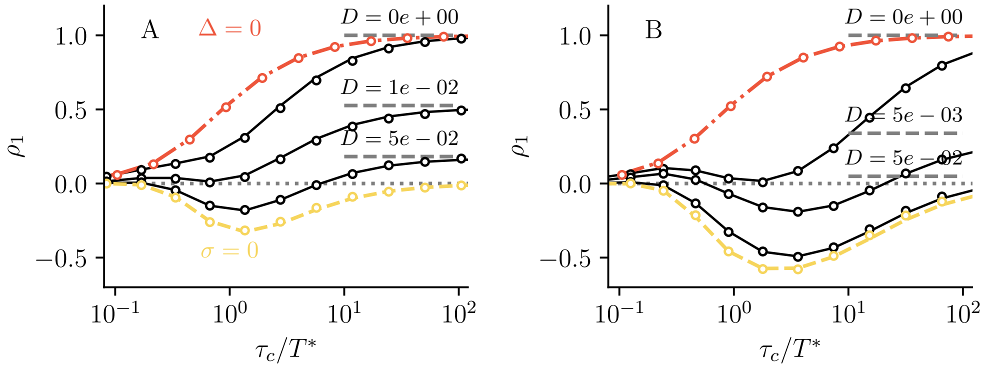

FIGURE 2.25: Serial correlation coefficient ρ_1 for the LIF model with adaptation-channel noise. Panels A and B show the SCC for two different parameter sets associated with weak and strong adaptation. In both cases, ρ_1 exhibits a non-monotonic behavior with respect to the common timescale $\tau_\eta = \tau_a = \tau_c$ given that the white noise intensity is not too small. The limit case of a vanishing adaptation ($\Delta = 0$) is shown by red circles and line, while the limit case of a vanishing correlated noise ($\sigma = 0$) is shown by yellow circles and line. The black circles and lines show the SCC for the full model with different white noise intensities. In the limit $\tau_c \to \infty$ the SCC reduces to $\rho_{1,\eta}$ indicated by dashed lines. Parameters A: $\gamma = 1$, $\mu = 5$, $\Delta = 2$, $\sigma = 0.2$; B: $\gamma = 1$, $\mu = 20$, $\Delta = 20$, $\sigma = 0.2$.

determined by the autocorrelation of the noise. Specifically for the OU process, adjacent intervals are positively correlated. For the red line in Fig. 2.25, we have additionally switched off the white noise ($D = 0$) so that ρ_1 approaches one for $\tau_c/T^* \gg 1$. For $\sigma = 0$, the stochastic part of the adaptation-channel noise vanishes ($\eta(t) = 0$), the white noise is the only remaining source of fluctuations in the system, and the SCC reduces to

$$\lim_{\sigma \to 0} \rho_k = \rho_{k,a}. \tag{2.4.60}$$

This is so because $\sigma = 0$ implies $\rho_{1,\eta} = 0$ (Eq. 2.4.49) if the intensity of the white noise does not vanish at the same time[5]). Furthermore, the prefactors become $A = 1 - \alpha\nu\beta$ and $C = 1 - \alpha\nu\beta$ so that their ratio equals $A/C = 1$. As we have explained in detail in Sec. 2.4.3 and as it is known from the literature, adjacent intervals are negatively correlated in this case. The respective SCC ρ_1 has a minimum for some intermediate time close to $\tau_c \approx T^*$ and vanishes in both the limit $\tau_c \to 0$ and $\tau_c \to \infty$ (yellow lines). The first case is easily understood: For $\tau_c \to 0$, the adaptation quickly decays towards $a = 0$, in particular, fast compared to the deterministic ISI T^*. The values a_i at the beginning of each interval are, therefore, almost independent of the specific length of the preceding interval. Instead, a_i is essentially given by the amplitude of the kick Δ/τ_c. The adaptation decays infinitely slowly in the opposite limit $\tau_c \to \infty$. At the same time, however, the kick amplitude Δ/τ_c also vanishes so that $a(t)$ remains finite. As a result, the specific values a_i attained at the beginning of intervals hardly differ. In both cases, interval correlations vanish because the dependence of a_i on the length of the preceding interval is exactly what correlates the intervals.

For intermediate cases, where we consider the full adaptation-channel-noise model, the behavior of the SCC depends on the specific choice of parameters, especially on the variance of the OU process σ^2 and the strength of the adaptation Δ, but also on the noise intensity of the white noise D. Without an additional white noise, the SCC can be a monotonic function of τ_c if Δ is sufficiently small (Fig. 2.25A). For larger values of Δ, the SCC becomes non-monotonic again but remains positive for all values of τ_c (Fig. 2.25B). This changes when an additional white noise is

---

[5] The fact that $\lim_{\sigma \to 0} \rho_{1,\eta} = 0$ only holds if there is an additional noise source can be somewhat counterintuitive. Shouldn't it be enough to require that the fluctuations of $\eta(t)$ vanish?This is not the case because the correlation coefficient is the ratio between the covariance $\langle \delta T_i \delta T_{i+1} \rangle$ and the variance $\langle \delta T_i^2 \rangle$, and both approach zero for $\sigma \to 0$ when the OU process is the only noise source. This is no longer the case in the presence of additional white noise because then the variance remains finite regardless of σ.

introduced, which can change the sign of the SCC ρ_1. This illustrates how fluctuations from channels with different timescales can interact to shape the SCC of the ISI. For larger values of D, the SCC approaches the purely white noise-driven case. This is so because, according to Eq. 2.4.49 the SCC $\rho_{1,\eta}$ vanishes for $D \gg \sigma^2\tau_\eta$ (which also implies $A/C = 1$). In any case in the limit $\tau_c \to \infty$ the SCC approaches

$$\lim_{\tau_c\to\infty} \rho_1 = \rho_{1,\eta}, \tag{2.4.61}$$

which for the LIF model is explicitly solved by

$$\lim_{\tau_c\to\infty} \rho_{1,\eta} = \frac{1}{1+\gamma\frac{D}{\sigma^2}\cot(\gamma T^*/2)}, \tag{2.4.62}$$

where $\cot(x) = \cos(x)/\sin(x)$ is the cotangent. The limit is depicted in Fig. 2.25A and B by dashed lines.

2.4.6 Network noise

So far, we have considered neuron models driven by a positively correlated noise because it is thought to arise from synaptic filtering of the uncorrelated presynaptic spike train or from slow ion channels (channel noise). The power spectrum of such noise is low-pass filtered, i.e., it has increased power at low frequencies and decreased power at high frequencies. This applies to neurons in the sensory periphery, where the variability in spike times is mainly caused by channel noise due to a lack of synaptic input. However, our theory can also be applied to neurons in a recurrent neural network under certain conditions. Recall that our theory relies on the assumption that the neuron model fires even in the absence of noise, i.e., that the model operates in the mean-driven regime. This severely limits the applicability of the theory in the context of recurrent neural networks because many neurons in the cortex operate in the excitable regime. However, most neural networks exhibit a large heterogeneity in cellular parameters and the type and strength of synaptic connections. This results in a large distribution of firing rates and CVs, varying between 0.2 and 1.5 [151, 152]. Cells that fire regularly with CVs as low as 0.2 can be assumed to be mean-driven. It should be noted that such low CVs could, in principle, also be realized in the excitable regime by a mechanism known as coherence resonance but would require fine-tuning of the parameters so that the model is very close to the bifurcation point (separating the excitable from the mean-driven regime) and the noise intensity is just right [92, 100, 116].

Here we consider a mean-driven neuron subject to correlated noise, as it would arise from a recurrent network in the asynchronous irregular state. We can think of our model neuron as either being part of this network or receiving feedforward input from it. Such network noise can be approximated by a Gaussian process that fluctuates around a certain mean and has a temporal correlation function that depends on the connectivity [153, 154]. In a typical situation where the population firing rate is not too high, it has been shown both experimentally [155] and theoretically [131, 153, 156] that the power spectrum of the fluctuations has reduced power at low frequencies (cf. Fig. 2.26A) and is otherwise flat. Such fluctuations are called *green* noise and are negatively correlated (in contrast to the positively correlated *red* noise).

As it was shown by Vellmer and Lindner [131], such a power spectrum can be generated if the previously independent noise sources in Eq. 2.4.1 are perfectly anti-correlated $\xi_v(t) = -\xi_\eta$. In this case, we can interpret the sum of the white noise and filtered version of itself as a single random process $\zeta = \sqrt{2D}\xi_v(t) + \eta(t)$. The power spectrum of this new process is given by

$$S_{\zeta\zeta}(\omega) = 2D - \frac{4\sqrt{D\sigma^2\tau_\eta} - 2\sigma^2\tau_\eta}{1+\tau_\eta^2\omega^2}, \tag{2.4.63}$$

with a constant high-frequency limit given by the intensity of the white noise $\lim_{\omega\to\infty} S(\omega) = 2D$ and a comparatively reduced power at low frequencies $\lim_{\omega\to 0} = (\sqrt{2D} - \sqrt{2\sigma^2\tau_\eta})^2 < 2D$.

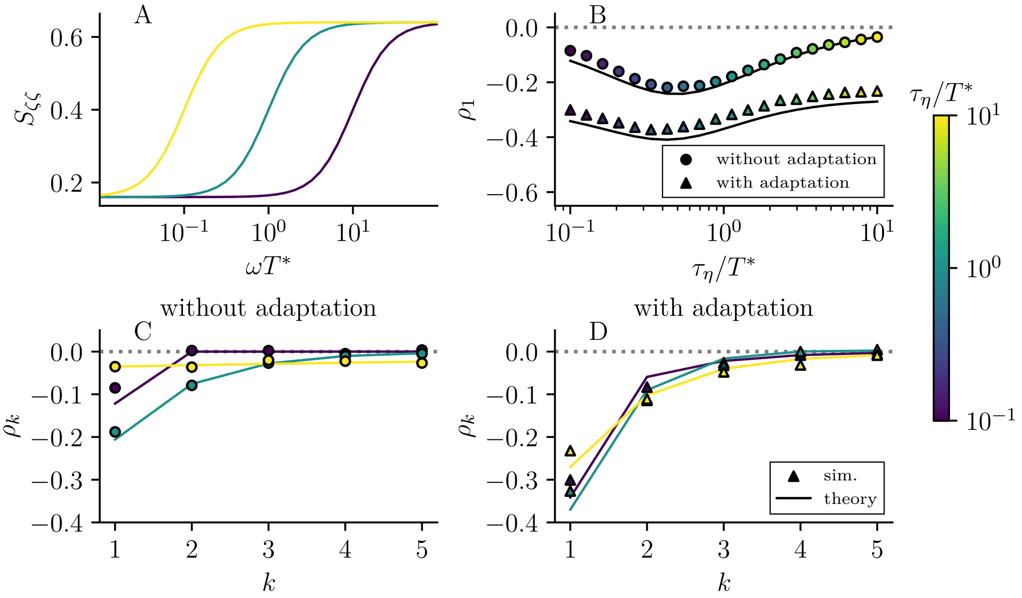

FIGURE 2.26: Serial correlation coefficient for LIF model with network-noise-like fluctuations. Panel A shows the power spectrum $S_{\zeta\zeta}$ of the input noise with reduced power at low frequencies. Panel B shows the SCC ρ_1 for a LIF model without (circles) and with (triangles) adaptation. The SCC has a minimum for intermediate values of τ_η since the noise becomes white both in the limit $\tau_\eta \to 0$ and $\tau_\eta \to \infty$. Panels C and D show the pattern of interval correlation for the LIF model without and with adaptation, respectively. Even in the absence of the adaptation (C), a correlated noise with reduced power at low frequencies can result in negative interval correlations. For the adaptive LIF (D), negative correlations are amplified by the network-noise-like fluctuations. Parameters C: $\gamma = 1$, $\mu = 5$, $\gamma = 1$, $\tau_a = 0$, $\Delta = 0$, $2\sigma^2\tau_\eta = 0.16$, $2D = 0.64$, $T^* \approx 0.22$; D: $\gamma = 1$, $\mu = 5$, $\gamma = 1$, $\tau_a = 2$, $\Delta = 2$, $2\sigma^2\tau_\eta = 0.16$, $2D = 0.64$, $T^* \approx 0.67$.

Furthermore, the turning point between these limits is given by $\omega = 1/\tau_\eta$. The respective autocorrelation function can be calculated using the Wiener–Khinchin theorem

$$C_{\zeta\zeta}(\tau) = 2D\delta(\tau) - \left(2\sqrt{\frac{D\sigma^2}{\tau_\eta}} - \sigma^2\right) e^{-|\tau|/\tau_\eta}, \tag{2.4.64}$$

so that τ_η is similar to a correlation time. Strictly speaking, the process $\zeta(t)$ has a no correlation time, defined as the ratio of the integrated correlation function to the variance, simply because the variance of the white noise $\xi(t)$ diverges. Finally, a numerical inspection of the network spectrum Eq. 2.4.63 by [131] revealed that τ_η is related to the (inverse) mean firing rate r_0 or likewise the mean ISI $\langle T_{\text{net}}\rangle$ of the recurrent network so that we roughly chose $\tau_\eta \approx \langle T_{\text{net}}\rangle/\omega$. The remaining parameters D and σ^2 that determine the power spectrum depend specifically on properties of the synaptic connections, see [131].

In Fig. 2.4.63A, we show the power spectrum of the process $\zeta(t)$ for three different values of the parameter τ_η. In all cases, the parameters D and σ^2 are chosen so that the low-frequency limit of the power spectrum is a quarter of the high-frequency limit $S_{\zeta\zeta}(\omega \to 0)/S_{\zeta\zeta}(\omega \to \infty) = 1/4$, similar to what was found by [131]. Note that this means that the product $\sigma^2\tau_\eta$ is fixed. In Fig. 2.4.63B, we calculate the first correlation coefficient ρ_1 for a LIF model with and without adaptation driven by the correlated noise $\zeta(t)$. As was demonstrated previously, the SCC for an IF model without adaptation, purely driven by a correlated noise, can be calculated according to

$$\rho_k = \frac{\int d\omega\, |\tilde{Z}(\omega)|^2 S_{\zeta\zeta}(\omega) e^{ik\omega T^*}}{\int d\omega\, |\tilde{Z}(\omega)|^2 S_{\zeta\zeta}(\omega)}, \tag{2.4.65}$$

where, compared to Eq. 2.4.20, the noise intensity does not appear explicitly in the denominator but is included in the power spectrum. For an IF model with adaptation driven by the high-pass filtered noise $\zeta(t)$, our result for the general SCC (Eq. 2.4.47) still applies because the correlation function Eq. 2.4.64 decays exponentially with a single timescale[6]. In this case, the SCC (Eq. 2.4.65) agrees with the specific SCC $\rho_{k,\eta}$.

In both cases shown in Fig. 2.26B, the SCCs measured from stochastic simulations (symbols) are in good agreement with the theoretical predictions (lines). Here we have chosen the parameters D and $\sigma^2\tau_\eta$ such that the resulting CV is between $0.2-0.5$, i.e., in the lower physiological range of cortical neurons. The agreement between theory and simulations could be improved by considering a weaker noise. The negatively correlated green noise induces negative ISI correlations (Fig. 2.26C), which become even stronger with an additional adaptation current (Fig. 2.26D). Moreover, the SCC depends non-monotonically on τ_η because the noise becomes uncorrelated in the limit $\tau_\eta \to 0$ but also in the limit $\tau_\eta \to \infty$. For $\tau_\eta \to 0$, this is clear and can be seen from the correlation function, but also from the power spectrum. The latter is reduced across all frequencies because the turning point of the spectrum is given by $\omega = 1/\tau_\eta$. Hence, for $\tau_\eta \to 0$, we obtain a flat power spectrum with reduced power compared to the white noise power spectrum:

$$\lim_{\tau_\eta \to 0} S_{\zeta\zeta}(\omega) = (\sqrt{2D} - \sqrt{2\sigma^2\tau_\eta})^2. \tag{2.4.66}$$

A similar argument applies for large values of $\tau_\eta \to \infty$, except that the turning point lies at $\omega \to 0$ in this limit. As a result, the power spectrum is gain constant over all frequencies and coincides with the white noise spectrum:

$$\lim_{\tau_\eta \to \infty} S_{\zeta\zeta}(\omega) = 2D. \tag{2.4.67}$$

Most relevant are intermediate values of τ_η. We have already noted that τ_η is roughly associated with the mean ISI of the neurons in the network. For a mean-driven cell with ISI $\langle T \rangle \approx T^*$ that fires somewhat faster than the network average, it is most relevant to consider values of τ_η that are somewhat larger than T^*. This is because from $\tau_\eta = \langle T_{\text{net}} \rangle / \pi$ and $\langle T_{\text{net}} \rangle > T^*$ it follows that $\tau_\eta / T^* > 1$. Interestingly, this is where the negative ISI correlations are most pronounced.

2.4.7 Range of validity

We emphasized in Sec. 2.3.2 that the PRC is essentially the linear response function of the phase variable, so our main result Eq. 2.4.47 is a first-order approximation of the perturbation amplitude. Therefore, one may wonder how well the result approximates the SCC as the perturbation becomes stronger.

To answer this question, we return to the most general case discussed in Sec. 2.4.4, the adaptive GIF driven by white and colored noise. We choose a specific set of parameters for the corresponding deterministic system and separately vary the two parameters associated with the amplitude of the perturbation, namely the intensity of the white noise D and the variance of the colored noise σ^2. We then measure the CV C_V and the SCC ρ_1 and compare the latter to the theoretical prediction according to Eq. 2.4.47. This allows to quantify the range of validity with respect to the output variability of the interspike intervals.

In Fig. 2.27A we fix the variance σ^2 and vary the white noise intensity. For small intensities of the white noise D, the SCC ρ_1 is mainly determined by the correlated noise and thus positive. As the intensity increases, the SCC becomes negative, an effect we have already discussed in Sec. 2.4.5. Additionally, we observe an increase in the output variability as shown in Fig. 2.27A$_1$. In Fig. 2.27A we fix the white noise intensity D and increase the variance σ^2. For small variances, the SCC ρ_1 is mainly determined by the combination of the adaption and white noise and, therefore, negative. This changes when the variance is increased. Again, this also leads to a likewise increase of the output variability as shown in Fig. 2.27B$_1$.

In the first case, we find quantitative agreement between the SCC obtained from stochastic simulations and the theory up to $D = 0.1$ and $C_V \approx 0.3$, indicated by a vertical dotted line in Fig. 2.27A. In the second case, the qualitative agreement is found up to $\sigma^2\tau_\eta = 0.1$, but the resulting $C_V \approx 0.15$ is smaller in this case. In both cases, we also examine how the pattern of interval correlations ρ_k deviates from the theoretical prediction (inset in Fig. 2.27A$_2$ and B$_2$). We find that although the SCC is not quantitatively predicted, the general pattern is still well described. In particular, in the inset of Fig. 2.27A$_2$, the theory reproduces the fact that the SCC

---

[6] Recall, that the evaluation of the sum in Eq. 2.4.40 relies on this condition.

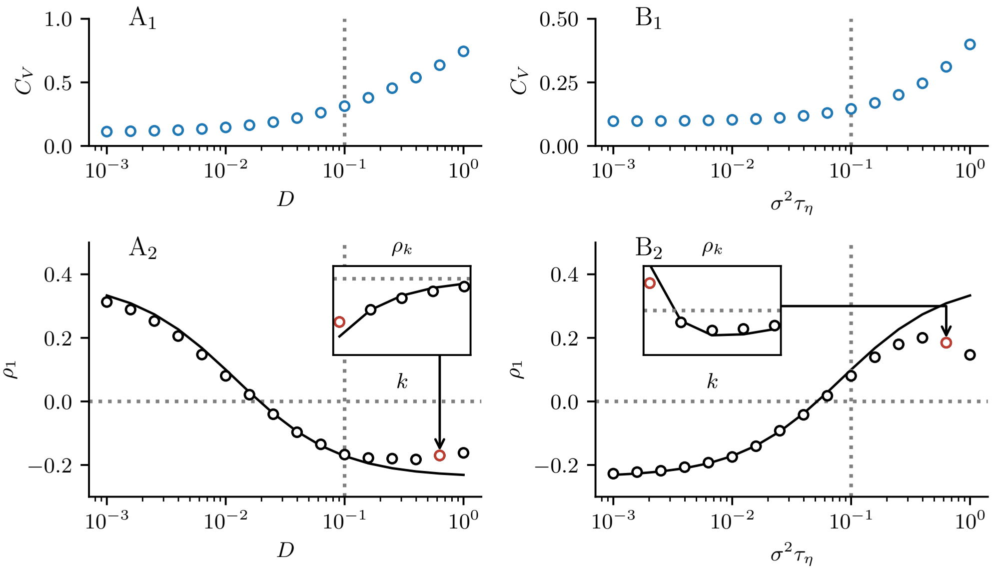

FIGURE 2.27: Range of validity for an adaptive GIF with varying noise strength. Panels A and B show the CV C_V and SCC ρ_1 as functions of the two small parameters D and $\sigma^2\tau_\eta$ of the weak-noise theory. In panel A, the variance $\sigma^2 = 0.1$ is fixed, and the white noise intensity D is increased. We find quantitative agreement between simulation results (circles) and the theory (line) up to $D = 0.1$. Beyond this point, both the predicted SCC ρ_1 begin to deviate from the simulation results. However, the qualitative agreement remains. In panel B the white noise intensity $D = 0.1$ is fixed, and the variance is increased. Again we find quantitative agreement up to $\sigma^2\tau_\eta = 0.1$ and qualitative agreement even beyond this point. Parameters A and B: $\gamma = 1$, $\mu = 20$, $\beta = 1.5$, $\tau_w = 1.5$, $\tau_a = 10$, $\Delta = 10$, $T^* \approx 0.57$.

is a monotonically decreasing function of k, and even for the more complicated pattern shown in the inset of Fig. 2.27B$_2$ the theory reproduces the sign change between ρ_1 and ρ_2 as well as the subsequent minimum at $k = 3$. Thus, the qualitative agreement is maintained even for higher output variability.

2.4.8 Traub-Miles model with an M-type current

So far, all models we have used and discussed are of the integrate-and-fire type. In fact, already in Sec. 2.4.1 we have pointed out that the reset upon spiking of all variables, except for the adaptation and noise, is important for the derivation of the general SCC. This is because variables that suffer a hard reset are guaranteed to be on the limit cycle at the beginning of an ISI and therefore do not contribute to the perturbation from the limit cycle. Conversely, this means that any variable that is *not* reset is unlikely to take the exact value it would have on the limit cycle at the beginning of an interval and therefore contributes to the perturbation from the limit cycle, the deviation of the spike time and eventually to the SCC. Such variables would have to be treated similarly to the adaptation variable, which significantly complicates the calculations presented in Sec. 2.4.2.

Nevertheless, here we consider a conductance-based neuron model and explain why we can expect our theory to provide a reasonable approximation to the SCC despite the lack of a reset. In particular, we use a variation of the Traub-Miles model introduced in Sec. 2.2.1 endowed with a slow potassium current [101] and apply an additional correlated and uncorrelated noise:

$$\begin{aligned} C\frac{dV}{dt} &= -I_{\text{ion}} - I_{\text{adap}} + I + \eta + \sqrt{2D}\xi_v(t), \\ \tau_\eta \frac{d\eta}{dt} &= -\eta + \sqrt{2\sigma^2\tau_\eta}\xi_\eta(t). \end{aligned} \tag{2.4.68}$$

Here I is a constant current, and the fast ionic currents are summarized in I_{ion}. The latter includes the fast sodium, leak, and potassium currents, each given in terms of the respective reversal potentials E_y, the maximum conductances g_y, and the gating variables h, n, and m:

$$I_{\text{ion}} = g_{\text{Na}} h m^3 (V - E_{\text{Na}}) + g_{\text{L}}(V - E_{\text{L}}) + g_{\text{K}} n^4 (V - E_{\text{K}}),$$
$$\frac{dx}{dt} = a_x(V)(1-x) - b_x(V)x, \quad \text{with} \quad x = h, m, n. \tag{2.4.69}$$

Finally, spike-frequency adaptation is mediated by a slow ion current, namely the potassium current

$$I_{\text{adap}} = \bar{g} z (V - E_{\text{K}}),$$
$$\tau_z \frac{dz}{dt} = h(V) - z, \quad \text{with} \quad h(V) = \frac{1}{1 + \exp\left(-\frac{V+20}{5}\right)}. \tag{2.4.70}$$

The functions $a_x(V)$, $b_x(V)$, and $h(V)$, as well as the values of the parameters occurring therein, are given in Table 2.1.

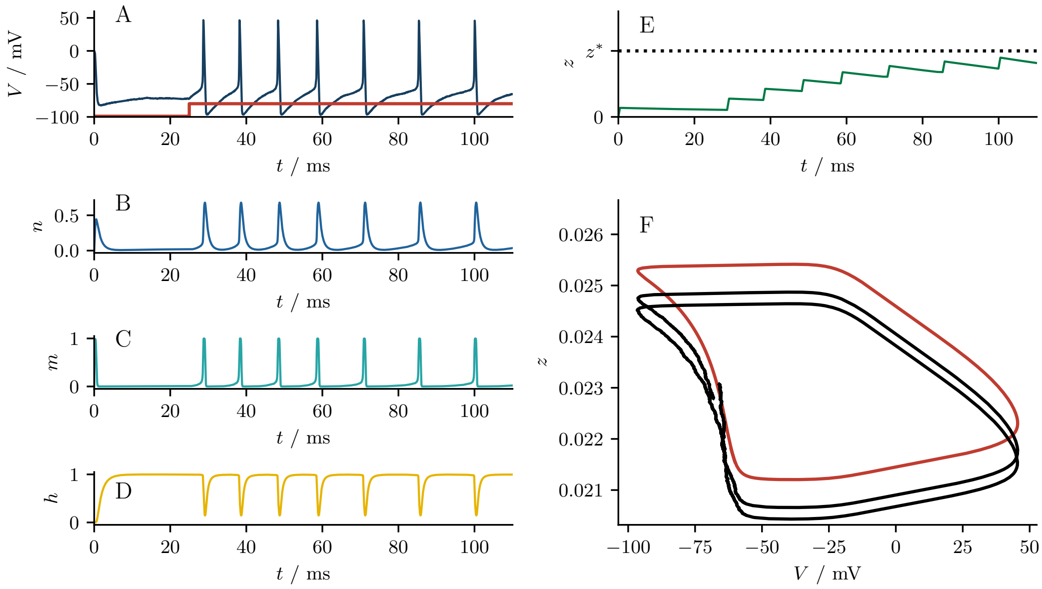

FIGURE 2.28: The Traub-Miles model with a slow M-type current. Panels A, B, C, and D show the membrane potential $V(t)$ and standard gating variable $n(t)$, $m(t)$, and $h(t)$, respectively. The model is additionally endowed with an M-type current that is governed by the additional gating variable $z(t)$ shown in panel E. At $t = 25$ms, a constant current $I = 5pA$ (red line in panel A) is applied, causing the model to enter the mean-driven regime. Due to the slow buildup of the adaptation variable $z(t)$, the initial high firing rate decreases until the adaptation variable reaches its stationary value, indicated by a dotted line in panel E. Panel F shows the stationary deterministic limit cycle (red line) together with a noisy trajectory of the model. Parameters: Table 2.1 and $I = 5$pA, $\tau_z = 100$ms, $\bar{g} = 5$nS, $\tau_\eta = 10$ms, $\sigma^2 = 0.1\text{pA}^2$, $D = 0.1\text{pA}^2$ms, $T^* \approx 18.9$ms.

An exemplary trajectory of the voltage (blue lines) in response to a constant current simulation (red line) is shown in Fig. 2.28A. The trajectories of the gating variables $n(t)$, $m(t)$ and $h(t)$, which affect the fast ion currents, are shown in Fig. 2.28B, C, and D. Evidently, the three gating variables $n(t)$, $m(t)$, and $h(t)$ are fast compared to a typical ISI. This is most obvious for the two variables n and m, which return to 0 almost immediately after the spike, and less obvious for the variable h, which decays to 1 a somewhat slower, but still fast compared to a typical ISI. This means that values of the gating variables after a spike bear little relation to the length of the preceding ISI and could as well be reset to a set of fixed values. Therefore, we can expect our theory to work for this model as well. In contrast, the variable $z(t)$ (Fig. 2.28E)shows a completely different behavior, increasing rapidly when the voltage is sufficiently depolarized and decreasing slowly otherwise. This behavior is very similar to the spike-triggered adaptation in our model (Eq. 2.4.21) and can mediate correlations between intervals. In Fig. 2.28F, we show the limit cycle in the V-z-plane because.

We must first determine the PRC to apply our theory to this model. Since the model is highly nonlinear, we use the direct method and apply small current pulses $\epsilon\delta(t-\tau)$ (where t is measured with respect to the last spike time) to the deterministic model at a certain phase τ on the limit cycle. This results in a deviation of the spike time from which we can infer the PRC at a given phase according to Eq. 2.3.15. Doing this for different phases τ allows us to determine the entire PRC as shown in Fig. 2.29A$_1$. Note that the PRC is strictly positive, so we expect similar SCCs as discussed in Sec. 2.4.3. In Fig. 2.29A$_2$, we show the corresponding values of the voltage on the limit cycle for each phase τ and define the peak of the spike as the point where $\tau = 0$. Additionally, our theory requires knowledge of the deterministic period T^*, the peak adaptation value a^*, and the timescale of the adaptation current τ_a. The latter is simply given by $\tau_a = \tau_z$ as seen from Eq. 2.4.70. The values T^* and a^* must be determined numerically. For the specific parameters we find $T^* = 18.9\,\mathrm{ms}$ and $a^* = I^*_{\mathrm{adap}}/C = 4.2\,\mathrm{mV\,ms}^{-1}$ corresponding to a weak perturbation defined by the parameter ν.

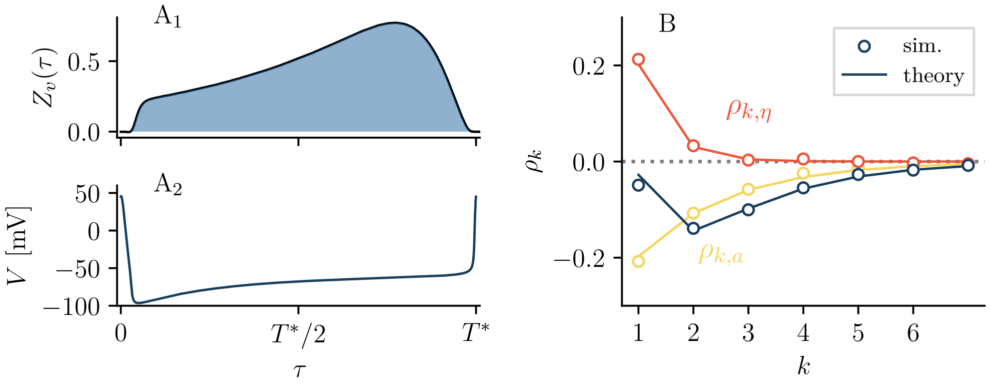

FIGURE 2.29: Serial correlation coefficient for the Traub-Miles model with a slow M-type current. Panel A$_1$ and A$_2$ show the PRC $Z_v(\tau)$ and the corresponding (deterministic) trajectory of the voltage over the period T^*. The phase $\tau = 0$ is defined by the voltage reaching its maximum. Panel B shows the general SCC ρ_k and the two specific SCCs $\rho_{k,a}$, $\rho_{k,\eta}$ similar to what we have shown in Fig. 2.21. Because the PRC is positive, we expect and indeed observe patterns of interval correlations similar to those for the LIF model.

We show the SCC in three scenarios similar to the discussions around Fig. 2.21. First, for the Traub-Miles model without a spike-triggered adaptation ($\bar{g} = 0$) but driven by a correlated noise (red), second for the Traub-Miles model with a spike-triggered adaptation but without a correlated noise ($\sigma^2 = 0$) (yellow), and finally for the full model, i.e. the Traub-Miles model with a spike-triggered adaptation driven by a correlated noise (blue). We find good agreement between the SCC obtained from stochastic simulations (circles) and the theory (lines) in all three cases. This demonstrates that our theory can also be applied to conductance-based models.

2.5 Summary

In this chapter, we have seen that randomness and adaptation are two essential features of neural spike generation. Randomness results from various internal noise sources (thermal noise, channel noise) and external noise sources (network noise) [9, 33]. Adaptation is often the result of a slow inhibitory current. These two features are not only reflected in the spontaneous activity of neurons but also affect the signal transmission properties when the neuron is stimulated with an information-carrying time-dependent signal [101, 157–167], and their synchronization properties in a large recurrent network [143, 168–170]. Therefore, it is an important goal in computational neuroscience to understand spiking neuron models that incorporate these features.

In Sec. 2.2, we have argued that while detailed conductance-based models describe the generation of the action potential in terms of different ion currents and have certainly been very insightful when it comes to the dynamics that shape the action potential, they are at the same time high-dimensional, nonlinear, and as a consequence difficult to treat analytically. However, because neurons often integrate postsynaptic potentials and fire a stereotypical action potential when a certain voltage threshold is exceeded, it is reasonable to focus on the often much simpler subthreshold dynamics and to replace the action potential with a fire-and-reset mechanism. This led us to the class of integrate-and-fire models, which provide a phenomenological description of neuronal spiking while remaining analytically tractable. Indeed, much effort has been devoted to the theoretical treatment of this class of models, see e.g. [9, 33, 38, 39, 62]. Moreover, it has been shown that stochastic integrate-and-fire models endowed with an adaptation current can mimic the response of pyramidal cells to different stimuli to an astonishing degree [42, 123, 171, 172].

Returning to the theoretical treatment of integrate-and-fire models, it is often assumed that interspike intervals are statistically independent, in which case the ISIs T_i are fully characterized by the probability density $p_{\mathrm{ISI}}(t)$. Put differently, neural spiking is assumed to be a renewal process [45, 76]. While this assumption allows for a far-reaching theory of recurrent neural networks [75, 173], we have seen that it is not always justified because slow processes can affect neural spike generation over multiple ISIs. The two most important mechanisms by which intervals become correlated are a temporally correlated input noise and slow inhibitory adaptation currents. The latter are often responsible for the ubiquitous phenomenon known as spike-frequency adaptation. As a consequence, the ISIs are no longer statistically independent but correlated, i.e., neural spiking is nonrenewal. In this case, the ISIs T_i are no longer fully characterized by the probability density but depend on the entire history of ISIs $T_{i-1}, T_{i-2}, \dots$ (or spike times $t_i, t_{i-1}, t_{i-2}, \dots$). A relatively simple linear measure to quantify interval correlations is given by the serial correlation coefficient ρ_k, which indicates whether the deviations of two intervals from the mean are on average proportional ($\rho_k > 0$), anti-proportional ($\rho_k < 0$) or uncorrelated ($\rho_k = 0$). This coefficient has been calculated analytically in several special cases, assuming that the noise is slow [66, 174], or weak [74, 92, 95, 115, 175], or that the adaptation is weak [97, 176], but the literature on nonrenewal neural spiking is disproportionally smaller. In particular, the SCC has not been calculated for the most realistic setup of an adaptive neuron model driven by an uncorrelated and correlated noise. Here, we have filled this gap.

However, since even the linear measure of interval correlations, namely the serial correlation coefficient, is difficult to calculate, we resorted to approximative methods. Specifically, we used an approach based on the phase reduction of a dynamical system that possesses a limit cycle in the deterministic limit [132, 135] detailed in Sec. 2.3. In this framework, weak perturbations of the dynamical system can be translated into spike time deviations by the phase response curve, i.e., the linear response function of the phase variable. Therefore, our theory is subject to two limitations: first, we must restrict ourselves to neuron models that operate in the mean-driven regime, i.e., that fire tonically in the deterministic limit, and second, the perturbations to which this system is subjected must be weak. We note that the theory presented here relies heavily on a previous approach developed by [74], who calculated the SCC from the phase response curve for a stochastic multidimensional IF model with adaptation but driven only by white noise. In Sec. 2.4, we generalize their approach to include an additional colored noise and derive a qualitatively new expression for the SCC given by Eq. 2.4.47: ρ_k as a function of the delay k is not limited to a single geometric sequence, but can be expressed as the sum of two geometric sequences. These two sequences can be interpreted well since they correspond exactly to the SCCs that would be obtained if adaptation and colored noise were considered separately. This is a very useful but highly non-trivial result due to the interplay of correlated noise and adaptation. The resulting patterns of interval correlations that such a sum can account for have not been theoretically explained.

The derived expression has been tested in a number of special cases. We have shown that how adaptation and correlated noise affect the interval correlations depends crucially on the shape of the PRC. For neurons with strictly positive PRC, an adaptation current results in negative interval correlations, and positively correlated input noise results in positive interval correlations. For neurons with a partially negative PRC, the situation is more complicated, and even the qualitative behavior of the SCC depends on the timescale of the correlation-inducing processes. In this case, adaptation currents can induce positive correlations, and positively correlated noise can induce negative correlations. The PRC is closely related to i) the neuron type, determined by the spike-onset bifurcation, and ii) the neuron class, determined by the shape of the F-I curve. In Type I neurons with a SNIC bifurcation, the PRC is purely positive, and the F-I curve is continuous

[145]. In Type II neurons with a subcritical Hopf bifurcation, the PRC may be partially negative, and the F-I curve has a discontinuity at the rheobase [99]. We have seen that the behavior of Type I and Type II neurons can be mimicked by the leaky and the generalized IF models, respectively.

Furthermore, two biophysically relevant cases have been studied. First, we have considered a case where a finite population of adaptation channels causes both the adaptation and the correlated noise and showed that in this case, the SCC ρ_1 has a minimum with respect to the timescale of the adaptation channels. Second, we investigated a case where the noise resembles that of a recurrent network in the asynchronous irregular state. In this case, the power spectrum has reduced power at low frequencies, corresponding to a negatively correlated noise process. We have shown that this is another independent process that can give rise to negative interval correlations. Finally, we have shown that the theory also applies to the conductivity-based Traub-Miles model with an M-type current and correlated noise, demonstrating the broad applicability of the theory.

Chapter 3

Nonrenewal spiking in Ca^{2+} signaling

3.1 Introduction

Cells communicate with each other primally through extracellular chemical messengers, of which there are four types: paracrine, neurotransmitter, hormone, and neurohormone [177]. These first messengers often bring about the desired cellular response by binding to one of the more than 700 different G protein-coupled receptors (GPCRs)[178] located in the cell or plasma membrane (PM) and increasing the intracellular concentration of a second messenger. Remarkably, despite the multitude of possible responses, there are only two major second messengers: cyclic adenosine monophosphate (cAMP) and Ca^{2+}. In this chapter, we focus on Ca^{2+} as a second messenger. Many of the Ca^{2+}-dependent cellular events are triggered by the activation of calmodulin (CaM). This intracellular Ca^{2+}-binding protein is not itself enzymatically active but phosphorylates target proteins, resulting in the cellular response. Among the processes regulated by Ca^{2+} through CaM are muscle contraction and relaxation, synaptic neurotransmitter secretion, fertilization, and apoptosis [23–26, 28]. Interestingly, similar to neuronal signals, Ca^{2+} signals often occur in the form of short, pulse-like increases in the intracellular Ca^{2+} concentration, so-called Ca^{2+} oscillations or spikes [24, 28].

To utilize Ca^{2+} as a second messenger, most cells maintain an extraordinary low resting intracellular Ca^{2+} concentration of about 100 nM that is four to five orders of magnitude lower than the extracellular Ca^{2+} concentration [19, 29]. The increase in the intracellular Ca^{2+} concentration can then be brought about either by Ca^{2+} entry from the extracellular medium through PM channels or by Ca^{2+} release from intracellular storage compartments, primarily the ER. We focus on the latter case, where the release of Ca^{2+} from the ER is initiated by binding a first messenger to a GPCR. This activates the inositol 1,4,5-trisphosphate (IP_3) pathway (see Fig. 3.1): the G protein activates the enzyme phospholipase C (PLC). PLC cleaves phosphatidylinositol 4,5-bisphosphate (PIP_2) into IP_3 and diacylglycerol (DAG). IP_3 diffuses through the cytosol and binds to the designated IP_3 receptor (IP_3R). The IP_3R channels are usually found in clusters of about 2 to 10 channels that collectively release Ca^{2+} in the form of short bursts called puffs or sparks. This increases the cytosolic Ca^{2+} concentration and eventually lead to the initiation of a cell-wide Ca^{2+} spike via a positive feedback mechanism. The cytosolic Ca^{2+} concentration in turn regulate various cellular functions in the form of stimulus-dependent spike-patterns [24, 28]. Among the processes that intracellular Ca^{2+} regulates in a specifically frequency-dependent manner are the transcription factors NFAT1 to NFAT4 (again via CaM), airway smooth muscle contraction, and the Ca^{2+}/CaM-dependent protein kinase II [20–22, 27].

The response of two different cell types to an agonist stimulation is shown in Fig. 3.2. In Fig. 3.2A, a human embryonic kidney (HEK) cell was stimulated with carbamylcholine, a structural analog of the neurotransmitter acetylcholine. In Fig. 3.2B, a HeLa cell was stimulated with histamine, a neurotransmitter or hormone. In both cases, the agonist binds to a corresponding receptor, which activates a G protein and induces Ca^{2+} spikes via the IP_3 pathway. Two essential features of the Ca^{2+} signal are immediately apparent. First, the timing of the spikes is somewhat random. Second, the intervals between spikes increase as more spikes are fired - similar to the spike-frequency adaptation phenomenon discussed in the previous chapter. Thus stochasticity and adaptation are two essential features of Ca^{2+} signaling.

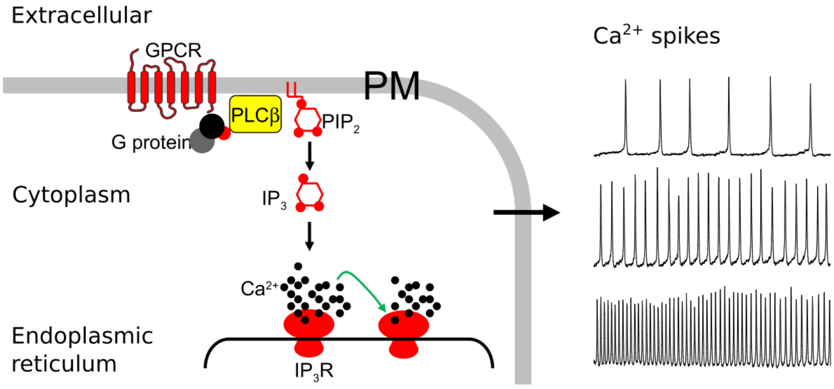

FIGURE 3.1: IP_3 pathway. Upon binding of an extracellular agonist to a GPCR, the G-protein's alpha subunit activates PLC, which hydrolyzes PIP_2 into IP_3 and DAG. IP_3 diffuses through the cytosol and binds to the IP_3R in the ER membrane leading to the release of stored Ca^{2+} into the cytosol. The resulting Ca^{2+} spikes trigger various intracellular responses. From *K. Thurley et al. Science signaling 7.331 (2014): ra59-ra59*. Reprinted with permission from AAAS. Modified with permission from M. Falcke.

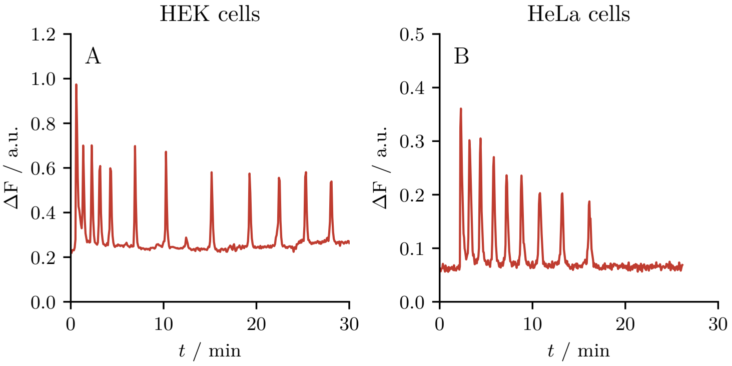

FIGURE 3.2: IP_3-mediated Ca^{2+} spiking in stimulated HEK and HeLa cells. Changes in the free cytosolic Ca^{2+} concentration are measured indirectly by changes in the Ca^{2+} indicator Fura-2 fluorescence ratio ΔF. Panel A and B show example measurements from HEK cells stimulated with 10 µM carbamylcholine (CCh) and HeLa cells stimulated with 100 µM histamine, respectively. Fluorescence signals were measured as described in [7, 8]. The data was provided, and permission was granted by M. Falcke.

In recent decades, Ca^{2+} spikes have often been perceived as a deterministic oscillation [179–183]. As a result, the focus has been on the dynamical properties that contribute to the generation of periodic Ca^{2+} spikes, and the Ca^{2+} current generated by the stochastic activity of the IP_3 receptors has often been considered in the thermodynamic limit. This neglects fluctuations in the cytosolic Ca^{2+} concentration caused by the puffs and the stochasticity of the spike times. To gain a comprehensive theoretical understanding of Ca^{2+} signaling, it is essential to employ stochastic models that accurately account for these fluctuations. Although stochastic models exist [24, 63, 64, 184–187], they do not focus on the spiking statistics as a point process. Specifically, higher-order spiking statistics associated with nonrenewal spike generation have not yet been considered, to the best of our knowledge.

In this chapter, we propose a phenomenological two-component model for the generation of Ca^{2+} spikes that accounts for the stochastic nature of the puffs, explains the observed transient by the depletion of the ER, and focuses on the spiking statistics as a point process. The first component describes the stochastic activity of clusters of IP_3Rs. The second component describes the dynamics of the intracellular Ca^{2+} concentration ($[Ca^{2+}]_i$) and the ER Ca^{2+} concentration ($[Ca^{2+}]_{er}$). We follow the idea that because the release of Ca^{2+} from the ER controls the generation of the cell-wide Ca^{2+} spikes, the cumulative depletion of the ER with each spike can explain the observed transients [30–32]. Based on this idea, we derive expressions for spiking statistics during the transient and in the stationary state. The effects of ER depletion on stationary second-order statistics are analyzed and compared with experimental data.

We use a kinetic model to describe the activity of IP$_3$R clusters. This model class is frequently used in mathematical cell biology and computational neuroscience to describe the activity of ion channels [48]. To describe the formation of Ca^{2+} spikes, we adopt the successful integrate-and-fire framework from computational neuroscience. These models describe spike generation phenomenologically and can be extended to include additional variables, such as slow processes affecting spike generation over multiple spikes. Moreover, integrate-and-fire models emphasize the excitable nature of the system, as we have explained in the previous chapter. We have already pointed out that Ca^{2+} spiking has long been perceived as a classical oscillatory system, while already the earliest models of neuronal spiking take into account characteristics of an excitable system [109, 110]. However, biophysically in both systems, it is recognized that spike generation involves a strong positive feedback mechanism, and also Ca^{2+} spiking is more commonly viewed as an excitable stochastic system [63, 64, 184]. Thus, applying the successful integrate-and-fire framework from computational neuroscience to the fundamental biophysical process of Ca^{2+} signaling seems a logical step that has not yet been taken.

This chapter is organized as follows. In the remainder of this first section, we provide a more comprehensive overview of the biophysical processes involved in the generation of the Ca^{2+} spike. In Sec. 3.2, we discuss a small number of kinetic models that describe the gating of the Ca^{2+} release channels and dynamic models that capture the change in the Ca^{2+} concentrations of different compartments in the cell. We will see that the modeling approaches used so far in the context of Ca^{2+} signaling are not fundamentally different from those used in computational neuroscience. In Sec. 3.3, we present our two-component model for the generation of Ca^{2+} spikes. The first component describes the stochastic opening and closing of the IP$_3$-receptor clusters. The second component describes the dynamics of the Ca^{2+} concentrations in the cytosol and the ER. Based on the observation that IP$_3$R channel activity is fast compared to the spike generation, we approximate the stochastic activity of the channel clusters by a Gaussian white noise. This process is completely determined by its mean and noise intensity. We show that regardless of the specific model, the noise intensity can be determined from the transition rate matrix by a system of algebraic equations. In Sec. 3.4, we first consider a simplified version of the model in which the Ca^{2+} concentration in the ER is assumed to be constant. In this case, the model generates a quasi-renewable spike train. This allows us to analytically calculate a large part of the spike train statistics using the Fokker-Planck equation associated with the Langevin approximation of the two-component model. We also ask to what extent the reduced model is able to reproduce the stationary statistics of ISI sequences observed in stimulated HEK cells. In Sec. 3.5, we return to the full two-dimensional model. This model generates a nonrenewal spike train and exhibits a distinct transient. Although the white noise approximation remains valid, the associated two-dimensional FPE is no longer analytically solvable. Instead, we use a slow adaptation approximation to calculate first-order stationary statistics. We also provide an intuitive explanation for the observed second-order stationary interval correlations based on the considerations of Chap. 2. Most importantly, we calculate statistics of the transient, specifically the number of transient intervals and the cumulative refractory period. The former quantifies the length of the transient, while the latter quantifies how much the intervals adapt during the transient. Finally, we fit our model to reproduce transient and first-order stationary statistics from spike sequences of single stimulated HEK cells. This provides a set of model parameters for each stimulated HEK cell. We find that the model predicts a rather weak depletion and slow replenishment of the ER. We then ask whether the (second-order stationary) interval correlations predicted by the model for the specific parameter sets are consistent with the experimentally observed interval correlations. It turns out that interval correlations of sequences of single cells can only be determined imprecisely due to the limited number of intervals. Therefore, statements about whether these correlations are well reproduced by our model are also difficult to make. However, when the observed interval correlations of all sequences are plotted as functions of the transient statistics, the observed trends are reproduced by our model.

3.1.1 Physiology of Ca^{2+} signaling

To generate Ca^{2+} spikes effectively, cells maintain an extraordinarily low resting Ca^{2+} concentration of about 100 nM inside the cell, which is 4 to 5 and 3 to 4 orders of magnitude lower than the Ca^{2+} concentration in the extracellular medium and the ER, respectively [19, 29]. This enormous gradient is maintained by different Ca^{2+}-ATPases and exchangers that compensate for the passive leakage of Ca^{2+} from the ER and the extracellular medium into the cytosol. Plasma membrane Ca^{2+}-ATPases (PMCAs) pump one Ca^{2+} per hydrolyzed ATP out of the cell and are complemented by Na^{+}/Ca^{2+} exchangers (NCXs), which exchange one Ca^{2+} ion for three Na^{+} ions, and Na^{+}/Ca^{2+}-K^{+} exchangers (NCKXs), which cotransport one Ca^{2+} and one K^{+} ion in exchange for four Na^{+} ions. Removal of Ca^{2+} from the cytosol into the ER is mainly accomplished by sarco/endoplasmic reticulum Ca^{2+}-ATPases (SERCAs), which pump two Ca^{2+} into the ER per hydrolyzed ATP.

When the cell is stimulated, an extracellular signaling molecule binds to the GPCR on the PM, activates the IP_3 pathway, and triggers the flood-like release of Ca^{2+} from the ER into the cytosol. This happens as follows: Upon activation of the GPCR, the Gα subunit dissociates from the G protein, allowing it to bind to and activate PLC, an enzyme located on the inner side of the PM. PLC then hydrolyzes PIP_2 into two second messengers: IP_3 and DAG. While DAG remains in the membrane, IP_3 diffuses through the cell and can bind to the designated IP_3R, a Ca^{2+} release channel, located in the ER membrane [188]. These receptors form spatially dense and functionally coupled clusters, scattered across the ER membrane with reported distances of 1 µm to 7 µm [189] (compared to the 20 nm IP_3R diameter [190, 191]). Opening a cluster of IP_3Rs results in a discharge-like release of Ca^{2+} from the ER into the cytosol. The local releases are called Ca^{2+} puffs and are thought to be the elementary events of cell-wide Ca^{2+} spike [189, 192]. Because channel/cluster gating happens in thermal contact with the surrounding molecules in the cell, it is a stochastic process, and the timing of the puffs is random [47, 193]. This noise is also reflected in the generation of cell-wide spikes because only a small number of IP_3 channels (<8%) in functional clusters contribute to Ca^{2+} release [194, 195].

However, the binding of IP_3 is only a prerequisite for opening the receptor channel. In addition, the IP_3R must bind Ca^{2+}. This has two effects. First, the channels in a cluster are locally strongly coupled because the Ca^{2+} concentration in the vicinity of an open channel can reach very high values within microseconds [196]. Thus, the opening of a single channel essentially triggers the opening of the entire cluster [197]. Second, the clusters in the cell are globally coupled by the cytosolic Ca^{2+} concentration, which is increased by the opening of the IP_3Rs clusters. In both cases, Ca^{2+} facilitates its own release. This positive feedback mechanism is known as Ca^{2+}-induced Ca^{2+} release (CIRC) and is thought to be responsible for the rapid increase in cytosolic Ca^{2+} concentration during the rising phase of the Ca^{2+} spike. Interestingly, the open probability of the IP_3 channels depends biphasic on Ca^{2+}, i.e., it decreases again at high cytosolic Ca^{2+} concentrations [198–200]. This negative feedback acts on a slower timescale, is responsible for the termination of the puff, and at least contributes to the termination of the spike [201]. However, the molecular mechanism of this negative feedback remains unclear.

After reaching the peak Ca^{2+} concentration during the spike, Ca^{2+} is rapidly pumped back into the ER by SERCA pumps or is expelled from the cell by PMCA pumps and Ca^{2+} exchangers. While a large fraction of the Ca^{2+} released during the spike is pumped back into the ER, a smaller fraction is lost to the extracellular medium. Due to the limited Ca^{2+} capacity of the ER, this leads to cumulative depletion and would only allow the generation of transient signals until the ER runs out of Ca^{2+}. The relatively constant level of Ca^{2+} in the ER, which allows the continuous generation of Ca^{2+} spikes, is maintained by a mechanism known as store-operated Ca^{2+} entry (SOCE) [202]: ER depletion leads to Ca^{2+} influx across the cell membrane via Ca^{2+} release-activated Ca^{2+} (CRAC) channels. These channels have a small but selective conductance. The molecular basis of how PM Ca^{2+} channels lead to ER replenishment has remained a mystery for nearly two decades [203]. Today it is known that ER depletion activates stromal interaction molecule 1 (STIM1) located in the ER membrane. Upon activation, STIM1s migrate and accumulate at ER-PM junctions where the ER is close enough to the PM for STIM1 to bind and open the CRAC channels (Orai1). This leads to an influx of Ca^{2+} at the ER-PM junction, which is immediately moved into the ER by SERCA pumps. A study by Suzuki et al. [204] indicates that although SOCE involves a Ca^{2+} flux through the cytosol, the cytosolic Ca^{2+} concentration remains largely unaffected due to the rapid reuptake into the ER.

3.2 Modeling IP$_3$R kinetics and Ca^{2+} dynamics

In the previous chapter, we worked with established models describing the generation of neuronal spikes. In particular, we have first discussed biophysically detailed conductance-based models and then turned to more phenomenological integrate-and-fire models, which still capture the response of real neurons to an astonishing degree [44]. Formulating such a simplified model to describe the generation of Ca^{2+} spikes is an essential part of this chapter. We will propose a two-component model describing the kinetics of Ca^{2+} channels, specifically clusters of IP$_3$Rs, on the one hand, and the dynamics of the relevant Ca^{2+} concentrations on the other hand. To place the model in the existing literature, in the following, we discuss two kinetic models describing the activity of IP$_3$R channels [179, 205] and one dynamic model describing the change of various Ca^{2+} concentrations and other agents in the cell that contribute to the Ca^{2+} spike generation [182]. The considered dynamic model is far from being the only model that could be discussed here but was chosen because it distinguishes a large number of different compartments in the cell and Ca^{2+} fluxes between them. The model provides an extensive overview, although it does not claim to provide a complete description.

3.2.1 Kinetic models: IP$_3$-receptor channel gating

We have explained in Sec. 3.1 that Ca^{2+} puffs are thought to be the building blocks of the cell-wide Ca^{2+} spikes. A comprehensive understanding of the generation of Ca^{2+} spikes thus requires understanding the activity of the Ca^{2+} release channels. Since the gating of ion channels occurs in thermal contact with the surrounding molecules in the cell, it is a stochastic process [47, 63]. We have explained previously in Sec. 1.1 that channel gating is commonly described by continuous-time Markov chains. A simple example is the two-state channel model with voltage-dependent rates that we have briefly introduced in the context of neural spike generation in Sec. 2.2.1.

In the context of Ca^{2+} spiking the channel activity is not voltage- but ligand-gated. In particular, cytosolic Ca^{2+} and IP$_3$ are regulators for all types of IP$_3$ receptor channels. This observation has led to the hypothesis that regulating gating processes may be related to binding and unbinding specific agents. For example, De Young and Keizer have proposed a kinetic model that assumes the presence of three binding sites (two for activating and inhibiting Ca^{2+} and one for IP$_3$) to describe IP$_3$R gating [179]. More recent models, like the Siekmann model, diverge from this mechanistic point of view and adopt a more data-driven strategy [205]. Both models will be presented in the following.

De Young-Keizer model

The De Young and Keizer (DYK) model assumes that an IP$_3$R channel consists of three identical and independent subunits. Each subunit consists of an activating Ca^{2+} binding site, an inhibiting Ca^{2+} binding site, and an IP$_3$ binding site. Each binding site can be occupied or unoccupied, resulting in eight (2^3) states for each subunit. The states are denoted s_{ijk} where i,j, and k indicate the state of the IP$_3$, the activating Ca^{2+}, and the inhibiting Ca^{2+} binding sites. An index is 1 if the respective molecule is bound and 0 if not. According to De Young and Keizer, an IP$_3$R channel is said to be open when for all three subunits the IP$_3$ and activating Ca^{2+} sites are occupied and the inhibiting Ca^{2+} site is unoccupied, i.e., when all three subunits are in the state s_{110}.

The schematic diagram of the kinetic model for a single subunit with all eight different states s_{ijk} is shown in Fig. 3.3A. The transition rates between the states on the front and back faces of the cube and the transition rates between these two faces are illustrated in Fig. 3.3B and C, respectively. State transitions are governed by second-order rate constants ($a_i[\mathrm{Ca}^{2+}]_\mathrm{i}$ or $a_i[\mathrm{IP}_3]$) for binding processes and by first-order rate constants (b_i) for unbinding processes. De Young and Keizer have distinguished five pairs of binding and unbinding constants a_i and b_i. The ratio between these two constants defines the dissociation constant, $d_i = b_i/a_i$, corresponding to the concentration at which the binding probability reaches half its maximum. Note that the fact that five different pairs are distinguished implies that the binding sites are not independent. For example, unbinding of Ca^{2+} at the inhibiting site depends on whether IP$_3$ is bound or not. The model parameters used by De Young and Keizer are given in Table 3.1.

The arguably most commonly calculated statistic of a channel model is the open probability p_open. This is because it is closely related to the mean current through the channel. We have already pointed out that for the DYK model, an IP$_3$R channel is said to be open when all three subunits are in the state s_{110}. Since the subunits are independent, the open probability is simply given by $p_{\text{open}} = p_0(110)^3$. Here, $p_0(ijk)$ denotes the stationary probability of the state s_{ijk}, which can be computed using the stationary master equation

$$0 = Q \cdot \boldsymbol{p}_0 \tag{3.2.1}$$

with the transition rate matrix

$$Q = \begin{pmatrix} -q_{11} & b_4 & b_5 & 0 & b_1 & 0 & 0 & 0 \\ a_4[\text{Ca}^{2+}] & -q_{22} & 0 & b_5 & 0 & b_3 & 0 & 0 \\ a_5[\text{Ca}^{2+}] & 0 & -q_{33} & b_4 & 0 & 0 & b_1 & 0 \\ 0 & a_5[\text{Ca}^{2+}] & a_4[\text{Ca}^{2+}] & -q_{44} & 0 & 0 & 0 & b_3 \\ a_1[\text{IP}_3] & 0 & 0 & 0 & -q_{55} & b_2 & b_5 & 0 \\ 0 & a_3[\text{IP}_3] & 0 & 0 & a_2[\text{Ca}^{2+}] & -q_{66} & 0 & b_5 \\ 0 & 0 & a_1[\text{IP}_3] & 0 & a_5[\text{Ca}^{2+}] & 0 & -q_{77} & b_2 \\ 0 & 0 & 0 & a_3[\text{IP}_3] & 0 & a_5[\text{Ca}^{2+}] & a_2[\text{Ca}^{2+}] & -q_{88} \end{pmatrix}, \tag{3.2.2}$$

where $q_{jj} = -\sum_{i\neq j} q_{ij}$, and the stationary probability vector

$$\boldsymbol{p}_0 = \begin{pmatrix} p_0(000) & p_0(001) & p_0(010) & p_0(011) & p_0(100) & p_0(101) & p_0(110) & p_0(111) \end{pmatrix}^T. \tag{3.2.3}$$

The solution of Eq. 3.2.1 together with the normalization condition $\sum_{ijk} p(ijk) = 1$ is straightforward and the open probability for an IP$_3$ receptor channel is given by [179]

$$p_{\text{open}} = p_0(110)^3 = \left[\frac{[\text{Ca}^{2+}]_\text{i}[\text{IP}_3]d_2}{([\text{Ca}^{2+}]_\text{i}[\text{IP}_3] + [\text{IP}_3]d_2 + d_1 d_2 + [\text{Ca}^{2+}]_\text{i} d_3)([\text{Ca}^{2+}]_\text{i} + d_5)}\right]^3. \tag{3.2.4}$$

If the dissociation constants d_i are chosen accordingly, Eq. 3.2.4 can quantitatively reproduce the experimentally observed biphasic dependence of the open probability on $[\text{Ca}^{2+}]_\text{i}$. In Fig. 3.4, we compare the open probability according to Eq. 3.2.4 with simulation results of the DYK model as a function of the $[\text{Ca}^{2+}]_\text{i}$ and the IP$_3$ concentrations.

We note that in addition to the channel model, the full DYK model includes a differential equation describing the change of the cytosolic Ca^{2+} concentration

$$\frac{d[\text{Ca}^{2+}]_\text{i}}{dt} = c_1(\nu_1 p_0(110)^3 + \nu_2)([\text{Ca}^{2+}]_{\text{er}} - [\text{Ca}^{2+}]_\text{i}) - \nu_3[\text{Ca}^{2+}]_\text{i}^2/([\text{Ca}^{2+}]_\text{i}^2 + k_3^2). \tag{3.2.5}$$

The first term describes the release of Ca^{2+} from the ER into the cytosol and consists of two components, the mean Ca^{2+} current through the IP$_3$Rs and a constant Ca^{2+} leak current. The second

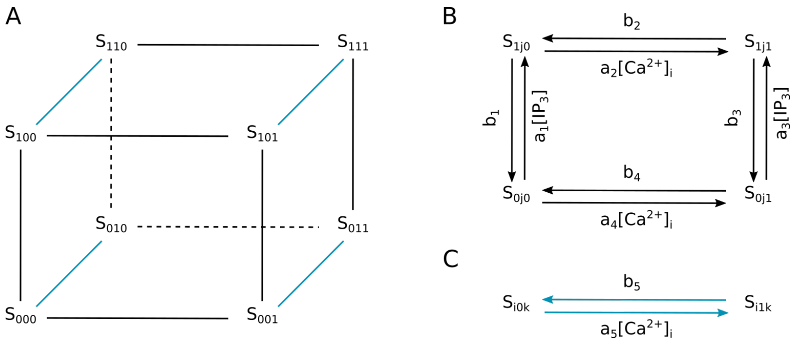

FIGURE 3.3: A schematic diagram of the kinetics of a single IP$_3$-receptor channel subunit according to De Young and Keizer [179]. The states are denoted by s$_{ijk}$, where i, j, and k indicate whether IP$_3$, activating Ca^{2+}, and inhibitory Ca^{2+} are bound (bound = 1, unbound = 0). A shows the whole model, including all eight possible states. B and C show parts of the whole model according to the color code. B shows the kinetics of the front and back faces of the cube. C shows the kinetics of the transitions between the two faces shown in B.

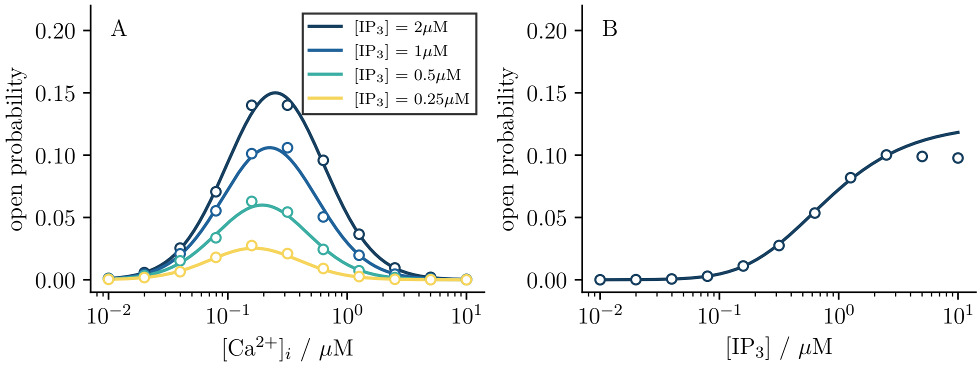

FIGURE 3.4: Open probability of the DYK model. (A) Open probability as a function of [Ca^{2+}]$_\mathrm{i}$. The solid line indicates the open probability of the full model calculated from the stationary master equation. The circles show the open probability obtained from stochastic simulations of the DYK model. (B) Open probability as function of [IP$_3$] with [Ca^{2+}]$_\mathrm{i}$ = 1μM. Solid line and circles as in (A).

TABLE 3.1: **Simulation parameters for the De Young-Keizer IP$_3$R model where [179]**

Parameter	Value	Description	Parameter	Value	Description
IP$_3$R binding constants			IP$_3$R dissociation constants $(d_i = b_i/a_i)$		
a_1 [μM^{-1}s^{-1}]	400	IP$_3$	d_1 [μM]	0.13	IP$_3$
a_2 [μM^{-1}s^{-1}]	0.2	Ca^{2+} inhibition	d_2 [μM]	1.049	Ca^{2+} inhibition
a_3 [μM^{-1}s^{-1}]	400	IP$_3$	d_3 [nM]	943.4	IP$_3$
a_4 [μM^{-1}s^{-1}]	0.2	Ca^{2+} inhibition	d_4 [nM]	144.5	Ca^{2+} inhibition
a_5 [μM^{-1}s^{-1}]	20	Ca^{2+} activation	d_5 [nM]	82.34	Ca^{2+} activation

term describes the removal of Ca^{2+} from the cytosol back into the ER by SERCA pumps. Eq. 3.2.5 is similar to the model we propose in that a kinetic channel model is coupled to a differential equation describing the dynamics of [Ca^{2+}]$_\mathrm{i}$. However, De Young and Keizer considered the Ca^{2+} dynamics only in the thermodynamic limit, where the Ca^{2+} current through the IP$_3$ receptors does not depend on the current states of the channels but only on the open probability p_{110}^3. Fluctuations of the Ca^{2+} concentration due to the stochastic nature of the ion channels are neglected.

We have already pointed out that the DYK channel model can reproduce the biphasic dependence of the open probability on [Ca^{2+}]$_\mathrm{i}$. At the same time, together with Eq. 3.2.5, oscillations of the cytosolic Ca^{2+} concentration with a period of about 20s can be explained. A disadvantage of the DYK model is that the rates given in Table 3.1 were chosen in accordance with the properties of the oscillating Ca^{2+} concentration rather than with the gating properties of the channels. In other words, it was assumed that the timescale of the Ca^{2+} oscillation is reflected in the binding rates of the channel (specifically in the delayed negative feedback of the inhibiting Ca^{2+} binding site). However, Thurley et al. [206] have shown that the timescale of the ISI is not reflected in the kinetics of the channels

Siekmann model

The second model we discuss is the Siekmann model [205]. This model departs from the mechanistic view of De Young and Keizer and follows a more data-driven strategy. Unlike many previous studies, Siekmann et al. do not attempt to formulate a model based on the binding and unbinding processes of different ligands but instead extract transition rates from experimental data in an arbitrary functional form.

Similar to Gin et al. [207], they derive their model by statistical analysis of an extensive single-channel data set. To this end, they used patch-clamp data from type 1 and type 2 IP$_3$R channels

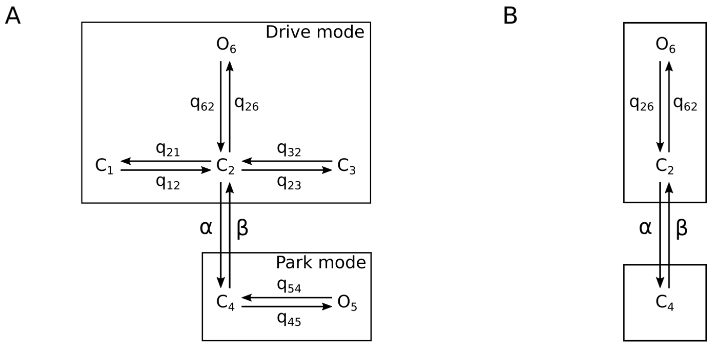

FIGURE 3.5: (A) schematic diagram of the kinetics of a single IP$_3$-receptor channel according to Siekmann et al. [205]. (B) shows a simplification of the Siekmann-model.

expressed in the nuclear membrane of DT40 cells, where two states (open and closed) are distinguished. Siekmann et al. observed that the channels alternate between periods with a high open probability of about 70% and periods with a low open probability close to zero. Thus, contrary to the DYK model's predictions, channels can occasionally have episodes with high open probabilities even when the stationary open probability is relatively low. In agreement with this observation, the authors follow the suggestion of Ionescu et al. [208] that IP$_3$Rs are mainly regulated by mode switching and propose a kinetic model with a drive and a park mode as depicted in Fig. 3.5A. Four states are distinguished in the drive mode: three closed states C_1, C_2, C_3, and one open state O_6. In park mode, there are only two states; one closed state C_4 and one open state O_5. This takes into account that the open probability in the park mode does not vanish entirely.

The transition rate matrix Q corresponding to the schematic diagram in Eq. 3.5A is as follows

$$Q = \begin{pmatrix} -q_{12} & q_{21} & 0 & 0 & 0 & 0 \\ q_{12} & -q_{21} - q_{23} - \alpha - q_{26} & q_{32} & \beta & 0 & q_{62} \\ 0 & q_{23} & -q_{32} & 0 & 0 & 0 \\ 0 & \alpha & 0 & -\beta - q_{45} & q_{54} & 0 \\ 0 & 0 & 0 & q_{45} & -q_{54} & 0 \\ 0 & q_{26} & 0 & 0 & 0 & -q_{62} \end{pmatrix} \tag{3.2.6}$$

and the probability vector is given by

$$\boldsymbol{p}(t) = \begin{pmatrix} p(1,t) & p(2,t) & p(3,t) & p(4,t) & p(5,t) & p(6,t) \end{pmatrix}^{\mathrm{T}}. \tag{3.2.7}$$

Again, the stationary master equation allows us to compute the stationary probability and thus the open probability, for which Siekmann et al. have given an exact expression (Eq. 1-10 in [205]) that is not repeated here.

Interestingly, they find that the transition rates within the two modes q_{ij} are rather independent of Ca^{2+} and IP$_3$. Conversely, the transition rates α and β between the modes depend on Ca^{2+} and IP$_3$ but have not been specified by the authors. This gap was later closed by Cao et al. [209, 210] who constructed the rates to reproduce both the stationary [211] and the time-dependent [212] behavior of an IP$_3$R. The resulting functions are complicated and entail a large number of parameters. For the sake of simplicity, we restrict ourselves here to the stationary case where the two rates are given by

$$\alpha = q_\alpha + V_\alpha(1 - m_\alpha^* h_\alpha^*), \tag{3.2.8}$$

$$\beta = q_\beta + V_\beta m_\beta^* h_\beta^* \tag{3.2.9}$$

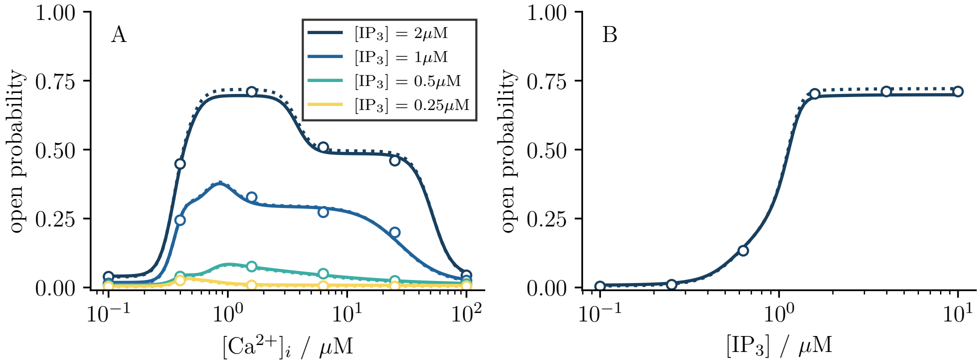

FIGURE 3.6: Open probability of the Siekmann model. (A) Open probability as a function of $[Ca^{2+}]_i$. The solid line indicates the open probability of the full model calculated from the stationary master equation. The dotted line shows the open probability of the simplified Siekmann model, also calculated from the stationary master equation. The circles show the open probability obtained from stochastic simulations of the simplified Siekmann model. (B) Open probability as function of $[IP_3]$ with $[Ca^{2+}]_i = 1\,\mu M$. Solid line, dotted line, circles as in (A).

with

$$m_\alpha^* = \frac{[Ca^{2+}]_i^{n_{m_\alpha}}}{[Ca^{2+}]_i^{n_{m_\alpha}} + K_{m_\alpha}^{n_{m_\alpha}}}, \qquad h_\alpha^* = \frac{[Ca^{2+}]_i^{n_{h_\alpha}}}{[Ca^{2+}]_i^{n_{h_\alpha}} + K_{h_\alpha}^{n_{h_\alpha}}}, \tag{3.2.10}$$

$$m_\beta^* = \frac{[Ca^{2+}]_i^{n_{m_\beta}}}{[Ca^{2+}]_i^{n_{m_\beta}} + K_{m_\beta}^{n_\beta}}, \qquad h_\beta^* = \frac{[Ca^{2+}]_i^{n_{h_\beta}}}{[Ca^{2+}]_i^{n_{h_\beta}} + K_{h_\beta}^{n_{h_\beta}}}. \tag{3.2.11}$$

Compared to the Markov model proposed by De Young and Keizer, which is completely determined by ten parameters, the Markov scheme proposed by Siekmann et al. [205] with the $[Ca^{2+}]$ and $[IP_3]$ dependent rates α and β according to [209] has an impressive number of 20 or 51 parameters (depending on whether, for example, q_α is considered as a single parameter or as consisting of four parameters, see Table 3.2). However, it was quickly realized that the probability of finding the states C_1, C_3, and O_5 in the full Siekmann model is small [64]. This led to the formulation of the simplified Siekmann model where only three different states are distinguished, as illustrated in Fig. 3.5.

In Fig. 3.6A, we compare the theoretical prediction of the open probability as given by Siekmann et al. [205] of the full Siekmann model (solid line) to the reduced Siekmann model (dotted line). There is little difference between the two models. Interestingly, the open probability, both as a function of $[Ca^{2+}]_i$ and as a function of $[IP_3]$, is very different from the open probability obtained from the DYK model. This is true for the shape of the open probability as a function of $[Ca^{2+}]_i$, but also for the value of $[Ca^{2+}]_i$ at which the maximum is reached (note the different Ca^{2+} ranges in Fig. 3.3 and Fig. 3.6).

Despite the differences between the two models, we have seen that IP_3R channel gating is usually described by Markov chains and that the open probability is the first statistic of interest for these models.

3.2.2 Dynamic model: Ca^{2+} oscillations

For the DYK model, we have already seen that the kinetics of the IP_3 receptors is only one component needed to describe the generation of Ca^{2+} spikes. The second component is the dynamics of the cytosolic Ca^{2+} concentration $[Ca^{2+}]_i$ or, more generally, the dynamics of the various agents in the cell. The goal here is to provide an overview of the various dynamical quantities commonly considered relevant to the generation of Ca^{2+} spikes. To this end, we consider the deterministic model proposed by Schuster, Marhl, and Höfer [182].

This model is far from being the only deterministic point model that could be considered (see, for instance [179, 180, 183, 213–215]), but to the best of our knowledge, distinguishes the largest number of different processes and can therefore be considered a most comprehensive model. The

TABLE 3.2: **Simulation parameters for the Siekmann model [209]**

Parameter	Value	Parameter	Value
q_{12} [s^{-1}]	$1.24 \cdot 10^3$	V_α [s^{-1}]	$60 + \frac{437}{[\mathrm{IP}_3]^3+1.73}$
q_{21} [s^{-1}]	$8.8 \cdot 10^1$	V_β [s^{-1}]	100
q_{23} [s^{-1}]	3	n_{m_α}	$6.3 + \frac{1.72[\mathrm{IP}_3]^2}{[\mathrm{IP}_3]^2+1.44}$
q_{32} [s^{-1}]	$6.9 \cdot 10^1$	n_{m_β}	$5.9 + \frac{7.6}{[\mathrm{IP}_3]^2+1.44}$
q_{26} [s^{-1}]	$1.05 \cdot 10^4$	n_{h_α}	$\frac{8.2[\mathrm{IP}_3]^2}{[\mathrm{IP}_3]^2+2.25}$
q_{62} [s^{-1}]	$4.01 \cdot 10^3$	n_{h_β}	$3.2 + \frac{4.88[\mathrm{IP}_3]^2}{[\mathrm{IP}_3]^2+1.69}$
q_{45} [s^{-1}]	$1.10 \cdot 10^1$	K_{m_α}	$0.48 + \frac{0.1}{[\mathrm{IP}_3]^2+1.44}$
q_{54} [s^{-1}]	$3.33 \cdot 10^3$	K_{m_β}	$0.4 + \frac{0.26[\mathrm{IP}_3]^4}{[\mathrm{IP}_3]^4+168}$
q_α [s^{-1}]	$1 + \frac{7.5}{[\mathrm{IP}_3]^2+0.25}$	K_{h_α}	$79.75 + \frac{25}{[\mathrm{IP}_3]^2+1.44}$
q_β [s^{-1}]	$\frac{1.8[\mathrm{IP}_3]^2}{[\mathrm{IP}_3]^2+0.34}$	K_{h_β}	$0.17 + \frac{70[\mathrm{IP}_3]^3}{[\mathrm{IP}_3]^3+274.6}$

model reads as follows

$$\begin{aligned}
\frac{d[\mathrm{IP}_3]}{dt} &= \nu_{\mathrm{plc}} - \nu_{\mathrm{d}}, \\
\frac{d[\mathrm{Ca}^{2+}]_{\mathrm{i}}}{dt} &= \nu_{\mathrm{in}} - \nu_{\mathrm{out}} + \nu_{\mathrm{rel}} - \nu_{\mathrm{serca}} + \nu_{\mathrm{mo}} - \nu_{\mathrm{mi}} - \textstyle\sum_j \nu_{b,j}, \\
\frac{d[\mathrm{Ca}^{2+}]_{\mathrm{er}}}{dt} &= \rho_{\mathrm{er}}(\nu_{\mathrm{serca}} - \nu_{\mathrm{rel}}), \\
\frac{d[\mathrm{Ca}^{2+}]_{\mathrm{m}}}{dt} &= \rho_{\mathrm{m}}(\nu_{\mathrm{mi}} - \nu_{\mathrm{mo}}), \\
\frac{dB_j}{dt} &= \nu_{b,j},
\end{aligned} \tag{3.2.12}$$

where $[\mathrm{IP}_3]$ is the IP$_3$ concentration, $[\mathrm{Ca}^{2+}]_{\mathrm{i}}$, $[\mathrm{Ca}^{2+}]_{\mathrm{er}}$, $[\mathrm{Ca}^{2+}]_{\mathrm{m}}$ are the Ca^{2+} concentrations in the cytosol, the ER, and the mitochondrion, and B_j is the bound concentration of the j-th Ca^{2+} buffer. The model implicitly distinguishes between three compartments within the cell, the cytosol, the ER, and the mitochondrion, even though they are not spatially separated in a point model.

The dynamics of IP$_3$ concentration is determined by the rate of IP$_3$ formation by phospholipase C (PLC) ν_{plc} and the rate of IP$_3$ degradation by hydrolysis ν_{d}. In its simplest form, ν_{plc} is a constant, while $\nu_{\mathrm{d}} = \hat{\nu}_{\mathrm{d}}[\mathrm{IP}_3]$ depends linearly on the IP$_3$ concentration. In some cells, $[\mathrm{Ca}^{2+}]_{\mathrm{i}}$ may also positively influence IP$_3$ formation, depending on the specific PLC isotype [216]. The second line, which governs the dynamics of the cytosolic Ca^{2+} concentration, distinguishes the largest number of different Ca^{2+} currents. The seven terms fall into four categories. First, the influx and efflux of Ca^{2+} across the cell membrane are described by the terms ν_{in} and ν_{out}. Here, ν_{out} describes the active removal of Ca^{2+} from the cytosol into the extracellular medium, e.g. by PMCAs, and typically depends (nonlinearly) on $[\mathrm{Ca}^{2+}]_{\mathrm{i}}$. Second, the Ca^{2+} fluxes across the ER membrane are described by ν_{rel} and ν_{serca}. The first term ν_{rel} captures the release of Ca^{2+} from the ER into the cytosol, usually including a leak term and the release through IP$_3$Rs. Both are diffusive currents that depend on the difference between $[\mathrm{Ca}^{2+}]_{\mathrm{er}}$ and $[\mathrm{Ca}^{2+}]_{\mathrm{i}}$. In addition, the Ca^{2+} current through IP$_3$Rs usually includes a nonlinear term reflecting the dependence of the IP$_3$Rs open probability on $[\mathrm{Ca}^{2+}]_{\mathrm{i}}$ (see below). The active reuptake of Ca^{2+} from the cytosol into the ER by SERCA pumps is described by the second term ν_{serca} and (like the PMCAs) also depends nonlinearly on $[\mathrm{Ca}^{2+}]_{\mathrm{i}}$ (see below). Third, the Ca^{2+} currents across the mitochondrial membrane

ν_{mi} and ν_{mo}, which are rarely considered, and fourth, the binding and unbinding of Ca^{2+} to the j-th Ca^{2+} buffer B_j, described by $\nu_{b,j}$. The currents across the ER and the mitochondrial membrane affect the respective Ca^{2+} concentrations $[\mathrm{Ca}^{2+}]_{\mathrm{er}}$ and $[\mathrm{Ca}^{2+}]_{\mathrm{m}}$ with opposite signs and a prefactor $\rho_{\mathrm{er}} = V_{\mathrm{er}}/V_{\mathrm{i}}$ and $\rho_{\mathrm{m}} = V_{\mathrm{m}}/V_{\mathrm{i}}$, which account for the volume ratios between the cytosol and the ER and mitochondrion, respectively. We emphasize again that, to the best of our knowledge, no model has yet been published that accounts for all of the above processes.

For Eq. 3.2.12 to have a periodic solution, at least two of the above variables must be considered. $[\mathrm{Ca}^{2+}]_{\mathrm{i}}$ should, of course, be one of them. Furthermore, at least one of the two variables must exert positive feedback on itself[1]. CICR provides such feedback. Apart from the early models in which the delayed negative feedback that high Ca^{2+} concentrations exert on IP$_3$R channels was assumed to be responsible for the oscillations of the cytosolic Ca^{2+} concentration (for instance, in the DYK model), later models assumed that the transport of Ca^{2+} between the cytosol and the ER was responsible for the observed oscillations [217–219]. Moreover, when the IP$_3$ formation depends on $[\mathrm{Ca}^{2+}]_{\mathrm{i}}$, the interaction between $[\mathrm{Ca}^{2+}]_{\mathrm{i}}$ and [IP$_3$] may be sufficient to observe oscillations [181].

Despite the wide variety of models and mechanisms that have been proposed to describe the formation of Ca^{2+} oscillations or spikes, there are some common features that most models share. First, almost all models assume that CICR is the relevant positive feedback mechanism for the occurrence of Ca^{2+} oscillations or spikes. Second, almost all models describe Ca^{2+} release from the ER by a combination of a leak current and a Ca^{2+}-dependent Ca^{2+} current. The latter is associated with the Ca^{2+} release via the IP$_3$R channels and is usually described by Hill equations as follows

$$\nu_{\mathrm{rel}} = (k_1 + k_2 \frac{[\mathrm{Ca}]_{\mathrm{i}}^{\alpha}}{K_{\mathrm{act}}^{\alpha} + [\mathrm{Ca}]_{\mathrm{i}}^{\alpha}} \frac{K_{\mathrm{inh}}^{\beta}}{K_{\mathrm{inh}}^{\beta} + [\mathrm{Ca}]_{\mathrm{i}}^{\beta}})([\mathrm{Ca}^{2+}]_{\mathrm{er}} - [\mathrm{Ca}^{2+}]_{\mathrm{i}}) \tag{3.2.13}$$

or

$$\nu_{\mathrm{rel}} = (k_1 + k_2 \frac{[\mathrm{Ca}]_{\mathrm{i}}^{\alpha}}{K_{\mathrm{act}}^{\alpha} + [\mathrm{Ca}]_{\mathrm{i}}^{\alpha}} \frac{[\mathrm{Ca}]_{\mathrm{er}}^{\beta}}{K_{\mathrm{inh}}^{\beta} + [\mathrm{Ca}]_{\mathrm{er}}^{\beta}})([\mathrm{Ca}^{2+}]_{\mathrm{er}} - [\mathrm{Ca}^{2+}]_{\mathrm{i}}). \tag{3.2.14}$$

Here, k_1, k_2 are rate constants, K_{act}, K_{inh} are dissociation constants and α, β are Hill coefficients. The first term captures the Ca^{2+} leak from the ER into the cytosol, whereas the second term describes the release of Ca^{2+} from the ER through the IP$_3$Rs. Whether the release of Ca^{2+} from the ER into the cytosol is described by equation Eq. 3.2.13 or Eq. 3.2.14 depends on which process is thought to be responsible for the termination of the Ca^{2+} release. In Eq. 3.2.13, the term $K_{\mathrm{inh}}^{\beta}/(K_{\mathrm{inh}}^{\beta} + [\mathrm{Ca}]_{\mathrm{i}}^{\beta})$, and thus a high cytosolic Ca^{2+} concentration, is responsible for the termination of the Ca^{2+} release. This reflects the negative feedback a high cytosolic Ca^{2+} concentration exerts on the opening probability of the IP$_3$Rs. In contrast, in Eq. 3.2.14, the term $[\mathrm{Ca}]_{\mathrm{er}}^{\beta}/(K_{\mathrm{inh}}^{\beta} + [\mathrm{Ca}]_{\mathrm{er}}^{\beta})$, and thus the depletion of the ER, is responsible for the termination of the Ca^{2+} release.

Third, the active reuptake of Ca^{2+} from the cytosol into the ER by the SERCA pumps is also typically described by a Hill equation:

$$\nu_{\mathrm{serca}} = k_3 \frac{[\mathrm{Ca}]_{\mathrm{i}}^{\gamma}}{K_{\mathrm{serca}}^{\gamma} + [\mathrm{Ca}]_{\mathrm{i}}^{\gamma}}. \tag{3.2.15}$$

Finally, if an additional buffer is considered, the dynamics are governed by a second-order rate constant for the binding of Ca^{2+} to the buffer and by a first-order rate constant for the unbinding processes:

$$\nu_b = k_+(B_T - B)[\mathrm{Ca}^{2+}]_{\mathrm{i}} - k_- B. \tag{3.2.16}$$

Here B_T is the total buffer concentration and k_+ and k_- are the binding and unbinding constants.

---

[1] This is because in the simplest two-dimensional case $\dot{x} = f_1(x,y)$, $\dot{y} = f_2(x,y)$ oscillations require complex eigenvalues $\lambda_{1,2}$ with a positive real part given by the trace of the corresponding Jacobi matrix $\mathrm{Re}(\lambda_{1,2}) = df_1/dx + df_2/dy > 0$.

The term $B_T - B$ corresponds to the free buffer concentration, assuming that the total buffer concentration is constant.

3.3 An integrate-and-fire approach to Ca^{2+} signaling

In this section, we propose a phenomenological two-component model for the generation of Ca^{2+} spikes that takes into account the stochastic nature of the Ca^{2+} puffs and treats the Ca^{2+} spike as a stochastic point process. The first component describes the stochastic opening and closing of clusters of IP$_3$Rs by a Markov chain. We have shown in Sec. 3.2.1 that modeling IP$_3$Rs by Markov models follows a certain tradition [179, 205]. However, our approach differs somewhat because we do not describe single IP$_3$ receptor channels but a cluster of such channels. The second component is a phenomenological IF model describing the dynamics of the intracellular and ER Ca^{2+} concentrations. Similar to the generation of neural spikes, we follow the idea that Ca^{2+} spikes can be viewed as the result of a summation or *integration* process combined with a *fire* mechanism that triggers a spike whenever the intracellular Ca^{2+} concentration exceeds a critical value. Here, the release of Ca^{2+} into the cytosol by the puffs represents the process that is integrated, and the positive feedback induced by CICR constitutes the fire mechanism by which a cell-wide spike is triggered. Additionally, we endow the model with a slow adaptation-like variable that captures the depletion and replenishment of the ER Ca^{2+} concentration and allows to capture the observed transient.

3.3.1 IP$_3$R channel cluster: Cyclic Markov model

We begin by describing the Markov model that characterizes the activity of a cluster of IP$_3$-receptor channels. We have already pointed out that our considerations do not start from a single channel. Of course, several single-channel models, such as the introduced DYK or Siekmann models, could be used to derive a cluster model. However, because the channels in a cluster are strongly coupled and thus highly cooperative, cluster models derived from single-channel dynamics are very complex [220, 221]. However, despite the complexity of the dynamics, they yield relatively simple waiting time distributions for both the closed and open cluster states [206, 221–223]. Therefore, we take a different approach and derive a simplified model based on experimentally available statistics of the puff strength and the interpuff interval (IPI).

In our model, the states of a single cluster over time t form a CTMC, denoted $y(t)$. The Markov chain is then mapped to an observable stochastic process $x(t)$ that describes the number of open channels within a cluster at time t. The process $x(t)$ eventually enters into the dynamics of the intracellular Ca^{2+} concentration (see Sec. 3.3.2). A schematic diagram of the cluster model is shown in Fig. 3.7. The complete state space of the Markov chain is given by $S = [O_N, \ldots, O_1, C_M, \ldots, C_1]$ and consists of two subspaces $S_O = [O_N, \ldots, O_1]$ containing the open states and $S_C = [C_M, \ldots, C_1]$ containing the closed states. The probability that a certain state $s \in S$ is occupied at time t is given by $p(s,t)$ and governed by the master equation

$$\dot{\boldsymbol{p}} = Q \cdot \boldsymbol{p} \tag{3.3.1}$$

with the transition rate matrix (each blank entry corresponds to a zero):

$$Q = \left(\begin{array}{ccc|ccc}
-\lambda_{\mathrm{close}} & & & & & \lambda_{\mathrm{open}}/N \\
\lambda_{\mathrm{close}} & \ddots & & & & \vdots \\
 & \ddots & \ddots & & & \lambda_{\mathrm{open}}/N \\ \hline
 & & \lambda_{\mathrm{close}} & -\lambda_{\mathrm{ref}} & & \\
 & & & \lambda_{\mathrm{ref}} & \ddots & \\
 & & & & \ddots & -\lambda_{\mathrm{open}}
\end{array}\right) \tag{3.3.2}$$

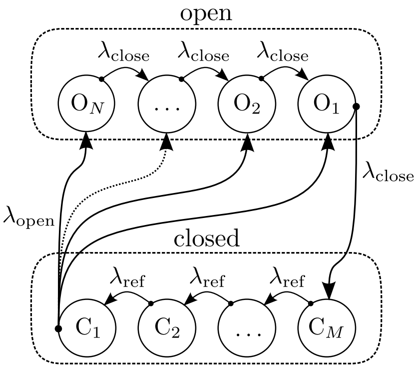

FIGURE 3.7: Schematic diagram of the kinetics of a cluster of IP$_3$-receptor channels. The model consists of N open and M closed states. States are labeled according to the corresponding number of open channels the state represents.

Parameter	Value
N	5
M	3
λ_{close}	$50\,\text{s}^{-1}$
λ_{ref}	$20\,\text{s}^{-1}$
ν^*_{open}	$0.1\,\text{s}^{-1}$
α	3.0
β	3.0
q	1.0

TABLE 3.3: Default parameters of the cluster model. The rate ν^*_{open} corresponds to the single-channel opening rate $\nu_{\text{open}}(c_{\text{i}}, q)$ at the resting concentration $c_{\text{i}} = c^*_0$ and $q = 1$.

and the probability vector:

$$\boldsymbol{p}(t) = \begin{pmatrix} p(O_N, t) & \dots & p(O_1, t) & p(C_M, t) & \dots & p(C_1, t) \end{pmatrix}^T . \tag{3.3.3}$$

Additionally, we assign every state s a natural number by the nonlinear transformation:

$$f(s) = \begin{cases} n, & \text{for } s = O_n \text{ with } n = 1, \dots, N \\ 0, & \text{for } s = C_m \text{ with } m = 1, \dots, M \end{cases} \tag{3.3.4}$$

to map the Markov process $y(t)$ to the stochastic process $x(t)$ representing the number of open channels in a cluster. The transformation maps every closed state C_m to 0 (no channels are open) and every open state O_n to n (the corresponding number of open channels). Fig. 3.8 presents exemplary time series of the process $y(t)$ and $x(t) = f(y(t))$ illustrating the transformation. Consistent with the pulse-like release of Ca^{2+} by the puffs, the model generates short episodes where the cluster is open, followed by relatively long intervals where the cluster remains closed.

Before turning to the statistical analysis of the puffs generated by our model, we motivate the Markov model in more detail and describe the biophysical properties that have been taken into account. The transition rate matrix Q consists of four submatrices (see Eq. 3.3.2), which results from the division of the state space into an open and a closed subspace. The shapes and biophysical justifications of each submatrix are described below, beginning with the upper-right submatrix and proceeding in a counterclockwise direction. The first three submatrices determine the statistics of the puff itself, particularly the puff strength A, defined as the integral of the number of channels open during a single puff. This quantity is closely related to the amount of Ca^{2+} released per puff, hence the name. The fourth submatrix determines the statistics of the time between two puffs, the IPI I. Both puff strength and IPI are highlighted in Fig. 3.8.

The upper-right $N \times M$ submatrix captures the transition from the closed state C_1 to an arbitrary open state O_n, describing the opening of the cluster. Biophysically, the firing of a puff is a cooperative event triggered by the opening of a single channel. This significantly elevates the *local* Ca^{2+} concentration, increases the open probability of the remaining channels within the same cluster, and causes a certain uniformly distributed number of them to respond and open as well [224, 225]. We assume that this response is instantaneous. The transition from the closed state C_1 to any open state O_n can then be described by a single transition with rate λ_{open}. The fact that in our model, the transition to each open state is equally likely reflects the observed uniform distribution of the number of responding channels n_0. The notion that any channel can trigger the cluster opening is reflected by the linear dependence of λ_{open} on the cluster size N (see Eq. 3.3.7). That λ_{open} is a linear function of N has been shown experimentally [197].

Upon initiation of a puff, the channels close successively as described by the upper-left $N \times N$ (and lower-left $M \times N$) submatrix. Intuitively, it could be assumed that the channels within a cluster close independently, leading to a closing rate of the cluster that is directly proportional to

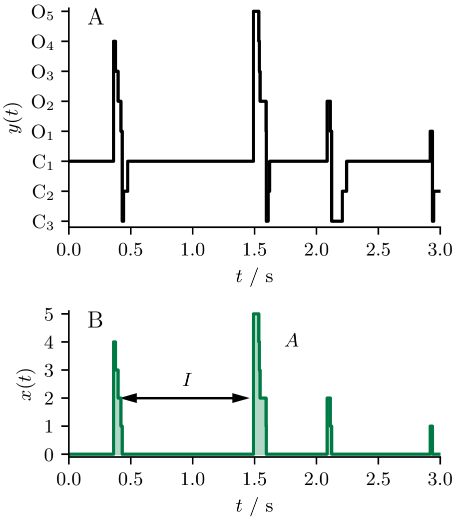

FIGURE 3.8: Transforming the Markov process $y(t)$ into the stochastic process $x(t)$. Panel A shows a time series of the process $y(t)$. Panel B shows the transformed process $x(t)$. While the individual open states O_n remain distinguishable after the transformation, the closed states C_m all collapse to zero and lose their distinctiveness. The opening of a cluster is the basis for the Ca^{2+} puff. The integrated number of open channels during a single opening event is related to the amount of Ca^{2+} release per puff and defines the puff strength A. The time between two opening events defines the interpuff interval I.

the number of currently open channels n. However, Wiltgen et al. [201] have demonstrated that the mean dwell time (the inverse closing rate) exhibits minimal dependence on n. This finding suggests that channel closing is also a cooperative process, although the underlying mechanisms are poorly understood. Our model describes the transition from the state O_n to O_{n-1} by a constant closing rate λ_{close} independent of n. The constant closing rate results in a staircase-like shape of the puff shown in Fig. 3.8B, where the mean dwell time in each state (i.e., the average width of the steps) is identical.

Finally, the lower-right $M \times M$ submatrix determines the statistics of the IPI. Experimentally, IPIs are known to be highly stochastic but have a (small) refractory period [197, 206]. The latter is due to a negative feedback that occurs during the opening of a channel/cluster: The local Ca^{2+} concentration in the vicinity of an open channel/cluster reaches very high values within microseconds [196] and reduces the probability of an immediate reopening for a relative refractory period [188, 199]. This is most likely due to an inhibitory Ca^{2+} binding site on IP_3R, which has a much higher affinity for Ca^{2+} binding and acts on a slower timescale compared to the activation site [226, 227]. While this feedback is a subject of ongoing debate, even studies that consider such feedback unlikely come to the conclusion that the IP_3R has more than one closed state [228]. Thus, IPIs cannot be modeled by a single transition. We introduce a series of refractory states that must be traversed after a puff before a new puff can be initiated. Specifically, the closed states $C_M, \ldots, C_2$ must be traversed with transition rates λ_{ref} before the cluster reaches the state C_1 and can open again with the rate λ_{open}. At this point, the cycle starts anew with the opening of the cluster.

To complete the cluster model, we specify the dependence of the rates on Ca^{2+} and IP_3. We have already explained that the local positive feedback in a cluster is captured by the dependence of the opening rate on the cluster size N. The global feedback that the opening of one cluster exerts on the other cluster through an increase in $[Ca^{2+}]_i$ has not yet been accounted for. Unfortunately, to the best of our knowledge, there is no quantitative study that relates cluster activity to $[Ca^{2+}]_i$. In the absence of direct measurements, we choose the Ca^{2+} dependence of the opening rate by analogy with the biphasic Ca^{2+} dependence of the open probability of a single channel, usually described by a combination of Hill equations [199, 200, 229]. Since we describe the dynamics of the cytosolic Ca^{2+} concentration by an IF model, we restrict ourselves to cytosolic Ca^{2+} concentrations close to the resting concentration. This eliminates the need to include a term that captures the decrease in open probability at high Ca^{2+} concentrations. We chose

$$\begin{aligned}\lambda_{\text{open}}([\text{Ca}^{2+}]_\text{i}) &= N\nu_{\text{open}}([\text{Ca}^{2+}]_\text{i}) \\ &= N\hat{\nu}_{\text{open}}\frac{[\text{Ca}^{2+}]_\text{i}{}^{\alpha}}{K_{\text{act}}^{\alpha}+[\text{Ca}^{2+}]_\text{i}{}^{\alpha}}\frac{[\text{IP}_3]^{\beta}}{K_{\text{stim}}^{\beta}+[\text{IP}_3]^{\beta}},\end{aligned} \tag{3.3.5}$$

where N is the number of channels in a cluster and ν_{open} ($\hat{\nu}_{\text{open}}$) can be interpreted as the Ca^{2+}-dependent (maximal) opening rate of a single channel. The two remaining rates λ_{ref} and λ_{close} are chosen independent of both $[Ca^{2+}]_i$ and $[IP_3]$. Mak, McBride, and Foskett [200] have shown that the mean open time of a single channel is independent of the Ca^{2+} concentration. Therefore, it is plausible that the closing rate, which determines the open time, is also independent of $[Ca^{2+}]_i$. Similarly, the refractory period observed in the ISI is likely due to negative feedback from the local Ca^{2+} concentration in the vicinity of the open cluster. This concentration has little to do with the cell-wide cytosolic Ca^{2+} concentration. Therefore, we assume that λ_{ref} is independent of $[Ca^{2+}]_i$ and chose both rates to be constants (Table 3.3):

$$\begin{aligned}\lambda_{\text{ref}} &= \text{const.} \\ \lambda_{\text{close}} &= \text{const.}\end{aligned} \tag{3.3.6}$$

In the following, neither $[Ca^{2+}]_i$ nor $[IP_3]$ will be given in absolute units but relative to the respective dissociation constant. For this purpose we introduce the two variables $c_\text{i} = [Ca^{2+}]_\text{i}/K_{\text{act}}$ and $q = [IP_3]/K_{\text{stim}}$. Estimates of K_{act} have been obtained by fitting combinations of the Hill equation to the open probabilities of individual channels and are typically between 100 nM to 500 nM [188, 230]. However, it was also noted that the fit parameters are not uniquely determined, so the results should be taken with caution. We have chosen an intermediate value of $K_{\text{act}} = 250\,\text{nM}$. This parameter is not explicitly included in our model but allows us to relate the dimensionless quantity c_i to physiological Ca^{2+} concentrations. The dependence of the cluster opening rate on c_i and q is then given by

$$\lambda_{\text{open}}(c_\text{i}) = N\hat{\nu}_{\text{open}}\frac{c_\text{i}^{\alpha}}{1+c_\text{i}^{\alpha}}\frac{q^{\beta}}{1+q^{\beta}} \tag{3.3.7}$$

and the single channel opening rate by

$$\nu_{\text{open}}(c_\text{i}) = \hat{\nu}_{\text{open}}\frac{c_\text{i}^{\alpha}}{1+c_\text{i}^{\alpha}}\frac{q^{\beta}}{1+q^{\beta}}. \tag{3.3.8}$$

Often it is more convenient to express the opening rate relative to a given rate at a reference concentration c_i^*. This is because the maximum rate may be difficult to obtain experimentally, whereas the opening rate at a given Ca^{2+} concentration (for instance, the resting Ca^{2+} concentration) is readily available. Expressing the Ca^{2+} dependent rate by means of a reference rate can be accomplished by a simple transformation of Eq. 3.3.8

$$\nu_{\text{open}} = \nu_{\text{open}}^*(c_\text{i}^*, q^*)\cdot\left(\frac{c_\text{i}}{c_\text{i}^*}\right)^{\alpha}\frac{1+(c_\text{i}^*)^{\alpha}}{1+c_\text{i}^{\alpha}}, \tag{3.3.9}$$

where we have assumed that the relative IP_3 concentration q^* has not changed. In Table 3.3 we have given ν_{open}^* relative to the cytosolic resting concentration $c_\text{i}^* = c_0^*$ and at an intermediate stimulation $q^* = 1$. The value $c_0^* = 0.2$ was chosen in accordance with physiological resting concentrations, which are usually of the order of $[Ca^{2+}]_0^* \approx 50\,\text{nM}$ [29].

For the kinetic model presented, the open probability can be calculated as the fraction of time the cluster is open:

$$p_{\text{open}}(c_\text{i}) = \frac{\tau_{\text{open}}}{\tau_{\text{open}}+\tau_{\text{close}}(c_\text{i})}. \tag{3.3.10}$$

Here τ_{open} and $\tau_{\text{close}}(c_\text{i})$ are the mean open and closed times, corresponding to the mean duration of a puff and the mean interval between puffs (the IPI), respectively. These mean open/closed

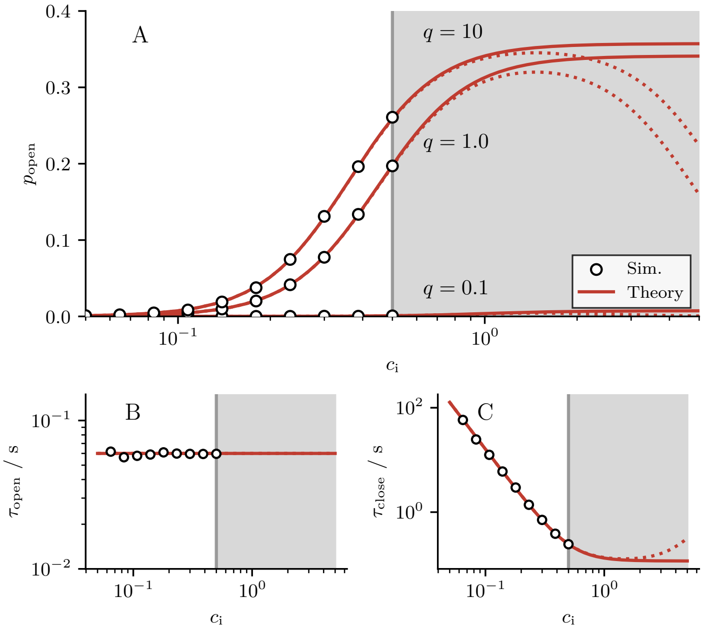

FIGURE 3.9: Open probability and mean dwell times of an IP_3R cluster. Panel A shows the open probability $p_\mathrm{open}(c_\mathrm{i})$ for three different IP_3 concentrations q. Theoretical predictions of $p_\mathrm{open}(c_\mathrm{i})$ according to Eq. 3.3.13 (solid red lines) are confirmed by simulation results (blue circles). Panel B shows the mean dwell times in the open states τ_open that is independent of c_i. Panel C shows the mean dwell time in the closed states τ_close that depends on c_i. Dotted lines in panel A and C indicate the open probability and dwell times with a biphasic opening rate according to Eq. 3.3.14. Parameters are chosen according to Table 3.3.

intervals and the mean values considered below are calculated as time averages, not ensemble averages. That is, we consider one long realization of the stochastic process $x(t)$ and calculate the mean open (closed) time as the average of the sequence of occurring open and closed intervals. In contrast, to calculate the ensemble average, many realizations $x_n(t)$ must be considered, and the mean intervals are obtained by averaging over all open or closed intervals found at time t. However, since the time t is more likely to fall into a longer interval, such an average introduces a bias in the sampling of the intervals; in general, the length of the intervals will be overestimated [46]. Returning to the calculation of the mean open time, we first calculate the conditional mean open time $\tau_\mathrm{open}(n_0) = n_0/\lambda_\mathrm{close}$ for a given number of responding channels n_0 and then average again over the number of responding channels:

$$\tau_\mathrm{open} = \frac{1}{N}\sum_{n_0=1}^{N}\frac{n_0}{\lambda_\mathrm{close}} = \frac{N+1}{2\lambda_\mathrm{close}}. \tag{3.3.11}$$

We recall that n_0 is uniformly distributed according to $p(n_0) = 1/N$. The mean closed time is given by the sum over the mean dwell times in the M closed states:

$$\tau_\mathrm{close}(c_\mathrm{i}) = \frac{1}{\lambda_\mathrm{open}(c_\mathrm{i})} + \frac{M-1}{\lambda_\mathrm{ref}}. \tag{3.3.12}$$

Combining Eq. 3.3.10, 3.3.11, and Eq. 3.3.12 yields

$$p_\mathrm{open}(c_\mathrm{i}) = \frac{\frac{N+1}{2\lambda_\mathrm{close}}}{\frac{N+1}{2\lambda_\mathrm{close}} + \frac{1}{\lambda_\mathrm{open}(c_\mathrm{i})} + \frac{M-1}{\lambda_\mathrm{ref}}}. \tag{3.3.13}$$

The open probability and the mean dwell times as functions of c_i are shown in Fig. 3.9. In our model and in agreement with experimental results [200], the increase of p_open with c_i is due to a decrease of τ_close with c_i. The gray area indicates concentrations that are inaccessible in our IF model because they are above the firing threshold c_T (see Sec. 3.3.2). The specific value of $c_T = 0.5$ has been chosen so that an increase in c_i still results in significant positive feedback, i.e., so that $p_\mathrm{open}(c_\mathrm{i})$ is not yet saturated. This value corresponds to a cytosolic Ca^{2+} concentration of about 125 nM.

Finally, to make a relation to the existing literature, we show in Fig. 3.9 also the open probability and dwell times for an opening rate with a true biphasic c_i-dependence

$$\Lambda_\mathrm{open} = N\hat{\nu}_\mathrm{open}\frac{c_\mathrm{i}^\alpha}{1+c_\mathrm{i}^\alpha}\frac{K^\alpha}{K^\alpha+c_\mathrm{i}^\alpha}\frac{s^\beta}{1+s^\beta}, \tag{3.3.14}$$

where $K = K_\mathrm{inh}/K_\mathrm{act}$ is the ratio between the dissociation constants of the activation and inhibition Ca^{2+} binding site of the IP$_3$R and was set to $K = 10$. It turns out that for the specific choice of K, this additional term affects the dynamics of the cluster only at high Ca^{2+} concentrations, which are not described in our IF model.

Puff strength and interpuff interval of the IP$_3$R cluster model

So far, we have motivated the cluster model and computed the open probability. Here, we go beyond the open probability and compute statistics of the puff strength A, the IPI $I(c_\mathrm{i})$ and, most importantly, the mean $\mu_x(c_\mathrm{i})$ and the noise intensity $D_x(c_\mathrm{i})$ of a single cluster. In almost all cases, the statistics depend on the cytosolic Ca^{2+} concentration through the Ca^{2+}-depend opening rate $\lambda_\mathrm{open}(c_\mathrm{i})$. However, since cluster activity is often fast compared to the rate of change of [Ca^{2+}]$_\mathrm{i}$, we assume that this dependence is merely parametric and calculate all statistics for fixed values of c_i.

We start by calculating statistics of the puff strength A, a quantity closely related to the amount of Ca^{2+} released during a puff. Two exemplary puffs with strength A_i an A_{i+1} are shown in Fig. 3.10A$_1$. To calculate the mean $\langle A\rangle$ and the variance Var(A) of the puff strength, it is convenient first to calculate the conditional mean $\langle A|n_0\rangle$ and the conditional variance Var$(A|n_0)$ for a given number of responding channels n_0. The conditional and unconditional statistics are related by the law of total mean and total variance [231]:

$$\langle A\rangle = \langle\langle A|n_0\rangle_A\rangle_{n_0}, \tag{3.3.15}$$

$$\mathrm{Var}(A) = \langle \mathrm{Var}(A|n_0)_A\rangle_{n_0} + \mathrm{Var}(\langle A|n_0\rangle_A)_{n_0}. \tag{3.3.16}$$

The relation for the total mean is clear. We calculate the mean puff strength for a given number of responding channels $\langle A|n_0\rangle_A$ and obtain the total mean $\langle A\rangle$ by averaging again over the number of responding channels $\langle\langle A|n_0\rangle_A\rangle_{n_0}$. For the variance, it turns out that the same procedure, i.e., calculating $\langle \mathrm{Var}(A|n_0)_A\rangle_{n_0}$, does only account for a portion of the total variance Var(A). Additionally, the variance of the conditional mean $\langle A|n_0\rangle_A$ must be taken into account. This can be understood by realizing that even if A was a deterministic function of n_0 (if Var$(A|n_0)_A$ would vanish), the mere fact that n_0 is a stochastic quantity would still lead to a variance of A.

To determine the conditional puff strength $(A|n_0)$, we consider it to be the sum of n_0 independent random numbers corresponding to the area under each "step" of the puff, denoted $(a|n)$:

$$(A|n_0) = \sum_{n=1}^{n_0}(a|n). \tag{3.3.17}$$

For example, the number of responding channels for the second puff in Fig. 3.10A$_1$ is $n_0 = 5$, so that the total puff strength can be considered to be the sum of five independent random variables. During each step, the area $(a|n) = nt_{O_n}$ is the product of the deterministic number of open channels n and the stochastic dwell time t_{O_n} in the state O_n. Since the transition from any open state is a Poisson process described by the transition rate λ_close, all dwell times are exponentially distributed according to $p(t) = \lambda_\mathrm{close}\exp(-\lambda_\mathrm{close}t)$ and independent of n. Consequently, $(a|n)$ does also follow an exponential distributed with the rate $\lambda_n = \lambda_\mathrm{close}/n^2$ and the mean $\langle a|n\rangle = n/\lambda_\mathrm{close}$

---

[2] The distribution of a random variable that is the product of two other random variables $z = x\cdot y$ can be calculated by $p_z(z') = \int_{-\infty}^{\infty} dx\ p_x(x')p_y(z'/x')/|x'|dx'$ [232]. In our case n is deterministic, i.e. $p_n(n') = \delta(n'-n)$ and $p_t(t') = \lambda_\mathrm{close}\exp(-\lambda_\mathrm{close}t')$ so that $p(a'|n) = p_t(z'/n)/n = (\lambda_\mathrm{close}/n)\exp(-(\lambda_\mathrm{close}/n)z')$.

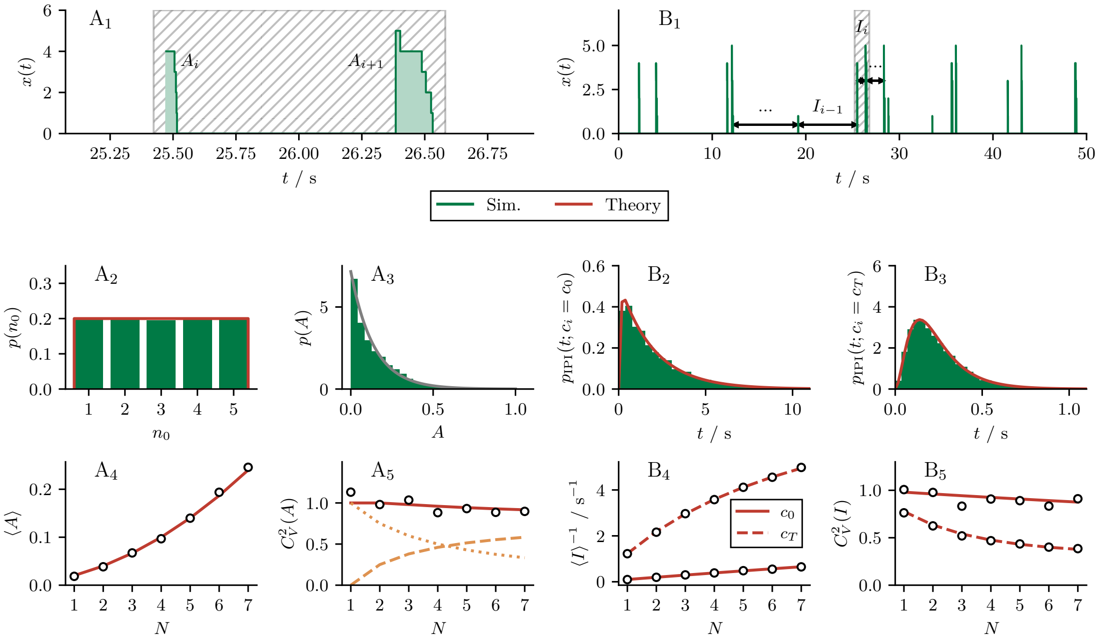

FIGURE 3.10: Statistics of the puff strength and interpuff interval. Panels A$_1$ - A$_5$ depict statistics of the puff strength A. Panels B$_1$ - B$_5$ depict statistics of the interpuff interval I. Panel A$_1$ shows a short time series of $x(t)$, which includes two successive puffs with strength A_i and A_{i+1}. Panel A$_2$ displays the distribution of responding channels n_0, which is uniform by construction. Panel A$_3$ shows the distribution of puff strengths A together with an exponential fit (gray line). Panel A$_4$ shows the mean puff strength $\langle A \rangle$, which is a quadratic function of the cluster size N. Panel A$_5$ shows the (squared) CV of the puff strength. Orange lines indicate the contribution of $\langle \mathrm{Var}(A|n_0) \rangle / \langle A \rangle^2$ (dotted) and $\mathrm{Var}(\langle A|n_0 \rangle)/\langle A \rangle^2$ (dashed) to the total $C_V^2(A)$. Panel B$_1$ shows a long time series of $x(t)$, where two IPIs are highlighted. The green highlighted area in B$_1$ corresponds to the highlighted area in A$_1$. Panels B$_2$ and B$_3$ show the IPI distribution at the resting and threshold Ca^{2+} concentrations, respectively. Panels B$_4$ and B$_5$ show the inverse mean of the IPI, i.e., the puff rate, and the (squared) CV of the IPI as a function of the cluster size N again for the resting and threshold Ca^{2+} concentration. Parameters are chosen according to Table 3.3 and $c_\mathrm{i} = c_0^*$ if not states otherwise.

as well as the variance $\mathrm{Var}(a|n) = (n/\lambda_\mathrm{close})^2$ are readily obtained. For the entire puff with a specific number of open channels $(A|n_0)$, the mean and variance are then given by

$$\langle A|n_0 \rangle = \sum_{n=1}^{n_0} \langle a|n \rangle \quad = \sum_{n=1}^{n_0} \frac{n}{\lambda_\mathrm{close}} = \frac{1}{2\lambda_\mathrm{close}} n_0(n_0+1), \tag{3.3.18}$$

$$\mathrm{Var}(A|n_0) = \sum_{n=1}^{n_0} \mathrm{Var}(a|n) = \sum_{n=1}^{n_0} \frac{n^2}{\lambda_\mathrm{close}^2} = \frac{1}{6\lambda_\mathrm{close}^2} n_0(n_0+1)(2n_0+1). \tag{3.3.19}$$

To obtain the total mean, we take a second average of Eq. 3.3.18 over the uniformly distributed number of responding channels:

$$\langle A \rangle = \langle \langle A|n_0 \rangle \rangle = \frac{1}{N} \sum_{n_0=1}^{N} \frac{1}{2\lambda_\mathrm{cls}} n_0(n_0+1) = \frac{1}{6\lambda_\mathrm{cls}} (N+1)(N+2). \tag{3.3.20}$$

This demonstrates that the fact that the channels do not close independently results in a mean puff strength that is a quadratic function of the cluster size N as shown in Fig. 3.10A$_3$. This would not be the case with N independent channels.

To calculate the total variance, we use the conditional variance (Eq. 3.3.19) and the conditional mean (Eq. 3.3.18):

$$\langle \mathrm{Var}(A|n_0)_A\rangle_{n_0} = \frac{1}{12\lambda_{\mathrm{close}}^2}(N+1)^2(N+2), \tag{3.3.21}$$

$$\mathrm{Var}(\langle A|n_0\rangle_A)_{n_0} = \frac{1}{60\lambda_{\mathrm{close}}^2}(N+1)(N+2)(3N^2+6N+1) - \frac{1}{36\lambda_{\mathrm{close}}^2}(N+1)^2(N+2)^2. \tag{3.3.22}$$

Adding these two equations yields a rather cumbersome expression for the variance of the puff strength. However, it turns out that the expression for the squared CV is much simpler:

$$C_V^2(A) = \frac{\langle \mathrm{Var}(A|n_0)\rangle + \mathrm{Var}(\langle A|n_0\rangle)}{\langle A\rangle^2} = \frac{4N^2+18N+8}{5N^2+15N+10}. \tag{3.3.23}$$

This expression implies that the CV is bound between 1 and 0.8 (cf. Fig. 3.10A$_4$). The maximum value is assumed for $N=1$, in which case we are dealing with a Poisson process with $C_V^2(A)=1$. The minimal value is assumed for infinite cluster sizes $\lim_{N\to\infty} C_V^2(A) = 0.8$. Moreover, Eq. 3.3.23 allows us to derive insights into the origin of this strong variability. It demonstrates that for $N \to \infty$, the randomness of the number of responding channels n_0 guarantees the strong variability of the puff strength. This is shown in Fig. 3.10A$_4$ where the contribution of $\langle \mathrm{Var}(A|n_0)\rangle/\langle A\rangle^2$ (dotted line) and $\mathrm{Var}(\langle A|n_0\rangle)/\langle A\rangle^2$ (dashed line) to the total (squared) CV are highlighted. It turns out that due to this strong variability, the puff strength is very well described by a single exponential distribution (grey line in Fig. 3.10A$_3$).

We now turn to the IPI I, which is the time between two puffs (excluding the puff duration). Unlike the puff strength A, the IPI I depends on c_{i} through the opening rate $\lambda_{\mathrm{open}}(c_{\mathrm{i}})$. A sample sequence of puffs with the IPIs highlighted is shown in Fig. 3.10B$_1$. The gray shaded area corresponds to the gray shaded area in Fig. 3.10A$_1$. Calculating the statistics of the IPI is straightforward because the IPI is given by the sum of M independent random variables

$$I = \sum_{m=1}^{M} t_{C_m}, \tag{3.3.24}$$

where t_{C_m} denotes the dwell time in the state C_m. Since the dwell times are independent and exponentially distributed according to $p(t_{C_m}) = \lambda_{\mathrm{ref}}\exp(-\lambda_{\mathrm{ref}}t_{C_m})$ for $m = 2,\dots,M$ and $p(t_{C_1}) = \lambda_{\mathrm{open}}\exp(-\lambda_{\mathrm{open}}t_{C_1})$ for $m=1$, the mean, variance, and CV of the IPI are readily obtained:

$$\langle I\rangle = \sum_{m=1}^{M}\langle t_{C_m}\rangle = \frac{1}{\lambda_{\mathrm{open}}} + \frac{M-1}{\lambda_{\mathrm{ref}}}, \tag{3.3.25}$$

$$\mathrm{Var}(I) = \sum_{m=1}^{M}\mathrm{Var}(t_{C_m}) = +\frac{1}{\lambda_{\mathrm{open}}^2} + \frac{M-1}{\lambda_{\mathrm{ref}}^2}, \tag{3.3.26}$$

$$\begin{aligned} C_V^2(I) = \mathrm{Var}(I)/\langle I\rangle^2 &= \frac{1+(M-1)(\lambda_{\mathrm{open}}/\lambda_{\mathrm{ref}})^2}{(1+(M-1)\lambda_{\mathrm{open}}/\lambda_{\mathrm{ref}})^2} \\ &= 1-(M-1)\frac{2\lambda_{\mathrm{ref}}/\lambda_{\mathrm{open}}+M-2}{(\lambda_{\mathrm{ref}}/\lambda_{\mathrm{open}}+M-1)^2}. \end{aligned} \tag{3.3.27}$$

First, we discuss the rather simple dependence on the number of closed states M. According to Eq. 3.3.25, the mean IPI increases with M because more states have to be traversed before a puff is fired. For the same reason, and according to Eq. 3.3.27, the IPI becomes more regular as M increases, starting at $C_V(I)=1$ for $M=1$ and then decreasing monotonically as $C_V(I) \propto 1/\sqrt{M}$. It is also interesting to ask how the cluster size N affects the IPI. We recall that the opening rate depends linearly on the cluster size $\lambda_{\mathrm{open}} = N\nu_{\mathrm{open}}$ (see Eq. 3.3.9). According to Eq. 3.3.25, we expect the mean IPI to decrease with increasing N before it saturates at $(M-1)/\lambda_{\mathrm{ref}}$. How quickly this limit is reached depends on the opening rate $\lambda_{\mathrm{open}}(c_{\mathrm{i}})$ and thus on the cytosolic Ca^{2+} concentration c_{i}. Specifically, the higher the Ca^{2+} concentration, the larger the opening rate and the faster the limit is reached. In Fig. 3.10B$_4$, the inverse mean IPI $\langle I\rangle^{-1}$ (the puff rate) is plotted as a function of the cluster size N for two different values of the Ca^{2+} concentration. For $c_\mathrm{i} = c_0^*$, the opening rate is much smaller than the refractory rate, the mean IPI is mainly determined by the dwell time in the state C_1, and the puff rate depends approximately linearly on the cluster size $\langle I \rangle^{-1} \approx N/\lambda_\mathrm{open}$ (solid line in Fig. 3.10B$_4$). For the larger value of $c_\mathrm{i} = c_T$, the dwell times in the refractory states account for a larger fraction of the mean IPI, and the puff rate depends more nonlinearly on N (dashed line in Fig. 3.10B$_4$). Similar to the mean, the CV of the IPI depends on the cluster size through the opening rate, as demonstrated in Fig. 3.10B$_5$. When N is small, the IPI is again mainly determined by the dwell time in the state C_1 and forms approximately a Poisson process with a CV close to one. For larger values of N, the cluster opens more frequently, and the IPI is mainly determined by the concatenation of the $M-1$ refractory states. This results in a more regular IPI. The opening rate also depends on the cytosolic Ca^{2+} concentration. At the resting concentration $c_\mathrm{i} = c_0^*$ there is little variation in the CV because the mean dwell time in the state C_1 dominates the IPI over a moderate range of cluster sizes (solid line in Fig. 3.10B$_5$). This is no longer the case when the Ca^{2+} concentration is increased to $c_\mathrm{i} = c_T$ (dashed line in Fig. 3.10B$_5$). In any case, for $N \to \infty$ (implying $\lambda_\mathrm{open} \to \infty$) the CV saturates at $\lim_{N\to\infty} C_V(I) = 1/\sqrt{M-1}$ for $M > 1$.

To compute the complete probability density function of the IPI $p_\mathrm{IPI}(t)$, we convolve M exponential distributions describing the dwell times in the closed states. The first $M-1$ dwell times are described by the rate λ_ref, while the last dwell time is described by the rate λ_open. This results in a convolution integral that can be expressed by the lower incomplete gamma function $\gamma(a,t) = \int_0^t dt'\, t'^{a-1} e^{-t'}$:

$$\begin{aligned} p_\mathrm{IPI}(t) &= \lambda_\mathrm{open} p(C_1, t) \\ &= \lambda_\mathrm{open} \left(\frac{\lambda_\mathrm{ref}}{\lambda_\mathrm{ref} - \lambda_\mathrm{open}} \right)^{M-1} \frac{\gamma(M-1, (\lambda_\mathrm{ref} - \lambda_\mathrm{open})t)}{(M-2)!} e^{-\lambda_\mathrm{open} t}. \end{aligned} \tag{3.3.28}$$

This provides a simple expression for $p_\mathrm{IPI}(t)$ that is confirmed in Fig. 3.10B$_2$ and B$_3$ for the resting and threshold Ca^{2+} concentration $c_\mathrm{i} = c_0^*$ and $c_\mathrm{i} = c_T$ respectively. At higher Ca^{2+} concentrations, a decrease in mean IPI and an increase in refractory period (relative to mean IPI) are observed.

Stationary mean and noise intensity of the IP$_3$R cluster model

Most importantly, we demonstrate that the mean $\mu_x(c_\mathrm{i})$ and noise intensity $D_x(c_\mathrm{i})$ of the cluster activity $x(t)$ can be calculated by algebraic equations. These two statistics provide a full description of a stochastic process when considered in the limit of a vanishing correlation time. That an algebraic equation determines the stationary mean is obvious since it is related to the stationary probability vector governed by the (algebraic) stationary master equation. This is less obvious for the noise intensity.

Following standard procedures we calculate the mean μ_x as the product of the state vector $\boldsymbol{x}$ and the stationary probability vector $\boldsymbol{p_0}$ [49, 57]

$$\begin{aligned} \mu_x &= \sum_{s\in S} x(s) p_0(s) \\ &= \boldsymbol{x} \cdot \boldsymbol{p_0}, \end{aligned} \tag{3.3.29}$$

where the stationary probability vector satisfies

$$0 = Q \cdot \boldsymbol{p_0} \tag{3.3.30}$$

and the normalization condition

$$\sum_{s\in S} p_0(s) = 1. \tag{3.3.31}$$

For our specific model the solution to Eq. 3.3.30 and Eq. 3.3.31 reads:

$$p_0(s) = \begin{cases} \frac{N+1-i}{N}\frac{1}{\tau_{\text{total}}\lambda_{\text{close}}}, & \text{if } s \in [O_N, \dots, O_1] \\ \frac{1}{\tau_{\text{total}}\lambda_{\text{ref}}}, & \text{if } s \in [C_M, \dots, C_2] \\ \frac{1}{\tau_{\text{total}}\lambda_{\text{open}}}, & \text{if } s = C_1 \end{cases}, \tag{3.3.32}$$

where $\tau_{\text{total}}(c_{\text{i}}) = \tau_{\text{open}} + \tau_{\text{close}}(c_{\text{i}})$ can be interpreted as the mean period of the cyclic Markov chain. This expression allows us to evaluate the sum in Eq. 3.3.29

$$\mu_x = \frac{1}{6\lambda_{\text{close}}} \frac{(N+1)(N+2)}{\frac{1}{\lambda_{\text{open}}} + \frac{M-1}{\lambda_{\text{ref}}} + \frac{N+1}{2\lambda_{\text{close}}}} = \frac{\langle A \rangle}{\tau_{\text{total}}} \tag{3.3.33}$$

and reveals that the mean cluster activity is equal to the mean puff strength $\langle A \rangle$ over the mean period of the Markov chain $\tau_{\text{total}}(c_{\text{i}})$.

Calculating the noise intensity D_x is more advanced. First of all, we note that the noise intensity of a stochastic process is defined by the integral over its autocorrelation function

$$D_x = \int_0^\infty d\tau\, C_{xx}(\tau), \tag{3.3.34}$$

where $C_{xx}(\tau) = \langle x(t)x(t+\tau)\rangle - \langle x \rangle^2$. Calculating the correlation function $C_{xx}(\tau)$, more precisely the first term of the correlation function $\langle x(t)x(t+\tau)\rangle$ requires knowledge of the time-dependent transition probability $\boldsymbol{p}(t)$. This probability is, in turn, determined by the time-dependent master equation (Eq. 3.3.1), a set of first-order linear differential equations. Thus, it is not immediately clear that D_x can be determined by a much simpler algebraic equation. However, taking advantage of the fact that we only need to know the integral of the correlation functions allows us to avoid solving the time-dependent master equation. A similar trick was used to calculate the correlation time and diffusion coefficient for systems described by an FPE [61, 233, 234]. We express the correlation function in terms of transition and stationary probabilities

$$\begin{aligned} D_x &= \int_0^\infty d\tau\, \langle x(t+\tau)x(t)\rangle - \langle x \rangle^2 \\ &= \int_0^\infty d\tau \sum_{s_1, s_2} [x(s_2)x(s_1)p(s_2, t+\tau|s_1, t)p_0(s_1) - x(s_2)x(s_1)p_0(s_2)p_0(s_1)] \\ &= \sum_{s_1, s_2} x(s_2)x(s_1) \int_0^\infty d\tau\, [p(s_2, t+\tau|s_1, t) - p_0(s_2)]p_0(s_1) \\ &= \sum_{s_1, s_2} x(s_2)f(s_2|s_1)x(s_1)p_0(s_1). \\ &= \sum_{s_1, s_2} x(s_2)f(s_2|s_1)y(s_1) \\ &= \boldsymbol{x}^T \cdot F \cdot \boldsymbol{y}, \end{aligned} \tag{3.3.35}$$

where we have introduces $y(s) = x(s)p_0(s)$ and the auxiliary function $f(s_2|s_1) = \int_0^\infty d\tau\, [p(s_2, t+\tau|s_1, t) - p_0(s_2)]$. The term inside the parentheses $p(s_2, t+\tau|s_1, t) - p_0(s_2)$ can be well understood. It describes the probability of finding a state s_2 at time $t+\tau$ given that the state s_1 was observed at time t minus the stationary probability of finding the state s_2. It should be clear that this difference tends to zero for $\tau \to \infty$ because the initial condition (i.e., the fact that the state s_1 was taken at time t) plays no role in this limit. The function $f(s_2|s_1)$ is the integral of this probability and answers the question of whether the state s_2 occurs more frequently ($f(s_2|s_1) > 0$) or less frequently ($f(s_2|s_1) < 0$) over a long period after the state s_1 was attained at the beginning of that period. Since the more frequent observation of one state must come at the expense of a less frequent observation of another state, we expect the sum $\sum_{s_2} f(s_2|s_1) = 0$ to vanish. To determine $f(s_2|s_1)$, we consider the master equation in a somewhat unusual representation that highlights the "initial" condition $p(s_1, t) = 1$ (at time t)

$$\begin{aligned}\dot{p}(s_3, t+\tau|s_1, t) &= \sum_{s_2} q_{s_3,s_2} p(s_2, t+\tau|s_1, t)\\ \dot{p}(s_3, t+\tau|s_1, t) &= \sum_{s_2} q_{s_3,s_2}[p(s_2, t+\tau|s_1, t) - p_0(s_2)]\\ \int_0^\infty d\tau\, \dot{p}(s_3, t+\tau|s_1, t) &= \int_0^\infty d\tau \sum_{s_2} q_{s_3,s_2}[p(s_2, t+\tau|s_1, t) - p_0(s_2)]\\ p_0(s_3) - \delta_{s_3,s_1} &= \sum_{s_2} q_{s_3,s_2} f(s_2|s_1).\end{aligned} \tag{3.3.36}$$

To get from the first to the second line, we have subtracted the derivative of the stationary probability $0 = \dot{p}_0(s_3) = \sum_{s_2} q_{s_3,s_2} p_0(s_2)$ on both sides. Eq. 3.3.36 can be written in a corresponding matrix representation

$$\boldsymbol{p_0} - \boldsymbol{e}(s_1) = Q \cdot \boldsymbol{f}(s_1) \tag{3.3.37}$$

with the unit vector $\boldsymbol{e}(s_1)$ in the s_1-direction and the vector $\boldsymbol{f}(s_1) = \sum_{s_2} f(s_2|s_1)\boldsymbol{e}(s_2)$. Finally, as for the stationary probability, Eq. 3.3.37 does not determine $\boldsymbol{f}(s_1)$ uniquely but only up to a constant. We have already hinted at the additional condition required to uniquely determine $\boldsymbol{f}(s_1)$, namely that the sum over this vector must vanish. This can be seen as follows

$$\sum_{s_2} f(s_2|s_1) = \int_0^\infty d\tau \sum_{s_2}[p(s_2, t+\tau|s_1, t) - p_0(s_2)] = \int_0^\infty d\tau\, [1-1] = 0. \tag{3.3.38}$$

Eq. 3.3.37 can be written more compactly so that all initial conditions s_1 are considered simultaneously

$$P_0 - \mathbb{1} = Q \cdot F, \tag{3.3.39}$$

where P_0 is matrix with entries $p_{ij} = p_0(i)$, $\mathbb{1}$ is the unit matrix, and F is a matrix with entries $f_{ij} = f(i|j)$. In summary, the mean can be calculated according to

$$\mu_x = \boldsymbol{x} \cdot \boldsymbol{p_0} \quad \text{with} \quad 0 = Q \cdot \boldsymbol{p_0} \tag{3.3.40}$$

and the normalization condition Eq. 3.3.31, while the noise intensity can be calculated according to

$$D_x = \boldsymbol{x}^T \cdot F \cdot \boldsymbol{y} \quad \text{with} \quad P_0 - \mathbb{1} = Q \cdot F, \tag{3.3.41}$$

and the additional conditions Eq. 3.3.38. These two statistics fully determine the stochastic process in the white noise limit.

In Fig. 3.11, we study how the different cluster parameters affect the mean $\mu_x(c_\mathrm{i})$ and noise intensity $D_x(c_\mathrm{i})$ as a function of c_i. Black lines indicate default parameters. We note again that both statistics have been calculated under the assumption that the correlation time of the process $x(t)$ is small compared to any other timescale in the system. That is, we assumed that the process $x(t)$ adiabatically adjusts to $c_\mathrm{i}(t)$. The dependence of the mean on c_i and the different cluster parameters can be well understood using the analytical expression we have derived in Eq. 3.3.33 and is repeated here for convenience:

$$\mu_x(c_\mathrm{i}) = \frac{\langle A \rangle}{\tau_\mathrm{total}(c_\mathrm{i})}. \tag{3.3.42}$$

First of all, $\mu_x(c_\mathrm{i})$ increases monotonically with c_i because $\tau_\mathrm{total}(c_\mathrm{i})$ decreases monotonically with c_i. Second, the mean increases with ν^*_open (Fig. 3.11A$_1$), decreases with λ_close (Fig. 3.11B$_1$), and increases again with λ_ref (Fig. 3.11C$_1$). This is because increasing ν^*_open and λ_ref shortens the period $\tau_\mathrm{total}(c_\mathrm{i})$, while decreasing λ_close strengthens the mean puff $\langle A \rangle$. Third, the mean increases with the cluster size N because larger clusters open more frequently and generate stronger puffs (Fig. 3.11D$_1$). Conversely, the number of refractory states M decreases the mean by increasing

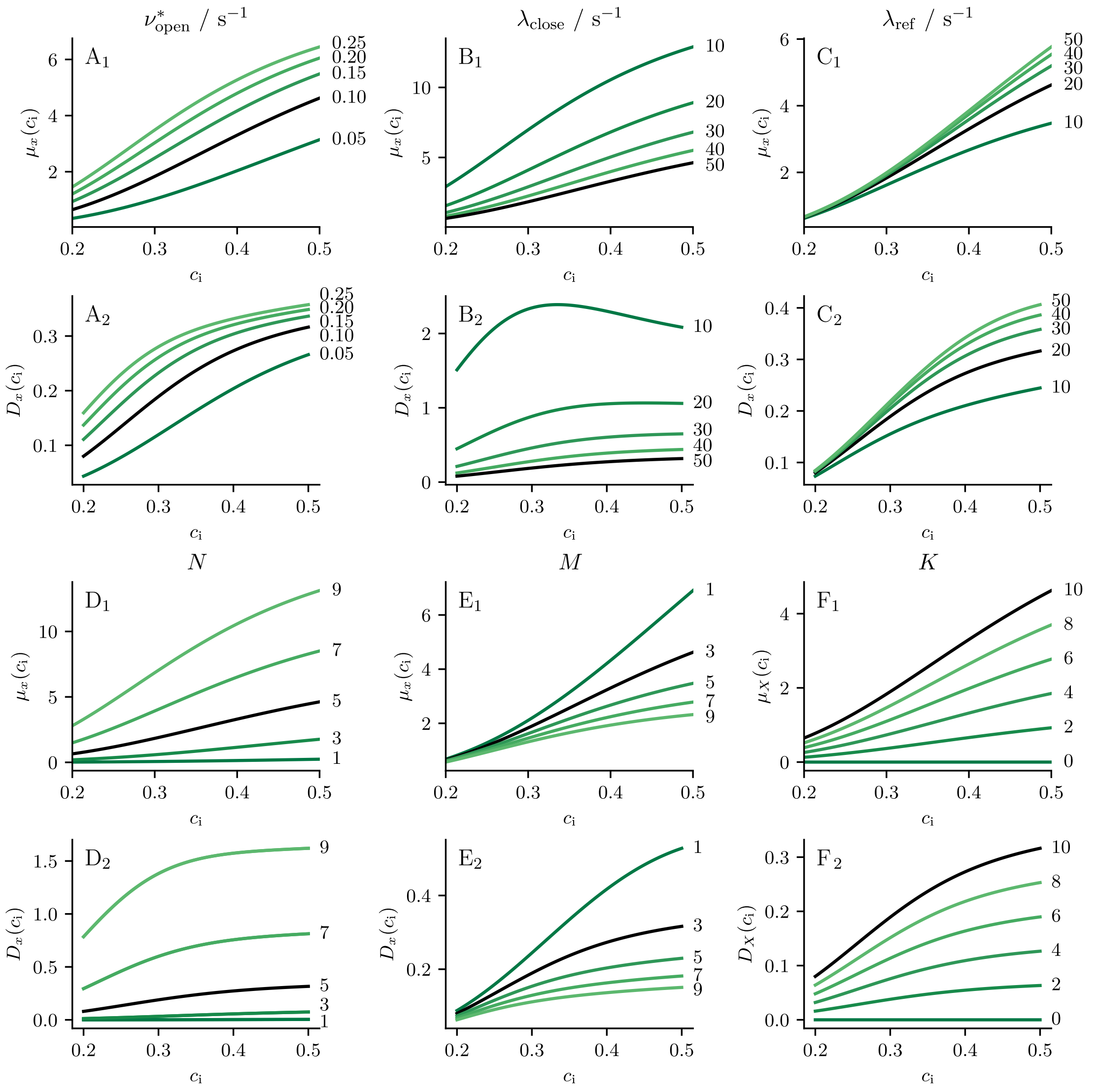

FIGURE 3.11: Mean $\mu_x(c_i)$ (A_1 to E_1) and noise intensity $D_x(c_i)$ (A_2 to E_2) of the cluster activity $x(t)$. Panels A, B, and C show the mean and noise intensity as a function of the rates ν^*_{open}, λ_{close}, and λ_{ref}, respectively. Panels D and E show the mean and noise intensity for varying cluster sizes N and number refractory states M. Panel F_1 and F_2 show the mean and noise intensity for the superposition of K independent cluster $X(t) = \sum_k^K x_k(t)$. In all panels, the black lines indicate the mean and noise intensity obtained using the default parameters specified in Table 3.3.

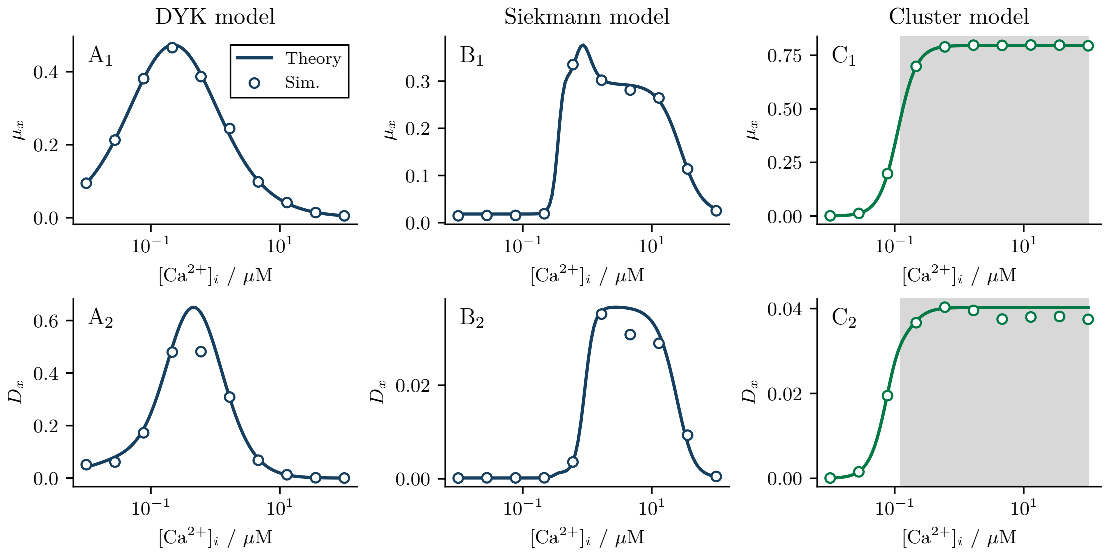

FIGURE 3.12: Comparison of the mean μ_x and noise intensity D_x of different channel/cluster models. Panels A, B, and C show the two statistics for the DYK model, the Siekmann model, and our cluster model, respectively. Circles show simulation results, while solid lines are theoretical predictions. The gray area in panels C_1 and C_2 indicates Ca^{2+} concentrations that are inaccessible in our IF model.

the period $\tau_{\text{total}}(c_{\text{i}})$ (Fig. 3.11E_1). The dependence on c_{i} and the cluster parameters is less clear for the noise intensity because we do not have an explicit solution to Eq. 3.3.41. In most cases we observe an increase with c_{i}, except for small closing rates λ_{close} (Fig. 3.11A_2 - E_2). In addition, we observe that the overall dependence of the noise intensity on the cluster size N and closing rate λ_{close} is strong compared to the dependence on the other parameters. This is presumable because these two parameters affect the puff itself. In Fig. 3.11F_1 and Fig. 3.11F_2 we show that for the superposition of K clusters, $X(t) = \sum_k^K x_k(t)$, the mean and the noise intensity depend linearly on K, as expected for independent processes.

Finally, we demonstrate that our theory does not only apply to our specific model but holds more general. To this end, we simulate the De Young-Keizer and Siekmann model along with our cluster model and compare in Fig. 3.12 the mean and noise intensity calculated from stochastic simulations with the theoretical prediction according to Eq. 3.3.40 and Eq. 3.3.41. To provide some comparability between the models, we return to physical Ca^{2+} concentrations given in µM. For all three models, we find good agreement between simulation results (circles) and theoretical predictions (lines), demonstrating the broad applicability of the theory. Discrepancies between simulation results and theoretical predictions are likely due to inaccuracies in calculating the noise intensity using the simulation data since the numerical calculation and integration of the correlation function $C_{xx}(\tau)$ can be error-prone. It should be noted that the noise intensity of the DYK model is almost 20 times larger than that of the Siekmann model, which has to do with the much larger correlation time of the DYK model (not shown). This is so because the noise intensity can also be formulated as the product of the variance and the correlation time[3] and the DYK model is constructed such that the timescale of the inhibitory Ca^{2+} binding site ($0.2\,\mu\mathrm{M}^{-1}\,\mathrm{s}^{-1}$) of the channel model essentially determines the timescale of the interspike intervals. This means that the DYK model contains significantly slower time scales than the Siekmann model, resulting in a longer correlation time.

3.3.2 Ca^{2+} dynamics: Integrate-and-fire model

Here we present the IF part of the two-component model describing the dynamics of the cytosolic Ca^{2+} concentration $[\mathrm{Ca}^{2+}]_{\text{i}}$ and the Ca^{2+} concentration in the ER $[\mathrm{Ca}^{2+}]_{\text{er}}$. To this end, we will

---

[3] The fact that $D_x = \sigma_x^2 \tau_x$ is somewhat trivial given the definitions of the correlation time $\tau_x = \int_0^\infty d\tau\, C_{xx}(\tau)/\sigma_x^2$ and the noise intensity $D_x = \int_0^\infty d\tau\, C_{xx}(\tau)$.

TABLE 3.4: Default parameters of the Ca^{2+} dynamics

Parameter	Value
K	10
c_0^*	0.2
c_T	0.5

explain the various terms that affect the two concentrations and discuss the general behavior of the model. Only then will we discuss the biophysical motivation in more detail.

The IF model is as follows

$$\begin{aligned}\dot{c}_\mathrm{i} &= -(c_\mathrm{i} - c_0(c_\mathrm{er}))/\tau + j_\mathrm{puff}(c_\mathrm{i}, c_\mathrm{er}),\\ \dot{c}_\mathrm{er} &= -(c_\mathrm{er} - 1)/\tau_\mathrm{er} - \varepsilon c_\mathrm{er} \textstyle\sum_i \delta(t - t_i),\\ &\text{if } c_\mathrm{i}(t) = c_T \to t_i = t \text{ and } c_\mathrm{i}(t) = c_R,\end{aligned} \tag{3.3.43}$$

where c_i is the dimensionless cytosolic Ca^{2+} concentration and c_er is the dimensionless ER Ca^{2+} concentration. Recall that $c_\mathrm{i} = [\mathrm{Ca}^{2+}]_\mathrm{i}/K_\mathrm{act}$ is given relative to the dissociation constant of the activation Ca^{2+} binding site of the IP$_3$R. In contrast to that, $c_\mathrm{er} = [\mathrm{Ca}^{2+}]_\mathrm{er}/[\mathrm{Ca}^{2+}]_\mathrm{er}^\mathrm{max}$ is given relative to the maximum Ca^{2+} concentration in the ER (see below). Consequently, c_er is bound between 0 (empty) and 1 (full) and can be interpreted as the filling level of the ER. Returning to the dynamical equations, the first term on the r.h.s. of the first line is a *deterministic* linear Ca^{2+} current with timescale τ that determines how quickly the resting concentration $c_0(c_\mathrm{er}) = c_0^* c_\mathrm{er}$ is reached when no puffs are fired. The second term on the r.h.s. is the *stochastic* puff Ca^{2+} current that results from the stochastic opening and closing of K independent IP$_3$R clusters:

$$j_\mathrm{puff}(c_\mathrm{i}, c_\mathrm{er}) = p c_\mathrm{er} \sum_k^K x_k(t). \tag{3.3.44}$$

Here, p is a permeability-like parameter, and $x_k(t)$ is the number of open channels in the k-th cluster at time t. The random processes $x_k(t)$ have been described in Sec. 3.3.1. The dynamics of the cytosolic Ca^{2+} concentration are completed by a fire-and-reset rule: whenever $c_\mathrm{i}(t) = c_T$, a spike is said to be fired at $t = t_i$ and $c_\mathrm{i}(t)$ is immediately reset to c_R. For the sake of simplicity, we reset the model to the resting concentration, i.e., $c_R = c_0(c_\mathrm{er})$. The second line in Eq. 3.3.43 describes the dynamics of the ER Ca^{2+} concentration $c_\mathrm{er}(t)$. The first term is again a deterministic linear current with timescale τ_er that determines how quickly the ER is replenished and $c_\mathrm{er}(t)$ returns to its steady-state value $c_\mathrm{er}^\mathrm{max} = 1$. The second term describes the depletion of the ER. Whenever a spike is fired, $c_\mathrm{er}(t)$ is immediately decreased by $\varepsilon c_\mathrm{er}(t_i^-)$, where the minus indicates that the decrease is meant to be proportional to the concentration right *before* the spike at time t_i. This distinction between times immediately before a spike t_i^- and immediately after a spike t_i^+ is relevant because the δ-function applied at the spike time leads to an ambiguity in the value $c_\mathrm{er}(t_i)$, depending on whether the kick has already been applied or not. Mathematically speaking, the left and right limits $\lim_{\epsilon\to 0} c_\mathrm{er}(t_i - \epsilon) \neq \lim_{\epsilon \to 0} c_\mathrm{er}(t_i + \epsilon)$ do not agree. The stochasticity in the $c_\mathrm{er}(t)$ dynamics results from the randomness of the spike times t_i at which the δ function is applied. The ER Ca^{2+} concentration dynamics are very similar to a spike-triggered adaptation [18] described in the previous chapter. However, there are two differences: first, spike generation is inhibited more strongly by lower values of $c_\mathrm{er}(t)$, and second, the spike-triggered term is multiplicative in the sense that it depends on $c_\mathrm{er}(t)$ itself. The model parameters that are not changed are given in Table 3.4.

Dynamics of the IF model

In the following, we will consider two different versions of the model. The first model is a renewal version, where we assume that the ER Ca^{2+} concentration remains constant at its maximum value $c_\mathrm{er}(t) = 1$. As we will see below, this loosely corresponds to the situation where the Ca^{2+} is conserved throughout the cell. The renewal model [5] is discussed in detail in Sec. 3.4, can be treated analytically to a large extent but does not reproduce all features of Ca^{2+} spiking observed experimentally. The second model is the adaptive version that takes into account the depletion and

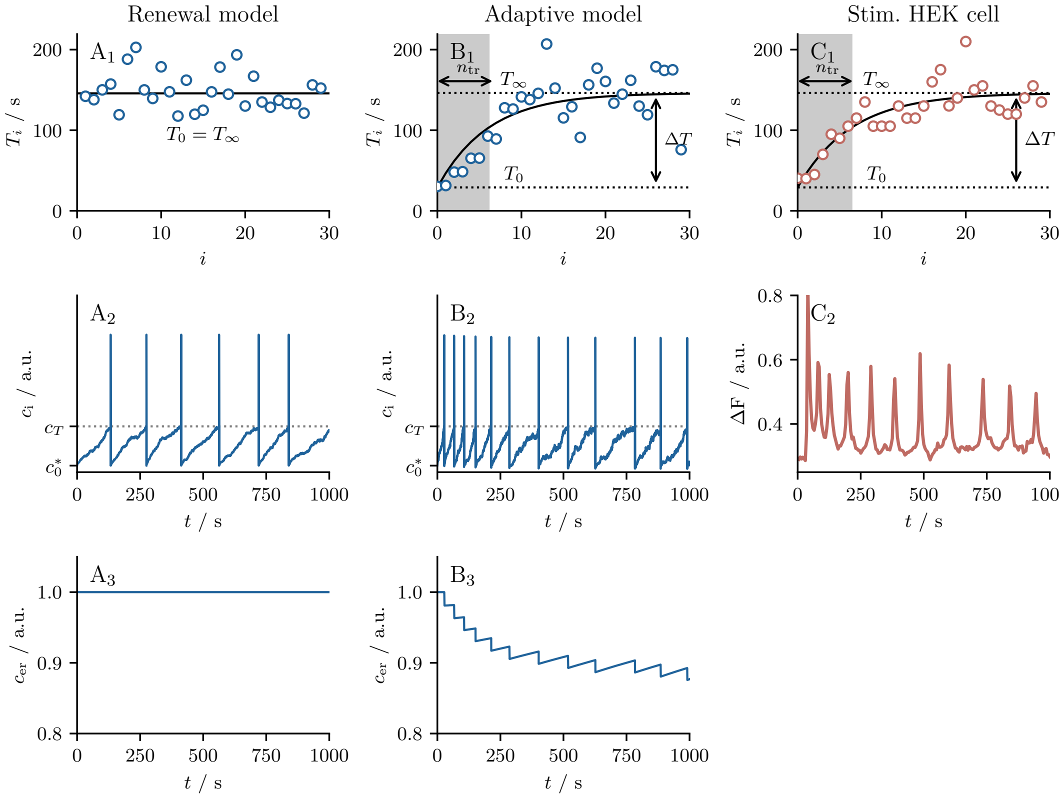

FIGURE 3.13: Comparison of ISI sequences and Ca^{2+} dynamics in two different models (A, B) and experimental data (C). Panels A$_1$, B$_1$, and C$_1$ show ISI sequences obtained from simulations of the renewal model, simulations of the adaptive model, and measurements of stimulated HEK cells, respectively. In all three panels, the assumed mean $\langle T_i \rangle$ as a function of the index i is highlighted by a black line. In panel A$_1$, the mean is independent of i. In panels B$_1$ and C$_1$ the mean is assumed to follow the exponential function $T_\infty - (T_\infty - T_0)\exp(-i/n_{\rm tr})$. The gray area indicates the indices for which $i \leq n_{\rm tr}$ holds. The horizontal dotted lines show the initial interval T_0 (lower) and stationary interval T_∞ (upper). The difference defines the cumulative refractory period $\Delta T = T_\infty - T_0$. Panels A$_2$, B$_2$, and C$_2$ show the time courses of cytosolic Ca^{2+} concentrations. Dotted lines in A$_2$ and B$_2$ show the firing threshold. ISIs for the experimental data have been determined peak-to-peak. Panels A$_3$ and B$_3$ show the time courses of the ER Ca^{2+} concentrations. Parameters A: $\tau = 11.8$s, $p = 5.74 \cdot 10^{-3}$; B: $\tau = 5.48$s, $p = 1.47 \cdot 10^{-2}$, $\tau_{\rm er} = 981$s, $\varepsilon = 1.90 \cdot 10^{-2}$. The remaining parameters are as in Table 3.3 and 3.4.

replenishment of the ER. This version was just introduced. The adaptive model [6] is discussed in more detail in Sec. 3.5, is more difficult to treat analytically but reproduces a large number of experimentally observed features of Ca^{2+} spiking.

Fig. 3.13 provides an overview of the dynamics of the two model variants and compares the resulting ISI sequences with experimentally measured ISI sequences of stimulated HEK cells. In Fig. 3.13A and B, both model versions are subjected to a constant IP$_3$ stimulation $q = 1$ applied at $t_0 = 0$. Prior to the stimulation $t < t_0$, the concentrations rest at $c_{\rm i} = c_0^*$ and $c_{\rm er} = 1$, all IP$_3$R channels are closed, the puff current is zero and there are no spikes generated in this state (not shown). Upon stimulation, the IP$_3$R channels are activated and give rise to a stochastic Ca^{2+} current such that $c_{\rm i}(t)$ begins to rise toward the threshold while $c_{\rm er}(t)$ remains at 1. The first time the threshold is reached, a spike is fired at time t_1. The difference between the first spike time and the stimulation time defines the initial ISI, $T_0 = t_1 - t_0$. Every subsequent spike is defined as usual $T_i = t_{i+1} - t_i$. It is only now, after the first spike, that the models begin to differ. In the case of the renewal model, $c_{\rm i}$ is reset to $c_R = c_0^*$ and the second (and any subsequent)

ISI is statistically equivalent to the first interval[4]. This is evident from the fact that the mean interval (back line in Fig. 3.13A_1) is independent of the index i. In case of the adaptive model $c_{\mathrm{er}}(t)$ is decreased by $\varepsilon c_{\mathrm{er}}(t_1^-)$ and $c_{\mathrm{i}}(t)$ is reset to $c_R = c_0^* c_{\mathrm{er}}(t_i^+)$. Note that $c_{\mathrm{er}}(t_1^-) = 1$ and $c_{\mathrm{er}}(t_1^+) = 1 - \varepsilon$ because no spike was fired prior to the first spike. After the reset, $c_{\mathrm{i}}(t)$ rises towards the threshold again, and $c_{\mathrm{er}}(t)$ is slowly replenished. During the first few intervals, the replenishment of $c_{\mathrm{er}}(t)$ between two spikes cannot compensate for the depletion during a spike. This leads to a cumulative decrease of $c_{\mathrm{er}}(t)$ and, due to the resulting inhibition of the puff current and decrease of the reset value (both proportional to $c_{\mathrm{er}}(t)$), also to a cumulative refractoriness in the sequence of ISIs as shown in Fig. 3.13B_1 where the black line represents a fit of the ISI sequence by the exponential function $T_\infty - (T_\infty - T_0)\exp(-i/n_{\mathrm{tr}})$. The part of the ISI sequence where the interval statistics explicitly depend on i is called the transient.

While the renewal model can capture some stationary statistics of the experimental ISI sequence shown in Fig. 3.13C_1, only the adaptive model can reproduce the transient.

Motivation of the IF dynamics

So far, we have presented the IF part of our model in an ad hoc manner and discussed the emerging dynamics. In the following, we take a step back and motivate the model in more detail. While we will eventually move to a dimensionless description, we begin our consideration with physical concentrations. As we have emphasized many times, in an IF model, the spiking variable, here the intracellular Ca^{2+} concentration, is described only over a small part of the physiological range up to a certain threshold. This threshold is usually well below the peak concentration reached during the spike. The spike itself is not modeled but replaced by a fire-and-reset rule. This has the advantage that the often nonlinear processes that cause the intracellular Ca^{2+} concentration to rise and fall during the spike can be neglected.

Our model distinguishes between IP_3-independent and IP_3-dependent currents that affect the cytosolic Ca^{2+} concentration $[Ca^{2+}]_i$. The IP_3-independent currents include all active and passive Ca^{2+} currents across the plasma membrane and the membrane of the ER. Since we consider only small changes in the cytosolic Ca^{2+} concentration, these currents are linearized and combined into a single current

$$J_{\mathrm{lin}} = \frac{[Ca^{2+}]_i - [Ca^{2+}]_0^*}{\tau}. \tag{3.3.45}$$

This term gives rise to a stable cytosolic resting Ca^{2+} concentration $[Ca^{2+}]_0^*$ in the absence of a stimulus and perturbations to $[Ca^{2+}]_i$ decay towards this value with the time constant τ. The IP_3-dependent Ca^{2+} current is the puff current, which describes the discharge of Ca^{2+} from the ER into the cytosol through clusters of IP_3 receptor channels

$$J_{\mathrm{puff}} = \hat{p}[Ca^{2+}]_{\mathrm{er}} \sum_k^K x_k(t). \tag{3.3.46}$$

This current mediates the positive feedback mechanism CICR and the nonlinearity of the spike generation. In Eq. 3.3.46, we have already made a simplifying assumption because the puff current is a diffusive current between the cytosol and ER, which, according to Fick's first law [47], should depend on the difference $[Ca^{2+}]_{\mathrm{er}}$- $[Ca^{2+}]_i$. However, since the ER Ca^{2+} concentration (100-500μM) is usually three to four orders of magnitude larger than the cytosolic Ca^{2+} concentration (50-100nM) [19, 29, 235] we neglect the dependence on $[Ca^{2+}]_i$ in this difference.

Consistent with our assumption that only two subthreshold currents need to be distinguished, of which the IP_3-independent one is linear in c_{i}, the Parker lab [236, 237] has recently shown that the main share of Ca^{2+} release into the cytosol during the rising phase of the spike is due to the discharge of Ca^{2+} from the ER through clusters of IP_3Rs and that the return to the resting concentration after a spike, when puffs are absent, is well described by an exponential decay with a single timescale.

---

[4] We note that the first interval T_0 is not fully equivalent to the subsequent intervals T_i with $i \geq 1$, because the clusters are initiated in the state C_1 and not according to the stationary probabilities of the states. However, this has little effect on the ISI statistics because the correlation time of $x(t)$ is small compared to $\langle T_0 \rangle$.

What we have not considered so far is that the resting concentration $[\mathrm{Ca}^{2+}]_0^*$ results from the balance of different Ca^{2+} currents across the cell membrane and across the ER membrane. Since the latter depends on the Ca^{2+} concentration in the ER, which is itself a dynamic variable in our model, the resting concentration is not fixed but varies. To study this dependence, we distinguish two types of IP$_3$-independent currents: those through the cell membrane and those through the ER membrane:

$$J_{\mathrm{lin}} = -\frac{[\mathrm{Ca}^{2+}]_{\mathrm{i}}}{\tau_s} + \frac{V_{\mathrm{er}}}{V_{\mathrm{i}}}\frac{[\mathrm{Ca}^{2+}]_{\mathrm{er}}}{\tau_l} - \frac{[\mathrm{Ca}^{2+}]_{\mathrm{i}} - [\mathrm{Ca}^{2+}]_0^*}{\tau_{p_m}}. \tag{3.3.47}$$

The first two terms describe currents across the ER membrane, specifically the active Ca^{2+} reuptake from the cytosol into the ER by SERCA pumps with timescale τ_s and the passive leak current from the ER into the cytosol with timescale τ_l. The factor $V_{\mathrm{er}}/V_{\mathrm{i}}$ accounts for the volume ratio between ER and cytosol. The third term describes Ca^{2+} currents across the plasma membrane, again in a linearized way with the timescale τ_{p_m}. Note that, strictly speaking, the second term should again depend on $[\mathrm{Ca}^{2+}]_{\mathrm{er}} - [\mathrm{Ca}^{2+}]_{\mathrm{i}}$, a difference that we approximate by $[\mathrm{Ca}^{2+}]_{\mathrm{er}}$ for the same reason as before. We combine the three currents in Eq. 3.3.47 into a single linear term

$$J_{\mathrm{lin}} = -\frac{[\mathrm{Ca}^{2+}]_{\mathrm{i}} - [\mathrm{Ca}^{2+}]_0}{\tau} \tag{3.3.48}$$

with timescale

$$\tau = \frac{\tau_s \tau_{p_m}}{\tau_{p_m} + \tau_s} \tag{3.3.49}$$

and resting concentration

$$[\mathrm{Ca}^{2+}]_0 = \left(\frac{[\mathrm{Ca}^{2+}]_0^*}{\tau_{p_m}} + \frac{[\mathrm{Ca}^{2+}]_{\mathrm{er}}}{\hat{\tau}_l}\right)\tau, \quad \hat{\tau}_l = \frac{V_{\mathrm{i}}}{V_{\mathrm{er}}}\tau_l. \tag{3.3.50}$$

To make a relation to the maximum resting concentration $[\mathrm{Ca}^{2+}]_0^*$, which is assumed when no spikes are fired, and the ER is not depleted, we consider a variation of the ER Ca^{2+} concentration from the maximal concentration $[\mathrm{Ca}^{2+}]_{\mathrm{er}} = [\mathrm{Ca}^{2+}]_{\mathrm{er}}^{\max} - \Delta[\mathrm{Ca}^{2+}]_{\mathrm{er}}$ and substitute this expression into Eq. 3.3.50. This yields

$$[\mathrm{Ca}^{2+}]_0 = \left(\frac{[\mathrm{Ca}^{2+}]_0^*}{\tau_{p_m}} + \frac{[\mathrm{Ca}^{2+}]_{\mathrm{er}}^{\max}}{\hat{\tau}_l}\right)\tau - \Delta[\mathrm{Ca}^{2+}]_{\mathrm{er}}\frac{\tau}{\hat{\tau}_l}, \tag{3.3.51}$$

a relation that can be simplified by realizing that when no spikes are fired, and all concentrations are at rest, the two currents across the ER membrane must balance (because $[\mathrm{Ca}^{2+}]_{\mathrm{er}} = \mathrm{const.}$). Put differently, for $[\mathrm{Ca}^{2+}]_{\mathrm{i}} = [\mathrm{Ca}^{2+}]_0^*$ and $[\mathrm{Ca}^{2+}]_{\mathrm{er}} = [\mathrm{Ca}^{2+}]_{\mathrm{er}}^{\max}$ the Ca^{2+} leakage from the ER into the cytosol and the Ca^{2+} removal from the cytosol into the ER by SERCA pumps are equal:

$$\frac{[\mathrm{Ca}^{2+}]_0^*}{\tau_s} = \frac{[\mathrm{Ca}^{2+}]_{\mathrm{er}}^{\max}}{\hat{\tau}_l}. \tag{3.3.52}$$

Combining Eq. 3.3.51 and 3.3.52 yields

$$[\mathrm{Ca}^{2+}]_0 = [\mathrm{Ca}^{2+}]_0^*\left(1 - \left[1 - \frac{[\mathrm{Ca}^{2+}]_{\mathrm{er}}}{[\mathrm{Ca}^{2+}]_{\mathrm{er}}^{\max}}\right]\frac{\tau_{p_m}}{\tau_s + \tau_{p_m}}\right). \tag{3.3.53}$$

Finally, we reinsert Eq. 3.3.53 into 3.3.48 and return to dimensionless variables by dividing both the left and right-hand side by K_{act} to obtain

$$j_{\mathrm{lin}} = -(c_{\mathrm{i}} - c_0(c_{\mathrm{er}}))/\tau, \tag{3.3.54}$$

with

$$c_0(c_{\mathrm{er}}) = c_0^*(1 - \alpha[1 - c_{\mathrm{er}}]), \tag{3.3.55}$$

where we have introduced the dimensionless ER Ca^{2+} concentration $c_{\text{er}} = [\text{Ca}^{2+}]_{\text{er}}/[\text{Ca}^{2+}]_{\text{er}}^{\text{max}}$. In the following, we will additionally assume $\alpha = 1$. This means that the Ca^{2+} current across the plasma membrane is significantly slower than the Ca^{2+} current across the ER membrane due to the SERCA pumps. This implies $\tau_{p_m} \gg \tau_s$, which is consistent with other theoretical studies [64, 181, 214]. The puff current is much easier to motivate. We take Eq. 3.3.46 and scale the current to match the scaling of the linear current

$$j_{\text{puff}} = p c_{\text{er}} \sum_k^K x_k(t) \tag{3.3.56}$$

with $p = \hat{p}[\text{Ca}^{2+}]_{\text{er}}^{\text{max}}/K_{\text{act}}$.

We now turn to the equations governing the ER Ca^{2+} concentration dynamics. The Ca^{2+} currents across the ER membrane that contribute to the subthreshold dynamics of the cytosolic Ca^{2+} concentration should also occur there. This concerns the first two currents in Eq. 3.3.47 and the puff current given by Eq. 3.3.46, that affect the ER Ca^{2+} concentration with a reversed sign and a prefactor that accounts for the volume ratio

$$J_{\text{er}} = \frac{V_{\text{i}}}{V_{\text{er}}}\left(\frac{[\text{Ca}^{2+}]_{\text{i}}}{\tau_s} - \frac{V_{\text{er}}}{V_{\text{i}}}\frac{[\text{Ca}^{2+}]_{\text{er}}}{\tau_l} - \hat{p}[\text{Ca}^{2+}]_{\text{er}} \sum_k^K x_k(t)\right). \tag{3.3.57}$$

The three terms inside the parentheses are of the order of $[\text{Ca}^{2+}]_{\text{i}} \approx 100\,\text{nM}$ (strictly speaking, per second) and will have little effect on $[\text{Ca}^{2+}]_{\text{er}} \approx 100\,\mu\text{M}$. This is true even if the inverse volume ratio $V_{\text{i}}/V_{\text{e}} \approx 10$ is considered so that the Ca^{2+} currents affecting the subthreshold dynamics of the Ca^{2+} concentration in the cytosol can be neglected for the ER. Instead, we consider only the larger depletion of the ER *during* a Ca^{2+} spike and the replenishment by store-operated Ca^{2+} entry (SOCE). Thus, we distinguish two cases for the ER Ca^{2+} concentration dynamics. First, when a spike is fired ($t = t_i$) the concentration is depleted immediately according to

$$\frac{d}{dt}[\text{Ca}^{2+}]_{\text{er}} = -\varepsilon[\text{Ca}^{2+}]_{\text{er}}\delta(t - t_i). \tag{3.3.58}$$

This term takes into account that the concentration in the ER before the spike is not equal to the concentration after the spike. Although a large fraction of the Ca^{2+} released into the cytosol during the spike is transported back into the ER by SERCA pumps, a smaller fraction is transported out of the cell into the extracellular medium by Ca^{2+} pumps and exchangers in the cell membrane, leading to a net loss of Ca^{2+} with each spike. The fraction of the ER Ca^{2+} concentration lost to the extracellular medium is described by the parameter ε, which describes the *relative* net loss of Ca^{2+} during a spike. For $\varepsilon = 0$, all Ca^{2+} released during the spike is pumped back into the ER, whereas for $\varepsilon = 1$, the entire Ca^{2+} in the ER is lost during each spike. Consistent with our previous assumption about the strength of SERCA and PM currents, we expect the parameter ε to be small. The situation where ε is not only small but zero is considered in Sec. 3.4. Second, in the absence of a spike ($t \neq t_i$), we assume that the ER Ca^{2+} concentration is replenished exponentially via store-operated Ca^{2+} entry and the dynamics are governed by

$$\frac{d}{dt}[\text{Ca}^{2+}]_{\text{er}} = -([\text{Ca}^{2+}]_{\text{er}} - [\text{Ca}^{2+}]_{\text{er}}^{\text{max}})/\tau_{\text{er}}. \tag{3.3.59}$$

Combining Eq. 3.3.58 and 3.3.59 and dividing both the left and right hand side by $[\text{Ca}^{2+}]_{\text{er}}^{\text{max}}$ yields the equation used in our model:

$$\dot{c}_{\text{er}} = (c_{\text{er}} - 1)/\tau_{\text{er}} - \varepsilon c_{\text{er}} \textstyle\sum_i \delta(t - t_i). \tag{3.3.60}$$

3.4 Spiking statistics of the renewal model

We begin with a study of the renewal version of our model, which is obtained by assuming a constant and maximal Ca^{2+} concentration in the endoplasmic reticulum ($c_{\text{er}} = 1$). We will first focus on how the noise resulting from the stochastic activity of the IP$_3$R clusters can be treated mathematically. We will see that the timescale separation between puffs and spikes suggests a

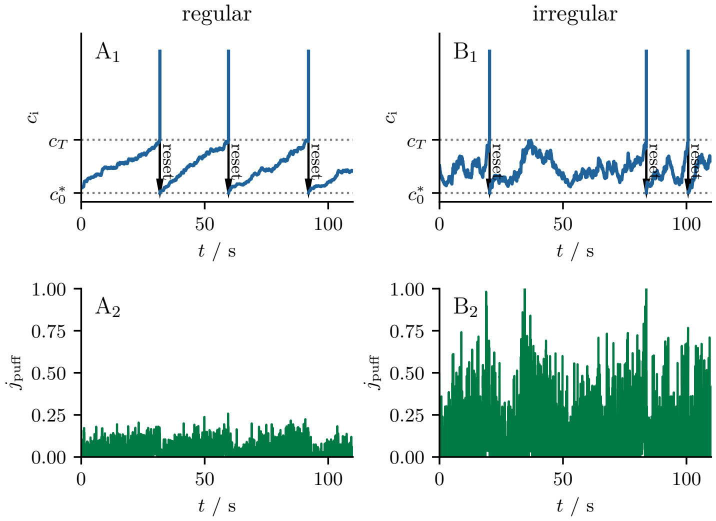

FIGURE 3.14: Firing regimes of the renewal model. Panels A (B) show the model in the regular (irregular) firing regime where the variability of the ISI is small (large) with $C_V(T) \approx 0.2$ ($C_V(T) \approx 0.8$). Panels A$_1$ (B$_1$) and A$_2$ (B$_2$) show the dynamics of $c_{\rm i}(t)$ and $j_{\rm puff}(t)$, respectively. In Panel A, the puff current and the leak current are weak, and $c_{\rm i}(t)$ gradually increases towards the threshold. In Panel B, the puff current and leak current are strong and may even balance on average between resting and threshold concentrations. In this case, $c_{\rm i}(t)$ is subject to significant fluctuations. Parameters A: $\tau = 5$s, $p = 0.015$; B: $\tau = 1$s, $p = 0.06$.

diffusion approximation of the puff current. This, in turn, allows the two-component model to be treated in the Fokker-Planck framework and many spike and ISI statistics to be calculated analytically.

The renewal version of the model is as follows:

$$\begin{aligned} \dot{c}_{\rm i} &= -(c_{\rm i} - c_0^*)/\tau + j_{\rm puff}(c_{\rm i}), \\ \text{if } c_{\rm i}(t) &= c_T \rightarrow t_i = t \text{ and } c_{\rm i}(t) = c_R, \end{aligned} \tag{3.4.1}$$

where the first term $-(c_{\rm i} - c_0^*)/\tau$ is a deterministic linear current, while the second term $j_{\rm puff} = p\sum_k^K x_k(t)$ is the stochastic puff current. Unless stated otherwise, the parameters are chosen according to Table 3.3 and 3.4. As a result, two parameters remain to be varied, τ and p.

In Fig. 3.14, we illustrate the dynamics of the renewal model (Eq. 3.4.1) using two parameter sets, resulting in either regular firing (Fig. 3.14A) or irregular firing (Fig. 3.14B). The observed behavior can be intuitively understood. In the first case, where the model fires regularly, the timescale parameter τ is large, while the permeability-like parameter p is small. Consequently, a substantial number of puffs is necessary to initiate a spike, and $c_{\rm i}$ gradually increases towards the firing threshold. In this firing regime, the model resembles the perfect IF model [238], where the leak term is absent. In fact, as τ approaches infinity, it takes, on average, $n = (c_R - c_T)/p\langle A\rangle$ puffs to reach the threshold. For the specific parameter set used, this amounts to $n \approx 150$ puffs. Although there is substantial variability in the timing of individual puffs (cf. Fig. 3.10B$_5$), the time necessary for the puff count to reach 150 and to initiate a Ca^{2+} spike demonstrates relatively low variability. In contrast, in the second case, where the model fires irregularly, the timescale τ is comparable to the mean IPI. The superposition of $K = 10$ clusters results in a puff current that is still fast compared to the leak current, but a significant portion of the Ca^{2+} released into the cytosol by the puffs is removed between two puffs. In this case, the leak and puff currents may even balance for a certain period, causing $c_{\rm i}(t)$ to fluctuate between the resting and threshold concentrations. This behavior contrasts with the gradual increase toward the firing threshold observed in Fig. 3.14A. Consequently, in this case, the model is more of a coincidence detector, where the initiation of the Ca^{2+} spike requires a small number of puffs to occur in quick succession.

While the qualitative behavior of the model can be well understood, quantitative statements about firing statistics are challenging due to the hierarchical organization of Ca^{2+} spiking into

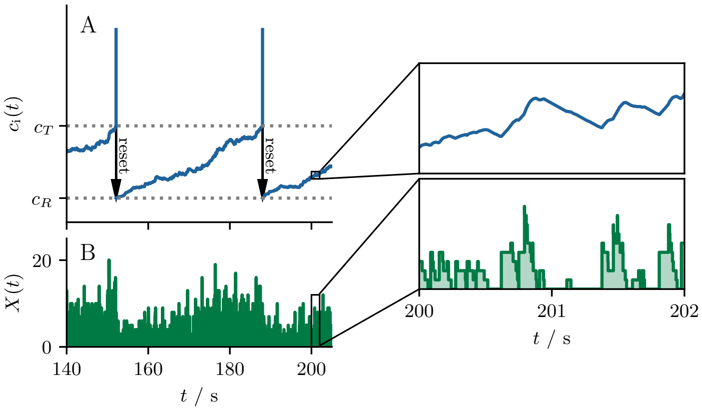

FIGURE 3.15: Illustration of the timescale separation between the slow dynamics of $c_i(t)$ (Panel A) and the fast dynamics of the cluster activity $\sum x_k(t)$ (Panel B). The inset highlights the many transitions of $X(t)$ that occur before a significant change in $c_i(t)$ is observed, further emphasizing the timescale difference. Parameters $\tau = 5$s, $p = 0.015$.

puffs and spikes. As we have seen, the puffs give rise to a stochastic Ca^{2+} current that influences the dynamics of the cytosolic Ca^{2+} concentration and impacts various statistics. Like any *real* noise, the puff current has a finite correlation time. Consequently, the process $c_i(t)$ is not Markovian. Although the pair $(c_i(t), y(t))$ is Markovian and could be described by a corresponding Kolmogorov forward equation, the resulting system of differential equations governing the probability densities would be high-dimensional. However, the timescale separation between the puff and leak currents enables a diffusion approximation, where the stochastic puff current $j_{\text{puff}}(c_i)$ is replaced by a deterministic mean and a Gaussian white noise. In this approximation, $c_i(t)$ becomes a Markov process, and the corresponding probability density $P(c_i, t)$ can be treated in the Fokker-Planck framework.

3.4.1 Diffusion approximation of the puff current

In the following, we present the derivation of the diffusion approximation of the stochastic puff current

$$j_{\text{puff}}(c_i) \approx \mu(c_i) + \sqrt{2D(c_i)}\xi(t), \tag{3.4.2}$$

where $\mu(c_i)$ is the c_i-dependent mean puff current and $\xi(t)$ is a Gaussian white noise with c_i-dependent noise intensity $D(c_i)$. This approximation allows to formulate an Langevin equation corresponding to Eq. 3.4.1. As emphasized above, the motivation for this approximation stems from the observed timescale separation between the slower leak current and the faster cluster activity. This timescale separation is illustrated in Fig. 3.15, by means of typical time series of $c_i(t)$ and $X(t) = \sum x_k(t)$ in the regular firing regime. The inset of the figure further highlights this separation by displaying the dynamics over two seconds, demonstrating that the summed cluster states $X(t)$ undergo numerous transitions before $c_i(t)$ changes significantly. We note that in the past, discrete-time Markov chains have been approximated by Langevin equations [239, 240]. Typically, these approximations assume that the fraction of channels (or clusters, in our case) in each state of the Markov chain can be treated as a continuous random variable that is Gaussian distributed. This assumption requires a large number of channels/clusters compared to the number of states and results in a stochastic process that is not necessarily uncorrelated. In contrast, our approach relies solely on the observed timescale separation and allows for a diffusion approximation even for a small number of channels/clusters.

To derive the Langevin approximation we consider Eq. 3.4.1 integrate over a short time window Δt:

$$c_i(t + \Delta t) = c_i(t) - \int_t^{t+\Delta t} dt' \, (c_i(t') - c_0^*)/\tau + \int_t^{t+\Delta t} dt' \, pX(t') \tag{3.4.3}$$

and define the stochastic process

$$\bar{X}(t;\Delta t) = \frac{1}{\Delta t}\int_t^{t+\Delta t} dt' X(t'), \tag{3.4.4}$$

that can be viewed as a moving average or box-filtered version of the summed cluster activity $X(t)$. As a result of the filtering, $\bar{X}(t;\Delta t)$ is a continuous random process with a piecewise continuous derivative. As we have already pointed out in Sec. 1.2, in order to formulate a Langevin equation, the time window Δt must approximately satisfy two opposing conditions. First, the time window should be chosen *small* enough so that the integral over the leak current can be approximated by the typical Euler integration scheme:

$$\int_t^{t+\Delta t} dt' \, (c_\mathrm{i}(t') - c_0^*)/\tau \approx (c_\mathrm{i}(t) - c_0^*)\Delta t/\tau. \tag{3.4.5}$$

Second, the time window should be *large* enough so that the summed cluster activity $X(t)$ undergoes multiple transitions. If this is the case, the moving average $\bar{X}(t,\Delta t)$ can be considered the sum of multiple puffs with independent strength. If a sufficiently large number of puffs falls into the time window, and hence a sufficiently large number of random variables is summed, the process $\bar{X}(t;\Delta t)$ will - according to the central limit theorem - be Gaussian distributed and fully characterized by its mean μ_X and variance $\sigma_X(\Delta t)$ (neglecting the bar):

$$\int_t^{t+\Delta t} dt' \, pX(t') = p\bar{X}(t;\Delta t)\Delta t \approx p(\mu_X + \sigma_X(\Delta t)\nu(t))\Delta t. \tag{3.4.6}$$

Here $\nu(t)$ is a Gaussian distributed random process with zero mean and unit variance. If both conditions can be satisfied at the same time, Eq. 3.4.3 can be approximated as follows

$$c_\mathrm{i}(t+\Delta t) \approx c_\mathrm{i}(t) - (c_\mathrm{i}(t) - c_0^*)\Delta t/\tau + p\mu_X\Delta t + p\sigma_X(\Delta t)\nu(t)\Delta t. \tag{3.4.7}$$

This equation closely resembles an Euler integration scheme of a Langevin equation. The only difference is that the random process $\nu(t)$ is not uncorrelated but possesses a nonvanishing correlation time τ_X inherited from the process $\bar{X}(t;\Delta t)$. However, if the correlation time is significantly shorter than any other timescale in the system (specifically, the timescale of the leak current τ), we can find a time window Δt such that the process $\nu(t)$ is practically uncorrelated at two different times Δt apart. In this limit the variance scales as $\sigma_X(\Delta t) \propto 1/\sqrt{\Delta t}$ (see below) and Eq. 3.4.7 corresponds exactly to the Euler integration scheme of a Langevin equation.

The filtered cluster activity and its convergence to a Gaussian distributed random process for a fixed cytosolic Ca^{2+} concentration $c_\mathrm{i} = c_T$ is illustrated in Fig. 3.16 where typical time series of $\bar{X}(t;\Delta t)$ for three different values $\Delta t = 0$s, $\Delta = 0.1$s and $\Delta t = 1.0$s are shown in Fig. 3.16A$_1$, B$_1$ and C$_1$, respectively. Note that for $\Delta t = 0$ the original process $X(t) = \sum_k x_k(t)$ is recovered. The corresponding probability densities are shown by histograms in Fig. 3.16A$_2$, B$_2$ and C$_2$. The red lines show Gaussian distributions with mean μ_x and variance $\sigma_X^2(\Delta t)$. Note that the mean does not depend on Δt, while the variance does. This is expected for a moving average. Specifically, for $\Delta t \to \infty$, we expect no fluctuations in $\bar{X}(t;\Delta t)$. For the time bin $\Delta t = 0$ (Fig. 3.16A) and $\Delta t = 0.1$ (Fig. 3.16B), the variance is still large enough for the Gaussian approximation to predict incorrectly that the process $\bar{X}(t;\Delta t)$ can take negative values (not shown). This changes if we choose a time bin $\Delta t = 1.0$ (Fig. 3.16C), in which case $\bar{X}(t;\Delta t)$ closely follows a Gaussian distribution (Fig. 3.16C$_2$).

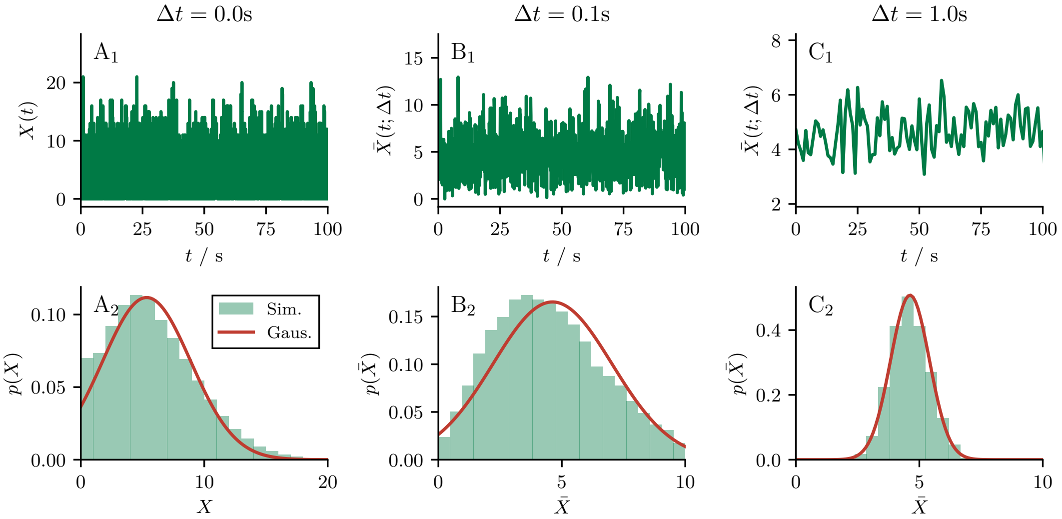

FIGURE 3.16: Diffusion approximation of the cluster activity $X(t) = \sum x_k(t)$ for a fixed Ca^{2+} concentration $c_{\mathrm{i}} = c_T$. Panels A, B, and C shows time series of the filtered cluster activity $\bar{X}(t;\Delta t)$ and histograms of the corresponding probability density $p(\bar{X})$ for three different time windows $\Delta t = 0$s, $\Delta t = 0.1$s and $\Delta t = 1$s, respectively. Note that for $\Delta t = 0$, the original process $X(t)$ is recovered. As shown in A$_2$, B$_2$, and C$_2$, the larger the time window Δt, the better the probability distribution $p(\bar{X})$ can be described by a Gaussian distribution (red line).

Mean and variance of the filtered cluster activity

We now turn to the calculation of the mean μ_X and the variance $\sigma_X(\Delta t)$ of the filtered cluster activity $\bar{X}(t;\Delta t)$. We begin by calculating the mean μ_X. Since the K clusters are statistically independent and identical, it is clear that the mean of the sum is equal to the sum of the means:

$$\begin{aligned}\mu_X = \langle \bar{X}(t;\Delta t)\rangle &= \frac{1}{\Delta t}\int_t^{t+\Delta t} dt_1\, \langle \sum_k^K x_k(t_1)\rangle \\ &= \frac{1}{\Delta t}\int_t^{t+\Delta t} dt_1\, K\langle x(t_1)\rangle \\ &= K\mu_x,\end{aligned} \tag{3.4.8}$$

where the mean of a single cluster μ_x can be calculated according to Eq. 3.3.40. The variance is somewhat more complicated but can be related to the correlation function of a single cluster $C_{xx}(\tau)$:

$$\begin{aligned}\sigma_X^2 &= \langle \Delta\bar{X}(t;\Delta t)^2\rangle \\ &= \frac{1}{\Delta t^2}\iint_t^{t+\Delta t} dt_1 dt_2 \sum_{k_1,k_2}^K \langle \Delta x_{k_1}(t_1)\Delta x_{k_2}(t_2)\rangle \\ &= \frac{1}{\Delta t^2}\iint_t^{t+\Delta t} dt_1 dt_2 \left[\sum_{k_1=1}^K \langle \Delta x_{k_1}(t_1)\Delta x_{k_1}(t_2)\rangle + \sum_{k_1\neq k_2}^K \langle \Delta x_{k_1}(t_1)\Delta x_{k_2}(t_2)\rangle\right], \\ &= \frac{K}{\Delta t^2}\iint_t^{t+\Delta t} dt_1 dt_2\, C_{xx}(t_2 - t_1).\end{aligned} \tag{3.4.9}$$

To get from the second to the third line, we split the double sum into two parts, one considering only the terms with $k_1 = k_2$ and the other considering the remaining terms with $k_1 \neq k_2$. To get from the third to the last line, we additionally used the fact that the clusters are independent of each other, i.e., the second sum over different clusters vanishes. Eq. 3.4.9 can be simplified further using that the correlation function does only depend on the difference $\tau = t_2 - t_1$ (but not on

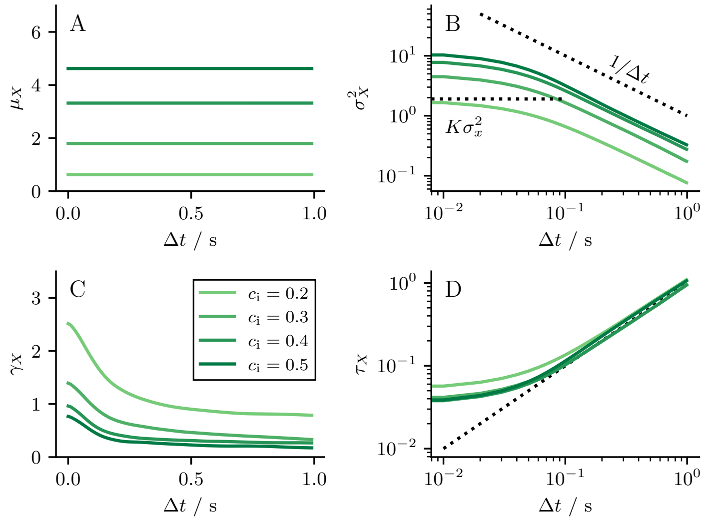

FIGURE 3.17: Statistics of $\bar{X}(t;\Delta t)$ as a function of the time window Δt. All statistics are obtained from stochastic simulations of the cluster model at a fixed Ca^{2+} concentration c_i (color coded). Panel A shows that the mean μ_X is independent of Δt. Panel B shows the variance σ_X^2, which is given by Kσ_x^2 (horizontal dotted line) for $\Delta t = 0$ and decreases as $\sigma_X^2 \propto 1/\Delta t$ (diagonal dotted line) for large time windows. Both the mean and the variance increase with c_i as the open probability and the number of transitions increases. Panel C shows that the skewness decreases with Δt and c_i, improving the quality of the Gaussian approximation. Panel D shows the correlation time τ_X, which starts at a small c_i-dependent value, but converges to $\tau_X \approx \Delta t$ for large values of Δt.

absolute time) and is symmetric $C_{xx}(\tau) = C_{xx}(-\tau)$:

$$\begin{aligned}\sigma_X^2 &= \frac{K}{\Delta t^2}\iint_t^{t+\Delta t} dt_1 dt_2\, C_{xx}(t_2 - t_1)\\ &= \frac{2K}{\Delta t}\int_0^{\Delta t} d\tau\, C_{xx}(\tau)(1-\tau/\Delta t).\end{aligned} \tag{3.4.10}$$

Finally, if, according to our initial assumption, the time window is much larger than the correlation time of the cluster activity $\Delta t \gg \tau_x$, then the integral in Eq. 3.4.10 can be approximated by

$$\int_0^{\Delta t} d\tau\, C_{xx}(1-\tau/\Delta t) \approx \int_0^\infty d\tau\, C_{xx}(\tau), \tag{3.4.11}$$

which allows to relate the variance σ_X^2 of the filtered cluster activity to the noise intensity D_x of a single cluster by

$$\sigma_X^2 = \frac{2KD_x}{\Delta t}. \tag{3.4.12}$$

This is interesting not only because it shows that in the white noise limit, the relevant quantity to describe the strength of the fluctuations of a random process is the noise intensity but also because it provides a practical way to measure the noise intensity of a random process with a finite correlation time. To emphasize this again, to obtain the noise intensity of a random process $x(t)$, we introduce the box-filtered process $\bar{x}(t;\Delta t)$, increase the time bin Δt until the variance of this filtered process $\sigma^2(\Delta t)$ scales as $1/\Delta t$, and obtain the noise intensity by $D_x = \sigma^2(\Delta t)\Delta t$ (alternatively, one can plot $\sigma^2(\Delta t)\Delta t$ directly until it saturates for large Δt).

In Fig. 3.17 we show the mean μ_X, variance σ_X^2, skewness $\gamma_X = \langle(\bar{X} - \langle\bar{X}\rangle)^3\rangle/\sigma_X^3$ and correlation time τ_X of the filtered cluster activity $\bar{X}(t;\Delta t)$ as functions of Δt for different values of the cytosolic Ca^{2+} concentration c_i. In accordance with Eq. 3.4.8, the mean μ_X does not depend on the time window Δt but increases with c_i (Fig. 3.17A). In contrast, the variance initially shows a weak dependence on Δt when the time window is small and scales as $\sigma_X^2 \propto 1/\Delta t$ when the time window is large. This is so because for $\Delta t \to 0$, the variance can be approximated by

$$2K \int_0^{\Delta t} d\tau\, C_{xx}(1 - \tau/\Delta t) \approx K C_{xx}(0) = K\sigma_x^2, \tag{3.4.13}$$

which is shown for $c_\mathrm{i} = 0.2$ by the horizontal dotted line. The scaling for large values of Δt is as in Eq. 3.4.12. Additionally, we observe an overall increase in the variance with c_i due to an increased number of transitions between cluster states. Finally, in Eq. 3.17C and D, we show the skewness γ_X and correlation time τ_X, both should be small for $\bar{X}(t, \Delta t)$ to be approximately Gaussian distributed and uncorrelated. The skewness quickly decreases as Δt increases. Unfortunately, whether or not the skewness vanishes for $\Delta t \to \infty$ is unclear. The correlation time τ_X shown in Fig. 3.17D even increases with Δt. This is so because the filtering of the cluster activity introduces a new correlation time set by the time window Δt. However, this is no issue because the time window Δt also corresponds to the integration step in Eq. 3.4.3, and the random process considered at two different times $\nu(t)$ and $\nu(t + \Delta t)$ is practically uncorrelated. In addition, there is a general decrease in skewness and correlation time with c_i. This is again due to an increased number of transitions and shows that the quality of the diffusion approximation also depends on c_i.

3.4.2 Langevin and Fokker-Planck equation

We have shown in Sec. 3.4.1 that the puff current can be approximated by a c_i-dependent mean $\mu(c_\mathrm{i}) = pK\mu_x(c_\mathrm{i})$ and a Gaussian white noise with c_i-dependent intensity $D(c_\mathrm{i}) = p^2 K D_x(c_\mathrm{i})$. This allows reducing the two-component model (Eq. 3.3.43) to a one-dimensional integrate-and-fire model with a nonlinear drift and a multiplicative Gaussian white noise

$$\begin{aligned} \dot{c}_\mathrm{i} &= -(c_\mathrm{i} - c_0^*)/\tau + \mu(c_\mathrm{i}) + \sqrt{2D(c_\mathrm{i})}\,\xi(t), \\ &\text{if } c_\mathrm{i}(t) = c_T \to t_i = t \text{ and } c_\mathrm{i}(t) = c_R, \end{aligned} \tag{3.4.14}$$

where $\xi(t)$ is a zero mean Gaussian white noise $\langle \xi(t)\xi(t+\tau)\rangle = \delta(\tau)$. Since the noise intensity depends on the variable driven by the white noise (multiplicative noise), the stochastic differential equation (SDE) requires an interpretation [58]. This has to do with the infinite variance of the white noise. In the next section, we will discuss the problem of interpreting the SDE, the so-called Ito-Stratonovich dilemma, in somewhat more detail; here, we just note that following Wong and Zakai [241], we interpret the stochastic differential equation in the sense of Stratonovich. Returning to the model, we note that a one-dimensional IF model with a Gaussian white noise always generates a renewal point process because resetting c_i to a fixed value c_R at the end of an interval erases all memory of the previous ISI and the white noise $\xi(t)$ is by definition uncorrelated. We, therefore, refer to this variant as the renewal model.

Before we turn to the full stochastic system, we first consider the deterministic limit ($D = 0$), which allows us to distinguish the mean-driven from the excitable firing regime through the deterministic drift term:

$$f(c_\mathrm{i}) = -(c_\mathrm{i} - c_0^*)/\tau + \mu(c_\mathrm{i}). \tag{3.4.15}$$

In the mean-driven regime, this function is positive for all $c_\mathrm{i} < c_T$ but, in the excitable regime, has a zero for some value $c_\mathrm{i}^* < c_T$. This is illustrated in Fig. 3.18A$_2$ where the model possesses no fixed point between reset and threshold, while in Fig. 3.18B$_2$ there is a fixed point (black circle) for some value $c_\mathrm{i}^* < c_T$.

In Fig. 3.18A and B, the same parameters were used as previously in Fig. 3.14A and B. We can now understand what distinguishes the regular firing regime in Fig. 3.14A from the irregular firing regime in Fig. 3.14B. In the first case, the model operates in the mean-driven regime, spikes are fired periodically even in the deterministic limit ($D = 0$), and the noise from the puff current plays only a minor role. The system can be considered a deterministic oscillator subject to a weak noise, which results in rather regular ISIs. In the second case, the model operates in the excitable regime, and spikes are observed only due to the noise of the puff current. In particular, the deterministic system cannot reach the threshold but approaches the fixed point c_i^*. The transition

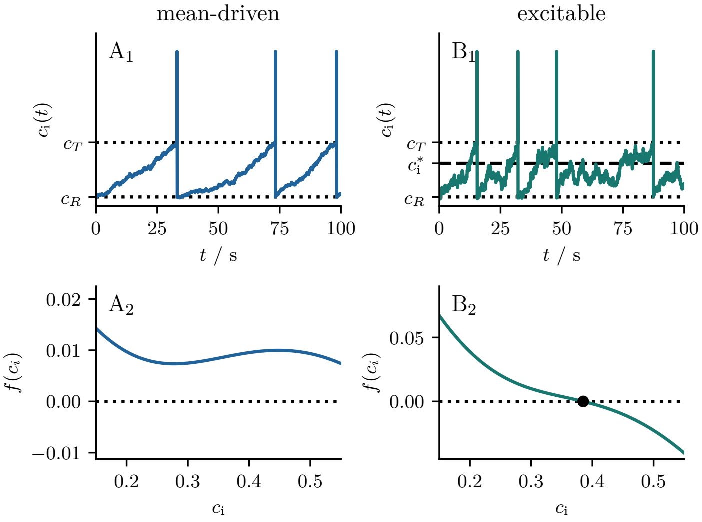

FIGURE 3.18: Firing regimes of the Langevin approximation. Panel A (B) shows the model in the mean-driven (excitable) firing regime. Panels A$_1$ and B$_1$ show the dynamics of $c_\mathrm{i}(t)$. Panel A$_2$ shows the drift function $f(c_\mathrm{i})$ in the mean-driven regime, which is positive for all values $c_R < c_\mathrm{i} < c_T$. Panel B$_2$ shows the drift function in the excitable regime, which has a zero $f(c_\mathrm{i}^*) = 0$ for some value $c_R < c_\mathrm{i}^* < c_T$. Consequently, the model has a fixed point at c_i^* (black circle). Parameters A: $\tau = 5$s, $p = 0.015$; B: $\tau = 1$s, $p = 0.06$.

from c_i^* to c_T is noise-induced, resulting in highly stochastic ISIs. We note that, in general, spiking can also be irregular in the mean-driven regime if the noise is strong enough or regular in the excitable regime if the difference between fixed point and threshold and the noise intensity are chosen just right. However, neither is the case here.

Eq. 3.4.14 allows us to determine the bifurcation point between these two firing regimes. The transition between the two firing regimes occurs when the fixed point falls exactly on the firing threshold $f(c_T) = 0$. This leads to a simple condition for the critical values of τ and p:

$$\tau p = \frac{c_T - c_0^*}{K\mu_x(c_T)}. \tag{3.4.16}$$

Apart from the fact that Eq. 3.4.14 allows us to determine the bifurcation point, the white-noise approximation is appealing because it permits to use the powerful arsenal of the theory of Markov processes [59, 60]. For example, the time evolution of the probability density $P(c_\mathrm{i}, t)$ can be determined using the Fokker-Planck equation.

Itô-Stratonovich Dilemma

Due to the multiplicative nature of the white noise - the intensity depends on the variable it acts upon - it becomes necessary to interpret the SDE to determine the corresponding FPE uniquely [58]. Formally, the interpretation of the SDE corresponds to the specification of the parameter a within the following FPE:

$$\frac{\partial}{\partial t}P(c_\mathrm{i}, t) = \frac{\partial}{\partial c_\mathrm{i}}\left[-f(c_\mathrm{i}) - aD'(c_\mathrm{i}) + \frac{\partial}{\partial c_\mathrm{i}}D(c_\mathrm{i})\right]P(c_\mathrm{i}, t) + r(t)\delta(c_\mathrm{i} - c_R). \tag{3.4.17}$$

The term $r(t)\delta(c_\mathrm{i} - c_R)$ is the counterpart of the reset rule of the IF model but does not affect the interpretation of the FPE. The most common interpretations are the ones by Itô ($a = 0$), by Stratonovich ($a = 1/2$), and by Klimontovich and Hänggi ($a = 1$). Unfortunately, it is unclear which of these interpretations (if any [242]) should be chosen for our model. Without diving too deeply into the sometimes confusing relationship between classical Riemann and stochastic integrals[5], we note that according to Wong and Zakai [241], a Langevin equation must be interpreted

---

[5] The interested reader is referred to Chapter 8 and 9 in [59]

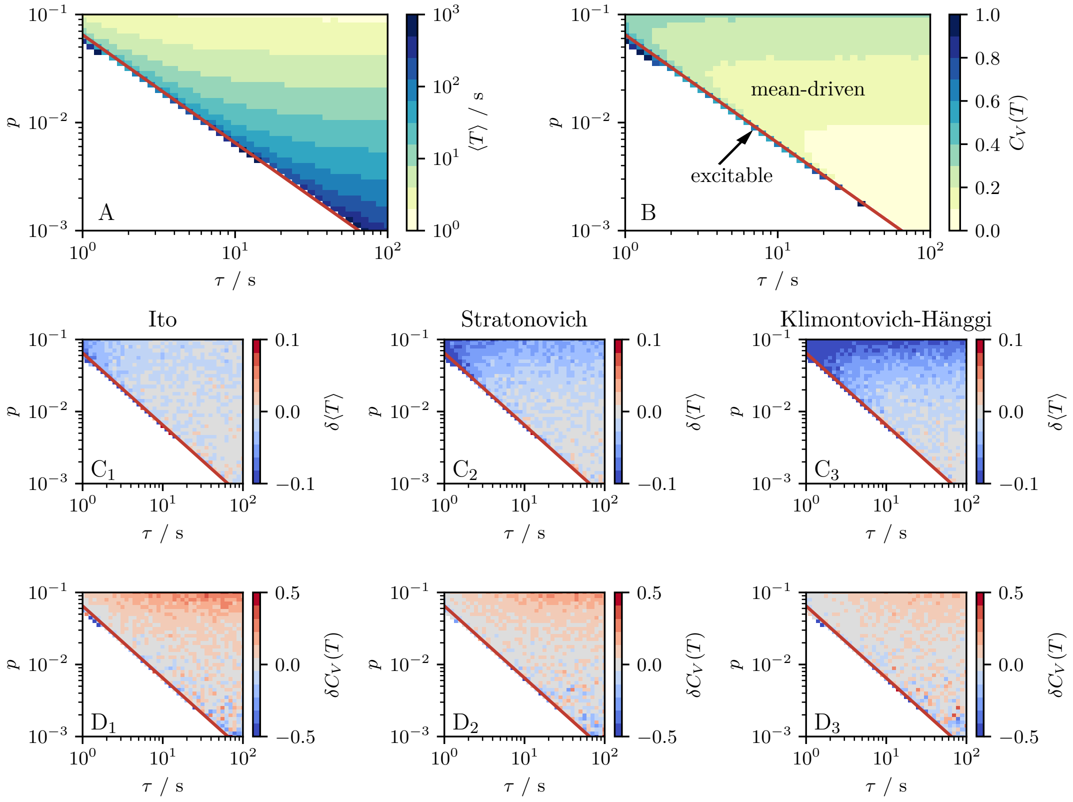

FIGURE 3.19: Statistics of the two-component model and interpretation of the Langevin approximation. Panels A and B show the mean $\langle T \rangle$ and the CV $C_V(T)$ obtained from stochastic simulations of the two-component model as a function of the parameters τ and p. The red lines indicate the bifurcation line according to Eq. 3.4.16. Above the bifurcation line (mean-driven regime), spikes are observed for all combinations of τ and p. Below the bifurcation line (excitable regime), spiking requires some fine-tuning of the parameters and is only observed close to the bifurcation line. The white area indicates the parameters for which no spikes were observed. In panels C and D, we show the relative deviation of the mean $\delta\langle T \rangle = (\langle T \rangle - \langle \hat{T} \rangle)/\langle T \rangle$ and the CV $\delta C_V(T) = (C_V(T) - \hat{C}_V(T)/C_V(T))$. Here $\langle T \rangle$ and $\langle \hat{T} \rangle$ ($C_V(T)$ and $\hat{C}_V(T)$) refer to the mean (CV) obtained from simulations of the two-component model and the Langevin approximation. The results for the most common interpretations are shown in C$_1$, C$_2$, and C$_3$ (D$_1$, D$_2$, and D$_3$).

in the Stratonovich sense if the white noise is an approximation of a continuous colored noise with piecewise continuous derivative. This is exactly the case for the process $\bar{X}(t; \Delta t)$. This result has been generalized by Blankenship and Papanicolaou [243] to hold for a large class of colored-noise processes, including jump processes, such as dichotomous noise or the process $X(t)$ generated by our cluster model. Thus, there is reason to believe that Eq. 3.4.14 must be interpreted in the Stratonovich sense. A rigorous derivation of this result would require to show that the Kolmogorov forward equation of Eq. 3.3.43, when considered in the limit of vanishing correlation time ($\tau_X = 0$), corresponds to the FPE 3.4.18.

Although we opt for the Stratonovich interpretation, Fig. 3.19 shows the effect of the three most common interpretations on the ISI statistics. To do this, we first determine the mean $\langle T \rangle$ and the CV $C_V(T)$ of the ISIs by stochastic simulations of the two-component model (Fig. 3.19A and B). We then determine the same statistics from the Langevin approximation in the three interpretations with the same parameters and denote the resulting means by $\langle \hat{T} \rangle$ and the CVs by $C_V(\hat{T})$. Finally, we determine the relative deviation between the mean resulting from the simulations of the two-component model and the means resulting from the simulations of the Langevin approximations $\delta\langle T \rangle = (\langle T \rangle - \langle \hat{T} \rangle)/\langle T \rangle$ (Fig. 3.19C) and similarly for the CVs $\delta C_V(T) = (C_V(T) - \hat{C}_V(T)/C_V(T))$ (Fig. 3.19D). It turns out that the question of interpretation does not play a significant role in our model for the parameter range where biophysically plausible ISIs and CVs are observed. While deviations between the three interpretations are observed for large values of p and small values of τ, this is also the parameter regime where the white-noise approximation describes the system poorly. For small values of τ, the puff current cannot be assumed to be white, whereas, for large values of p, the puff current cannot be assumed to be Gaussian distributed. Consequently, the deviations observed in this range are not necessarily due to the interpretation. For small values of p and large values of τ, where the diffusion approximation describes the system well, we observe minimal variation among the interpretations.

Stationary probability density function

We have motivated above that the FPE corresponding to Eq. 3.4.14 is given by

$$\begin{aligned}\frac{\partial}{\partial t}P(c_\mathrm{i},t) &= \frac{\partial}{\partial c_\mathrm{i}}\left[-f(c_\mathrm{i}) - D'(c_\mathrm{i})/2 + \frac{\partial}{\partial c_\mathrm{i}}D(c_\mathrm{i})\right]P(c_\mathrm{i},t) + r(t)\delta(c_\mathrm{i}-c_R)\\ &= -\frac{\partial}{\partial c_\mathrm{i}}J(c_\mathrm{i},t)\end{aligned} \tag{3.4.18}$$

with the drift function $f(c_\mathrm{i}) = -(c_\mathrm{i}-c_0^*)/\tau + \mu(c_\mathrm{i})$ and the Stratonovich drift $D'(c_\mathrm{i})/2$. The FPE is completed by the natural boundary condition, the absorbing boundary condition, and the normalization condition

$$\lim_{c_\mathrm{i}\to-\infty} P(c_\mathrm{i},t) = 0, \qquad P(c_T,t) = 0, \qquad \int_{-\infty}^{c_T} dc_\mathrm{i}\, P(c_\mathrm{i},t) = 1. \tag{3.4.19}$$

The second line in Eq. 3.4.18 relates the temporal derivative of the probability density to the spatial derivative of the probability current $J(c_\mathrm{i},t)$, which corresponds to a continuity equation for the probability density. We emphasize again that the IF model's reset rule in Eq. 3.4.14 finds its counterpart in the source term in Eq. 3.4.18 that is proportional to the probability current $J(c_\mathrm{i},t)$ across the threshold

$$r(t) = J(c_T,t) = -\left.\frac{\partial}{\partial c_\mathrm{i}}D(c_\mathrm{i})P(c_\mathrm{i},t)\right|_{c_\mathrm{i}=c_T}. \tag{3.4.20}$$

FPEs with such a source term have been extensively studied in the computational neuroscience literature [244–247]. However, to the best of our knowledge, the case of multiplicative noise is rarely considered.

Here, we calculate the stationary probability density $P_0(c_\mathrm{i})$ and the stationary firing rate r_0. To this end, we consider the stationary FPE

$$0 = \left[-f(c_\mathrm{i}) - D'(c_\mathrm{i})/2 + \frac{\partial}{\partial c_\mathrm{i}}D(c_\mathrm{i})\right]P_0(c_\mathrm{i}) + r_0\Theta(c_\mathrm{i}-c_R), \tag{3.4.21}$$

where we have omitted the time derivative because we are interested in the stationary case and subsequently integrate once with respect to c_i. As a result of this integration, the δ-function $\delta(c_\mathrm{i}-c_R)$ becomes a Heaviside function $\Theta(c_\mathrm{i}-c_R)$. To solve Eq. 3.4.21 we introduce two auxiliary functions, first $L(c_\mathrm{i}) = D(c_\mathrm{i})P_0(c_\mathrm{i})$ and second the effective drift function $g(c_\mathrm{i}) = f(c_\mathrm{i}) + D'(c_\mathrm{i})/2$, to obtain

$$\frac{\partial}{\partial c_\mathrm{i}}L(c_\mathrm{i}) = \frac{g(c_\mathrm{i})}{D(c_\mathrm{i})}L(c_\mathrm{i}) - r_0\Theta(c_\mathrm{i}-c_R), \tag{3.4.22}$$

which is solved by

$$L(c_\mathrm{i}) = r_0 e^{h(c_\mathrm{i})}\int_{c_\mathrm{i}}^{c_T} dx\, e^{-h(x)}\Theta(x-c_R), \quad \text{with} \quad h(x) = \int_{c_R}^{x} dy\, \frac{g(y)}{D(y)}. \tag{3.4.23}$$

The re-substituting of $P_0(c_\mathrm{i}) = L(c_\mathrm{i})/D(c_\mathrm{i})$ yields the stationary probability density:

$$P_0(c_\mathrm{i}) = r_0\frac{e^{h(c_\mathrm{i})}}{D(c_\mathrm{i})}\int_{c_\mathrm{i}}^{c_T} dx\, e^{-h(x)}\Theta(x-c_R). \tag{3.4.24}$$

This expression also allows us to calculate the stationary firing rate r_0 using the normalization of the probability density $\int dc_\mathrm{i}\, P_0(c_\mathrm{i}) = 1$. Put differently we can integrate c_i from $-\infty$ to c_T and obtain

$$r_0 = \left(\int_{c_R}^{c_T} dx_2\, e^{-h(x_2)} \int_{-\infty}^{x_2} dx_1\, \frac{e^{h(x_1)}}{D(x_1)} \right)^{-1}, \tag{3.4.25}$$

where we have used that the bounds of the integral can be interchanged and that the Heaviside function can be incorporated into the boundaries as follows

$$\int_{-\infty}^{x_T} dx_1 \int_{x_1}^{x_T} dx_2\, f(x_1, x_2)\theta(x_2 - x_R) = \int_{x_R}^{x_T} dx_2 \int_{-\infty}^{x_2} dx_1\, f(x_1, x_2). \tag{3.4.26}$$

Moments of the first-passage time

While the stationary FPE allows the calculation of the stationary probability density and the stationary firing rate, this approach makes higher moments of the ISI inaccessible. However, a second approach, where the ISI is interpreted as the first-passage time (FPT) from the reset c_R to the threshold c_T, allows to calculate the moments of the ISI density $\langle T^n \rangle$. This is usually done by formulating the Kolmogorov backward equation [57], which cannot be formulated for IF models with a reset mechanism. Instead, we follow the approach developed by Lindner [248] and calculate the moments of the FPT based on respective the Kolmogorov forward equation or FPE

$$\frac{\partial}{\partial t} P(c_\mathrm{i}, t) = \frac{\partial}{\partial c_\mathrm{i}} \left[-f(c_\mathrm{i}) - D'(c_\mathrm{i})/2 + \frac{\partial}{\partial c_\mathrm{i}} D(c_\mathrm{i}) \right] P(c_\mathrm{i}, t) = -\frac{\partial}{\partial c_\mathrm{i}} J(c_\mathrm{i}, t) \tag{3.4.27}$$

with the natural boundary condition, absorbing boundary condition, and initial condition:

$$\lim_{c_\mathrm{i} \to -\infty} P(c_\mathrm{i}, t) = 0, \qquad P(c_T, t) = 0, \qquad P(c_\mathrm{i}, 0) = \delta(c_\mathrm{i} - c_R). \tag{3.4.28}$$

Unlike Eq. 3.4.18, this FPE has no source term because for the *first*-passage time, the probability flux across the threshold is absorbed instead of reset. Still, the probability flux across the threshold at time t is related to the probability of finding a spike at time t:

$$p_{FP}(t) = J(c_T, t), \tag{3.4.29}$$

where $p_{FP}(t)$ is the FPT density. To compute the moments of the FPT, a hierarchy of differential equations can be derived. Although the case of multiplicative noise is rarely considered, the derivation of the hierarchy in this case is completely analogous to the case of additive noise [248], so we state the differential equations directly

$$-nJ_{n-1}(c_\mathrm{i}) = -g(c_\mathrm{i})J_n'(c_\mathrm{i}) + \frac{\partial}{\partial c_\mathrm{i}} D(c_\mathrm{i})J_n'(c_\mathrm{i}), \quad n > 0,. \tag{3.4.30}$$

where the auxiliary function $J_n(c_\mathrm{i})$ is defined as

$$J_n(c_\mathrm{i}) = \int_0^\infty dt\, t^n J(c_\mathrm{i}, t) \tag{3.4.31}$$

and $J_0(c_\mathrm{i}) = \Theta(c_\mathrm{i} - c_R)$. Eq. 3.4.30 is completed by the two boundary conditions:

$$J_n'(c_T) = n \int_0^\infty t^{n-1} P(c_t, t) = 0, \qquad \lim_{c_\mathrm{i} \to \infty} J_n(c_\mathrm{i}) = \int_0^\infty t^n \lim_{c_\mathrm{i} \to \infty} J(c_t, t) = 0. \tag{3.4.32}$$

Evaluating $J_n(c_\mathrm{i})$ at the threshold yields the n-moment of the FPT or equivalently the ISI density $J_n(c_T) = \langle T^n \rangle$. The solution to Eq. 3.4.30 can be obtained by first solving the homogeneous problem, then using the variation of parameters method to find the complete solution, and finally incorporating the boundary condition $J_n(c_\mathrm{i} \to -\infty) = 0$:

$$J_n(c_\mathrm{i}) = n \int_{\infty}^{c_\mathrm{i}} dy \frac{e^{h(y)}}{D(y)} \int_{y}^{c_T} dx\, e^{-h(x)} J_{n-1}(x). \tag{3.4.33}$$

For $n = 1$ this yields the mean ISI

$$\langle T \rangle = J_n(c_T) = \int_{c_R}^{c_T} dx_2\, e^{-h(x_2)} \int_{-\infty}^{x_2} dx_1 \frac{e^{h(x_1)}}{D(x_1)}, \tag{3.4.34}$$

where we have again used Eq. 3.4.26 to interchange the bounds of the integral. This expression agrees with the inverse firing rate in Eq. 3.4.25. For $n = 2$, we obtain the second moment:

$$\langle T^2 \rangle = 2 \int_{c_R}^{c_T} dx_4\, e^{-h(x_4)} \int_{-\infty}^{x_4} dx_3 \frac{e^{h(x_3)}}{D(x_3)} \int_{x_3}^{c_T} dx_2 e^{-h(x_2)} \int_{-\infty}^{x_2} dx_1 \frac{e^{h(x_1)}}{D(x_1)}. \tag{3.4.35}$$

The evaluation of the four nested integrals is even numerically challenging, but in the case of the variance, the expression can be simplified to include only two nested integrals [246]:

$$\left\langle \Delta T^2 \right\rangle = 2 \int_{-\infty}^{c_T} dx_3\, e^{-h(x_3)} \left(\int_{-\infty}^{x_3} dx_2 \frac{e^{h(x_2)}}{D(x_2)} \right)^2 \int_{x_3}^{c_T} dx_1\, e^{-h(x_1)} \Theta(x_1 - c_R). \tag{3.4.36}$$

3.4.3 Spiking statistics

So far, we have presented a one-dimensional Langevin approximation of the two-component model, formulated the corresponding FPE, and found analytical expressions for the stationary probability density along with the first and second moments of the ISI density.

Here, we compare these analytical results to numerical simulations of the two-component model (Eq. 3.3.43). We also provide an overview of how the spike statistics are influenced by the timescale of the leak current τ and the permeability-like parameter p. We have already pointed out that the Langevin approximation allows us to find an expression (Eq. 3.4.16) for the bifurcation line separating the mean-driven from the excitable regime, which is repeated here for convenience:

$$\tau p = \frac{c_T - c_0^*}{K \mu_x(c_T)}. \tag{3.4.37}$$

The dynamics of the two-component model in the mean-driven and excitable regimes have been shown in Fig. 3.14 and Fig. 3.18 for the two-component model and Langevin approximation, respectively. The associated statistics in the two firing regimes are depicted in Fig. 3.20.

Fig. 3.20A_1 and B_1, compares the stationary probability densities $P_0(c_\mathrm{i})$ obtained from stochastic simulations of the two-component model (histograms) with the corresponding theoretical predictions according to Eq. 3.3.32 (red line). The two show excellent agreement in the mean-driven regime and good agreement in the excitable regime. In the mean-driven regime, the probability density is close to uniform (Fig. 3.20A_1). This distribution arises from the minimal variation exhibited by the drift term $f(c_\mathrm{i})$ as a function of c_i (cf. Fig. 3.18A_2). Conversely, in the excitable regime, the deterministic drift term has a zero at the fixed point of the corresponding deterministic system c_i^* (cf. Fig. 3.18B_2). Consequently, the system spends more time near this fixed point, leading to a pronounced maximum in the probability density (Fig. 3.20B_1). However, the maximum does not align with the fixed point due to the interplay between the multiplicative noise and the nonlinear drift term in the model. It is also interesting to note that the theoretical prediction poorly describes the density near the reset in the excitable regime. This has to do with the finite correlation time of the noise. In the excitable regime, spikes are noise-induced, i.e., the drift $f(c_T) < 0$ is negative at the threshold, and the noise must take a positive value exceeding the negative drift to trigger a spike. Since the noise of the puff current has a small but finite correlation time, and the reset is instantaneous, the noise is more likely to take positive values for some time after the reset. As a result, the Ca^{2+} concentration quickly moves away from the reset point after the spike. This is not the case in the white noise approximation, where all memory is erased after the reset.

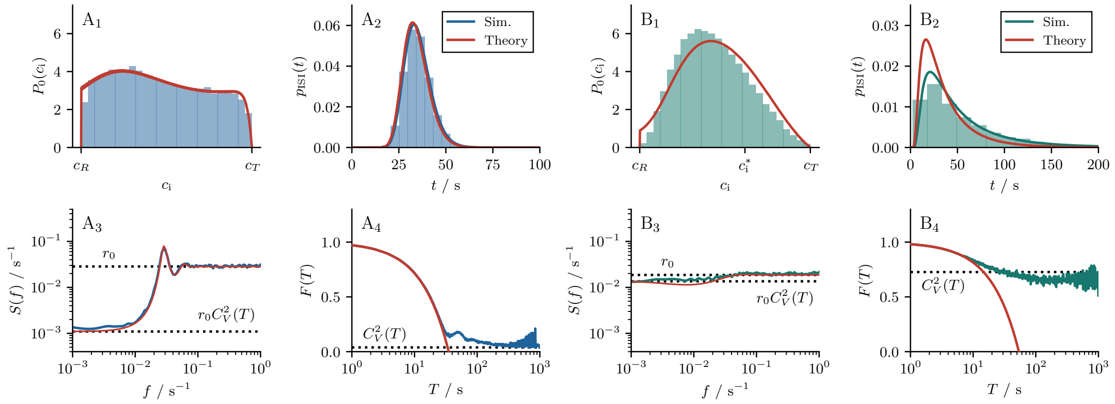

FIGURE 3.20: Spiking statistics of the two-component model. Panels A and B show the model in the mean-driven and excitable firing regimes. Panels A$_1$ and B$_1$ show the stationary probability density $P_0(c_i)$ obtained from stochastic simulations (histogram) and according to Eq. 3.4.24 (red line). The density shows a weak dependence on c_i in the mean-driven regime and has a pronounced peak below c_i^* in the excitable regime. Panel A$_2$ and B$_2$ compare the ISI density $p_{ISI}(t)$ from stochastic simulations (histogram) with an inverse Gaussian distribution. Mean $\langle T\rangle$ and CV $C_V(T)$ are obtained either from simulations (blue/green line) or Eq. 3.4.34 and Eq. 3.4.36 (red line). Panels A$_3$ and B$_3$ show the spike train power spectrum $S(f)$ from simulations (blue/green lines) and calculated according to Eq. 3.4.40 and Eq. 3.4.41 (red line). The high-frequency limit $S(f \to \infty) = r_0$ and low-frequency limits $S(0) = r_0 C_V^2(T)$ are highlighted by dotted lines. Panels A$_4$ and B$_4$ show the Fano factor of the spike count $F(T)$. Red lines indicate the approximation $F(T) = 1 - T/\langle T\rangle$. The horizontal dotted line shows the large time-window limit $F(T \to \infty) = C_V^2(T)$. Parameters A$_1$-A$_4$: $\tau = 5$s, $p = 0.015$; B$_1$-B$_4$: $\tau = 1$s, $p = 0.06$.

Fig. 3.20A$_2$ and B$_2$ illustrate the obtained ISI density from stochastic simulations of the two-component model (histograms). In the mean-driven regime, the ISI distribution exhibits a distinct peak (Fig. 3.20A$_2$). The corresponding ISI sequence is rather regular with a moderate CV of $C_V(T) = 0.2$. In contrast to that, in the excitable regime, the ISI density displays a pronounced skewness (Fig. 3.20B$_2$), and the corresponding ISI sequence is highly irregular with a CV of $C_V(T) = 0.8$. In both cases, we compare the ISI density obtained from stochastic simulations to an inverse Gaussian distribution

$$p_{IG}(t) = \sqrt{\frac{\langle T\rangle}{2\pi C_V^2(T) t^3}} \exp\left(-\frac{(t - \langle T\rangle^2)}{2\langle T\rangle C_V^2(T)}\right), \tag{3.4.38}$$

that is fully characterized by the mean $\langle T\rangle$ and CV $C_V(T)$ of the ISI. In Fig. 3.20A$_2$ and B$_2$, the inverse Gaussian distribution is shown by solid lines, where the mean and the CV of the ISI were computed from stochastic simulations of the two-component model (blue/green line) and calculated according to Eq. 3.4.34 and Eq. 3.4.36 (red line). The agreement of the two solid lines is thus also an indication of the quality of the Langevin approximation. In the mean-driven regime (Fig. 3.20A$_2$), the two solid lines are barely distinguishable, while in the excitable regime, the two lines are separated (Fig. 3.20B$_2$). This is not too surprising, as we have previously mentioned that in the mean-driven regime, the timescale τ tends to be larger, and the permeability-like parameter p tends to be smaller compared to the excitable regime. As a result, both the assumed timescale separation between the leak and puff current and the assumed Gaussian distribution of the puff current are better satisfied in the mean-driven regime. The fact that an inverse Gaussian distribution can describe the ISI density may be surprising. In the mean-driven regime, this is because the drift function $f(c_i)$ shows minimal dependence on c_i. In this firing regime, the model is similar to a perfect IF model, where the drift function is constant, and the ISI density is known to follow an inverse Gaussian distribution [238, 249]. Surprisingly, even in the excitable regime, the inverse Gaussian provides a good approximation to the ISI density when the mean and CV are determined from the stochastic simulation of the two-component model, Based on the assumption that ISIs follow an inverse Gaussian distribution, we can also calculate the power spectrum $S(f)$ of the spike train $z(t)$, that we have defined in Eq. 1.3.8 and is repeated here

$$S(f) = \lim_{T\to\infty} \frac{\langle |\tilde{z}_T(f)|^2\rangle}{T}, \tag{3.4.39}$$

where $\tilde{z}_T(f)$ is the (one-sided) Fourier transform of the spike train. If the spike train forms a renewal point process, it is completely determined by the ISI density (a first-order statistic), and the power spectrum (a second-order statistic) can be related to the Fourier transform of the ISI density $\tilde{p}_{\mathrm{ISI}}(f)$ according to Eq. 1.3.21:

$$S_{\mathrm{renew}}(f) = \frac{1}{\langle T\rangle} \frac{1 - |\tilde{p}_{\mathrm{ISI}}(f)|^2}{|1 - \tilde{p}_{\mathrm{ISI}}(f)|^2}. \tag{3.4.40}$$

For the inverse Gaussian distribution, the Fourier transform is known:

$$\tilde{p}_{\mathrm{IG}}(f) = \exp\left(\frac{1 - \sqrt{1 - 4\pi i f \langle T\rangle C_V^2(T)}}{C_V^2(T)}\right). \tag{3.4.41}$$

In Fig. 3.20A$_3$ and B$_3$, we compare the power spectrum calculated directly from the spike train of the two-component model using Eq. 3.4.39 (blue/green lines), with the power spectrum of an inverse Gaussian ISI distribution calculated according to Eq. 3.4.40 and Eq. 3.4.41 (red lines). The more regular spiking pattern in the mean-driven regime is evident by a peak in the power spectrum at the firing rate $f = r_0$. In the excitable regime, the spectrum appears relatively flat, closely resembling the power spectrum of a Poisson process (which would be constant). In both cases, the power spectrum of the spike train saturates at the firing rate r_0 for large values of f and approaches $r_0 C_V^2(T)$ for $f = 0$.

An interesting statistic of the spike *count* is the Fano factor that we have introduced in Eq. 1.3.10 and repeat here:

$$F(T) = \frac{\langle \Delta N(T)^2\rangle}{\langle N(T)\rangle}. \tag{3.4.42}$$

This measure compares the variance to the mean of the spike count $N(T)$ and is shown in Fig. 3.20A$_4$ and B$_4$ as a function of the counting window T. For small time windows T much smaller than the mean ISI, finding a spike in that window is essentially a Poisson process so that $\lim_{T\to 0} F(t) = 1$. We have shown previously (cf. Eq. 1.3.11) that for intermediate times, the Fano factor decreases linearly according to [66]

$$F(T) = 1 - T/\langle T\rangle \tag{3.4.43}$$

up to a characteristic time, which is roughly given by the mean ISI (red line in Fig. 3.20A$_4$ and B$_4$). For large values of T, the Fano factor saturates at the squared CV $\lim_{t\to\infty} F(t) = C_V^2(T)$ (dotted line) according to Eq. 1.3.12, which is confirmed by stochastic simulations. Finally, in Fig. 3.21A and B, we present the firing rate $r_0 = 1/\langle T\rangle$ as a function of the relative IP$_3$ concentration q. The arrow indicates the value of $q = 1$ used thus far. Each circle corresponds to a stochastic simulation of the two-component model and is color-coded based on the corresponding $C_V(T)$ obtained from the same simulation. The theoretical prediction of the firing rate, given by Eq. 3.4.25, exhibits excellent agreement with the simulation results in the mean-driven regime (Fig. 3.21A) and displays minor deviations in the excitable regime (Fig. 3.21B).

Extending our analysis beyond the two parameter sets examined previously, we revisit Fig. 3.19A and B, which show the mean and CV of the ISI obtained from stochastic simulations of the two-component model. In this analysis, we vary the two parameters, τ and p, over two orders of magnitude. As expected, the mean ISI (Fig. 3.19A) consistently decreases with an increase in the permeability-like parameter p, which is due to a corresponding increase in the mean $\mu(c_{\mathrm{i}})$ and the noise intensity $D(c_{\mathrm{i}})$ of the puff current. A similar behavior is observed when the timescale of the leak current, τ, is increased. The bifurcation line between excitable and mean-driven regimes

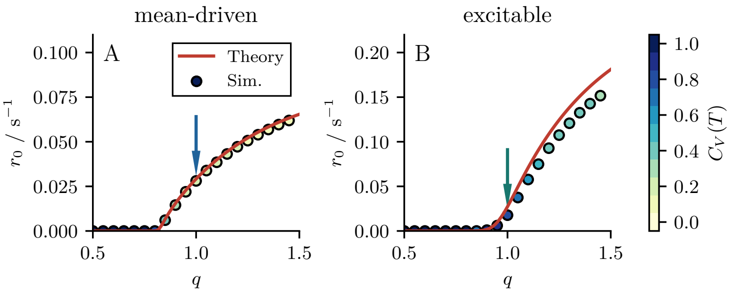

FIGURE 3.21: Firing rate of the two-component model. Panel A and B show the firing rate r_0 as a function of the relative IP$_3$ concentration q in the mean-driven and excitable regime, respectively. Arrows indicate the IP$_3$ concentration $q = 1$ that was used thus far. The firing rate determined by stochastic simulations (circles) is compared to the theoretical prediction according to Eq. 3.4.25 (red line). In addition, circles are color-coded to indicate the CV obtained from stochastic simulations. Parameters A: $\tau = 5$s, $p = 0.015$; B: $\tau = 1$s, $p = 0.06$.

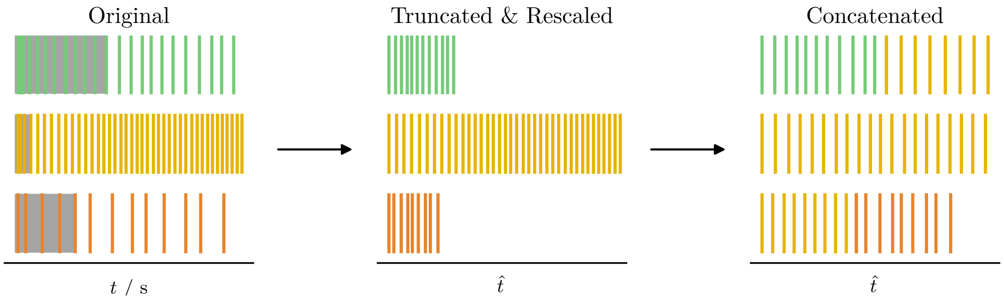

FIGURE 3.22: Illustration of the preprocessing of experimental spike trains from different stimulated HEK cells. The left panel shows exemplary spike trains from three different cells. The gray area shows the intervals that belong to the transient and are truncated. The middle panel shows the remaining spike times, where the time $\hat{t} = t/\langle T\rangle$ for each cell has been rescaled with respect to the mean ISI $\langle T\rangle$ of the remaining intervals. The right panel shows the concatenated spike train. The color coding is for orientation only. The spike trains of different cells are no longer distinguished.

according to Eq. 3.4.16 is shown by a red line. Because the noise in our model stems exclusively from the activity of the IP$_3$R clusters, it is often rather weak. Consequently, the excitable regime extends only to a small part below the bifurcation line, and for a large part of the parameter space, no spiking is observed (white area). The CV (Fig. 3.19B) shows a more complicated dependence on the parameters. It is close to one in the excitable regime [100] and drops drastically as soon as we cross the bifurcation line by increasing p or τ. The CV saturates in the limit of large τ when the leak current becomes negligible. In contrast, for large p, the CV continues to increase. This is probably due to the increasing noise intensity combined with the leak current becoming less important for $p \to \infty$.

3.4.4 Stimulated HEK cells

To test the model, we ask to what extent the renewal model can reproduce experimentally observed ISI sequences. To this end, we compare ISI statistics measured in stimulated HEK cells (see [7, 8]) with those obtained from the two-component model when fitted to the experimental data. Specifically, these are the ISI density, the spike train power spectrum, and the spike count Fano factor.

Unfortunately, measuring ISI sequences long enough to determine these statistics with sufficient precision is difficult. To solve this problem, we rescale and concatenate experimentally measured ISI sequences to obtain a single long ISI sequence, as suggested by Skupin and Falcke [250]. The procedure is illustrated in Fig. 3.22. Specifically, the procedure is as follows: In the first step, those sequences are selected from the available data in which the intervals approach a stationary value. This is the case for 29 out of 36 sequences. In the second step, the number of transient

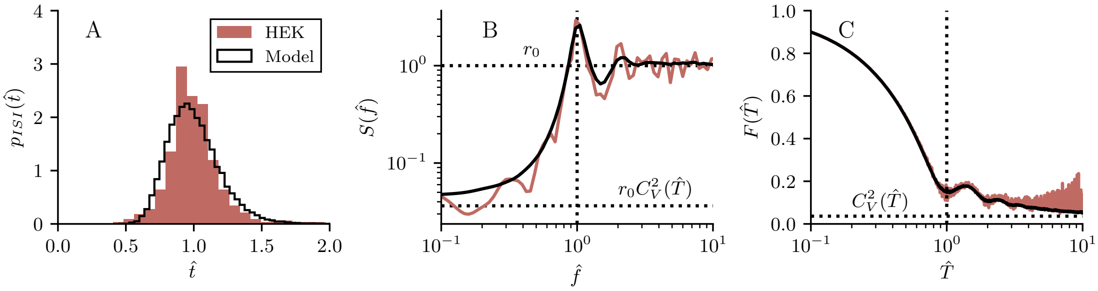

FIGURE 3.23: Comparison between ISI statistics of stimulated HEK cells and the two-component model. Spike trains from different cells were rescaled and combined as described in the main text. The resulting ISI sequence has a mean ISI $\langle T^{\mathrm{HEK}} \rangle \approx 155$s (before rescaling) and CV $C_V(T^{\mathrm{HEK}}) \approx 0.19$ (after rescaling). The model parameters $\tau = 11.1$ and $p = 0.006$ were chosen to reproduce the mean and CV. Panel A compares the ISI density $p_{\mathrm{ISI}}(\hat{t})$ as a function of rescaled time $\hat{t} = t/\langle T \rangle$. Panel B compares the power spectra $S(\hat{f})$ of the two ISI sequences where $\hat{f} = f\langle T \rangle$. Both spectra reach the low frequency limit $S(0) = r_0 C_V(\hat{T})$. Panel C shows the Fano factors $F(\hat{T})$ of the corresponding spike counts as a function of the rescaled time window $\hat{T} = T/\langle T \rangle$. Both the Fano factor of the experimental and simulated spike trains saturate at $C_V^2(\hat{T})$ for $\hat{T} \to \infty$ (horizontal dotted line).

intervals n_{tr} is determined by fitting the exponential function $T_\infty - (T_\infty - T_0)\exp(-i/n_{\mathrm{tr}})$ to the interval sequences. Three examples of stationary ISI sequences and the corresponding transient intervals are shown in the left panel of Fig. 3.22 in three different colors. In the third step, twice the number of transient intervals are truncated from the beginning of the sequence (grey area); on average, 9 out of 20 intervals. For the remaining intervals, the mean $\langle T \rangle$ is determined, and the time for each sequence is rescaled so that $\hat{t} = t/\langle T \rangle$. The rescaled sequences are shown in the middle panel of Fig. 3.22. Finally, we concatenate the truncated and rescaled sequences into one long ISI sequence that no longer discriminates between individual cells, as shown in the right panel of Fig. 3.22 (the color coding is for orientation only). From this concatenated sequence, we calculated the statistical measures of interest. We emphasize that rescaling the ISI sequences results in a mean ISI and firing rate equal to one. To determine the parameter set for the two-component model, we require that the ISI sequence of the model reproduce the mean and CV of the experimental data. Specifically, we require that the model reproduce the mean ISI of the data before rescaling $\langle T^{\mathrm{HEK}} \rangle \approx 155$s (before introducing $\hat{t} = t/\langle T \rangle$) and the CV of the data after rescaling $C_V(T^{\mathrm{HEK}}) \approx 0.19$. Given the large number of parameters in our model, we set the cluster parameters according to Table 3.3 and the number of clusters, resting Ca^{2+} concentration and threshold Ca^{2+} concentrations according to Table 3.3 as usual. To determine the remaining two parameters, we use the Nelder-Mead method [251] to minimize the loss function $f(x_1, x_2) = \sum_i |x_i - y_i|/x_i$, where $x_i \in [\langle T^{\mathrm{HEK}} \rangle, C_V(T^{\mathrm{HEK}})]$ are the target statistics obtained from the experimental data as described above, and $y_i \in [\langle T \rangle, C_V(T)]$ are the same output statistics of the model. The resulting values for the two parameters are $\tau = 11.1$ and $p = 0.006$. (We note that these values are very close to the bifurcation line, in fact, for the set of standard parameters according to Table 3.3 and Table 3.4 and for $\tau = 11.1$ the critical value for the permeability type parameter is $p^* = 0.0058$.)

In Fig. 3.23A, the ISI density $p_{\mathrm{ISI}}(\hat{t})$ of the concatenated ISI sequence obtained from stimulated HEK cells (red histogram) is compared to the rescaled ISI distribution obtained from stochastic simulations of the two-component model (black line). Given the limited amount and temporal precision of the experimental data (5s), the two densities are in good agreement, although the experimental density is slightly more peaked. Fig. 3.23B shows the power spectrum $S(\hat{f})$ of the experimental spike train (red line) and compares it to the power spectrum of the model (black line). The two spectra show excellent agreement with respect to the low-frequency limit, the height of the peak at $\hat{f} = 1$ ($f = 1/\langle T \rangle$), and the high-frequency limit. The agreement observed in the high-frequency limit is expected since the power spectrum always saturates at the firing rate $S(\hat{f} \to \infty) = r_0$. The low-frequency limit of the power spectrum is of particular interest because it is directly related to the stationary firing rate and the CV of the ISIs when the spike train is renewal:

$$S_{\mathrm{renew}}(0) = r_0 C_V^2(T). \tag{3.4.44}$$

We have pointed out previously that for a nonrenewable spike train, the sum of the correlation coefficients ρ_k is also included in the low-frequency limit:

$$S_{\text{nonrenew}}(0) = r_0 C_V^2(T) \left(1 + 2\sum_k \rho_k\right). \tag{3.4.45}$$

Therefore, the fact that the power spectrum saturates at $r_0 C_V^2(T)$ indicates that the concatenated spike train is renewal. In Fig. 3.23C, we compare the Fano factors of the experimental spike count (red line) and the simulated spike count (black line) and find good agreement. Again, the Fano factor saturates at the renewal limit $F(\hat{T} \to \infty) = C_V^2(T)$ for large time windows $\hat{T}$, indicating that the concatenated spike train is renewal to a good approximation.

The fact that the spike train appears to form a renewal point process and that the ISIs are uncorrelated is somewhat surprising since the experimental sequences of the ISIs often show long transients during which a strong cumulative refractory period builds up over many spike times (cf. Fig. 3.13C). Usually, such transients are attributed to a slow process that also correlates intervals and gives rise to a nonvanishing correlation coefficient $\rho_k \neq 0$. According to Skupin and Falcke [252] have shown that stimulated HEK cells do not exhibit statistically significant interval correlations. This paradox of a strong cumulative refractory period without significant interval correlations is addressed in Sec. 3.5.

3.4.5 Extension: Fast Ca^{2+} buffers

An important aspect of Ca^{2+} signaling that we have not considered so far is the presence of Ca^{2+} buffer proteins that can bind a significant portion (up to 99%) of the free Ca^{2+} both in the cytosol and ER [253, 254]. Here, we extend our model to account for an additional *fast* Ca^{2+} buffer in the cytosol and discuss the effect on the mean and CV of the ISI. The reaction scheme for a general Ca^{2+} buffer is as follows

$$\text{Ca}^{2+} + \text{B} \underset{k^-}{\overset{k^+}{\rightleftharpoons}} \text{CaB}, \tag{3.4.46}$$

where k^+ and k^- are rate constants for the binding and unbinding processes, respectively. Since we consider a fast Ca^{2+} buffer, these rates are chosen to be large compared to the rate of change of the cytosolic Ca^{2+} concentration. In terms of the differential equation governing the dynamics of the cytosolic Ca^{2+} concentration, a fast Ca^{2+} buffer can be described by a second differential equation describing the portion of the Ca^{2+} concentration currently bound to the buffer as follows (cf. Sec. 3.2.2):

$$\begin{aligned} \dot{c}_\text{i} &= -(c_\text{i} - c_0^*)/\tau + j_\text{puff}(c_\text{i}) - k^+ c_\text{i}(b_T - c_b) + k^- c_b, \\ \dot{c}_b &= k^+ c_\text{i}(b_T - c_b) - k^- c_b, \\ &\text{if } c_\text{i}(t) = c_T \to t_i = t \text{ and } c_\text{i}(t) = c_R, c_b(t) = c_b^*(c_R), \end{aligned} \tag{3.4.47}$$

where c_b is the portion of the cytosolic Ca^{2+} concentration bound to the buffer. A second equation for the free buffer concentration b does not need to be formulated because we assume that the total buffer concentration is a constant $b_T = b + c_b$. Note that because of the one-to-one binding, the bound Ca^{2+} concentration equals the bound buffer concentration $c_b = b_c$. Returning to Eq. 3.4.47, the first term in the second line describes the binding of a Ca^{2+} ion to a buffer protein, proportional to the rate constant k^+, the free Ca^{2+} concentration c_i and the free buffer concentration $b = b_T - c_b$. In contrast, the second term described the unbinding, proportional to the rate constant k^- and the buffered Ca^{2+} concentration c_b. In an IF model, a fast buffer requires an additional reset rule to ensure that even after the infinitely fast reset of c_i, the bound buffer concentration c_b is still in equilibrium with the free cytosolic Ca^{2+} concentration. This additional reset rule is given in the last line of Eq. 3.4.47 and states that c_b is reset to its equilibrium value $c_b^*(c_R)$ when a spike is triggered. For such a simple binding scheme, the equilibrium value $c_b^*(c_\text{i})$ can be calculated analytically by considering the second line in Eq. 3.4.47 and requiring that the temporal derivative vanishes

$$0 = k^+ c_\text{i}(b_T - c_b^*) - k^- c_b^* \quad \Longrightarrow \quad c_b^*(c_\text{i}) = \frac{c_\text{i} b_T}{K + c_\text{i}}, \tag{3.4.48}$$

where we have introduced the dissociation constant $K = k^-/k^+$.

The extension of our model complicates the description by the FPE. There are two reasons for this. First, we are now dealing with a two-dimensional system, which makes the treatment of the corresponding FPE much more difficult, and second, it is not clear to what extent the white noise approximation describes the system well in the presence of a fast buffer. However, Wagner and Keizer [255] have shown that a fast buffer can be eliminated and affects the dynamics of c_i only by a (c_i-dependent) constant β according to

$$\dot{c}_\mathrm{i} = \beta[-(c_\mathrm{i} - c_0^*)/\tau + j_\mathrm{puff}(c_\mathrm{i})], \quad \text{with} \quad \beta = \left(1 + Kb_T/(K + c_\mathrm{i})^2\right)^{-1}. \tag{3.4.49}$$

Assuming that the c_i dependence of β is weak ($K \gg c_\mathrm{i}$), one might conclude that the constant factor β can be eliminated by introducing a new time $\hat{t} = \beta t$ that grows slower than t so that adding a fast buffer leads to a rescaling of time. This is only true in the deterministic limit but not when the fluctuations of the puff current are taken into account, which has to do with the fact that the rates of the Markov model are not rescaled accordingly. To see that the mean and the noise intensity are affected differently by a rescaling of time, we consider the Langevin approximation of Eq. 3.4.49 and substitute $t = \hat{t}/\beta$:

$$\frac{dc_\mathrm{i}}{d\hat{t}} = -(c_\mathrm{i} - c_0^*)/\tau + \mu(c_\mathrm{i}) + \sqrt{2\beta D(c_\mathrm{i})}\xi(\hat{t}), \tag{3.4.50}$$

where, when measured in the new time $\hat{t}$, the deterministic drift $f(c_\mathrm{i}) = -(c_\mathrm{i} - c_0^*)/\tau + \mu(c_\mathrm{i})$ is unaffected by the fast buffer, but the noise intensity is not. To obtain this equation, we used the scaling property of white noise $\xi(\hat{t}/\beta) = \sqrt{\beta}\xi(\hat{t})$[6]. The factor β is guaranteed to be less than 1, so an additional fast buffer will always slow down the dynamics. It should be emphasized that the dependence of the noise intensity on β is not a property of the Langevin approximation. It is just expressed particularly well there. This is illustrated in Fig. 3.24, where we compare the mean and CV of the ISIs obtained from stochastic simulations of the two-component model (circles) and the Langevin approximation (lines), both with an additional fast buffer according to Eq. 3.4.47.

We now return to the question of how a fast buffer affects the mean and CV of the ISI. In the mean-driven regime, the mean ISI is largely determined by the drift $f(c_\mathrm{i})$. Since the drift is independent of β, this implies that the mean ISI measured in units of $\hat{t}$ is also independent of β. Going back to the original time $t = \hat{t}/\beta$, the mean ISI scales linearly with $1/\beta$ as the time t itself

$$\langle T \rangle = \frac{\langle T_0 \rangle}{\beta} \approx \langle T_0 \rangle (1 + b_T/K), \tag{3.4.51}$$

where $\langle T_0 \rangle$ refers to the mean ISI without a buffer $b_T = 0$. According to Eq. 3.4.51, the mean ISI is a linear function of the total buffer concentration b_T. This is demonstrated in Fig. 3.24A$_1$ by means of stochastic simulations of the two-component model with an additional fast buffer according to Eq. 3.4.47 (circles). As expected, the stochastic simulations show a linear dependence of $\langle T \rangle$ on b_T in the mean-driven regime, with a slope slightly overestimated by the theory. This is because the c_i dependence has been neglected (cf. the factor β in Eq. 3.4.49) The effect of a fast buffer on the CV is more complicated. However, when the model is mean-driven, and the noise is not too strong, the variance of the ISI can be estimated according to Arecchi and Politi [257] by

$$\begin{aligned} \langle \Delta T^2 \rangle &= 2\beta \int_{c_0^*}^{c_T} dc_\mathrm{i}\, D(c_\mathrm{i})/f(c_\mathrm{i})^3 \\ &= \langle \Delta T_0^2 \rangle / \beta, \end{aligned} \tag{3.4.52}$$

where we have assumed that the factor β is independent of c_i and thus can be placed before the integral. The step from the first to the second line, i.e., from a β-dependency to a $1/\beta$-dependency, results from the rescaling of time similar to equation Eq. 3.4.51 (which adds another factor $1/\beta^2$ to the variance). Combining Eq. 3.4.51 and Eq. 3.4.52 allows us to determine the dependence of

---

[6] The scaling property of a white noise can be derived from the fact that the correlation function must be preserved, i.e., $2D\delta(t - t') = 2D^*\delta(\hat{t} - \hat{t}')$. Using the scaling property of the Dirac delta function $\delta((\hat{t} - \hat{t}')/\beta) = |\beta|\delta(\hat{t} - \hat{t}')$ allows to relate the two intensities $D^* = \beta D$ so that one finds $\sqrt{\beta}\xi(\hat{t}) = \xi(\hat{t}/\beta)$ [256].

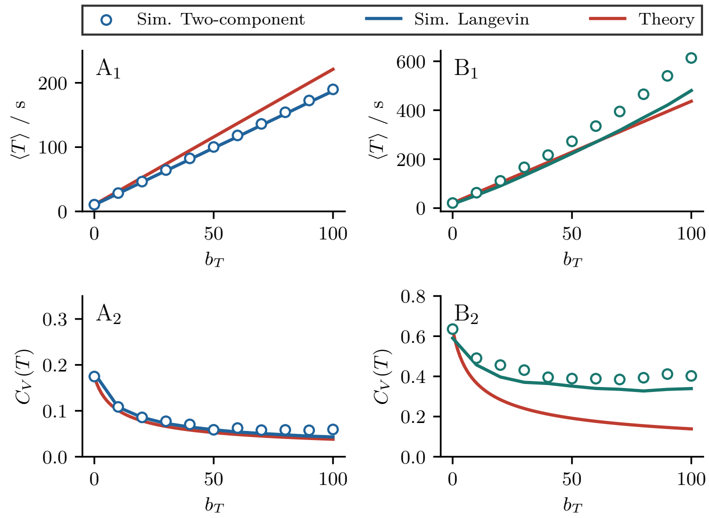

FIGURE 3.24: Spike-train statistics in the presence of a fast Ca^{2+} buffer. Panels A and B show spike-train statistics in the mean-driven and excitable regimes. Simulation results of the two-component model and the Langevin approximation are shown as blue/green circles and lines, respectively. Theoretical approximations according to Eq. 3.4.51 and Eq. 3.4.53 are shown by red lines. Panels A_1 and B_1 show the mean ISI $\langle T \rangle$ as a function of the total buffer concentration b_T. In the mean-driven (excitable) regime, the ISI scales linearly (superlinearly) with the total buffer concentration. Panels A_2 and B_2 show the CV $C_V(T)$. In the mean-driven regime, $C_V(T)$ exhibits a square root relationship with respect to the total buffer concentration b_T. In the excitable regime, $C_V(T)$ appears to saturate as b_T increases. Parameters: $k^+ = 10$, $k^- = 50$, A: $\tau = 5$s, $p = 0.025$; B: $\tau = 1$s, $p = 0.064$.

the CV on the total buffer concentration

$$C_V(T) = \frac{\sqrt{\langle \Delta T_0^2 \rangle / \beta}}{\langle T_0 \rangle / \beta} = \frac{C_V(T_0)}{\sqrt{1 + b_T/K}}, \tag{3.4.53}$$

where $C_V(T_0)$ refers again to the CV without a fast Ca^{2+} buffer $b_T = 0$. Eq. 3.4.53 is confirmed in Fig. 3.24A_2.

Finally, in Fig. 3.24B_1 and B_2, we consider the model in the excitable regime, where the spiking statistics depend strongly on the noise intensity and thus the buffer concentration. Specifically, in Fig. 3.24B_1, the ISI grows faster than linear with b_T. This is due to the fact that in the excitable regime, the jump from the deterministic fix point c_i^* to the threshold c_T is fluctuation driven. Adding a Ca^{2+} buffer (increasing b_T) reduces the noise intensity, which can lead to a superlinear increase in the mean interval in the excitable regime. Even more complicated is the dependence of the CV on the total buffer concentration in the excitable regime shown in Fig. 3.24B_2. After an initial decrease of the CV, we observe a minimal dependence of the CV on b_T; apparently, we are far from the weak-noise limit where the CV decreases with the noise intensity. This may indicate that we are dealing with an effect similar to coherence resonance [100].

3.5 Spiking statistics: nonrenewal model

We have seen in the previous section that the renewal model is analytically tractable and can reproduce certain stationary spiking statistics of stimulated HEK cells, such as ISI density, spike train power spectrum, and the Fano factor. However, many cell types exhibit an initial transient in response to the onset of a constant stimulation (cf. Fig. 3.13), during which the ISIs are not identically distributed but gradually increase until the stationary state is reached. Moreover, the intervals are not statistically independent but correlated in the stationary state. Neither the transient nor the interval correlations are described by the renewal model. In this section, we return to the full two-component model, describing the dynamics of Ca^{2+} concentration in the cytosol $c_i(t)$

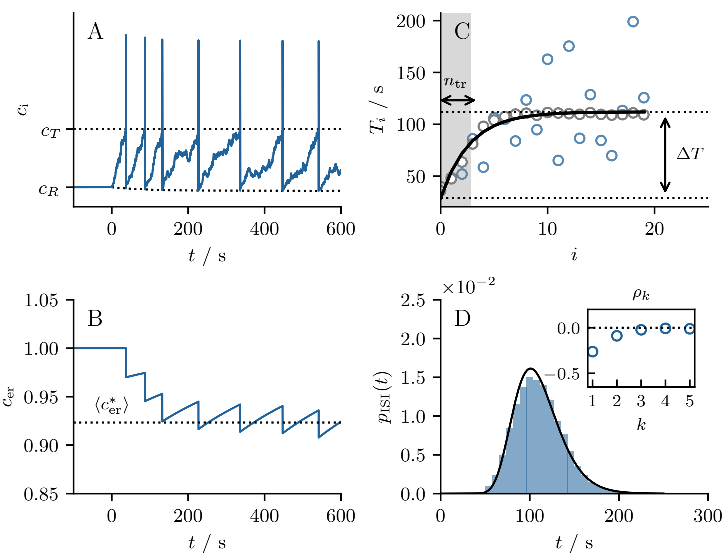

FIGURE 3.25: Spiking statistics of the nonrenewal model. Panel A and B show the time series of the Ca^{2+} concentration in the cytosol $c_{\mathrm{i}}(t)$ and the ER $c_{\mathrm{er}}(t)$ in response to a constant IP_3 stimulation $q = 1$ applied at $t = 0$. Dotted lines in A indicated the threshold c_T and reset $c_R = c_0^* c_{\mathrm{er}}(t_i^+)$. The dotted line B indicates the stationary mean value $\langle c^*_{\mathrm{er}} \rangle$. Panel C shows the stochastic sequence of ISIs $\{T_i\}$ by blue circles and the deterministic sequence of mean ISIs $\{\langle T_i \rangle\}$ by gray circles. The black line is a fit of Eq. 3.5.2 to the sequence of mean ISIs. The number of transient intervals n_{tr} and cumulative refractory period $\Delta T = T_\infty - T_0$ are highlighted by a horizontal and vertical arrow, respectively. Panel D depicts the stationary ISI density $p_{\mathrm{ISI}}(t)$ together with an inverse Gaussian distribution (black line). Parameters: $\tau = 5$s, $p = 0.015$, $\tau_{\mathrm{er}} = 300$s, $\varepsilon = 0.03$.

and Ca^{2+} concentration in the ER $c_{\mathrm{er}}(t)$. This model can account for the experimentally observed transient and some of the observed ISI correlations. We analyze how the cumulative depletion of the ER affects the statistics of the ISIs. This includes first-order stationary statistics, in particular the mean and CV of the ISI, and second-order stationary statistics, in particular the interval correlations. We then turn to a statistical description of the transient, characterized by its length and the strength of the adaptation of the ISI. We also discuss how, according to our model, the two transient statistics relate to the interval correlations and verify the relations using experimental interval sequences.

The nonrenewal version of the model is as follows:

$$\begin{aligned} \dot{c}_{\mathrm{i}} &= -(c_{\mathrm{i}} - c_0(c_{\mathrm{er}}))/\tau + j_{\mathrm{puff}}(c_{\mathrm{i}}, c_{\mathrm{er}}), \\ \dot{c}_{\mathrm{er}} &= -(c_{\mathrm{er}} - 1)/\tau_{\mathrm{er}} - \varepsilon c_{\mathrm{er}} \textstyle\sum_i \delta(t - t_i), \\ &\text{if } c_{\mathrm{i}}(t) = c_T \to t_i = t \text{ and } c_{\mathrm{i}}(t) = c_R. \end{aligned} \tag{3.5.1}$$

We have already discussed the characteristics of the model in Sec. 3.3.2 and repeat the main features here for convenience. In Fig. 3.25A and B, we show the cytosolic and ER Ca^{2+} concentrations $c_{\mathrm{i}}(t)$ and $c_{\mathrm{er}}(t)$ in response to a constant IP_3 stimulation applied at $t_0 = 0$. We emphasize again that prior to the stimulation ($t < t_0$) the concentrations are at $c_{\mathrm{i}}(t < t_0) = c_0^*$ and $c_{\mathrm{er}}(t < t_0) = 1$. That is, neither $c_{\mathrm{i}}(t)$ nor $c_{\mathrm{er}}(t)$ are affected by any noise because the IP_3 receptors - the only noise source in our model - are inactivated before the stimulation. Upon stimulation, when the IP_3Rs are activated, Ca^{2+} is released from the ER into the cytosol, and $c_{\mathrm{i}}(t)$ begins to rise toward the threshold. When the threshold is reached, and a spike is fired, $c_{\mathrm{er}}(t)$ is immediately decreased by $\varepsilon c_{\mathrm{er}}(t_i^-)$ and $c_{\mathrm{i}}(t)$ is reset to $c_0^* c_{\mathrm{er}}(t_i^+)$. After the spike, $c_{\mathrm{i}}(t)$ rises again, and $c_{\mathrm{er}}(t)$ is slowly replenished. During the transient, the depletion during a spike is, on average, larger than the replenishment between two spikes, resulting in a cumulative decrease in $c_{\mathrm{er}}(t)$ that builds up over several spike times (see Fig. 3.25B). Since the ER Ca^{2+} concentration affects the puff current and the reset value, the cumulative decrease also results in a transient in the sequence of ISIs that spans several spikes. This is illustrated in Fig. 3.25C where we show the stochastic ISI sequence

$\{T_i\}$ by blue circles and the deterministic sequence of mean intervals $\{\langle T_i\rangle\}$ by gray circles. During the transient, the statistics of the ISI depend on the index i. To characterize the transient, we introduce the fit function

$$T_\infty - (T_\infty - T_0)e^{-i/n_{\text{tr}}}, \tag{3.5.2}$$

with the number of transient intervals n_{tr} and the cumulative refractory period $\Delta T = T_\infty - T_0$. The black line in Fig. 3.25C shows a fit of Eq. 3.5.2 to the sequence of mean intervals. Note that we have used this fit function earlier to truncate the transient intervals from the sequence of ISIs obtained from stimulated HEK cells. After the transient, when the stationary state is reached, the ISI statistics are independent of i. In this case, all ISIs follow the same probability density $p_{\text{ISI}}(t)$ shown in Fig. 3.25D and are still well described by an inverse Gaussian distribution (black line). However, even in the stationary state, where the intervals are identically distributed, they are not statistically independent but weakly correlated (inset Fig. 3.25D). This is so because the statistics of a given interval T_{i+1} depends on the value $c_{\text{er}}(t_i^+)$ taken at the beginning of that interval. At the same time, $c_{\text{er}}(t_i^+)$ depends on the previous interval T_i, so that the interval T_{i+1} depends on T_i through the ER Ca^{2+} concentration $c_{\text{er}}(t_i^+)$.

Fokker-Planck equation

We start again by formulating the Langevin approximation corresponding to Eq. 3.5.1. In Sec. 3.4, we showed that when the Ca^{2+} concentration in the ER is fixed ($c_{\text{er}} = \text{const}$), the stochastic puff current $j_{\text{puff}}(c_{\text{i}})$ can be approximated by a Gaussian white noise with c_{i}-dependent mean $\mu(c_{\text{i}})$ and intensity $D(c_{\text{i}})$.

This approximation assumes that the number of open channels in a cluster $x(t)$ changes rapidly. More precisely, the correlation time of the random process $X(t) = \sum x_k(t)$ is assumed to be small compared to any other timescale in the system. This is still the case if we additionally consider the dynamics of the Ca^{2+} concentration in the ER, which we assume to mediate the adaptation of the ISIs. Therefore, the corresponding timescale τ_{er} must be chosen to be of the order of the stationary interval to observe an adaptation effect and is thus larger than τ and much larger than the correlation time of $X(t)$. Eq. 3.5.1 can then still be approximated by the Langevin equation:

$$\begin{aligned} \dot{c}_{\text{i}} &= -(c_{\text{i}} - c_0(c_{\text{er}}))/\tau + \mu(c_{\text{i}}, c_{\text{er}}) + \sqrt{2D(c_{\text{i}}, c_{\text{er}})}\xi(t), \\ \dot{c}_{\text{er}} &= -(c_{\text{er}} - 1)/\tau_{\text{er}} - \varepsilon c_{\text{er}} \textstyle\sum_i (t - t_i), \\ &\text{if } c_{\text{i}}(t) = c_T \to t_i = t \text{ and } c_{\text{i}}(t) = c_R, \end{aligned} \tag{3.5.3}$$

where the mean $\mu(c_{\text{i}}, c_{\text{er}}) = pc_{\text{er}}K\mu_x(c_{\text{i}})$ and the noise intensity $D(c_{\text{i}}, c_{\text{er}}) = (pc_{\text{er}})^2 KD_x(c_{\text{i}})$ of the puff current do not only depend on $c_{\text{i}}(t)$, but also on $c_{\text{er}}(t)$. The mean $\mu_x(c_{\text{i}})$ and the noise intensity $D_x(c_{\text{i}})$ of a single cluster still depend solely on $c_{\text{i}}(t)$ through the c_{i} dependence of the opening rate.

Eq. 3.5.3 possesses a corresponding two-dimensional FPE

$$\partial_t P(c_{\text{i}}, c_{\text{er}}, t) = \mathcal{L}P(c_{\text{i}}, c_{\text{er}}, t) + J_{\text{i}}(c_T, c_{\text{er}}/(1-\varepsilon), t)\delta(c_{\text{i}} - c_R) \tag{3.5.4}$$

with the Fokker-Planck operator

$$\mathcal{L} = -\partial_{c_{\text{i}}}[f(c_{\text{i}}, c_{\text{er}}) + D'(c_{\text{i}}, c_{\text{er}})/2 - \partial_{c_{\text{i}}} D(c_{\text{i}}, c_{\text{er}})] - \partial_{c_{\text{er}}} g(c_{\text{er}}) \tag{3.5.5}$$

and the two drift functions

$$\begin{aligned} f(c_{\text{i}}, c_{\text{er}}) &= -(c_{\text{i}} - c_0(c_{\text{er}}))/\tau + \mu(c_{\text{i}}, c_{\text{er}}), \\ g(c_{\text{er}}) &= -(c_{\text{er}} - 1)/\tau_{\text{er}}, \end{aligned} \tag{3.5.6}$$

as well as the Stratonovich drift $D'(c_{\text{i}}, c_{\text{er}})/2$. Again, the reset rule of the IF model in Eq. 3.5.3 finds its counterpart in the source term in Eq. 3.5.4, which is proportional to the probability current in the c_{i}-direction $J_i(c_{\text{i}}, t)$ across the firing threshold:

$$J_{\text{i}}(c_T, c_{\text{er}}, t) = -\partial_{c_{\text{i}}} D(c_{\text{i}}, c_{\text{er}}) P(c_{\text{i}}, c_{\text{er}}, t)\big|_{c_i = c_T}. \tag{3.5.7}$$

The factor $1/(1-\varepsilon)$ appearing in the source term in Eq. 3.5.4 reflects that a trajectory crossing the threshold at $(c_T, c_{\mathrm{er}}/(1-\varepsilon))$ is reset to (c_R, c_{er}). In terms of the probability density, this means that the change in the probability density at (c_R, c_{er}) is proportional to the probability current $J_{\mathrm{i}}(c_{\mathrm{i}}, c_{\mathrm{er}})$ at $(c_T, c_{\mathrm{er}}/(1-\varepsilon))$. Finally, the FPE is completed by the natural boundary condition, the absorbing boundary condition, and the normalization condition

$$\lim_{c_{\mathrm{i}}\to-\infty} P(c_{\mathrm{i}}, c_{\mathrm{er}}, t) = 0, \qquad P(c_{\mathrm{i}} = c_T, c_{\mathrm{er}}, t) = 0, \qquad \int_{-\infty}^{c_T} dc_{\mathrm{i}} \int_{-\infty}^{\infty} dc_{\mathrm{er}}\, P(c_{\mathrm{i}}, c_{\mathrm{er}}, t) = 1, \tag{3.5.8}$$

as well as the two reflecting boundary conditions

$$J_{\mathrm{er}}(c_{\mathrm{i}}, c_{\mathrm{er}} = 0, t) = J_{\mathrm{er}}(c_{\mathrm{i}}, c_{\mathrm{er}} = 1, t) = 0, \tag{3.5.9}$$

where $J_{\mathrm{er}}(c_{\mathrm{i}}, c_{\mathrm{er}})$ refers to the probability current in the c_{er}-direction. For the two-dimensional FPE, the firing rate $r(t)$ is given by the probability current across the threshold *line*:

$$r(t) = \int_0^1 dc_{\mathrm{er}}\, J_{\mathrm{i}}(c_T, c_{\mathrm{er}}, t). \tag{3.5.10}$$

Evaluating this integral is already demanding, not to mention higher moments or higher-order statistics. This is because it requires the solution of Eq. 3.5.4, a two-dimensional partial differential equation, which is a severe problem even numerically. In the following, we will therefore use approximation methods. For a detailed study of the two-dimensional FPE of IF models, see [131].

3.5.1 Stationary first-order interspike interval statistics

Here, we focus on first-order stationary interval statistics. That is, we assume that the onset of the stimulation of the model cell occurred in the distant past, and the interval statistics are independent of the absolute time that has elapsed since then. Moreover, we consider first-order statistics, which can be calculated from the ISI density $p_{\mathrm{ISI}}(t)$. Interval correlations are thus excluded here. As we have mentioned earlier, a renewal process with statistically independent intervals is completely determined by this density [46, 65].

Self-consistent firing rate

We begin by calculating the stationary firing rate r_0. To this end, we assume that the Ca^{2+} concentration in the ER can be approximated by its stationary mean value $\lim_{t\to\infty}\langle c_{\mathrm{er}}(t)\rangle = \langle c_{\mathrm{er}}^*\rangle$ (cf. Fig. 3.25B). Note that this assumption excludes the possibility of calculating higher-order statistics, which are mediated by the (time-dependent) values $c_{\mathrm{er}}(t_i)$. In other words, when $c_{\mathrm{er}}(t)$ is replaced by its stationary mean $\langle c_{\mathrm{er}}^*\rangle$, the intervals become statistically independent and identically distributed. This approach allows to derive *two* equations that must be solved simultaneously (self-consistently) to obtain the firing rate. The first equation is derived from the first line of Eq. 3.5.3. Assuming $c_{\mathrm{er}}(t) \approx \langle c_{\mathrm{er}}^*\rangle$, the system can be described by a one-dimensional FPE. The calculation of the firing rate is then analogous to the calculation in Sec. 3.4 but requires the knowledge of $\langle c_{\mathrm{er}}^*\rangle$. The second equation is obtained by averaging the second line of Eq. 3.5.3 and considering the limit $t\to\infty$.

The first expression is obtained by substituting $c_{\mathrm{er}}(t) \approx \langle c_{\mathrm{er}}^*\rangle$ in Eq. 3.5.3 and formulating the corresponding one-dimensional FPE

$$\frac{\partial}{\partial t} P(c_{\mathrm{i}}, t) = -\frac{\partial}{\partial c_{\mathrm{i}}}\left[f(c_{\mathrm{i}}; \langle c_{\mathrm{er}}^*\rangle) - D'(c_{\mathrm{i}}; \langle c_{\mathrm{er}}^*\rangle)/2 + \frac{\partial}{\partial c_{\mathrm{i}}} D(c_{\mathrm{i}}; \langle c_{\mathrm{er}}^*\rangle)\right] P(c_{\mathrm{i}}, t) + r(t)\delta(c_{\mathrm{i}} - c_R), \tag{3.5.11}$$

where the functions $f(c_{\mathrm{i}}; \langle c_{\mathrm{er}}^*\rangle)$, $D(c_{\mathrm{i}}; \langle c_{\mathrm{er}}^*\rangle)$, $D'(c_{\mathrm{i}}; \langle c_{\mathrm{er}}^*\rangle)$, and the reset point $c_R = c_0^*\langle c_{\mathrm{er}}^*\rangle$ depend parametrically on $\langle c_{\mathrm{er}}^*\rangle$. As we have already shown in Sec. 3.4.2, Eq. 3.5.11 can be used to calculate the firing rate according to

$$r_0(\tau, p, \langle c_{\mathrm{er}}^*\rangle) = \left(\int_{c_R}^{c_T} dx_2\, e^{-h(x_2; \langle c_{\mathrm{er}}^*\rangle)} \int_{-\infty}^{x_2} dx_1\, \frac{e^{h(x_1; \langle c_{\mathrm{er}}^*\rangle)}}{D(x_1; \langle c_{\mathrm{er}}^*\rangle)}\right)^{-1} \tag{3.5.12}$$

with

$$h(x) = \int_{c_R}^{x} dy \, \frac{g(y; \langle c_{\text{er}}^* \rangle)}{D(y; \langle c_{\text{er}}^* \rangle)} \tag{3.5.13}$$

as a function of the two parameters τ and p, but also as a function of the stationary mean $\langle c_{\text{er}}^* \rangle$. The expression cannot be evaluated because $\langle c_{\text{er}}^* \rangle$ is unknown. The second expression is obtained by considering the stationary average of the second line in Eq. 3.5.3:

$$0 = -(\langle c_{\text{er}}^* \rangle - 1)/\tau_{\text{er}} - \varepsilon \langle c_{\text{er}} \textstyle\sum_i (t - t_i) \rangle. \tag{3.5.14}$$

This equation involves two different mean values. First, the unconditional stationary mean $\langle c_{\text{er}}^* \rangle$, which appears in the first term, and second, the conditional mean, which appears in the second term. To see this, we write the average as an integral over a large time window

$$\begin{aligned} \langle c_{\text{er}} \textstyle\sum_i (t - t_i) \rangle &= \lim_{T \to \infty} \frac{1}{T} \int_0^T c_{\text{er}}(t) \sum_i \delta(t - t_i) \\ &= \lim_{T \to \infty} \frac{1}{T} \sum_{t_i \in [0,T]} c_{\text{er}}(t_i^-) \\ &= \lim_{T \to \infty} \frac{N(T)}{T} \langle c_{\text{er}}^* | t = t_i^- \rangle \\ &= r_0 \langle c_{\text{er}}^* | t = t_i^- \rangle, \end{aligned} \tag{3.5.15}$$

where $\langle c_{\text{er}}^* | t = t_i^- \rangle$ is the stationary mean of $c_{\text{er}}(t)$ right before a spike. Put differently, taking the average of $c_{\text{er}}(t)$ along with the spike train $z(t)$ introduces a sampling bias such that only those values of $c_{\text{er}}(t)$ are considered for which the time t was a spike time. It should be clear that this conditional mean is always larger than the unconditional mean $\langle c_{\text{er}}^* | t = t_i^- \rangle > \langle c_{\text{er}}^* \rangle$ because $c_{\text{er}}(t)$ takes its maximum value over a given ISI right before the spike at t_i^-. Substituting Eq. 3.5.15 into Eq. 3.5.14 yields

$$0 = -(\langle c_{\text{er}}^* \rangle - 1)/\tau_{\text{er}} - \varepsilon r_0 \langle c_{\text{er}}^* | t = t_i^- \rangle. \tag{3.5.16}$$

An expression that has brought us closer to finding a relation between the stationary firing rate r_0 and the stationary mean $\langle c_{\text{er}}^* \rangle$, but at the same time raises a new problem, since it is not clear how the unconditional and the conditional mean are related.

Intermezzo: The averages of the ER Ca^{2+} concentration

Before we continue to calculate the firing rate, we derive relations between the different mean values $\langle c_{\text{er}}^* \rangle$, $\langle c_{\text{er}}^* | t = t_i^- \rangle$, and $\langle c_{\text{er}}^* | t = t_i^+ \rangle$. To this end, note that between two spike times $t_i \leq t < t_{i+1}$, the governing differential equation for the ER Ca^{2+} concentration reduces to

$$\dot{c}_{\text{er}} = -(c_{\text{er}} - 1)/\tau_{\text{er}}, \tag{3.5.17}$$

which can be solved by

$$c_{\text{er}}(t) = 1 - [1 - c_{\text{er}}(t_i^+)] e^{-(t - t_i)/\tau_{\text{er}}} \quad \text{with} \quad t_i \leq t < t_{i+1}, \tag{3.5.18}$$

where $c_{\text{er}}(t_i^+)$ is the value taken immediately after the spike. This value is the initial condition for the next interval T_i. The final value $c_{\text{er}}(t_{i+1}^-)$, taken at the end of the interval, is also known. This somewhat trivial observation allows to establish less trivial relation between the two conditional means

$$\langle c_{\text{er}} | t = t_{i+1}^- \rangle = 1 - \langle [1 - c_{\text{er}}(t_i^+)] e^{-T_i/\tau_{\text{er}}} \rangle, \tag{3.5.19}$$

where we have substituted $T_i = t_{i+1} - t_i$. Note that on the r.h.s. of Eq. 3.5.19, we take the average over two correlated quantities, namely the value $c_{\text{er}}(t_i^+)$ taken at the beginning of the interval T_i, and precisely that interval. A second relation between the mean values can be derived using that exactly at a spike time $c_{\mathrm{er}}(t)$ is decreased by $\varepsilon c_{\mathrm{er}}(t_i^-)$, which allows to relate the values of c_{er} taken right before and right after a spike by

$$c_{\mathrm{er}}(t_i^+) = c_{\mathrm{er}}(t_i^-)(1-\varepsilon). \tag{3.5.20}$$

This equation can again be averaged to obtain

$$\langle c_{\mathrm{er}}(t)|t=t_i^+\rangle = \langle c_{\mathrm{er}}(t)|t=t_i^-\rangle(1-\varepsilon). \tag{3.5.21}$$

In the stationary case, the means do not depend on absolute time, and Eq. 3.5.19 and 3.5.21 become

$$\begin{aligned} \langle c_{\mathrm{er}}^*|t=t_i^-\rangle &= 1-\langle[1-c_{\mathrm{er}}(t_i^+)]e^{-T_i/\tau_{\mathrm{er}}}\rangle, && (3.5.22)\\ \langle c_{\mathrm{er}}^*|t=t_i^+\rangle &= \langle c_{\mathrm{er}}^*|t=t_i^-\rangle(1-\varepsilon). && (3.5.23) \end{aligned}$$

To link the two conditional means with the unconditional mean, we express the latter as integral over a large time window

$$\langle c_{\mathrm{er}}^*\rangle = \lim_{T\to\infty}\int_0^T dt\, c_{\mathrm{er}}(t) \tag{3.5.24}$$

and split the integral at the spike times where $c_{\mathrm{er}}(t)$ takes the values $c_{\mathrm{er}}(t_i^+)$

$$\begin{aligned} \langle c_{\mathrm{er}}^*\rangle &= \lim_{T\to\infty}\frac{1}{T}\sum_{t_i+T_i\in[0,T]}\int_0^{T_i} dt\, 1-[1-c_{\mathrm{er}}(t_i^+)]e^{-(t-t_i)/\tau_{\mathrm{er}}}\\ &= \lim_{T\to\infty}\frac{1}{T}\sum_{t_i+T_i\in[0,T]} T_i-\tau_{\mathrm{er}}[1-c_{\mathrm{er}}(t_i^+)][1-e^{-T_i/\tau_{\mathrm{er}}}]\\ &= 1-\frac{\tau_{\mathrm{er}}}{\langle T\rangle}\left([1-\langle c_{\mathrm{er}}^*|t=t_i^+\rangle]-\langle[1-c_{\mathrm{er}}(t_i^+)]e^{-T_i/\tau_{\mathrm{er}}}\rangle\right)\\ &= 1-\frac{\tau_{\mathrm{er}}}{\langle T\rangle}\left(\langle c_{\mathrm{er}}^*|t=t_i^-\rangle-\langle c_{\mathrm{er}}^*|t=t_i^+\rangle\right)\\ &= 1-\varepsilon\frac{\tau_{\mathrm{er}}}{\langle T\rangle}\langle c_{\mathrm{er}}^*|t=t_i^-\rangle. \end{aligned} \tag{3.5.25}$$

The first and second lines are obtained by using Eq. 3.5.18 and evaluating the integral. The get from the third to the fourth line and from the fourth to the fifth line was used Eq. 3.5.22 and Eq. 3.5.23, respectively. This establishes an exact relation between the conditional and unconditional mean values. The drawback of this expression is that it depends on the stationary mean interval $\langle T\rangle$. Alternatively, we can derive a simpler approximation assuming that $c_{\mathrm{er}}(t)$ is slowly replenished and evolves linearly according to

$$c_{\mathrm{er}}(t) \approx c_{\mathrm{er}}(t_i^+) + \frac{c_{\mathrm{er}}(t_{i+1}^-)-c_{\mathrm{er}}(t_i^+)}{T_i}t \quad \text{with} \quad t_i \le t < t_{i+1}. \tag{3.5.26}$$

Note that this expression does not correspond to a linear approximation of $c_{\mathrm{er}}(t)$ at $t = t_i^+$ (or $t = t_{i+1}^-$) in the sense of a Taylor expansion but provides a linear approximation so that both the values $c_{\mathrm{er}}(t_i^+)$ and $c_{\mathrm{er}}(t_{i+1}^-)$ are taken at the beginning and the end of the interval T_i. In this case, the unconditional mean and conditional mean are related by

$$\begin{aligned} \langle c_{\mathrm{er}}^*\rangle &\approx \frac{\langle c_{\mathrm{er}}|t=t_i^-\rangle+\langle c_{\mathrm{er}}|t=t_i^+\rangle}{2},\\ &\approx \langle c_{\mathrm{er}}^*|t=t_i^-\rangle(1-\epsilon/2) \end{aligned} \tag{3.5.27}$$

where we have used Eq. 3.5.23 again. This expression will be used in the following.

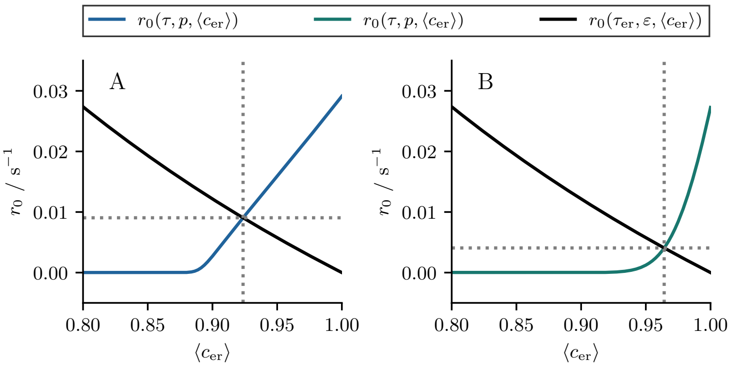

FIGURE 3.26: Self-consistent firing rate. Panels A and B illustrate the self-consistent calculation of the firing rate in the mean-driven and excitable regimes, respectively. The blue and green lines show the firing rate according to Eq. 3.5.12, while the black line shows the firing rate according to Eq. 3.5.28. The intersection point determines the stationary firing rate r_0 and the stationary mean value $\langle c^*_{\rm er}\rangle$, indicated by the dotted lines. Parameters: (A) $\tau = 5$s, $p = 0.015$, $\varepsilon = 0.03$, $\tau_{\rm er} = 300$s; (B) $\tau = 1$s, $p = 0.06$, $\varepsilon = 0.03$, $\tau_{\rm er} = 300$s.

Returning to the original problem, we insert Eq. 3.5.27 into Eq. 3.5.16, rearrange the terms, and find a second expression for the firing rate as a function of the two parameters $\tau_{\rm er}$ and ε, and the stationary mean $\langle c^*_{\rm er}\rangle$

$$r_0(\tau_{\rm er}, \varepsilon, \langle c^*_{\rm er}\rangle) = \frac{1-\langle c^*_{\rm er}\rangle}{\hat{\varepsilon}\tau_{\rm er}\langle c^*_{\rm er}\rangle}, \tag{3.5.28}$$

where $\hat{\varepsilon} = \varepsilon/(1-\varepsilon/2)$ accounts for the biased sampling problem introduced by the conditional mean value [66]. Together Eq. 3.5.12 and 3.5.28 permit the self-consistent calculation of the firing rate as is illustrated in Fig. 3.26, where the firing rates as a function of $\langle c_{\rm er}\rangle$ according to Eq. 3.5.12 and Eq. 3.5.28 are shown by blue/green lines and black lines, respectively. At the intersection of the two lines, both equations are satisfied simultaneously, and the stationary firing rate and stationary mean can be read off the y-axis and x-axis, respectively (horizontal and vertical lines in Fig. 3.26). We note that Eq. 3.5.12 is a monotonically increasing function of $\langle c_{\rm er}\rangle$, while Eq. 3.5.28 is a monotonically decreasing function of $\langle c_{\rm er}\rangle$, so the point of intersection and the firing rate are uniquely determined.

In Fig. 3.27A$_1$ and B$_1$, we compare the mean ISI obtained from stochastic simulations of the two-component model and the Langevin approximation with the theoretical prediction by the self-consistent method. First, we observe that the mean ISI increases with both $\tau_{\rm er}$ and ε. This is expected since an increase in either of these parameters decreases $\langle c^*_{\rm er}\rangle$. Furthermore, we observe excellent agreement between theory and simulations for all values of $\tau_{\rm er}$ and small values of ε. The fact that the net loss ε rather than timescale $\tau_{\rm er}$ serves as the limiting factor of the approximation ($c_{\rm er}(t) \approx \langle c^*_{\rm er}\rangle$) may seem surprising since the self-consistent method relies on the assumption that the Ca^{2+} concentration in the ER changes slowly - a property intuitively associated with the parameter $\tau_{\rm er}$. However, in the stationary state, the depletion during a spike (determined by ε) and the replenishment between two spikes (determined by the ratio $\langle T\rangle/\tau_{\rm er}$) must balance on average. Consequently, the ε parameter determines how strongly $c_{\rm er}(t)$ changes over an ISI. Conversely, the relative change of $c_{\rm er}(t)$ depends on the timescale only through the ratio $\langle T\rangle/\tau_{\rm er}$. Since $\langle T\rangle$ itself depends on $\tau_{\rm er}$ (cf. Fig. 3.27A$_1$), small values of $\tau_{\rm er}$ do not necessarily imply that $c_{\rm er}(t)$ changes significantly over an ISI.

As we have also shown in Sec. 3.4.2, the mean-adaptation approximation does, in principle, also allow to calculate of the variance $\langle \Delta T^2\rangle$ of the ISI according to

$$\left\langle \Delta T^2 \right\rangle = 2\int_{-\infty}^{c_T} dx_3\, e^{-h(x_3)} \left(\int_{-\infty}^{x_3} dx_2\, \frac{e^{h(x_2)}}{D(x_2)}\right)^2 \int_{x_3}^{c_T} dx_1\, e^{-h(x_1)}\Theta(x_1 - c_R) \tag{3.5.29}$$

and thus also the CV $C_V = \sqrt{\langle \Delta T^2\rangle}/\langle T\rangle$. However, the time dependence of $c_{\rm er}(t)$ is often crucial for the variability of the ISI and cannot be neglected. In the following, we discuss in which cases

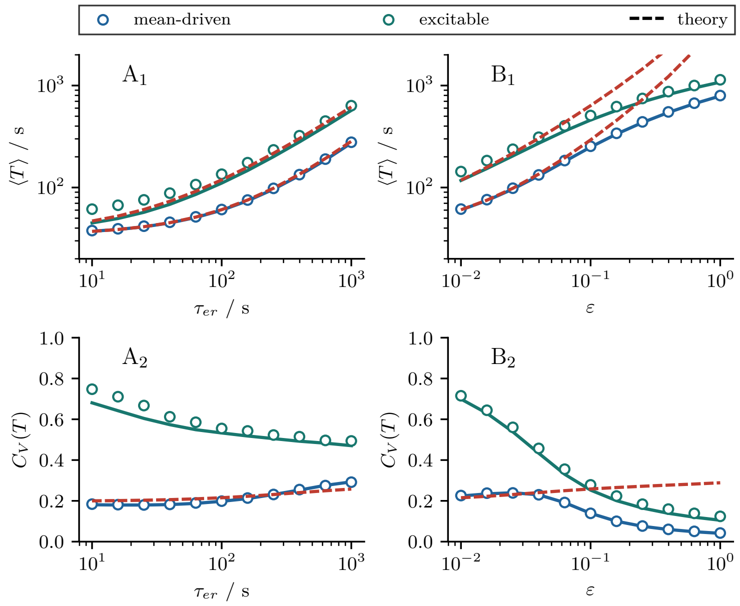

FIGURE 3.27: Stationary first-order interspike interval statistics. Panels A and B show the mean $\langle T \rangle$ and CV $C_V(T)$ as functions of τ_{er} and ε. Blue/green circles and lines indicate statistics calculated from stochastic simulations of the two-component model (Eq. 3.5.1) and the Langevin approximation (Eq. 3.5.3), respectively. Red lines indicate theoretical predictions according to Eq. 3.5.12, 3.5.28 and 3.5.29. Parameters Mean-driven: $\tau = 5$s, $p = 0.015$; Excitable: $\tau = 1$s, $p = 0.06$; A: $\varepsilon = 0.03$; B: $\tau_{\text{er}} = 300$s.

the CV can nevertheless be determined by means of Eq. 3.5.29 and Eq. 3.5.12.

Coefficient of variation

A distinctive feature of Ca^{2+} signaling is the persistence of the CV of the ISIs between different cells of a cell line stimulated with the same agonist, despite considerable cell-to-cell variability [7, 8]. This experimental finding is difficult to reproduce with the renewal model, where the ISI variability is solely due to the fluctuations of the cytosolic Ca^{2+} concentration caused by the random discharge of Ca^{2+} from the ER into the cytosol through IP_3R clusters. As a result, the noise acting on the cytosolic Ca^{2+} concentration is relatively weak, and spiking is either nearly deterministic in the mean-driven regime or highly stochastic in the excitable regime. In order to reproduce the ISI statistics of stimulated HEK cells with an intermediate CV, the parameters had to be chosen close to the bifurcation line in the mean-driven regime.

Introducing the ER Ca^{2+} concentration $c_{\text{er}}(t)$ as an adaptation variable solves this problem to some extent because it affects the variability of the ISIs differently, depending on the specific choice of parameters. On the one hand, it provides a second source of ISI variability by adding a stochastic component to the initial conditions $c_{\text{i}}(t_i^+)$ and $c_{\text{er}}(t_i^+)$. This can potentially increase the CV. On the other hand, the negative feedback of the adaptation variable can also give rise to a relative refractory period. This usually reduces the CV. It is easy to show that introducing an *absolute* refractory period always leads to a decrease in the CV. To see this, consider a new interval $T' = T + \tau_{\text{ref}}$ consisting of a stochastic time T and a deterministic absolute refractory period τ_{ref}. The mean of the new interval is given by $\langle T' \rangle = \langle T \rangle + \tau_{\text{ref}}$, while the variance $\langle \Delta T'^2 \rangle = \langle (T + \tau_{\text{ref}} - \langle T + \tau_{\text{ref}} \rangle)^2 \rangle = \langle \Delta T^2 \rangle$ is independent of the refractory period. Consequently, the CV of the interval T' is reduced compared to the CV of the interval T. The dependence of the CV on the parameters τ_{er} and ε is shown in Fig. 3.27A$_2$ and B$_2$, respectively. When τ_{er} and ε take small values, the nonrenewal model closely resembles the renewal model. In this scenario, the CV is approximate $C_V(T) \approx 0.20$ for the specific parameters in the mean-driven regime (blue lines and circles) and $C_V(T) \approx 0.75$ for the specific parameters in the excitable regime (green lines and circles). In the mean-driven regime, the CV exhibits a non-monotonic dependence on both parameters. Initially, as τ_{er} increases, there is a slight decrease in the CV, followed by an increase as τ_{er} continues to increase. Conversely, as the parameter ε increases, the CV experiences a slight

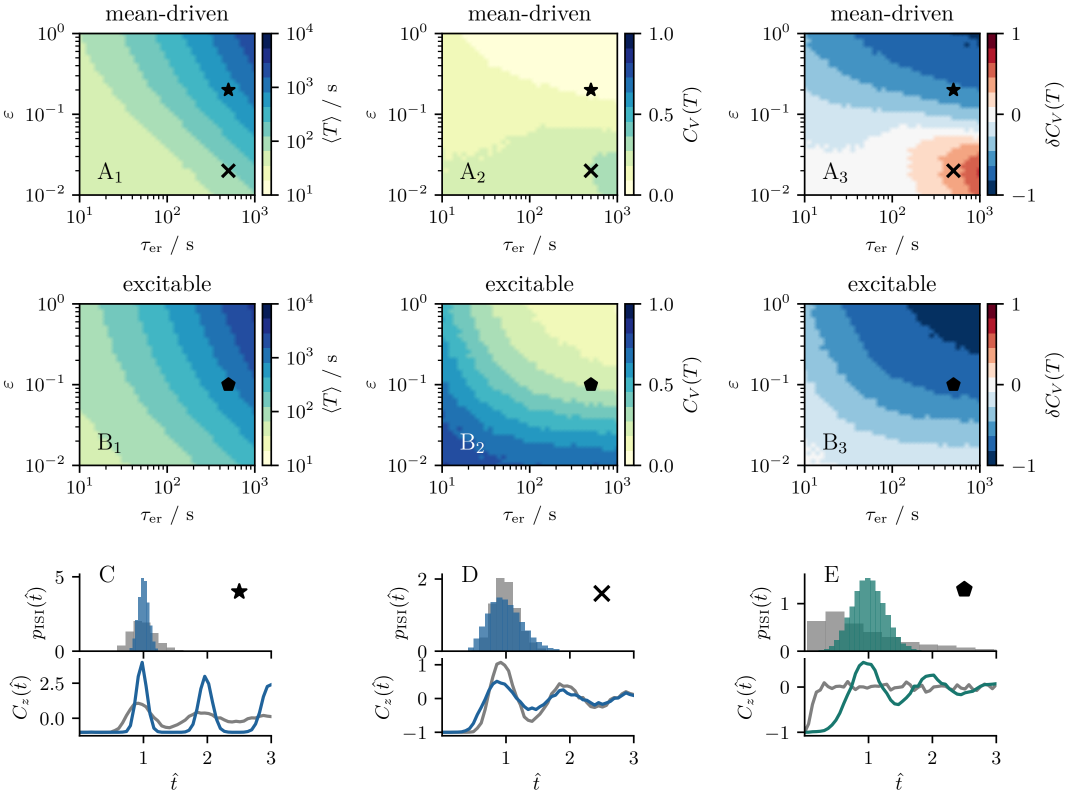

FIGURE 3.28: Ca^{2+} store depletion and interspike interval variability. Panels A and B show the mean $\langle T\rangle$, the CV $C_V(T)$, and the relative change of the CV compared to the renewal model $\delta C_V = (C_V - C_V^*)/C_V^*$, in the mean-driven and excitable regimes, respectively. Panels A_1 and B_1 show that the mean interval is prolonged when either τ_{er} or ε is increased. The effect on the CV shown in A_2, A_3 and B_2, B_3 is less obvious. In the mean-driven regime, the CV can either be increased as for the parameters marked by the cross ($\tau_{\mathrm{er}} = 500\mathrm{s}$, $\varepsilon = 0.02$) or decreased as for the parameters marked by the star ($\tau_{\mathrm{er}} = 500\mathrm{s}$, $\varepsilon = 0.2$). In the excitable regime, the CV is generally decreased, as shown for the parameters marked by the pentagon ($\tau_{\mathrm{er}} = 500\mathrm{s}$, $\varepsilon = 0.1$). Panels C, D, and E show the ISI density $p_{\mathrm{ISI}}(\hat{t})$ and the spike-train correlation function $C_z(\hat{t})$ for the three sets of parameter in the two regimes. Parameters Mean-driven: $\tau = 5\mathrm{s}$, $p = 0.015$; Excitable $\tau = 1\mathrm{s}$, $p = 0.06$.

initial increase before decreasing as ε is further increased. In the excitable regime, regardless of whether τ_{er} or ε is varied, we observe a general decrease in the CV with increasing adaptation strength. Thus, the introduction of an additional adaptation variable leads to a less pronounced difference in the ISI variability between the excitable and mean-driven regimes compared to the renewal model.

To provide a more comprehensive overview of the observed behavior, we show in Fig. 3.28A and B the mean $\langle T\rangle$, the CV $C_V(T)$, and most importantly, the relative change in the CV $\delta C_V = (C_V - C_V^*)/C_V^*$ over a wide range of the parameters τ_{er} and ε. Here, C_V^* refers to the CV obtained from stochastic simulations of the renewal model with the same values for the parameters τ and p as for the nonrenewal model. From Fig. 3.28A_3, it is evident that when the ER is significantly depleted during a single spike, roughly when $\varepsilon > 0.1$, the CV decreases compared to the renewal case, regardless of the value of τ_{er}. Recall that in the stationary case, larger values of ε imply stronger changes of $c_{\mathrm{er}}(t)$ over an interval because ε is closely related to the difference between the values of $c_{\mathrm{er}}(t)$ at the beginning and the end of an ISI. The strong depletion leads to a strong inhibition of the spiking probability right after a spike is fired, similar to a refractory period. This is illustrated in more detail for the specific parameters marked by the star in Fig. 3.28A_3 by comparing the ISI density $p_{\mathrm{ISI}}(\hat{t})$ and the spike-train autocorrelation function $C_z(\hat{t}) = \langle z(\hat{t}' + \hat{t})z(\hat{t}')\rangle - \langle z(\hat{t}')\rangle^2$ of the renewal model (gray histogram and line) and the nonrenewal model (blue histogram and line) in Fig. 3.28C. Since the depletion of the ER strongly affects the mean ISI (see Fig. 3.28A$_1$ and B$_1$), we rescale the time axis $\hat{t} = t/\langle T \rangle$ to allow for a comparison of the two statistics. Consistent with our reasoning, the ISI density of the nonrenewal model is more strongly peaked, and spiking is almost completely inhibited until right before the mean ISI $\hat{t} \approx 1$. In contrast to that, when the depletion of the ER during a single spike is small, roughly when $\varepsilon < 0.1$, and the replenishment is slow, the CV can even be increased. This is the case for the parameters marked by the cross in the lower right corner of Fig. 3.28A$_3$ and further illustrated in Fig. 3.28D where we again compare the ISI density and correlation function of the renewal model (gray histogram and line) and the nonrenewal model (blue histogram and line). We notice that the ISI density is broadened for the nonrenewal model, and the correlation function is flattened. For the specific value of ε, the change in $c_{\rm er}(t)$ over an ISI is rather small so that $c_{\rm er}(t)$ is approximately constant. In addition to reducing the reset point c_R, this essentially reduces the permeability according to $\hat{p} = p\langle c_{\rm er}^* \rangle$ so that the model operates closer to the bifurcation, which generally increases the CV in the mean-driven regime. The fact that in Fig. 3.27A$_2$, where ε is small, the dependence of the CV on $\tau_{\rm er}$ is accurately captured by the mean-adaptation approximation $c_{\rm er}(t) \approx \langle c_{\rm er}^* \rangle$ indicates that the effective reduction of the parameter p is indeed the mechanism through which the adaptation variable enhances the CV in the mean-driven regime. Finally, in the excitable regime, we consistently observe a decrease in the CV for all combinations of $\tau_{\rm er}$ and ε compared to the renewal case and a monotonic decrease in the CV as a function of these two parameters. Increasing either $\tau_{\rm er}$ or ε leads to a stronger inhibition of the spike generation over a certain period, which always reduces the CV compared to the renewal case, where spiking is almost Poissonian. This is illustrated in Fig. 3.28E, where the ISI density and correlation function of the renewal model show clear characteristics of a Poisson process (exponential ISI density, vanishing correlation function), except for a reduced firing probability immediately after a spike is fired. In contrast, when the depletion of the ER is taken into account, both the ISI density and the correlation function show characteristics of a more regular spiking process, often associated with the mean-driven regime but here mediated by the adaptation variable.

3.5.2 Stationary second-order interspike interval statistics

So far, we have considered stationary *first-order* ISI statistics that are based on the ISI density $p_{\rm ISI}(t)$. However, because the adaptation is usually mediated by a slow process that affects the spiking statistics over multiple spikes, the intervals are often also correlated by this process [18, 74, 97]. In our model, this slow process is the Ca^{2+} concentration in the ER $c_{\rm er}(t)$.

The intervals generated by our model are statistically dependent as shown by several second-order statistics in Fig. 3.29. The full picture of the dependence of subsequent intervals is provided by probability density $p(T_{i+1}, T_i)$ shown in Fig. 3.29A (dotted lines indicated the mean ISI $\langle T \rangle$). The conditional probability densities $p(T_{i+1}|T_i)$ for an interval T_i can be inferred as the density along a given vertical line and shows a dependence on T_i. For example, for $T_i < \langle T \rangle$, the probability is shifted to larger values of T_{i+1}. For $T_i > \langle T \rangle$, the probability is shifted to smaller values of T_{i+1}. Adjacent intervals are thus anticorrelated. The conditional mean $\langle T_{i+1}|T_i \rangle$ shown by the red line illustrates these anticorrelations more clearly.

As we have explained in detail in the previous chapter, such interval correlations can be quantified by the SCC

$$\rho_k = \frac{\langle \delta T_i \delta T_{i+k} \rangle}{\langle \delta T_i \rangle^2}, \tag{3.5.30}$$

where $\delta T_i = T_i - \langle T \rangle$ is the deviation of the i-th ISI T_i from the mean. In Fig. 3.29B, we show the pattern of interval correlations ρ_k as a function of the lag k (blue circles) and observed a pronounced anticorrelation that decays monotonically over a few lags according to

$$\rho_k \approx \rho_1 e^{-(k-1)/n_{\rm corr}}, \tag{3.5.31}$$

where $n_{\rm corr}$ is the number of correlated intervals. The fact that for our model, the SCC is initially negative and monotonically approaches 0 as k increases can be well understood in the framework developed in the previous chapter. Let us briefly recall the properties that the model must fulfill in order to apply the theory of the previous chapter. First, the model must operate in the

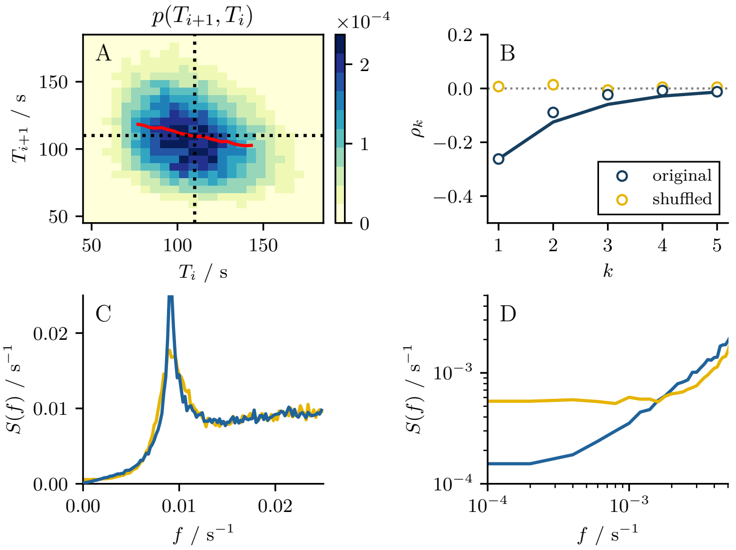

FIGURE 3.29: Stationary second-order interspike interval statistics. Panel A shows the joint probability density $P(T_{i+1}, T_i)$. The color code indicates the frequency at which a specific pair of adjacent intervals (T_{i+1}, T_i) is observed. The vertical and horizontal dotted lines indicate the mean $\langle T \rangle$. The red line indicates the conditional mean $\langle T_{i+1} | T_i \rangle$. Panel B shows the sequence of correlation coefficients ρ_k, indicating strong anticorrelations of adjacent intervals (ρ_1) that decay slowly with lag k. Panel C and D show the power spectrum $S(f)$ over a wide range of frequencies and at low frequencies, respectively. Panels B, C, and D also show the SCC and the power spectrum calculated for the same but shuffled ISI sequence (yellow circles and lines). Parameters: $\tau = 5$s, $p = 0.015$, $\tau_{\text{er}} = 300$s, $\varepsilon = 0.03$.

mean-driven regime, i.e., possess a deterministic limit cycle to define a phase. Second, the deviations from this limit cycle must be weak so that they can be described in the framework of the phase-response curve. If these two conditions are met, the theory predicts two possible patterns of interval correlation for a one-dimensional IF model with a spike-triggered adaptation variable [74]. In both cases, the SCC starts at negative values $\rho_1 < 0$ and approaches 0 either monotonically or oscillatory with the lag k. Schwalger and Lindner [74] have shown that the observed pattern is related to the drift $f(c_{\text{i}}, c_{\text{er}})$ at the reset point. If this drift is positive, the sequence ρ_k decays monotonically; if it is negative, the sequence decays oscillatory. In other words, if (in the deterministic limit) the cytosolic Ca^{2+} concentration $c_{\text{i}}(t)$ begins to rise toward the threshold immediately after the reset, the SCC will decay monotonically. This is the case for our model. The drift at the reset $c_R = c_0^* c_{\text{er}}$ is given by $f(c_R, c_{\text{er}}) = \mu(c_R, c_{\text{er}}) > 0$ and is guaranteed to be positive because the mean puff current is positive for all values of c_{er}. The fact that ρ_k decays monotonically, has consequences for the first SCC ρ_1, since the sum over all SCCs is bound according to

$$\textstyle\sum_k \rho_k \geq -1/2, \tag{3.5.32}$$

which implies $\rho_1 > -1/2$ when all SCCs are negative. Combining Eq. 3.5.31 and Eq. 3.5.32, evaluating the sum and rearranging terms, allows to derive an upper limit for the number of correlated intervals

$$n_{\text{corr}} \leq -\frac{1}{\ln(1 + 2\rho_1)}, \tag{3.5.33}$$

given $-1/2 \leq \rho_1 \leq 0$. In Fig. 3.29B we show the sequence ρ_k according to Eq. 3.5.31 with $n_{\text{corr}} = -1/\ln(1 + 2\rho_1)$ by the solid blue. The estimate provides a good approximation even though the actual sequence ρ_k decays somewhat faster. The corresponding power spectrum $S(f)$ in two different frequency ranges is shown in Fig. 3.29C and D. In both cases, we compare the power spectrum of the original spike train (blue line) to the power spectrum of the same spike train with the ISIs shuffled (yellow line). Shuffling the sequence of ISIs provides a simple method to decorrelate intervals without changing first-order statistics (cf. Fig. 3.29B). Because the low-frequency limit of a nonrenewal spike train is given by $S(0) = r_0 C_V^2(T)(1 + 2\sum_{k=1}^{\infty} \rho_k)$ the power

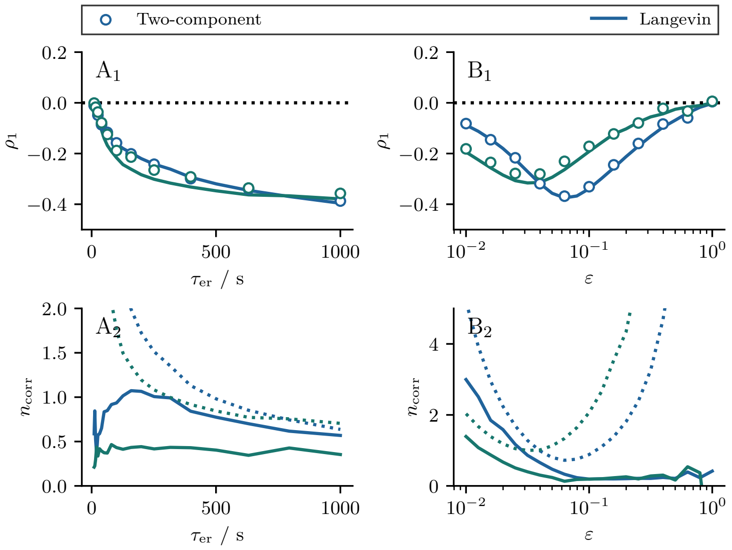

FIGURE 3.30: Serial correlation coefficient and number of correlated intervals. Panels A and B show the SCC ρ_k and the number of correlated intervals n_corr as functions of τ_er and ε. Blue/green circles and lines indicate statistics calculated in the mean-driven/excitable regime from stochastic simulations of the two-component model and the Langevin approximation. The number of transient intervals has been calculated according to Eq. 3.5.34 and thus relies on the assumption that the SCC decays monotonically with the lag k. Dotted lines in A$_2$ and B$_2$ show the theoretical (upper) limit of n_corr according Eq. 3.5.33. Parameters Mean-driven: $\tau = 5$s, $p = 0.015$; Excitable: $\tau = 1$s, $p = 0.06$; A: $\varepsilon = 0.03$; B: $\tau_\mathrm{er} = 300$s.

spectrum of the shuffled spike train has larger power compared to the original spike train.

Beyond the specific parameters used so far, we show in Fig. 3.30 the first SCC ρ_1 and the number of correlated intervals n_corr as functions of τ_er and ε in both the mean-driven and excitable regimes. First of all, the SCC shown in Fig. 3.30A$_1$ and B$_1$ is always negative as expected [74, 82, 97, 176, 258]. Secondly, no correlation coefficient falls below the $\rho_1 < -1/2$ limit resulting from the monotonic pattern of interval correlations. This suggests that the argument made earlier regarding the pattern of interval correlation may hold more generally beyond a weakly perturbed, mean-driven model. Thirdly, we find that ρ_1 decreases monotonically as a function of τ_er and exhibits a local minimum as a function of ε. The minimum with respect to ε results from the fact that the correlation coefficient must vanish for both $\varepsilon = 0$ and $\varepsilon = 1$. We pointed out earlier that two neighboring intervals are correlated by $c_\mathrm{er}(t_i^+)$, which depends on the interval T_i and serves as an initial condition for the interval T_{i+1}. For $\varepsilon = 0$, it is evident that $c_\mathrm{er}(t_i^+)$ does not depend on T_i, simply because $c_\mathrm{er}(t)$ does not change at all. Conversely, for $\varepsilon = 1$, the initial conditions $c_\mathrm{er}(t_i^+)$ are again independent of T_i, this time because the ER is completely depleted with each spike, i.e., $c_\mathrm{er}(t_i^+) = 0$. In both cases, the intervals are uncorrelated, and there is a minimum for some intermediate value of ε.

Finally, in Fig. 3.30A$_2$ and B$_2$ we show the number of correlated intervals n_corr as a function of τ_er and ε. To calculate the number of correlated intervals, we assume that the SCC decays monotonically according to Eq. 3.5.31, which allows us to derive the expression

$$n_\mathrm{corr} = \frac{1}{\ln(\rho_1/\rho_2)}. \tag{3.5.34}$$

Since the second correlation coefficient ρ_2 is difficult to measure (especially when it is close to zero, as is often the case here), we show only the results from numerical simulations of the more efficient Langevin approximation (blue/green solid lines). The results are compared to the theoretical upper limit according to Eq. 3.5.33 (dotted lines). Interestingly the limit $n_\mathrm{corr} = -1/\ln(1 + 2\rho_1)$ implies that if adjacent intervals are strongly anticorrelated, the number of correlated intervals n_corr is small. Since the SCC ρ_1 decreases with τ_er, this leads to the somewhat counterintuitive conclusion that the number of correlated intervals decreases as τ_er increases. This is shown in Fig. 3.30A$_2$, where, after an initial increase n_corr decreases with τ_er. At the same time, we find that

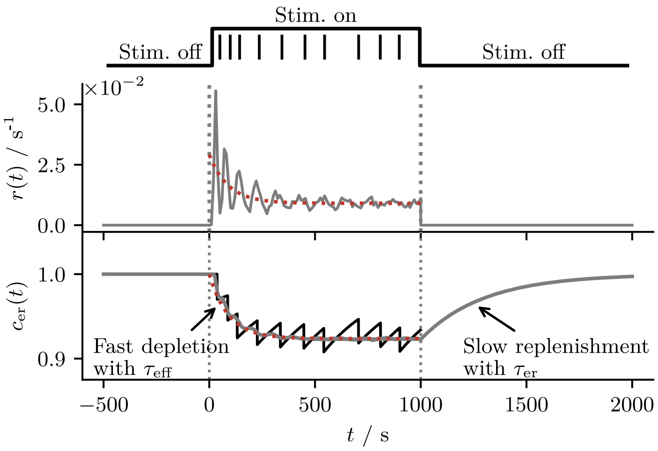

FIGURE 3.31: Timescale of ER depletion and replenishment. The upper and lower panels show the response of the firing rate $r(t)$ and the ER Ca^{2+} concentration $c_{\mathrm{er}}(t)$ to a constant IP$_3$ stimulation. The stimulation is activated at $t = 0$s and deactivated at $t = 1000$s, as illustrated by the upper black step function. Vertical lines below the stimulation line indicate spike times. The corresponding time series $c_{\mathrm{er}}(t)$ is depicted by black lines in the lower panel. Switching to an averaged description, the firing rate $r(t)$ and the ensemble average $\langle c_{\mathrm{er}}(t)\rangle$ are shown as gray lines. Notably, the effective timescale τ_{eff} at which $\langle c_{\mathrm{er}}(t)\rangle$ converges to its stationary value in response to the stimulus differs from the timescale τ_{er} at which $\langle c_{\mathrm{er}}(t)\rangle$ approaches its stationary value in the absence of a stimulus. The red line indicates the stationary firing rate $r_0(c_{\mathrm{er}}(t))$. Parameters: $\tau = 5$s, $p = 0.015$, $\tau_{\mathrm{er}} = 300$s, $\varepsilon = 0.03$.

for all values of τ_{er}, the number of correlated intervals rarely exceeds one. A larger number of correlated intervals is observed for small values of ε, as shown in Fig. 3.30B$_2$.

3.5.3 Timescale of the transient - Ca^{2+} store depletion

So far, our investigation has focused on the effect of the depletion of the intracellular Ca^{2+} store on *stationary* ISI statistics. To this end, we have assumed that the initial stimulation of the model cell occurred in the distant past, rendering the ISI statistics independent of the absolute time elapsed since then. However, there is a period of time when this assumption does not hold, and the spiking statistics do depend on the absolute time since stimulation. This period is called the transient. Here, we derive a timescale corresponding to the duration of this transient. In what follows, we will again focus on the computation of statistics that characterize the ISIs specifically during this transient. The mechanism underlying the time dependence of the spiking statistics is the cumulative depletion of the ER over multiple spikes. Therefore, it is suggestive to consider the timescale on which the variable $c_{\mathrm{er}}(t)$ approaches the stationary state as an estimate of the duration of the transient. This effective timescale τ_{eff}, at which the ER is depleted when spikes are fired repeatedly, should not be confused with the timescale τ_{er} at which the ER is replenished in the absence of spikes. The fact that these two timescales are different is demonstrated in Fig. 3.31, where a constant IP$_3$ stimulation is applied to the model over a period of time indicated by the top black line. This stimulation activates the IP$_3$Rs and triggers the release of Ca^{2+} from the ER into the cytosol, causing the model to fire spikes. The vertical black lines represent an exemplary sequence of spike times during the stimulation period. Even by visual inspection, it is clear that the reduction of $c_{\mathrm{er}}(t)$ with each spike significantly prolongs the ISIs. The corresponding time series of the variable $c_{\mathrm{er}}(t)$ is shown in the lower panel, represented by a black line.

To estimate the effective τ_{eff}, we consider the time-dependent ensemble average of the ER Ca^{2+} concentration $\langle c_{\mathrm{er}}(t)\rangle$ obtained from a large number of simulations N_{sim} of the two-component model where the Ca^{2+} concentrations are initiated at $c_{\mathrm{i},n}(0) = c_R$, $c_{\mathrm{er},n}(0) = 1$, and the clusters are initiated in the state C_1. The ensemble average is then calculated by

$$\langle c_{\mathrm{er}}(t)\rangle = \textstyle\sum_{n=1}^{N_{\mathrm{sim}}} c_{\mathrm{er},n}(t)/N_{\mathrm{sim}} \tag{3.5.35}$$

and the firing rate $r(t)$ can be estimated by the fraction of realizations $c_{\mathrm{i},n}(t)$ that have crossed the threshold c_T in the small time window $[t, t+\Delta t]$ divided by Δt. The instantaneous firing rate

$r(t)$ and the average $\langle c_{\text{er}}(t)\rangle$ are shown in Fig. 3.32 by gray lines. Interestingly, $r(t)$ exhibits a pronounced "ringing", characterized by alternating periods of high and low firing rates. This can also be observed for $\langle c_{\text{er}}(t)\rangle$, although less pronounced. Two factors contribute to this ringing. First, our model is constructed so that neither the Ca^{2+} concentration in the cytosol nor the Ca^{2+} concentration in the ER are subject to any noise when the model cell is not stimulated. Consequently, the initial conditions at the time of the stimulation $c_{\text{i}}(t = 0) = c_0$ and $c_{\text{er}}(t = 0) = 1$ are identical for each unit in the ensemble from which the firing rate is obtained. Second, the parameters are chosen so that the model operates in the mean-driven regime, where spiking is rather regular. Consequently, the first few spikes occur in relative synchrony across the ensemble, resulting in a pronounced peak in firing rate around multiples of the mean ISI at $t \approx n\langle T\rangle$ with $n = 1, 2, \ldots$. As the number of spikes increases, this effect diminishes as the ensemble diffuses. Interestingly, negative correlations counteract this diffusion because if, in a realization, an early spike is fired (short ISI), it is typically followed by a late spike (long ISI). The negative correlations in the ISIs thus maintain a higher degree of synchronization in the ensemble over a longer time.

To estimate the effective timescale, we assume that the time series of the averaged ER Ca^{2+} concentration $\langle c_{\text{er}}(t)\rangle$ can be fitted by a single exponential function

$$\langle c^*_{\text{er}}\rangle + (1 - \langle c^*_{\text{er}}\rangle)e^{-t/\tau_{\text{eff}}} \tag{3.5.36}$$

indicated by the lower red line in Fig. 3.32. The estimate of τ_{eff} according to this fitting procedure is shown in Fig. 3.32 (blue circles) and can differ significantly from τ_{er} depending on the parameters. We note that the assumed fit function Eq. 3.5.36 introduces some ambiguity in the interpretation of τ_{eff}, since the time series of $c_{\text{er}}(t)$ will, in general, not be described by Eq. 3.5.36. In the following, however, we will show in which case $c_{\text{er}}(t)$ is indeed solved by an exponential function and τ_{eff} can be interpreted as the timescale on which the stationary mean $\langle c^*_{\text{er}}\rangle$ is approached.

To derive an analytical approximation for the effective τ_{eff}, we consider the time-dependent ensemble average of the ER Ca^{2+} concentration governed by

$$\frac{d}{dt}\langle c_{\text{er}}\rangle = -(\langle c_{\text{er}}\rangle - 1)/\tau_{\text{er}} - \hat{\varepsilon}\langle c_{\text{er}}\rangle r(t), \tag{3.5.37}$$

where we have assumed that the relation between the conditional mean $\langle c_{\text{er}}(t)\rangle$ and $\langle c_{\text{er}}(t)|t = t_i^-\rangle$ that we derived earlier for the stationary case also holds during the transient. In addition, we assume that the firing rate adjusts adiabatically to $\langle c_{\text{er}}(t)\rangle$, which omits the previously explained "ringing" and allows the instantaneous firing rate to be approximated by the stationary firing rate $r(t) \approx r_0(\langle c_{\text{er}}\rangle(t))$ so that Eq. 3.5.37 becomes

$$\frac{d}{dt}\langle c_{\text{er}}\rangle \approx -(\langle c_{\text{er}}\rangle - 1)/\tau_{\text{er}} - \hat{\varepsilon}\langle c_{\text{er}}\rangle r_0(\langle c_{\text{er}}\rangle). \tag{3.5.38}$$

The firing rate $r_0(\langle c_{\text{er}}\rangle(t)$ is shown in Fig. 3.31 by the upper red line. Equation Eq. 3.5.38 cannot be solved due to the complex functional relation between the stationary firing rate and $\langle c_{\text{er}}\rangle$, as described by Eq. 3.5.12. In order to obtain an approximate solution for $\langle c_{\text{er}}(t)\rangle$, we expand the firing rate around $\langle c^*_{\text{er}}\rangle$, considering terms up to zeroth and first order. To simplify the subsequent derivations, we introduce the abbreviated notation $x(t) = \langle c_{\text{er}}(t)\rangle$ and $x = \langle c^*_{\text{er}}\rangle$.

In the zeroth-order approximation $r_0(x) \approx r_0(x^*)$, the firing rate is constant and independent of $x(t)$. Consequently, Eq. 3.5.37 simplifies and becomes a linear differential equation

$$\dot{x} = -(x - 1)/\tau_{\text{er}} - \hat{\varepsilon}x r_0(x^*), \tag{3.5.39}$$

which is solved by

$$x(t) = x^* + (x_0 - x^*)e^{-t/\tau_1}, \tag{3.5.40}$$

with the initial condition $x_0 = 1$ and the timescale

$$\tau_1 = \frac{\tau_{\text{er}}}{1 + \hat{\varepsilon}\tau_{\text{er}} r_0(x^*)}. \tag{3.5.41}$$

The solution to $x(t)$ in the zeroth-order approximation of the firing rate provided by Eq. 3.5.40 matches the assumed fit function according to Eq. 3.5.36, and it follows that $\tau_{\text{eff}} = \tau_1$. Notably, even in this case, where the firing rate is assumed to be independent of $x(t)$, the effective timescale τ_{eff} does not agree with τ_{er}, but is smaller. This is due to the fact that the adaptation is multiplicative, i.e., the amplitude of the spike-triggered term depends on c_{er} so that the second term in Eq. 3.5.39 also depends on c_{er}. In Fig. 3.32, we compare the effective timescale τ_{eff} with τ_1 and find that the latter is a poor approximation of the true timescale. This observation is not surprising since Fig. 3.26 has already revealed that the firing rate changes significantly with respect to the mean ER Ca^{2+} concentration.

A more accurate approximation can be obtained by expanding the firing rate up to the first order $r_0(x) \approx r_0(x^*) + r_0'(x^*)(x - x^*)$, where the prime denotes the derivative with respect to x. In this case, Eq. 3.5.37 becomes a quadratic differential equation

$$\dot{x} = -(x-1)/\tau_{\text{er}} - \hat{\varepsilon}x[r_0(x^*) + r_0'(x^*)(x - x^*)], \tag{3.5.42}$$

that can still be solved analytically by

$$x(t) = x^* \frac{1 + (x_0 - x^*)/(x_0 + x^*)e^{-t/\tau_2}}{1 - (x_0 - x^*)/(x_0 + x^*)e^{-t/\tau_2}}, \tag{3.5.43}$$

again with the initial condition $x_0 = 1$ and the timescale

$$\tau_2 = \frac{\tau_{\text{er}}}{\sqrt{(1 + \hat{\varepsilon}\tau_{\text{er}}[r_0(x^*) - r_0'(x^*)x^*])^2 + 4\hat{\varepsilon}\tau_{\text{er}} r_0'(x^*)}}. \tag{3.5.44}$$

As mentioned before, we cannot expect the two timescales τ_2 and τ_{eff} to coincide since they are derived from different functions and thus have different meanings. However, we can introduce a new quantity $\Delta x = x_0 - x^*$, which describes the difference between the (mean) ER Ca^{2+} concentration before stimulation and the mean ER Ca^{2+} concentration in the steady state, thus the cumulative depletion of the ER, and substitute Δx in Eq. 3.5.43 to obtain

$$x(t) = x_0 \frac{2x^* + \Delta x + \Delta x e^{-t/\tau_2}}{2x^* + \Delta x - \Delta x e^{-t/\tau_2}}. \tag{3.5.45}$$

Similar to the firing rate, this expression is expanded to the first order in Δx to obtain an exponential function with a single timescale:

$$x(t) \approx x^* + (x_0 - x^*)e^{-t/\tau_2}. \tag{3.5.46}$$

In essence, when the difference $x_0 - x^* = 1 - \langle c_{\text{er}}^* \rangle$ is small, indicating a weak cumulative ER depletion, we can approximate τ_{eff} with τ_2. In Fig. 3.32, we compare the effective timescale τ_{eff} with τ_2 and observe good agreement over a wide range of parameters, except for small values of τ_{er}, indicated by the gray area in Fig. 3.32A. This discrepancy does not reflect a failure of the theory itself but rather the limitations of estimating τ_{eff} from simulation data. This is because the model operates in the mean-driven regime and fires regularly for the specific parameters used in Fig. 3.32. We have already explained that this results in a fairly synchronous firing of the first spike across the ensemble. The difference between the time the stimulus was presented and the first spike was fired also results in a delay between stimulus presentation and the decrease in $\langle c_{\text{er}}(t) \rangle$ of the order of the first ISI. Consequently, an estimate of the effective timescale τ_{eff} by fitting $c_{\text{er}}(t)$ with an exponential function starting at $t = 0$ will always also reflect this delay. In most cases, this inaccuracy will not significantly affect the estimate of the effective timescale since the mean of the first ISI is usually much shorter than the effective timescale. However, if the timescale τ_{er} is small compared to the mean of the first ISI, this can lead to a significant overestimation of τ_{eff}. This is illustrated in Fig. 3.32 where τ_{eff} saturates roughly at the mean of the first ISI $\langle T_1 \rangle \approx 30$s.

Finally, we note that in Fig. 3.32 the model operates in the mean-driven regime. In this case, τ_2 provides a good approximation to the effective timescale τ_{eff} because the $r_0(\langle c_{\text{er}} \rangle)$ can be well approximated by a linear function (cf. Fig. 3.26A). This is not the case in the excitable regime (cf. Fig. 3.26B), and the estimation becomes worse (not shown).

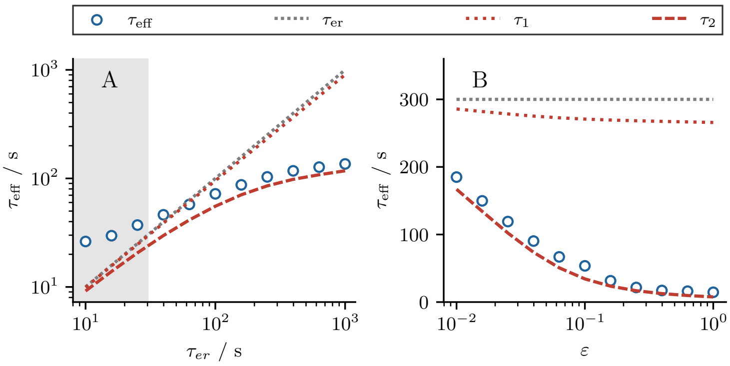

FIGURE 3.32: Effective timescale of ER depletion. Panel A and B show the effective timescale τ_{eff} has a function of τ_{er} and ε, respectively. Estimations of τ_{eff} from stochastic simulation of the two-component model are shown by blue circles. The timescale τ_{er} and the zero- and first-order approximations τ_1 and τ_2 are shown by black dotted lines, red dotted lines, and red dashed lines, respectively. The region where $\langle T_0 \rangle$ falls below the timescale τ_{er} is indicated by the gray area in panel A. Parameters: $\tau = 5$s, $p = 0.015$, $\tau_{\text{er}} = 300$s, $\varepsilon = 0.03$.

3.5.4 Transient interspike interval statistics

The method for the estimation of the effective timescale τ_{eff} detailed in Sec. 3.5.3 is based on the firing rate $r(t)$ and thus on the average over a large ensemble. This is usually infeasible in experimental settings. Here, we return to a description of the ISIs during the transient. As mentioned before, the sequence of mean ISIs $\langle T_i \rangle$ is well approximated by a single exponential function

$$T_\infty - (T_\infty - T_0)e^{-i/n_{\text{tr}}}, \tag{3.5.47}$$

described by three fit parameters, namely the initial (mean) interval T_0, the stationary (mean) interval T_∞, and the number of transient intervals n_{tr}. We use this fit function for both numerically simulated and experimentally measured ISI sequences. For the simulation data, we use the function to fit the interval sequence $\{\langle T_i \rangle\}$ averaged over many realizations. In the case of experimental sequences, the function is fitted to individual realizations $\{T_i\}$. For this reason, we refrain from referring to the fit parameters as mean values but emphasize that here the fit parameters T_0 and T_∞ correspond to the means of the initial interval $\langle T_0 \rangle$ and the stationary interval $\langle T \rangle$. Two of the three fit parameters are combined to define the cumulative refractory period $\Delta T = T_\infty - T_0$, which indicates how strongly the ISI adapts due to the depletion of the ER. The third fit parameter n_{tr} indicates the number of intervals over which the ISIs approach their stationary value. We note that the fit function was chosen ad hoc and does not necessarily reflect the actual dependence of the (mean) intervals T_i on the index i. This leads to some difficulty in the interpretation of the fit parameters, which does not so much affect the meaning of the cumulative refractory period ΔT, but rather the meaning of the number of transient intervals n_{tr}. The reason is that the interpretation of ΔT, i.e., the difference between the first and the stationary interval, is independent of the functional relation between T_i and i, whereas the interpretation of n_{tr} is not. This can be seen in Fig. 3.25C, where we have plotted a fit of Eq. 3.5.47 (black lines) to the sequence of mean ISIs (gray circles) and highlighted the cumulative refractory period ΔT as well as the number of transient intervals n_{tr}. A closer look reveals that the sequence of intervals deviates slightly from the fit function. Specifically, the first few mean intervals increase more slowly than the fit function, while the following intervals increase more rapidly until the stationary state is reached. Despite this difficulty, we provide estimates of the cumulative refractory period and the number of transient intervals in the following.

We begin by calculating the cumulative refractory period ΔT. Both the first and the stationary interval $T_0 = \langle T_0 \rangle$ and $T_\infty = \langle T \rangle$ can be calculated according to the self-consistent scheme detailed in Sec. 3.5.1. For the first interval, Eq. 3.5.12 can be solved directly since the value of the ER

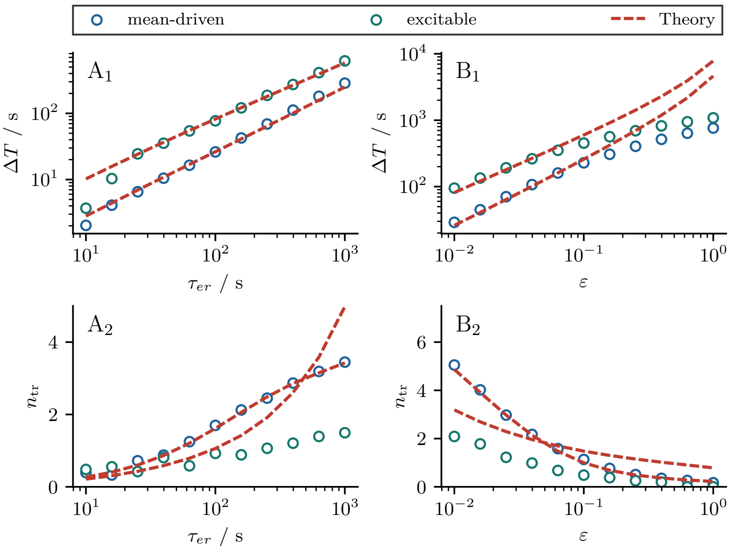

FIGURE 3.33: Transient interspike interval statistics. Panels A and B show transient statistics as functions of τ_{er} and ε, respectively. Panels A$_1$ and B$_1$ show the cumulative refractory period ΔT obtained from stochastic simulations of the two-component model in the mean-driven regime (blue circles) and excitable regime (green circle). Theoretical predictions according to Eq. 3.5.48 and Eq. 3.5.49 are shown by red lines. Panels A$_2$ and B$_2$ compare the number of transient intervals obtained by fitting Eq. 3.5.47 to a simulated sequence of mean ISI $\{\langle T_i \rangle\}$ to the theoretical prediction according to Eq. 3.5.50 where the effective timescale τ_{eff} is approximated by Eq. 3.5.44. Parameters Mean-driven: $\tau = 5$s, $p = 0.015$; Excitable $\tau = 1$s, $p = 0.06$; and A: $\varepsilon = 0.03$; B: $\tau_{\mathrm{er}} = 300$s.

Ca^{2+} concentration before the first spike is known, namely $c_{\mathrm{er}}(t < t_1) = 1$:

$$T_0 = \frac{1}{r_0(\langle c_{\mathrm{er}} \rangle = 1)}. \tag{3.5.48}$$

For the stationary interval, both Eq. 3.5.12 and Eq. 3.5.28 have to be solved simultaneously

$$T_\infty = \frac{1}{r_0(\langle c_{\mathrm{er}} \rangle = \langle c^*_{\mathrm{er}} \rangle)}. \tag{3.5.49}$$

We take the difference between the two intervals to obtain the cumulative refractory period $\Delta T = T_\infty - T_0$. In Fig. 3.33A$_1$ and B$_1$, we compare the theoretical prediction according to Eq. 3.5.48 and Eq. 3.5.49 (dashed red line) with the cumulative refractory period obtained by fitting Eq. 3.5.47 to the sequence of mean intervals $\{\langle T_i \rangle\}$ obtained from stochastic simulations of the two-component model (blue circles). As for the stationary mean interval, we observe a general increase in ΔT with respect to both τ_{er} and ε. Moreover, we find good agreement between the simulation results and the theory for all values of τ_{er} and for small values of ε. This is for the same reason we have discussed in the context of the stationary mean interval. Briefly, the mean-adaptation approximation $c_{\mathrm{er}}(t) \approx \langle c^*_{\mathrm{er}} \rangle$ fails for large values of ε.

The number of transient intervals n_{tr} can be estimated based on the approximation of the effective timescale $\tau_{\mathrm{eff}} \approx \tau_2$ derived in Sec. 3.5.3. To this end, we consider the simple estimate

$$n_{\mathrm{tr}} \approx \tau_{\mathrm{eff}} / T_0. \tag{3.5.50}$$

Recall that τ_{eff} is the length of the transients measured in units of time. The ratio τ_{eff}/T_0 is a dimensionless number that indicates how many intervals T_0 the transients would span. Thus, Eq. 3.5.50 can be considered as an upper bound on the number of transient intervals since $T_0 \leq T_i$ (provided that the timescale τ_{eff} is correctly described). In Fig. 3.33A$_2$ and B$_2$, we compare the number of transient intervals determined by fitting Eq. 3.5.47 to the sequence of mean intervals obtained from stochastic simulations of the two-component model (blue/green circles), and the number of transient intervals calculated according to Eq. 3.5.50 (red lines), where τ_{eff} is estimated

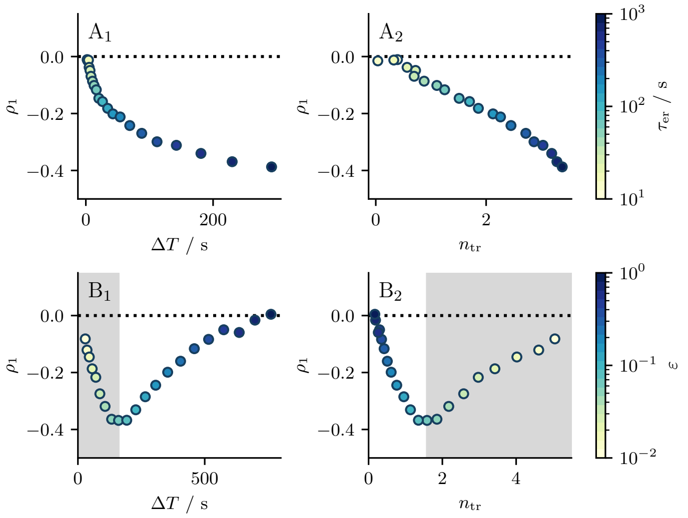

FIGURE 3.34: Stationary over transient interspike interval statistics. Panels A$_1$ and A$_2$ show the SCC ρ_1 as a function ΔT and n_{tr} when the parameter τ_{er} is varied. The color code indicates the value of τ_{er}. Panels B$_1$ and B$_2$ show the SCC ρ_1 as a function ΔT and n_{tr} when the parameter ε is varied. The gray area indicates the region where ε is small and ρ_1 increases monotonically with ε. In the white area, ε is larger, and ρ_1 decreases monotonically with ε. Parameters: $\tau = 5$s, $p = 0.015$; and A: $\tau_{\mathrm{er}} = 300$s, B: $\varepsilon = 0.03$.

according to Eq. 3.5.44 and T_0 according to Eq. 3.5.48. We find excellent agreement in the mean-driven regime (blue circles) and a general overestimation by the theory in the excitable regime (green circles). That the number of transient intervals in the excitation regime is poorly described by the theory is not surprising because already the estimation of the effective timescale by τ_2 is based on the assumption that the firing rate can be linearized around $\langle c_{\mathrm{er}}^* \rangle$. As shown in Fig. 3.26B, this is not the case in the excitable regime. It turns out that the number of transient intervals depends only moderately on τ_{er}. Even for large values of this timescale, such as $\tau_{\mathrm{er}} \approx 10^3$, one observes only a small number of transient intervals, $n_{\mathrm{tr}} \approx 3$ in the mean-driven regime (blue circles) and $n_{\mathrm{tr}} \approx 1$ in the excitable regime (green circles). Increasing the number of transient intervals from two to three in the mean-driven regime requires a tenfold increase in the timescale τ_{er} (note the logarithmic scale). Surprisingly, more transient intervals are observed when the parameter ε is decreased. This suggests that a large number of transient intervals is due to a weak depletion of the ER with each spike rather than due to a slow replenishment.

We also examine how the serial correlation coefficient ρ_1 relates to the experimentally more easily accessible number of transient interval n_{tr} and cumulative refractory period ΔT when the three statistics are varied as a function of ε and τ_{er}. It turns out that the dependence of the three statistics on τ_{er} shown in Fig. 3.34A$_1$ and A$_2$ is rather simple. Increasing τ_{er} leads to an increase in all three statistics, although the SCC ρ_1 and the number of transient intervals n_{tr} seem to saturate for large values of τ_{er}. As shown in Fig. 3.34B$_1$ and B$_2$, the case is more complicated when the parameter ε is varied. The nonmonotonic dependence of ρ_1 on ε leads to a nonmonotonic dependence of ρ_1 on both n_{tr} and ΔT. It is thus reasonable to distinguish two regions, one in which the intervals are more strongly correlated the larger ε (gray area) and one in which the intervals are less strongly correlated the larger ε (white area). If we restrict ourselves to small values of ε (gray area), i.e., a case where the ER is only slightly depleted with each spike, we can conclude that, regardless of whether ε or τ_{er} is changed, the ISIs are the more strongly correlated the larger the cumulative refractory period $|\rho_1| \propto \Delta T$. In contrast, the relation between the SCC ρ_1 and the number of transient intervals n_{tr} is ambiguous and depends on whether τ_{er} or ε is varied. Conversely, if we consider large values of ε (white area), where the ER is considerably depleted with each spike, we find that the ISIs are more strongly correlated the larger the number of transient intervals, $|\rho_1| \propto n_{\mathrm{tr}}$. In this case, the relation between the SCC ρ_1 and the cumulative refractory period ΔT becomes ambiguous. We expect the first case to be more relevant since experimental ISI sequences often show long transients associated with a small net loss ε.

Finally, in Fig. 3.35, we ask what conclusions can be drawn about the adaptation parameters

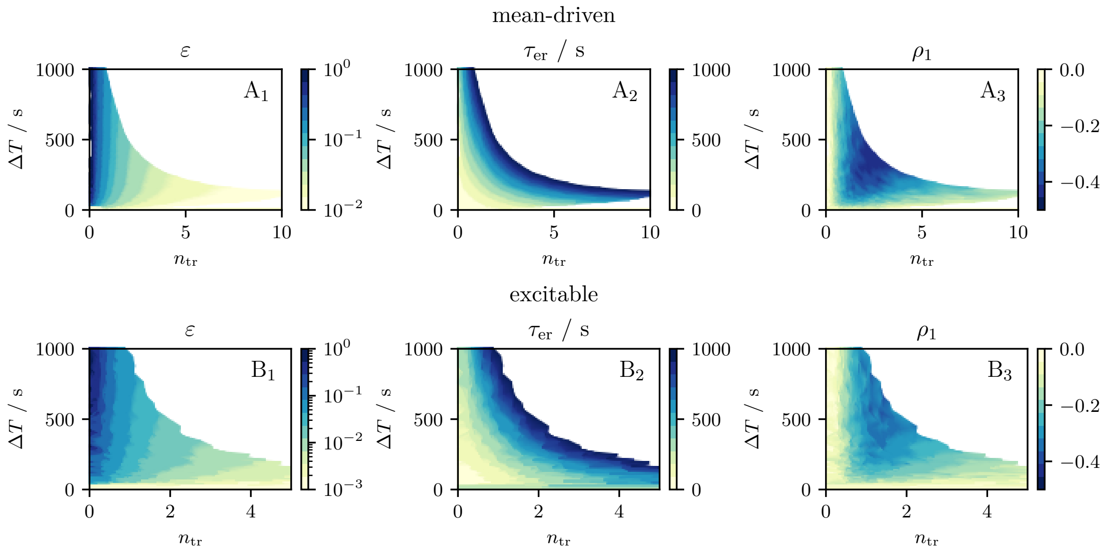

FIGURE 3.35: Summary of the behavior of the slow store Ca^{2+} dynamics. Panels A and B show the relations between the transient statistics n_{tr}, ΔT and the system parameters ε, τ_{er} as well as the SCC ρ_1 in the mean-driven (A) and excitable (B) regime. White regions in the plots show the pairs (n_{tr}, ΔT) which are not attained for $\tau_{er} < 10^3$s. Increasing τ_{er} beyond 10^3s has little effect on the boundaries of these regions. Long transients often indicate a small net loss (small ε) and slow replenishment (large τ_{er}). Large cumulative refractory periods can be realized by a large net loss or slow replenishment. Interval correlations are maximized for an intermediate number of transient intervals and intermediate cumulative refractory periods. Parameters Mean-driven: $\tau = 5$s, $p = 0.015$; Excitable $\tau = 1$s, $p = 0.06$.

τ_{er} and ε and the SCC ρ_1 when the statistics of the transient are known. These conclusions also depend on the two model parameters τ and p, which determine whether the model is mean-driven or excitable. Regardless of the firing regime, however, the results tend to be similar. Typically, long transients coincide with a small net loss of Ca^{2+} (small ε) and a slow replenishment process (large τ_{er}). Substantial adaptation of the ISI requires a substantial net loss unless the replenishment process is extremely slow. The SCC ρ_1 increases with ΔT except for very short transients (Fig. 3.35A$_3$ and B$_3$). The dependence of ρ_1 on n_{tr} is nonmonotonic. This was previously observed and attributed to the nonlinear dependence of the SCC on ε but is shown here over a wider range of transient statistics and in both firing regimes.

3.5.5 Stimulated HEK cells

Here, we ask to what extent the *nonrenewal* model can reproduce experimentally observed ISI sequences from stimulated HEK cells. In contrast to Sec. 3.4.4, where we tested the ability of the *renewal* model to reproduce stationary ISI statistics, we are now also interested in transient statistics. For this reason, we do not truncate the transients nor average the interval sequences of different cells as we did previously but consider the entire interval sequence of each cell individually. To fit our model to the data, we first determine four statistics of the experimental ISI sequence, namely the initial interval T_0^{HEK}, the stationary interval T_∞^{HEK}, the stationary CV $C_V(T^{\mathrm{HEK}})$, and the number of transient intervals n_{tr}^{HEK}. Based on these four statistics, the four model parameters p, τ, ε, and τ_{er} are determined so that the initial mean interval $\langle T_0 \rangle$, the stationary mean interval $\langle T \rangle$, the stationary CV $C_V(T)$, and the number of transient intervals n_{tr} obtained from the stochastic simulation of the model agree within a certain tolerance with the corresponding statistics from the experimental sequences. As in Sec. 3.4.4, we consider only those sequences that become stationary and exclude a small number of traces where the first intervals are not clearly distinguishable. For 24 out of 36 sequences, both conditions are met.

To determine the four statistics, we proceed in two steps. In a first step we fit Eq. 3.5.47 to the experimental ISI sequence $\{T_i\}$ in order to determine T_0^{HEK}, T_∞^{HEK}, and n_{tr}^{HEK}. To this end, we use the curve_fit function of the SciPy module [259] with the additional condition that all fitting parameters are positive. In a second step, we truncate the first $2n_{tr}$ (rounded up) intervals from

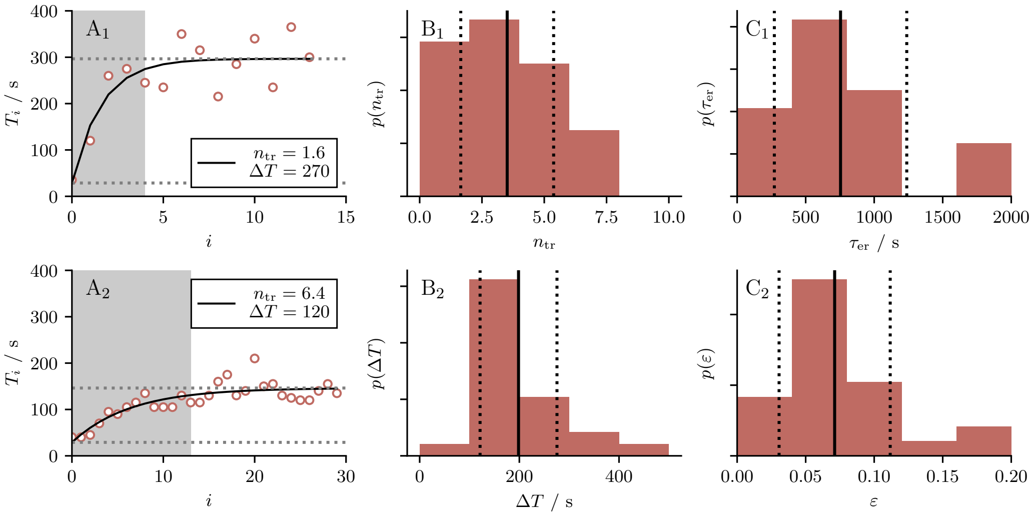

FIGURE 3.36: Transient interspike interval statistics from stimulated HEK cells. Panels A$_1$ and A$_2$ show two ISI sequences from stimulated HEK cells (red circles) with the corresponding least-square fit of Eq. 3.5.2 (black lines). The resulting number of transient intervals n_{tr} and the cumulative refractory period ΔT are given in the legend. Panels B$_1$ and B$_2$ show the frequency with which certain values of n_{tr} and ΔT are observed. The solid vertical lines indicate the mean, the dotted vertical lines indicate the mean plus or minus the standard deviation. Panels C$_1$ and C$_2$ show the frequency at which the resulting model parameter τ_{er} and ε are observed. Again the lines indicate the mean and the standard deviation.

the ISI sequence and calculate $C_V(T^{\mathrm{HEK}})$ from the remaining stationary sequence. We emphasize again that in contrast to Sec. 3.5.4 where sequences of *mean* intervals $\{\langle T_i \rangle\}$ have been considered, here single realizations $\{T_i\}$ are used. In Fig. 3.36A$_1$ and A$_2$, the fit procedure is illustrated by means of two experimental ISI sequences (red circles). The black lines show the least-square fit, while the gray area indicates the intervals that are truncated in order to determine the CV. As can be seen from these two figures, the cells are subject to considerable cell-to-cell variability. For instance, the cell in Fig. 3.36A$_1$ exhibits only a short transient but a large cumulative refractory period, whereas the opposite is true for the cell shown in Fig. 3.36A$_2$. In Fig. 3.36B$_1$ and B$_2$, we show the frequency with which certain values for the two transient statistics n_{tr} and ΔT are observed. The solid black line indicates the mean

$$\mu(x) = \frac{1}{n}\sum_{i=1}^{n} x_i, \tag{3.5.51}$$

whereas the dotted lines indicated the standard deviation

$$\sigma(x) = \sqrt{\frac{1}{n-1}\sum_{i=1}^{n}(x_i - \mu(x))^2}. \tag{3.5.52}$$

In both cases, x is a dummy variable. We find that both the number of transient intervals n_{tr} with a mean of $\mu(n_{\mathrm{tr}}) = 3.5$ and a variance of $\sigma(n_{\mathrm{tr}}) = 1.9$, as well as the cumulative refractory period ΔT with $\mu(\Delta T) = 200\,\mathrm{s}$ and $\sigma(\Delta T) = 80\,\mathrm{s}$ vary significantly across different cells.

To determine the four parameters τ, p, ε, and τ_{er} we require that the model reproduce the four statistics. To this end, we use again the Nelder–Mead method to minimize the loss function $f(x_1, \ldots, x_4) = \sum_i |x_i - y_i|/x_i$, where $x_i \in [T_0^{\mathrm{HEK}}, T_\infty^{\mathrm{HEK}}, C_V(T^{\mathrm{HEK}}), n_{\mathrm{tr}}^{\mathrm{HEK}}]$ are the target statistics obtained from the fit procedure described above and $y_i \in [\langle T_0 \rangle, \langle T \rangle, C_V(T), n_{\mathrm{tr}}]$ are the output statistics of the model.

A problem of the fit procedure arises from the fact that the output statistics of the model are themselves stochastic quantities when determined from a finite ISI sequence. This can give rise to serious problems for the Nelder-Mead method since the gradient of the cost function may not be determined correctly. In principle, this problem can be solved by longer simulation times, but this is often not feasible due to time constraints. Therefore, we use the numerically more efficient

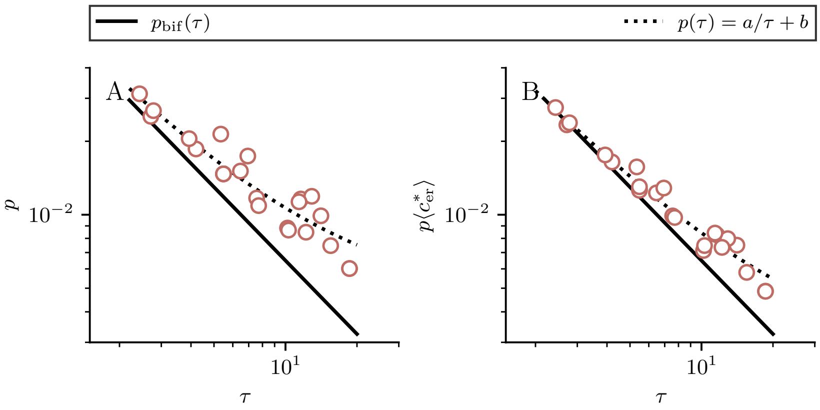

FIGURE 3.37: Parameters of the renewal model. Panel A shows that the two parameters τ and p obtained from the fit procedure (red circles) are highly correlated. This is because the model operates close to the bifurcation line (solid black line) given by Eq. 3.4.37 but still in the mean-driven regime. Panel B shows the "effective" permeability $p\langle c_{\mathrm{er}}^* \rangle$. The model would still operate in the mean-driven regime even when the stationary mean value $\langle c_{\mathrm{er}}^* \rangle$ is considered.

Langevin approximation to compute the output statistics. Unfortunately, this is still not sufficient to solve the minimization problem in a reasonable time. Therefore, we split the four-parameter minimization problem into two two-parameter minimization problems. We determined the parameters of the renewal model p and τ in the first step and the remaining two parameters of the nonrenewal model ε and τ_{er} in the second step. We recall that the first ISI of the nonrenewal model is statistically equivalent to the intervals of the renewal model. Therefore, to determine the parameters p and τ, we require that the mean ISI of the renewal model matches the fit parameter T_0^{HEK}. This does not suffice to determine two model parameters uniquely. In addition, we require that the CV of the renewal model reproduces the experimental CV of the stationary intervals. We note that this introduces a systematic error in the estimation of the model parameters because we are essentially assuming that the CV is unaffected by the depletion of the ER. As discussed in Sec. 3.5.1, this is not the case. However, it turns out that the change in variability due to the adaptation results in an absolute error in the CV that is usually well below 0.1 (with two exceptions where the error is just above 0.1). The resulting parameter pairs p and τ are shown in Fig. 3.37A. The solid black line indicates the bifurcation line separating the excitable from the mean-driven regime. It can be seen that, in order to reproduce the statistics of the stimulated HEK cells, the model always operates in the mean-driven regime but close to the bifurcation line. The proximity to the bifurcation leads to a strong correlation of the two parameters p and τ. Exactly on the bifurcation $p_{\mathrm{bif}}(\tau) = a/\tau$ with $a = (c_T - c_0^*)/(pK\mu_x(c_T))$ holds and also near the bifurcation the relation of the two parameters can be well described by the function $p = a/\tau + b$. The additional parameter b reflects that for large values of τ, the parameter p still has to take a finite value for the model to generate physiologically plausible interspike intervals. That the model operates in the mean-driven regime would still be the case when instead of p, the effective permeability $p\langle c_{\mathrm{er}}^* \rangle$ is considered, as shown in Fig. 3.37B.

To determine the remaining two parameters of the nonrenewal model, we require that the stationary interval $\langle T \rangle$ agrees with T_∞^{HEK} and that the number of transient intervals n_{tr}, which we obtain as a fit parameter from the numerical data, is equal to the number of transient intervals $n_{\mathrm{tr}}^{\mathrm{HEK}}$, which we obtain as a fit parameter from the experimental data. The distributions of the two parameters τ_{er} and ε are shown in Fig. 3.36C$_1$ and C$_2$ and reveal that the timescale τ_{er} with a mean of $\mu(\tau_{\mathrm{er}}) = 800$s and a variance of $\sigma(\tau_{\mathrm{er}}) = 500$s is rather large, while the depletion amplitude ε with $\mu(\varepsilon) = 0.07$ and $\sigma(\varepsilon) = 0.04$ is small. That the parameter ε is rather small has already been suspected due to the often large number of transient intervals observed.

Using the model parameters, we simulate long sequences of ISIs to determine the cumulative refractory period ΔT, the number of transient intervals n_{tr}, and the SCC ρ_1. In Fig. 3.38A$_1$ and A$_2$ we show the resulting correlation coefficient as a function of ΔT and n_{tr}, similarly to what was done in Fig. 3.34. We note that the distribution of correlation coefficients is not a numerical error but reflects the variability of the model parameters. First of all, we observe stronger interval correlations ρ_1 for larger cumulative refractory periods ΔT (Pearson correlation coefficient $\rho = -0.6$)

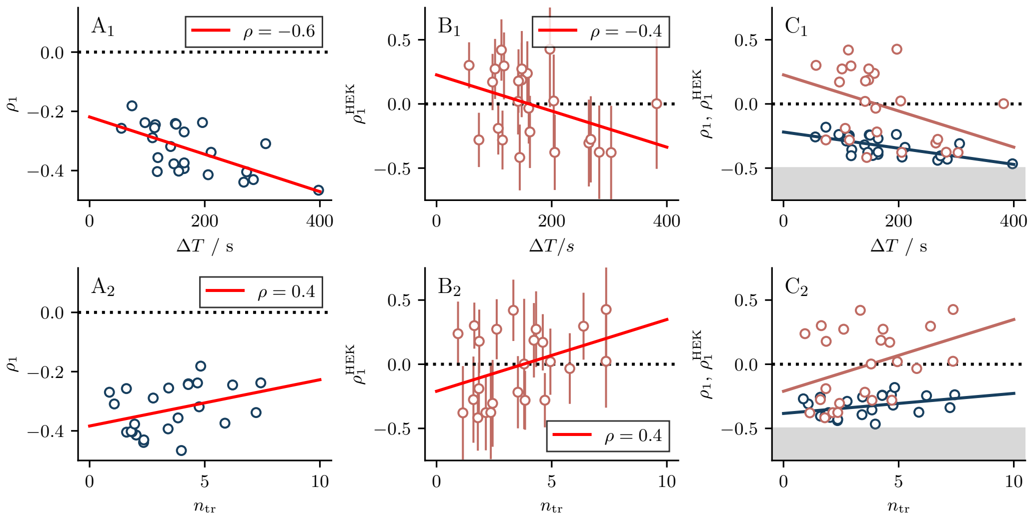

FIGURE 3.38: Stationary over transient interspike interval statistics. Panels A$_1$ and A$_2$ show the SCC ρ_1 as functions of the cumulative refractory period ΔT and number of transient intervals n_{tr}, obtained from stochastic simulations. Parameters have been chosen to reproduce experimental ISI sequences as described in the main text. The red line shows a linear regression. The corresponding Pearson correlation coefficient is given in the legend. Panels B$_1$ and B$_2$ show the same statistics as A$_1$ and A$_2$, except that the SCC ρ_1^{HEK} was determined from the stationary part of the experimental ISI sequence. The error bars correspond to the standard deviation $\sigma(\rho_1)$, determined according to Eq. 3.5.54. Panels C$_1$ and C$_2$ show both the SCC ρ_1 and ρ_1^{HEK}. The solid lines show the linear regressions. The gray area highlights the region $\rho_1 < -1/2$ that is inaccessible if the SCCs ρ_k decay monotonically with k.

and weaker interval correlations ρ_1 for larger numbers of transient intervals n_{tr} ($\rho = 0.4$). Based on our discussion of Fig. 3.34, the fact that adjacent intervals are the more anticorrelated the larger the cumulative refractory period ($|\rho_1| \propto \Delta T$) is to be expected. This is so because, for small values of ε, any increase in ΔT leads to a decrease in ρ_1. The relation is less clear for the correlation coefficient ρ_1 and the number of transient intervals n_{tr}. If the number of transient intervals increases because τ_{er} is varied, we expect more pronounced interval correlations ρ_1 for larger numbers of transient intervals n_{tr} (Fig. 3.34A$_2$). If the number of transient intervals increases because ε is varied (for ε small), we expect less pronounced interval correlations ρ_1 for larger numbers of transient intervals n_{tr} (gray area in Fig. 3.34B$_2$). Which of the two relations will dominate? We have already pointed out that for large values of τ_{er}, the number of transient intervals hardly changes with τ_{er}. In contrast, the number of transient intervals is much more sensitive to a change in ε. Since τ_{er} is indeed large and the relative standard deviation for both parameters τ_{er} and ε is similar (see Fig. 3.36B$_1$ and B$_2$), we expect the dependence on ε to reflects the relation between ρ_1 and n_{tr}. This is likely why we observe in Fig. 3.38A$_2$ that adjacent intervals become less strongly correlated as the number of transient intervals increases. In Fig. 3.38B$_1$ and B$_2$, we show ρ_1^{HEK} as a function of ΔT and n_{tr}, where the SCC has been determined from the stationary part of the experimental ISI sequences. We find that the general trend is also confirmed here, although the SCC is often positive, which our model cannot explain.

Before we discuss why this might be the case, it should be noted that the sequences of stationary intervals over which the sample SCC has been determined are often relatively short (17 intervals on average). As a consequence, the estimation of the SCC is rather imprecise, and the error is large.

According to Cox and Lewis [46] the variance of the SCC $\tilde{\rho}_k$ estimate from a finite sequence of n intervals can be approximated in leading order of $1/n$ by

$$\sigma^2(\tilde{\rho}_k) \approx \frac{1}{n-k}\left(1 + 2\sum_{k=1}^{\infty} \rho_k^2\right). \tag{3.5.53}$$

Assuming for simplicity that only the first correlation coefficient is finite and every other coefficient vanishes ($\rho_k = \rho_1 \delta_{1,k}$), this allows us to estimate the error of the SCC $\tilde{\rho}_k$ as follows

$$\sigma(\tilde{\rho}_1) \approx \sqrt{\frac{1}{n-1}(1+2\rho_1^2)}. \tag{3.5.54}$$

In addition to the difficulty of accurately determining the SCC from a relatively short sequence of intervals, there are two other possible explanations for the observed positive correlations between adjacent intervals. First, even slight nonstationarities may cause several consecutive intervals to be systematically above or below the mean. Such trends lead to positive correlations. Indeed, we have determined the SCC over the last $n - 2n_{\mathrm{tr}}^{\mathrm{HEK}}$, which are only approximately stationary. This can be seen in Fig. 3.36A$_1$ and A$_2$ by the fact that even after $2n_{\mathrm{tr}}^{\mathrm{HEK}}$ intervals, the black lines still systematically deviate from the stationary mean interval (upper dotted line). Second, the positive correlations could be due to processes not described by our model. Two possibilities come to mind. First, depending on the number of Orai1 ion channels responsible for SOCE, the slow replenishment of the ER could also be noisy. This could result in an additional slow noise leading to positive ISI correlations (cf. Chapter 2 and [96]). Second, the mitochondria are also known to store Ca^{2+} in addition to the ER. Although the release of Ca^{2+} from the ER via IP$_3$ receptors is the most important process for triggering Ca^{2+} spikes, a slow release of Ca^{2+} from the mitochondria could affect the intervals over multiple spike times or result in a small trend in the data. The distribution of the correlation coefficients in Fig. 3.36C$_1$ and C$_2$ might suggest this. In particular, Fig. 3.36C$_1$ clearly illustrates that the experimental correlation coefficients (red circle) fall into two well-separated groups, one with negative correlations that are well reproduced by our model (blue circles) and a second with positive correlations that our model cannot explain. This could suggest that, at least for the negative interval correlations, ER depletion is the relevant process. This hypothesis is supported by the fact that the lower bound $\rho_1 > -1/2$ predicted by us is not violated. Conversely, the process leading to positive correlations is not captured by our model.

3.6 Summary

This chapter has been concerned with the modeling of Ca^{2+} spikes and the analytical calculation of their statistics. To this end, we have developed a phenomenological but biophysically grounded model that describes the formation of Ca^{2+} spikes and accounts for randomness and adaptation in the spike generation. The model has two components: The first describes the number of open IP$_3$R channels in a cluster using a cyclic Markov chain; the second uses an integrate-and-fire approach to describe the dynamics of the cytosolic and the ER Ca^{2+} concentration. We have shown that the description of individual IP$_3$R channels using Markov chains has a certain tradition. In contrast, the description of Ca^{2+} spikes using the integrate-and-fire framework represents a new approach. In the past, Ca^{2+} spikes were often conceptualized as oscillations and considered from a dynamical systems point of view [179, 180, 182]. However, the fact that cell-wide Ca^{2+} spikes are rather stereotyped and reliably initiated by CICR suggests that we are dealing with an excitable system that can be described similarly to neural spike generation. Thus, it is reasonable to focus on Ca^{2+} spiking as a stochastic point process [65].

Regarding the first component of our model, which describes the activity of clusters of IP$_3$Rs, deriving such models from single-channel models is difficult because the channels are strongly coupled by local positive feedback. Since the resulting waiting time distributions for closed and open cluster states are often relatively simple, we took a different approach and built our model on various experimentally available puff statistics. Specifically, the following observations have been used to build the model:

1. Puffs occur randomly [193].
2. The opening of any channel can trigger a puff, i.e., the opening rate is a linear function of the number of channels in a cluster [197].
3. The number of responding channels in a cluster is uniformly distributed over the total number of channels in a cluster [225].

4. Dwell times in a cluster state with a given number of open channels are independent of this number [201].

5. The intervals between the puffs exhibit a refractory period [206].

In addition, we have assumed that the opening rate of the cluster depends on Ca^{2+}. Unfortunately, little is known about the exact nature of this dependence. However, since we have assumed that the opening of a single channel triggers the opening of the cluster, it is reasonable to assume that the cluster and channel opening rates depend similarly on Ca^{2+}. For the resulting cluster model, we were able to analytically calculate statistics of the puff strength and the interpuff intervals, assuming a static cytosolic Ca^{2+} concentration. This assumption is often fulfilled because the state of a cluster changes rapidly compared to the cytosolic Ca^{2+} concentration. Interestingly, it turns out that because the number of responding channels is uniformly distributed, the puff strength is highly stochastic and closely follows an exponential distribution. This may motivate the formulation of even simpler cluster models with only one open state. Most importantly, we have shown that the mean and noise intensity can be calculated from the transition rate matrix of the cluster model. While the calculation of the mean has been known, this was not the case for the noise intensity. Furthermore, we have shown that the method is generally applicable and not limited to our specific cluster model. This could also find application in models of cardiomyocytes and their Ca^{2+} release units.

The second component of our model describes the dynamics of the cytosolic and the ER Ca^{2+} concentrations. To this end, we have adopted the famous integrate-and-fire framework from computational neuroscience and modeled the cytosolic Ca^{2+} concentration only up to a certain threshold, at which point a spike is fired, and the cytosolic Ca^{2+} concentration is reset. We have assumed that the IP_3-independent currents below the threshold can be summarized into a linear leak current, whereas the IP_3-dependent puff current resulting from the cluster activity is Ca^{2+}-dependent and mediates the positive feedback (CICR). Moreover, we have shown that the puff current is stochastic, resulting in a cluster noise acting on the cytosolic Ca^{2+} concentration that is very similar to the channel noise acting on the membrane potential of neurons. For the dynamics of the ER Ca^{2+} concentration, we have assumed that some of the Ca^{2+} released into the cytosol during the spike is lost to the extracellular medium and that the ER is slowly replenished between spikes by SOCE. The resulting dynamics are very similar to those of spike-triggered adaptation.

We have seen that the two-component model is numerically expensive and difficult to treat analytically because the puff current is a complicated stochastic process that is neither Gaussian nor uncorrelated. However, the characteristic timescale of the puff current, or more precisely, the cluster activity, is usually small compared to the characteristic timescale of the leak current. This allowed us to derive a Langevin approximation of the two-component model where the number of open channels in a cluster is replaced by a Gaussian white noise that is fully determined by the mean and noise intensity of a cluster. Stochastic simulations of the Langevin approximation are orders of magnitude faster than simulations of the two-component model. Moreover, the Langevin approximation allows us to distinguish the mean-driven from the excitable regime and to formulate the corresponding Fokker-Planck equation, i.e., to use the powerful arsenal of the theory of Markov processes [59, 60].

We considered the two-component model and the corresponding Langevin approximation in two variants. The first was the renewal variant, where we assumed that the Ca^{2+} concentration in the ER is fixed. This corresponds to a situation where the ER is either weakly depleted or rapidly replenished. In this case, the model is one-dimensional, and the ISIs are statistically independent and identically distributed. Put differently, spiking is a renewal process. Solving the corresponding one-dimensional Fokker-Planck equation is a standard problem in the theory of stochastic processes and allowed us to derive expressions for the mean and the CV of the ISI [57, 248]. In addition to validating our simulation results, the Langevin approximation allows us to explore the effect of a fast Ca^{2+} buffer on spiking statistics. Contrary to popular belief, we have shown that a fast Ca^{2+} buffer is equivalent to a rescaling of time only in the deterministic limit. When the noise is taken into account, the statistics of the ISI depend on the fast Ca^{2+} buffer in a more complicated way. In short, the fast buffer reduces the noise intensity more strongly than the mean. We have shown that this can be well understood using the scaling properties of white noise and has different effects on the ISI statistics depending on whether the model operates in the mean-driven or excitable regime and how close it is to the bifurcation between these two regimes (coherence resonance). Finally, we demonstrated that the renewal model can quantitatively reproduce spiking statistics of stimulated HEK cells, ranging from ISI density to spike train power spectrum to spike-count Fano factors.

The second variant of the model is the nonrenewal version, which accounts for the cumulative ER depletion and is very similar to an adaptive integrate-and-fire model. Since spike generation is largely driven by the passive release of Ca^{2+} from the ER into the cytosol, a decrease in ER Ca^{2+} concentration affects spiking statistics. Most obviously, we have shown that ER depletion leads to a slowing of the spike generation. In addition, this adaptation reduces the difference in the ISI variability between the mean and excitable regimes, thereby increasing the robustness of the CV. However, ER depletion not only affects first-order stationary statistics but also causes intervals to be neither independent in stationary state nor identically distributed during the transient. We have described correlations between intervals by the SCC ρ_k. In terms of the previous chapter, our model corresponds to a Type 1 neuron model with a weak adaptation. This implies that, at least in the weakly perturbed mean-driven regime, the SCC decreases monotonically with lag k, which in turn implies a lower bound on the first correlation coefficient $\rho_1 > -1/2$. We have shown that this lower bound is obeyed not only in the mean-driven but also in the excitable regime. To characterize the transients, we have fitted the ISI sequences with a simple exponential function $T_\infty - (T_\infty - T_0)\exp(-i/n_{\mathrm{tr}})$, which allows to determine the cumulative refractory period $\Delta T = T_\infty - T_0$ and the number of transient intervals n_{tr}. We have provided approximations for both of these statistics. Interestingly, we have shown that the number of transient intervals, which characterizes the length of the transient, is not so much affected by the timescale at which the ER is replenished but by the amplitude at which the ER is depleted. In addition, we find that when ER depletion with each spike is not too strong (small ε), larger cumulative refractory periods are associated with stronger interval correlations and smaller number of transient intervals are associated with stronger interval correlations. This suggests that long transients indicate weak ER depletion with each spike. (However, the cumulative depletion can still be strong.)

Finally, we used the nonrenewal model to reproduce the transient statistics of ISI sequence from stimulated HEK cells. The resulting model parameters suggest that ER depletion with each spike is indeed weak. We note that this does not necessarily contradict the substantial depletion of the ER required to activate STIM1 and SOCE. This is so because the licensed IP_3Rs are well placed to locally deplete the stores closest to the ER-PM junctions where SOCE occurs [260]. We also determined the correlation coefficient of the experimental ISI sequence. It was found that the lower bound $\rho_1 > -1/2$ is always obeyed and that the trends with respect to the cumulative refractory period and the number of transient intervals predicted by the model are confirmed. However, it should be noted that we also frequently observe positive correlations between adjacent intervals in the experimental data. This cannot be explained by our model. Whether these positive correlations are due to an imprecise estimation of the correlation coefficient, a slow process that we have not accounted for, or weak nonstationarity, is not clear.

Chapter 4

Discussion and outlook

This thesis was concerned with the nonrenewal generation of spikes. We have studied two biophysical signaling systems. First, neural signaling, where the spikes are short electrical pulses, and second, Ca^{2+} signaling, where the spikes are chemical pulses. In both cases, the generation of the spike is a nonrenewal stochastic process. This not only implies a rich statistical structure of the spike train, but can also improve the transmission of a time-dependent signal or the performance in a signal detection task [70–73]. It is therefore an important theoretical task to understand spiking models that generate nonrenewable spike trains.

In the case of neurons, spiking is nonrenewal due to various slow processes. One of the most essential and ubiquitous processes often associated with negatively correlated intervals are self-inhibitory adaptation currents, which are responsible for the phenomenon of spike-frequency adaptation [18]. Positive correlations are often associated with a positively correlated input noise, which can result from slow channel gating, synaptic filtering, or slow network processes [85–91]. It is interesting to ask how these two processes, adaptation and correlated noise, interact with the dynamics of the membrane potential to shape the correlations between ISIs. So far, these two processes have only been considered separately and in a number of special cases, assuming a slow noise [66, 174], a weak noise [74, 92, 95, 115, 175], a weak adaptation [97, 176], or a discrete Markov-state description [96, 261]. The most realistic case, in which ISI correlations are evoked by a combination of adaptation and correlated noise, has not yet been theoretically understood.

In Chap. 2 of this thesis, we have extended the weak-noise theory developed by Schwalger and Lindner [74] to cover precisely this case. The theory is based on the phase reduction of a deterministic oscillator. Consequently, the system must be in the mean-driven firing regime, i.e., it must emit spikes even in the absence of fluctuations. In this case, perturbations of the higher dimensional system from its limit cycle can be translated into perturbations of the one-dimensional phase variable via the phase response curve and finally into shifts of the spike time. This approach has been very fruitful in computational neuroscience [136, 145, 262]. Here, it allowed the analytical calculation of the variance $\langle \delta T^2 \rangle$, the covariance $\langle \delta T_i \delta T_{i+k} \rangle$, and the correlation coefficients ρ_k of the ISIs in leading order of the perturbation. It turns out that the SCC ρ_k for an adaptive integrate-and-fire model driven by correlated noise can be expressed as the weighted sum of the two SCC that would result if the correlation-inducing processes were considered separately. We have also shown that how adaptation and correlated noise affect the interval correlations depends crucially on the shape of the PRC, which in turn is closely related to i) the neuron type, determined by the spike-onset bifurcation, and ii) the neuron class, determined by the shape of the F-I curve [99, 145]. In particular, the behavior can be counterintuitive for neuron models with partially negative PRC because adaptation currents can induce positive interval correlations, and positively correlated noise can induce negative interval correlations. Furthermore, two biophysically relevant special cases were studied, one where a finite population of adaptation channels causes both adaptation and correlated noise and another where the noise resembles that of a recurrent network in the asynchronous irregular state. Finally, although developed for IF models, we have shown that the theory also applies to the conductivity-based Traub-Miles model with an M-type current and correlated noise. In all these cases, the SCC can be predicted quantitatively, demonstrating the broad applicability of the theory.

We have studied the spontaneous activity of neurons under the influence of Gaussian noise. Two extensions of this case come to mind. First, as explained in the introduction, the assumption that the fluctuations are Gaussian distributed relies on the superposition of many small random events in a short interval - for example, due to the random opening and closing of a large number of ion channels or synaptic bombardment in the cortex. However, the effect of individual spikes on the postsynaptic voltage may not always be small. Some postsynaptic potentials can be as large as 1 mV to 10 mV [263–265] with distances from resting to threshold voltage between 10 mV to 20 mV in pyramidal cells [42, 264]. Thus, a small number of arriving spikes can be sufficient to elicit a response. In addition, at higher levels of processing, as the neural response becomes more selective, the spike trains become increasingly sparse [266, 267]. In both cases, the input spike trains are poorly represented by a Gaussian random process but can be more accurately described by shot noise. Although integrate-and-fire models driven by shot noise have been considered in the past to calculate first-order statistics such as the firing rate [114], response characteristics such as the susceptibility [268, 269], and even interval correlations in a neural population [270], renewal models are often considered, or the shot noise is assumed to be uncorrelated. The calculation of higher-order statistics for more complicated nonrenewal models driven by correlated shot noise may be feasible through a phase description of the spike generator. Second, while the spontaneous activity is certainly important, so are the response properties of neuron models driven by time-dependent signals. We have repeatedly pointed out that negative interval correlations can improve the signal-to-noise ratio for slow periodic signals by reducing the power of the spontaneous activity at low frequencies; furthermore, it has been shown that negative ISI correlations can improve the transmission of a broadband signal [70, 73, 271]. Conversely, positive interval correlations can also be beneficial if the increased power at a low frequency is compensated by reduced power at another frequency; a process known as noise shaping [272–274]. The computation of statistical measures related to the signal transmission, such as the cross-spectrum or coherence over a broader frequency range, or even a frequency-resolved mutual information [275], is also of interest. It has been shown that the cross-spectrum and coherence function depend crucially on whether an integrator or a resonator model is considered [276, 277]. Since this difference is well reflected in the PRC, it may turn out that such measures are analytically accessible in the framework presented here, even for more complicated models equipped with an adaptation mechanism or subject to correlated noise.

The limiting factor, however, is that the method relies on the phase reduction of a *deterministic* oscillator. For this case, the theory allows the calculation of second-order statistics, which are extremely difficult to determine otherwise. The generalization of the theory to stochastic oscillators that do not have a periodic solution in the deterministic limit is, of course, interesting. In the context of neuron models, this corresponds to a generalization of the theory to the excitable firing regime. The first step in this direction would be to generalize the notion of a phase to stochastic oscillators. Significant progress has been made in this regard recently [278–280]. Unfortunately, these theories are often based on the formulation of the Kolmogorov-backward operator, which has not yet been formulated for IF models with a reset rule. However, this difficulty does not in principle prevent the definition of a phase for stochastic IF models, as we have shown numerically for the adaptive leaky integrate-and-fire model [3]. It turns out that the stochastic (mean return-time) phase has interesting properties. For example, if one generates event times whenever a certain isochrone (instead of the firing threshold) is crossed, the intervals between these times do not show linear correlations. Despite the difficulties of determining the stochastic phase of an IF model, the theory presented here, the possible applications outline above, and the recent progress in reducing stochastic oscillators should encourage further research in this direction.

In Chap. 3, we have dealt with the nonrenewal spike generation in cells that use Ca^{2+} as a second messenger. We have seen that although neural and Ca^{2+} spikes are observed in different physical quantities and on different timescales, both signaling systems share some important principles concerning the generation of spikes. First, a spike is reliably initiated by a strong positive feedback mechanism as soon as a certain threshold is exceeded. Second, the generation of the spike is a stochastic process [33, 34, 64]. Third, the sequence of ISIs in response to the onset of a constant stimulus often shows an initial transient during which the (mean) ISIs gradually increase to a stationary value. In the case of Ca^{2+} signaling, the stochasticity is due to the random release of Ca^{2+} from the ER through IP_3Rs [184, 201, 206, 281], and the transient is thought to result from the depletion of the ER [30–32]. However, the literature on nonrenewable Ca^{2+} spike generation is thin. This may also be because mathematical models describing the generation of Ca^{2+} spikes often follow the spirit of conductance-based models and formulate high-dimensional and nonlinear current-balance equations [179, 180, 183, 213–215, 229]. Reduced models that follow the idea of the IF framework have not yet been developed. This is surprising given the many similarities in spike generation and the great success of the IF model in computational neuroscience. Here, we have formulated such a phenomenological but biophysically grounded model of Ca^{2+} spiking that accounts for the stochastic release of Ca^{2+} by the puffs and follows the idea that the transient is due to the cumulative depletion of the ER.

We have shown that the stochastic activity of the IP_3R channels described by a Markov chain generates a stochastic Ca^{2+} current that is neither uncorrelated nor Gaussian distributed. For this reason, the computation of ISI statistics is difficult. Experimentally, it is known that the timescale of the ISI is not reflected in the kinetics of the channels [206]. In particular, the ion channel activity is fast compared to the spike dynamics. This motivates a diffusion approximation in which the stochastic Ca^{2+} current is replaced by Gaussian white noise that is fully determined by the Ca^{2+}-dependent mean and noise intensity. We have developed a method to calculate both these statistics using the transition rate matrix that defines the Markov chain. While the calculation of the mean was known, the calculation of the noise intensity was not. This approximation allowed the formulation of a Langevin equation, the corresponding FPE, and the calculation of spiking statistics.

We then considered the model in two scenarios, one in which the Ca^{2+} concentration in the ER remains constant and one in which the ER is partially depleted with each spike. In the first case, spike formation is a renewal process. In this case, statistics such as the moments of the ISI density can be calculated analytically using the FPE [57, 248]. Although this model variant cannot account for the transient or the correlations between intervals, the power spectrum (including the low-frequency limit) of a normalized and concatenated spike sequence of different HEK cells can be well reproduced. In the second case, when the depletion of the ER is taken into account, spiking is a nonrenewal process, and the model can reproduce both transient and stationary statistics of individual HEK cells. For the nonrenewal model, we have shown that in agreement with other studies [187, 250, 282–284], the CV of the stationary ISIs is, to a large extent, determined by the recovery from the negative feedback after a spike and is provided with a certain robustness to a variation of other cell parameters. Furthermore, we find that ER depletion induces negative correlations between adjacent intervals ρ_1 that do not fall below $-1/2$. This is exactly what is expected according to the considerations in Chap. 2, because our model corresponds to a Type 1 neuron model with weak adaptation. Interestingly, the lower bound $\rho_1 > -1/2$ is also not violated in the excitable firing regime, possibly indicating that the results of the second chapter can be generalized. Beyond stationary statistics, we have described the ISI sequence during the transient by the exponential function $T_\infty - (T_\infty - T_0)\exp(-i/n_{\mathrm{tr}})$ and derived approximations for the cumulative refractory period $\Delta T = T_\infty - T_0$ and the number of transient intervals n_{tr}. We have also examined how the transient statistics are related to the adaptation parameters. It turned out that a large number of transient intervals tends to coincide with a weak depletion of the ER per spike. Experimental ISI sequences tend to have relatively long transients. We conclude that the ER is significantly depleted only over many spikes. This restricts the relevant parameter space and allows to draw conclusions about the relationship between ΔT and ρ_1 as well as n_{tr} and ρ_1. Specifically, we observe that for our model, larger cumulative refractory periods are associated with stronger interval correlations, and larger numbers of transient intervals are associated with weaker interval correlations. These trends are confirmed in the experimental data. However, positive correlations are also often observed. Whether this is due to poor statistics, weak nonstationarities in the data, or some slow process that we have not accounted for is not clear.

The analytical treatment of our model is based on a diffusion approximation of the Ca^{2+} released from the ER. Such approximations go back to Einstein [285] and Smoluchowski [286, 287] and have been used in the past to study the generation of Ca^{2+} spikes [288]. In our model, the release of Ca^{2+} is controlled by the stochastic activity of IP_3R clusters, which are described by a Markov chain. The transition rates of the Markov model were chosen to depend on the intracellular Ca^{2+} concentration but not explicitly on time. Thus, when $[Ca^{2+}]_i$ is fixed, the transitions between the discrete cluster states is a homogeneous Poisson process. In this case, we have shown how the noise intensity can be determined using an algebraic equation. Because the generation of Ca^{2+} spikes can also be described by inhomogeneous Poisson processes [284], the question arises whether the theory can be extended to apply to Markov models with explicitly time-dependent rates. In its current form, this is not the case.

The model proposed here is able to reproduce the spiking statistics of stimulated HEK cells. These cells are known to generate rather regular spike times with coefficients of variation of the interspike intervals on the order of 0.2. This variability is consistent with the notion that stimulated HEK cells are mean-driven oscillators subject to a weak noise. However, as we have shown, slow adaptation can lead to highly regular spiking even in the excitable regime. We cannot exclude that this is also the case for HEK cells. Indeed, CVs observed in other cell lines ranges from 0.17 in heptocytes to 0.90 in astrocytes [7, 8, 289]. In particular, the high variability in astrocytes is a strong indication that these cells are excitable. In our model, the range of parameters for which fluctuation-driven spikes are observed is small due to the rather weak noise resulting from the stochastic activity of the IP_3R channel clusters. Thus, the generation of ISI sequences with high variability requires fine-tuning of the model parameters, which seems unlikely to occur in biological systems given the large cell-to-cell variability.

This raises the question of whether there are other relevant sources of noise in the generation of Ca^{2+} spikes that we have not considered. Several processes could be important in this regard. The first is the cluster noise itself. So far, we have considered a population of homogeneous clusters. However, the number of channels per cluster actually varies [197, 225]. Taking this variability into account could imply that the puff current through all the different clusters is effectively determined by a few large clusters, since both the mean and the noise intensity of a cluster depend superlinearly on the number of channels. Indeed, it has been reported that in Xenopus oocytes Ca^{2+} spikes are often initiated at a few focal puff sites [290]. Second, we have considered only cluster noise caused by the IP_3Rs. This is plausible because the activity of functionally coupled channels in a cluster remains highly stochastic even for a large number of channels. However, it cannot be excluded that among the multitude of ion channels responsible for maintaining the Ca^{2+} gradient, generating the spike, or refilling the ER, there are some that generate a significant channel noise, for example, due to a relatively long correlation time. Third, we assumed that the dynamics of the ER Ca^{2+} concentration does not depend on the dynamics of the subthreshold intracellular Ca^{2+} concentration because $[Ca^{2+}]_{er}$ is orders of magnitude larger than $[Ca^{2+}]_i$ [19, 29]. The assumption that the ER Ca^{2+} concentration is significantly reduced only during the spike is consistent with other studies [30]. However, if the released Ca^{2+} is also included in the dynamics of the ER, fluctuations in the intracellular Ca^{2+} concentration would also be reflected there and feed back into the intracellular Ca^{2+} concentration. This could increase the overall noise intensity. Finally, we considered a point model that neglects the spatial extent of the cell and thus the local release of Ca^{2+}. It is known that such models, which assume that the intracellular Ca^{2+} concentration is homogeneously distributed throughout the cell, often underestimate the variability of interspike intervals [64]. Therefore, spatially extended models may be needed to describe cells that generate highly stochastic spike times. Such models exist and are often referred to as fire-and-diffuse models [63, 291–293] but are extremely difficult to treat analytically.

Finally, we have observed positive interval correlations in the experimental data that cannot be explained by our model. We have already pointed out that, due to the limited number of measurable interspike intervals, we cannot rule out the possibility that this is simply due to an inaccurate calculation of the correlation coefficient. Furthermore, such correlations may result from a weak nonstationarity in the data. Especially for the considered HEK cells with relatively low ISI variability, weak nonstationarity can lead to significant correlation coefficients. However, other biophysical processes not considered in our model could also be responsible for the observed positive correlations. As shown in the second chapter of this thesis, the primary processes to consider in this regard are those that generate temporally correlated noise. A possible candidate for this could be the already discussed counterpart of the fluctuations of the intracellular Ca^{2+} concentration in the ER Ca^{2+} concentration. In this case, the fluctuations of the intracellular Ca^{2+} concentration would be low-pass filtered by the dynamics of the ER Ca^{2+} concentration and thus re-enter the intracellular Ca^{2+} concentration as a correlated noise. Another possible process that we have not discussed is the storage and release of Ca^{2+} in and from mitochondria. Although mitochondria are unlikely to be of primary interest for the generation of Ca^{2+} spikes themselves, their precise role in Ca^{2+} signaling is a subject of ongoing research [294–298]. From a dynamical point of view, the abundance and small size of the mitochondria could lead to a slow stochastic release of Ca^{2+} if the kinetics of the channels involved are slow.

In any case, the universality of Ca^{2+} as a second messenger should be a strong incentive to further study this fascinating biophysical system and to solve some of the problems outlined above.

Publications

[1] L. Ramlow and B. Lindner. “Interspike interval correlations in neuron models with adaptation and correlated noise”. In: *PLoS Comput. Biol.* 17.8 (2021), e1009261.

[2] V. N. Friedhoff, L. Ramlow, B. Lindner, and M. Falcke. “Models of stochastic Ca^{2+} spiking”. In: *Eur. Phys. J.: Spec. Tops* 230.14 (2021), pp. 2911–2928.

[3] K. Holzhausen, L. Ramlow, S. Pu, P. J. Thomas, and B. Lindner. “Mean-return-time phase of a stochastic oscillator provides an approximate renewal description for the associated point process”. In: *Biol. Cybern.* (2022), pp. 1–17.

[4] J. Franzen, L. Ramlow, and B. Lindner. “The steady state and response to a periodic stimulation of the firing rate for a theta neuron with correlated noise”. In: *Journal of Computational Neuroscience* 51.1 (2023), pp. 107–128.

[5] L. Ramlow, M. Falcke, and B. Lindner. “An integrate-and-fire approach to Ca^{2+} signaling. Part I: Renewal model”. In: *Biophys. J.* 122.4 (2023), pp. 713–736.

[6] L. Ramlow, M. Falcke, and B. Lindner. “An integrate-and-fire approach to Ca^{2+} signaling. Part II: Cumulative refractoriness”. In: *Biophys. J.* 122.24 (2023), pp. 4710–4729.

Bibliography

[7] A. Skupin, H. Kettenmann, U. Winkler, M. Wartenberg, H. Sauer, S. C. Tovey, C. W. Taylor, and M. Falcke. “How does intracellular Ca^{2+} oscillate: By chance or by the clock?” In: *Biophys. J.* 94 (2008), p. 2404.

[8] K. Thurley, S. C. Tovey, G. Moenke, V. L. Prince, A. Meena, A. P. Thomas, A. Skupin, C. W. Taylor, and M. Falcke. “Reliable Encoding of Stimulus Intensities Within Random Sequences of Intracellular Ca^{2+} Spikes”. In: *Sci. Signal.* 7.331 (2014), ra59.

[9] W. Gerstner, W. M. Kistler, R. Naud, and L. Paninski. *Neuronal Dynamics From single neurons to networks and models of cognition*. Cambridge: Cambridge University Press, 2014.

[10] N. Spruston. “Pyramidal neurons: dendritic structure and synaptic integration”. In: *Nat. Rev. Neurosci.* 9.3 (2008), pp. 206–221.

[11] B. Wang, W. Ke, J. Guang, G. Chen, L. Yin, S. Deng, Q. He, Y. Liu, T. He, R. Zheng, et al. “Firing frequency maxima of fast-spiking neurons in human, monkey, and mouse neocortex”. In: *Front. Cell. Neurosci.* 10 (2016), p. 239.

[12] J. Grewe, A. Kruscha, B. Lindner, and J. Benda. “Synchronous Spikes are Necessary but not Sufficient for a Synchrony Code”. In: *PNAS* 114 (2017), E1977.

[13] E. M. Izhikevich. *Dynamical Systems in Neuroscience: The Geometry of Excitability and Bursting*. Cambridge, London: The MIT Press, 2007.

[14] E. R. Kandel, J. H. Schwartz, and T. M. Jessel. *Principles of Neural Science*. U. S.: McGraw-Hill Companies, 2000.

[15] B. Hille. *Ion channels of excitable membranes*. Sunderland: Sinauer, 2001.

[16] A. L. Hodgkin and A. F. Huxley. “A quantitative description of membrane current and its application to conduction and excitation in nerve”. In: *J. Physiol. (Lond.)* 10 (1952), p. 500.

[17] J. A. White, J. T. Rubinstein, and A. R. Kay. "Channel noise in neurons". In: *Trends Neurosci.* (2000), p. 131.

[18] J. Benda and A. V. M. Herz. "A universal model for spike-frequency adaptation". In: *Neural Comput.* 15 (2003), p. 2523.

[19] D. E. Clapham. "Calcium signaling". In: *Cell* 131.6 (2007), pp. 1047–1058.

[20] W. H. Li, J. Llopis, M. Whitney, G. Zlokarnik, and R. Y. Tsien. "Cell-permeant caged InsP3 ester shows that Ca^{2+} spike frequency can optimize gene expression". In: *Nature* 392.6679 (1998), pp. 936–941.

[21] R. E. Dolmetsch, K. Xu, and R. S. Lewis. "Calcium oscillations increase the efficiency and specificity of gene expression". In: *Nature* 392.6679 (1998), pp. 933–936.

[22] J. W. Putney. "Calcium signaling: Up, down, up, down.... What's the point?" In: *Science* 279.5348 (1998), pp. 191–192.

[23] M. J. Berridge, P. Lipp, and M. D. Bootman. "The versatility and universality of calcium signalling". In: *Nature Rev. Mol. Cell Biol.* 1.1 (2000), pp. 11–21.

[24] M. Falcke. "Reading the patterns in living cells - the physics of Ca^{2+} signaling". In: *Adv. Phys.* 53 (2004), p. 255.

[25] C. G. Schipke, A. Heidemann, A. Skupin, O. Peters, M. Falcke, and H. Kettenmann. "Temperature and nitric oxide control spontaneous calcium transients in astrocytes". In: *Cell Calcium* 43.3 (2008), pp. 285–295.

[26] R. Thul, T. C. Bellamy, H. L. Roderick, M. D. Bootman, and S. Coombes. "Calcium Oscillations". In: *Cellular Oscillatory Mechanisms*. Ed. by Miguel Maroto and Nicholas A. M. Monk. Vol. 641. Advances in Experimental Medicine and Biology. Springer New York, 2009, pp. 1–27. ISBN: 978-0-387-09794-7.

[27] E. Smedler and P. Uhlén. "Frequency decoding of calcium oscillations". In: *Biochim Biophys Acta Gen Subj* 1840.3 (2014), pp. 964–969.

[28] M. J. Berridge, M. D. Bootman, and P. Lipp. "Calcium - a life and death signal". In: *Nature* 395 (1998), p. 645.

[29] K. A. Campbell. *Intracellular calcium*. John Wiley & Sons, 2014.

[30] J. Sneyd, K. Tsaneva-Atanasova, D. I. Yule, J. L. Thompson, and T. J. Shuttleworth. "Control of calcium oscillations by membrane fluxes". In: *Proc. Natl. Acad. Sci.* 101.5 (2004), pp. 1392–1396.

[31] K. Ishii, K. Hirose, and M. Iino. "Ca^{2+} shuttling between endoplasmic reticulum and mitochondria underlying Ca^{2+} oscillations". In: *EMBO reports* 7.4 (2006), pp. 390–396.

[32] T. Takahashi, T. Kikuchi, Y. Kidokoro, and H. Shirakawa. "Ca^{2+} influx-dependent refilling of intracellular Ca^{2+} stores determines the frequency of Ca^{2+} oscillations in fertilized mouse eggs". In: *Biochemical and biophysical research communications* 430.1 (2013), pp. 60–65.

[33] H. C. Tuckwell. *Stochastic Processes in the Neuroscience*. Philadelphia, Pennsylvania: SIAM, 1989.

[34] A Aldo Faisal, Luc PJ Selen, and Daniel M Wolpert. "Noise in the nervous system". In: *Nat. Rev. Neurosci.* 9.4 (2008), pp. 292–303.

[35] W. A. Catterall. "Cellular and molecular biology of voltage-gated sodium channels". In: *Physiol. Rev.* 72 (1992), S15–S48.

[36] H. L. Roderick, M. J. Berridge, and M. D. Bootman. "Calcium-induced calcium release". In: *Curr. Biol.* 13.11 (2003), R425.

[37] P. Dayan and L. F. Abbott. *Theoretical Neuroscience*. Cambridge MA: MIT Press, 2001.

[38] A. N. Burkitt. "A Review of the Integrate-and-fire Neuron Model: I. Homogeneous Synaptic Input". In: *Biol. Cyber.* 95 (2006), p. 1.

[39] A. N. Burkitt. "A review of the integrate-and-fire neuron model: II. Inhomogeneous synaptic input and network properties". In: *Biol. Cyber.* 95 (2006), p. 97.

[40] Y. H. Liu and X. J. Wang. "Spike-frequency adaptation of a generalized leaky integrate-and-fire model neuron". In: *J. Comput. Neurosci.* 10 (2001), p. 25.

[41] R. Brette and W. Gerstner. "Adaptive exponential integrate-and-fire model as an effective description of neuronal activity". In: *J. Neurophysiol.* 94 (2005), p. 3637.

[42] L. Badel, S. Lefort, R. Brette, C. C. H. Petersen, W. Gerstner, and M. J. E. Richardson. "Dynamic I-V Curves Are Reliable Predictors of Naturalistic Pyramidal-Neuron Voltage Traces". In: *J. Neurophysiol.* 99 (2008), p. 656.

[43] W. Gerstner and R. Naud. "How good are neuron models?" In: *Science* 326.5951 (2009), pp. 379–380.

[44] Romain Brette. "What is the most realistic single-compartment model of spike initiation?" In: *PLoS Comput. Biol.* 11.4 (2015), e1004114.

[45] D. R. Cox. *Renewal Theory*. London: Methuen, 1962.

[46] D. R. Cox and P. A. W. Lewis. *The Statistical Analysis of Series of Events*. London: Chapman and Hall, 1966.

[47] P. Nelson. *Biological Physics: Energy, Information, Life*. W. H. Freeman, 2003.

[48] C. Koch. *Biophysics of Computation - Information Processing in Single Neurons*. New York, Oxford: Oxford University Press, 1999.

[49] N. G. van Kampen. *Stochastic Processes in Physics and Chemistry*. Amsterdam: North-Holland, 1992.

[50] James R Norris. *Markov chains*. 2. Cambridge university press, 1998.

[51] U. Behn. "Systems under influence of dichotomous noise". In: *Static Critical Phenomena in Inhomogeneous Systems*. Proceedings of XX Karpacz Winter School on Theoretical Physics (Springer Lecture Notes in Physics. Ed. by J. Sznajd A. Pekalski. Vol. 4206. Springer, 1984, p. 305.

[52] G. E. Uhlenbeck and L. S. Ornstein. "On the Theory of the Brownian Motion". In: *Phys. Rev.* 36 (1930), p. 823.

[53] M. C. Wang and G. E. Uhlenbeck. "On the Theory of the Brownian Motion-II". In: *Rev. Mod. Phys.* 17 (1945), p. 323.

[54] A. Einstein. "The motion of elements suspended in static liquids as claimed in the molecular kinetic theory of heat". In: *Ann. Phys.-Berlin* 17 (1905), p. 549.

[55] P. Langevin. "On the theory of Brownian Motion". In: *Comptes Rendus* 146 (1908), p. 530.

[56] B. Lindner. "Neural Noise and Neural Signals". In: *Lecture notes* (2022).

[57] C. W. Gardiner. *Handbook of Stochastic Methods*. Berlin: Springer-Verlag, 1985.

[58] N. G. Van Kampen. "Itô versus Stratonovich". In: *J. Stat. Phys.* 24.1 (1981), pp. 175–187.

[59] W. Horsthemke and R. Lefever. *Noise-Induced Transitions: Theory and Applications in Physics, Chemistry, and Biology*. Berlin: Springer, 1983.

[60] H. Risken. *The Fokker-Planck Equation*. Berlin: Springer, 1984.

[61] H. Risken. *The Fokker-Planck Equation* (second edition). Berlin: Springer, 1989.

[62] A. V. Holden. *Models of the Stochastic Activity of Neurones*. Berlin: Springer-Verlag, 1976.

[63] S. Rüdiger. "Stochastic models of intracellular calcium signals". In: *Physics Reports* 534.2 (2014), pp. 39–87.

[64] G. Dupont, M. Falcke, V. Kirk, and J. Sneyd. *Models of calcium signalling*. Vol. 43. Springer, 2016.

[65] D. R. Cox and V. Isham. *Point Processes*. London: Chapman and Hall, 1980.

[66] J. W. Middleton, M. J. Chacron, B. Lindner, and A. Longtin. "Firing statistics of a neuron model driven by long-range correlated noise". In: *Phys. Rev. E.* 68 (2003), p. 021920.

[67] R. Becker. *Theory of Heat*. New York: Springer, 1967.

[68] R. Kubo. "Fluctuation-dissipation theorem". In: *Rep. Prog. Phys.* 29 (1966), p. 255.

[69] R. L. Stratonovich. *Topics in the Theory of Random Noise*. New York: Gordon and Breach, 1967.

[70] M. J. Chacron, B. Lindner, and A. Longtin. “Noise shaping by interval correlations increases information transfer”. In: *Phys. Rev. Lett.* 93 (2004), p. 059904.

[71] B. Lindner, M. J. Chacron, and A. Longtin. “Integrate-and-fire neurons with threshold noise - A tractable model of how interspike interval correlations affect neuronal signal transmission”. In: *Phys. Rev. E.* 72 (2005), p. 021911.

[72] R. Ratnam and M. E. Nelson. “Nonrenewal Statistics of Electrosensory Afferent Spike Trains: Implications for the Detection of Weak Sensory Signals”. In: *J. Neurosci.* 20 (2000), p. 6672.

[73] M. J. Chacron, A. Longtin, and L. Maler. “Negative interspike interval correlations increase the neuronal capacity for encoding time-dependent stimuli”. In: *J. Neurosci.* 21 (2001), p. 5328.

[74] T. Schwalger and B. Lindner. “Patterns of interval correlations in neural oscillators with adaptation”. In: *Front. Comp. Neurosci.* 7 (2013), p. 164.

[75] W. Gerstner. “Time structure of the activity in neural network models”. In: *Phys. Rev. E.* 51 (1995), p. 738.

[76] D. H. Perkel, G. L. Gerstein, and G. P. Moore. “Neuronal Spike Trains and Stochastic Point Processes”. In: *Biophys. J.* 7 (2006), p. 419.

[77] S. Hagiwara. “Analysis of interval fluctuation of the sensory nerve impulse”. In: *Jpn. J. Physiol.* 14 (1954), p. 234.

[78] A. B. Neiman and D. F. Russell. “Two Distinct Types of Noisy Oscillators in Electroreceptors of Paddlefish”. In: *J. Neurophysiol.* 92 (2004), p. 492.

[79] M. P. Nawrot, C. Boucsein, V. Rodriguez-Molina, A. Aertsen, S. Grun, and S. Rotter. “Serial interval statistics of spontaneous activity in cortical neurons in vivo and in vitro”. In: *Neurocomp.* 70 (2007), p. 1717.

[80] T. A. Engel, L. Schimansky-Geier, A. V. M. Herz, S. Schreiber, and I. Erchova. “Subthreshold membrane-potential resonances shape spike-train patterns in the entorhinal cortex”. In: *J. Neurophysiol.* 100 (2008), p. 1576.

[81] F. Farkhooi, M. F. Strube-Bloss, and M. P. Nawrot. “Serial correlation in neural spike trains: Experimental evidence, stochastic modeling, and single neuron variability”. In: *Phys. Rev. E.* 79 (2009), p. 021905.

[82] O. Avila-Akerberg and M. J. Chacron. “Nonrenewal spike train statistics: causes and consequences on neural coding”. In: *Exp. Brain Res.* 210 (2011), p. 353.

[83] A. J. Peterson, D. Irvine, and P. Heil. “A model of synaptic vesicle-pool depletion and replenishment can account for the interspike interval distributions and nonrenewal properties of spontaneous spike trains of auditory-nerve fibers”. In: *J. Neurosci.* 34.45 (2014), pp. 15097–15109.

[84] S. Song, J. A. Lee, I. Kiselev, V. Iyengar, J. G. Trapani, and N. Tania. “Mathematical modeling and analyses of interspike-intervals of spontaneous activity in afferent neurons of the zebrafish lateral line”. In: *Sci. Rep.* 8.1 (2018), pp. 1–14.

[85] T. Schwalger, K. Fisch, J. Benda, and B. Lindner. “How noisy adaptation of neurons shapes interspike interval histograms and correlations”. In: *PLoS Comp. Biol.* 6 (2010), e1001026.

[86] K. Fisch, T. Schwalger, B. Lindner, A. Herz, and J. Benda. “Channel noise from both slow adaptation currents and fast currents is required to explain spike-response variability in a sensory neuron”. In: *J. Neurosci.* 32 (2012), p. 17332.

[87] T. Tetzlaff, S. Rotter, E. Stark, M. Abeles, A. Aertsen, and M. Diesmann. “Dependence of neuronal correlations on filter characteristics and marginal spike train statistics”. In: *Neural Comput.* 20.9 (2008), pp. 2133–2184.

[88] R. Moreno-Bote and N. Parga. “Response of Integrate-and-Fire Neurons to Noisy Inputs Filtered by Synapses with Arbitrary Timescales: Firing Rate and Correlations”. In: *Neural Comput.* 22 (2010), p. 1528.

[89] A. Litwin-Kumar and B. Doiron. “Slow dynamics and high variability in balanced cortical networks with clustered connections”. In: *Nat. Neurosci.* 15 (2012), p. 1498.

[90] S. Ostojic. "Two types of asynchronous activity in networks of excitatory and inhibitory spiking neurons". In: *Nat. Neurosci.* 17 (2014), p. 594.

[91] S. Wieland, D. Bernardi, T. Schwalger, and B. Lindner. "Slow fluctuations in recurrent networks of spiking neurons". In: *Phys. Rev. E* 92 (2015), 040901(R).

[92] B. Lindner. "Interspike interval statistics of neurons driven by colored noise". In: *Phys. Rev. E.* 69 (2004), p. 022901.

[93] F. Droste and B. Lindner. "Integrate-and-fire neurons driven by asymmetric dichotomous noise". In: *Biol. Cybern.* 108 (2014), p. 825.

[94] F. Müller-Hansen, F. Droste, and B. Lindner. "Statistics of a neuron model driven by asymmetric colored noise". In: *Phys. Rev. E.* 91.2 (2015), p. 022718.

[95] T. Schwalger, F. Droste, and B. Lindner. "Statistical structure of neural spiking under non-Poissonian or other non-white stimulation". In: *J. Comput. Neurosci.* 39 (2015), p. 29.

[96] T. Schwalger and B. Lindner. "Theory for serial correlations of interevent intervals". In: *Eur. Phys. J. Spec. Topics* 187 (2010), p. 211.

[97] E. Urdapilleta. "Onset of negative interspike interval correlations in adapting neurons". In: *Phys. Rev. E.* 84 (2011), p. 041904.

[98] R. D. Traub and R. Miles. *Neuronal networks of the hippocampus*. Vol. 777. Cambridge University Press, 1991.

[99] A. Hodgkin. "The local electric changes associated with repetitive action in a medullated axon". In: *J. Physiol.* 107 (1948), p. 165.

[100] B. Lindner, J. García-Ojalvo, A. Neiman, and L. Schimansky-Geier. "Effects of noise in excitable systems". In: *Phys. Rep.* 392 (2004), p. 321.

[101] B. Ermentrout. "Linearization of F-I curves by adaptation". In: *Neural Comput.* 10 (1998), p. 1721.

[102] R.R. De Ruyter van Steveninck, G. D. Lewen, S. P. Strong, R. Koberle, and W. Bialek. "Reproducibility and Variability in Neural Spike Trains". In: *Science* 275 (1997), p. 1805.

[103] M. N. Shadlen and W. T. Newsome. "The Variable Discharge of Cortical Neurons: Implications for Connectivity, Computation, and Information Coding". In: *J. Neuroci.* 18 (1998), p. 3870.

[104] Z. F. Mainen and T. J. Sejnowski. "Reliability of spike timing in neocortical neurons". In: *Science* 268 (1995), p. 1503.

[105] N. Brenner, O. Agam, W. Bialek, and R. de Ruyter van Steveninck. "Statistical properties of spike trains: Universal and stimulus-dependent aspects". In: *Phys. Rev. E.* 66 (2002), p. 031907.

[106] J. DeFelipe and I. Fariñas. "The pyramidal neuron of the cerebral cortex: morphological and chemical characteristics of the synaptic inputs". In: *Prog. Neurobiol.* 39.6 (1992), pp. 563–607.

[107] A. Destexhe and D. Paré. "A combined computational and intracellular study of correlated synaptic bombardment in neocortical pyramidal neurons in vivo". In: *Neurocomp.* 32-33 (2000), p. 113.

[108] F. Gabbiani and S. J. Cox. *Mathematics for neuroscientists*. Academic Press, 2017.

[109] L. Lapicque. "Recherches quantitatives sur l'excitation électrique des nerfs traitéecomme une polarization". In: *J. Physiol. Pathol. Gen.* 9 (1907), p. 620.

[110] L. F. Abbott. "Lapicque's introduction of the integrate-and-fire model neuron (1907)". In: *Brain Res. Bull.* 50.5-6 (1999), pp. 303–304.

[111] L. M. Ricciardi. *Diffusion Processes and Related Topics on Biology*. Berlin: Springer-Verlag, 1977.

[112] H. C. Tuckwell. *Introduction to Theoretical Neurobiology*. Cambridge: Cambridge University Press, 1988.

[113] R. D. Vilela and B. Lindner. “A comparative study of three different integrate-and-fire neurons: Spontaneous activity, dynamical response, and stimulus-induced correlation”. In: *Phys. Rev. E.* 80 (2009), p. 031909.

[114] M. J. E. Richardson and R. Swarbrick. “Firing-Rate Response of a Neuron Receiving Excitatory and Inhibitory Synaptic Shot Noise”. In: *Phys. Rev. Lett.* 105 (2010), p. 178102.

[115] C. Bauermeister, T. Schwalger, D. Russell, A. B. Neiman, and B. Lindner. “Characteristic Effects of Stochastic Oscillatory Forcing on Neural Firing: Analytical Theory and Comparison to Paddlefish Electroreceptor Data”. In: *PLoS Comput. Biol.* 9 (2013), e1003170.

[116] A. S. Pikovsky and J. Kurths. “Coherence resonance in a noise-driven excitable system”. In: *Phys. Rev. Lett.* 78 (1997), p. 775.

[117] N. Fourcaud-Trocmé, D. Hansel, C. van Vreeswijk, and N. Brunel. “How spike generation mechanisms determine the neuronal response to fluctuating inputs”. In: *J. Neurosci.* 23 (2003), p. 11628.

[118] P. E. Latham, B. J. Richmond, P. G. Nelson, and S. Nirenberg. “Intrinsic Dynamics in neuronal networks. I. Theory”. In: *J. Neurophysiol.* 83 (2000), p. 808.

[119] D. Hansel and G. Mato. “Existence and stability of persistent states in large neuronal networks”. In: *Phys. Rev. Lett.* 86 (2001), p. 4175.

[120] E. M. Izhikevich. “Resonate-and-fire neurons”. In: *Neural Netw.* 14 (2001), p. 883.

[121] N. Brunel, V. Hakim, and M. J. E. Richardson. “Firing-rate resonance in a generalized integrate-and-fire neuron with subthreshold resonance”. In: *Phys. Rev. E.* 67 (2003), p. 051916.

[122] M. J. E. Richardson, N. Brunel, and V. Hakim. “From subthreshold to firing-rate resonance”. In: *J. Neurophysiol.* 89 (2003), p. 2538.

[123] L. Badel, S. Lefort, T. K. Berger, C. C. H. Petersen, W. Gerstner, and M. J. E. Richardson. “Extracting non-linear integrate-and-fire models from experimental data using dynamic I-V curves”. In: *Biol. Cybern.* 99 (2008), p. 361.

[124] D. A. Brown and P. R. Adams. “Muscarinic suppression of a novel voltage-sensitive K+ current in a vertebrate neurone”. In: *Nature* 283.5748 (1980), pp. 673–676.

[125] D. V. Madison and R. A. Nicoll. “Control of the repetitive discharge of rat CA 1 pyramidal neurones in vitro.” In: *J. Physiol.* 354.1 (1984), pp. 319–331.

[126] I. A. Fleidervish, A. Friedman, and M. J. Gutnick. “Slow inactivation of Na+ current and slow cumulative spike adaptation in mouse and guinea-pig neocortical neurones in slices.” In: *J. Physiol.* 493.1 (1996), pp. 83–97.

[127] A. Treves. “Mean-field analysis of neuronal spike dynamics”. In: *Network: Comput. Neural Syst.* 4 (1993), p. 259.

[128] H. Markram, Y. Wang, and M. Tsodyks. “Differential signaling via the same axon of neocortical pyramidal neurons”. In: *P. Natl. Acad. Sci. USA* 95 (1998), p. 5323.

[129] R. S. Zucker and W. G. Regehr. “Short-term synaptic plasticity”. In: *Ann. Rev. Physiol.* 64 (2002), p. 355.

[130] L. F. Abbott and W. G. Regehr. “Synaptic Computation”. In: *Nature* 431 (2004), p. 796.

[131] Sebastian Vellmer and Benjamin Lindner. “Theory of spike-train power spectra for multidimensional integrate-and-fire neurons”. In: *Phys. Rev. Res.* 1.2 (2019), p. 023024.

[132] J. Guckenheimer. “Isochrons and Phaseless Sets”. In: *J. Math. Biol.* 1.3 (1975), p. 259.

[133] F. C. Hoppensteadt and E. M. Izhikevich. *Weakly Connected Neural Networks*. New York: Springer-Verlag, 1997.

[134] N. W. Schultheiss, A. A. Prinz, and R. J. Butera. *Phase response curves in neuroscience: theory, experiment, and analysis*. Springer Science & Business Media, 2011.

[135] G Bard Ermentrout and David H Terman. *Mathematical foundations of neuroscience*. Vol. 35. Springer Science & Business Media, 2010.

[136] T. Netoff, M. Schwemmer, and T. Lewis. “Experimentally estimating phase response curves of neurons: theoretical and practical issues”. In: *Phase Response Curves in Neuroscience* (2012).

[137] J. Guckenheimer and P. Holmes. *Nonlinear oscillations, dynamical systems, and bifurcations of vector fields*. Vol. 42. Springer Science & Business Media, 2013.

[138] A. T. Winfree. *The geometry of biological time*. Vol. 2. Springer, 1980.

[139] M. A. Schwemmer and T. J. Lewis. "The theory of weakly coupled oscillators". In: *Phase response curves in neuroscience*. Springer, 2012, pp. 3–31.

[140] B. Gutkin, G. B. Ermentrout, and A. D. Reyes. "Phase-response curves give the responses of neurons to transient inputs". In: *J. Neurophysiol.* 94.2 (2005), p. 1623.

[141] D. Wilson and B. Ermentrout. "Augmented phase reduction of (not so) weakly perturbed coupled oscillators". In: *SIAM Review* 61.2 (2019), pp. 277–315.

[142] E. Brown, J. Moehlis, and P. Holmes. "On the phase reduction and response dynamics of neural oscillator populations". In: *Neural Comp.* 16 (2004), p. 673.

[143] J. Ladenbauer, M. Augustin, L. J. Shiau, and K. Obermayer. "Impact of Adaptation Currents on Synchronization of Coupled Exponential Integrate-and-Fire Neurons". In: *PLoS Comput Biol* 8 (2012), e1002478.

[144] Y. Park, K. M. Shaw, H. J. Chiel, and P. J. Thomas. "The infinitesimal phase response curves of oscillators in piecewise smooth dynamical systems". In: *Eur. J. Appl. Math.* 29.5 (2018), pp. 905–940.

[145] B. Ermentrout. "Type I membranes, phase resetting curves, and synchrony". In: *Neural Comput.* 8 (1996), p. 979.

[146] T. Schwalger. "The interspike-interval statistics of non-renewal neuron models". PhD thesis. Humboldt-Universität zu Berlin, 2013.

[147] M. Messer, K. M. Costa, J. Roeper, and G. Schneider. "Multi-scale detection of rate changes in spike trains with weak dependencies". In: *J. Comp. Neurosci.* 42.2 (2017), pp. 187–201.

[148] S. B. Lowen and M. C. Teich. "Auditory-nerve action potentials form a nonrenewal point process over short as well as long time scales". In: *J. Acoust. Soc. Am.* 92 (1992), p. 803.

[149] C. Lewis, G. Gebber, P. Larsen, and S. Barman. "Long-term correlations in the spike trains of medullary sympathetic neurons". In: *J. Neurophysiol.* 85.4 (2001), pp. 1614–1622.

[150] M. J. Chacron, A. Longtin, M. St-Hilaire, and L. Maler. "Suprathreshold stochastic firing dynamics with memory in P-type electroreceptors". In: *Phys. Rev. Lett.* 85 (2000), p. 1576.

[151] W. R. Softky and C. Koch. "The highly irregular firing of cortical cells is inconsistent with temporal integration of random EPSPs". In: *J. Neurosci.* 13 (1993), p. 334.

[152] Y. Mochizuki, T. Onaga, H. Shimazaki, T. Shimokawa, Y. Tsubo, R. Kimura, A. Saiki, Y. Sakai, Y. Isomura, S. Fujisawa, K. Shibata, D. Hirai, T. Furuta, T. Kaneko, S. Takahashi, T. Nakazono, S. Ishino, Y. Sakurai, T. Kitsukawa, J. W. Lee, H. Lee, M. W. Jung, C. Babul, P. E. Maldonado, K. Takahashi, F. I. Arce-McShane, C. F. Ross, B. J. Sessle, N. G. Hatsopoulos, T. Brochier, A. Riehle, P. Chorley, S. Gruen, H. Nishijo, S. Ichihara-Takeda, S. Funahashi, K. Shima, H. Mushiake, Yukako Yamane, Hiroshi Tamura, Ichiro Fujita, Naoko Inaba, Kenji Kawano, Sergei Kurkin, Kikuro Fukushima, Kiyoshi Kurata, Masato Taira, Ken-Ichiro Tsutsui, T. Ogawa, H. Komatsu, K. Koida, K. Toyama, B. J. Richmond, and S. Shinomoto. "Similarity in Neuronal Firing Regimes across Mammalian Species". In: *J. Neurosci.* 36 (2016), p. 5736.

[153] B. Dummer, S. Wieland, and B. Lindner. "Self-consistent determination of the spike-train power spectrum in a neural network with sparse connectivity". In: *Front. Comp. Neurosci.* 8 (2014), p. 104.

[154] R.F. Pena, S. Vellmer, D. Bernardi, A.C. Roque, and B. Lindner. "Self-consistent scheme for spike-train power spectra in heterogeneous sparse networks". In: *Front. Comp. Neurosci.* 12.9 (2018).

[155] W. Bair, C. Koch, W. Newsome, and K. Britten. "Power spectrum analysis of bursting cells in area MT in the behaving monkey". In: *J. Neurosci.* 14 (1994), p. 2870.

[156] A. Lerchner, G. Sterner, J. Hertz, and M. Ahmadi. "Mean field theory for a balanced hypercolumn model of orientation selectivity in primary visual cortex". In: *Network : Computation in Neural Systems* 17 (2006), p. 131.

[157] M. J. Chacron, K. Pakdaman, and A. Longtin. “Interspike Interval Correlations, Memory, Adaptation, and Refractoriness in a Leaky Integrate-and-Fire Model with Threshold Fatigue”. In: *Neural Comput.* 15 (2003), p. 253.

[158] J. Benda, A. Longtin, and L. Maler. “Spike-frequency adaptation separates transient communication signals from background oscillations”. In: *J. Neurosci.* 25 (2005), p. 2312.

[159] J. Benda and R. M. Hennig. “Spike-frequency adaptation generates intensity invariance in a primary auditory interneuron”. In: *J. Comput. Neurosci.* 24 (2008), p. 113.

[160] S. A. Prescott and T. J. Sejnowski. “Spike-Rate Coding and Spike-Time Coding Are Affected Oppositely by Different Adaptation Mechanisms”. In: *J. Neurosci.* 28 (2008), p. 13649.

[161] K. Wimmer, K. Jannis Hildebrandt, R. M. Hennig, and K. Obermayer. “Adaptation and Selective Information Transmission in the Cricket Auditory Neuron AN2”. In: *PLoS Comput. Biol.* 4 (2008), e1000182.

[162] S. Peron and F. Gabbiani. “Spike frequency adaptation mediates looming stimulus selectivity in a collision-detecting neuron”. In: *Nat. Neurosci.* 12 (2009), p. 318.

[163] J. Benda, L. Maler, and A. Longtin. “Linear Versus Nonlinear Signal Transmission in Neuron Models With Adaptation Currents or Dynamic Thresholds”. In: *J. Neurophysiol.* 104 (2010), p. 2806.

[164] F. Farkhooi, E. Muller, and M. P.Nawrot. “Adaptation reduces variability of the neuronal population code”. In: *Phys. Rev. E* 83 (2011), 050905(R).

[165] F. Farkhooi, A. Froese, E. Muller, R. Menzel, and M. P. Nawrot. “Cellular Adaptation Facilitates Sparse and Reliable Coding in Sensory Pathways”. In: *PLoS Comput. Biol.* 9 (2013), e1003251.

[166] T. Deemyad and J. Kroeger. “Sub- and suprathreshold adaptation currents have opposite effects on frequency tuning”. In: *J. Physiol.* 590 (2012), p. 4839.

[167] C. Pozzorini, R. Naud, S. Mensi, and W. Gerstner. “Temporal whitening by power-law adaptation in neocortical neurons”. In: *Nat. Neurosci.* 16 (2013), p. 942.

[168] B. Ermentrout, M. Pascal, and B. Gutkin. “The effects of spike frequency adaptation and negative feedback on the synchronization of neural oscillators”. In: *Neural Comput.* 13 (2001), p. 1285.

[169] G. Fuhrmann, H. Markram, and M. Tsodyks. “Spike Frequency Adaptation and Neocortical Rhythms”. In: *J. Neurophysiol.* 88 (2002), p. 761.

[170] P. Zhou, S. D. Burton, N. Urban, and G. B. Ermentrout. “Impact of neuronal heterogeneity on correlated colored-noise-induced synchronization”. In: *Front. Comput. Neurosci.* 7 (2013), p. 113.

[171] R. Jolivet, F. Schürmann, T. K. Berger, R. Naud, W. Gerstner, and A. Roth. “The quantitative single-neuron modeling competition”. In: *Biol. Cybern.* 99 (2008), p. 417.

[172] P. M. Harrison, L. Badel, M. J. Wall, and M. J. E. Richardson. “Experimentally Verified Parameter Sets for Modelling Heterogeneous Neocortical Pyramidal-Cell Populations”. In: *PLoS Comput. Biol.* 11 (2015), p. 8.

[173] N. Brunel. “Dynamics of sparsely connected networks of excitatory and inhibitory spiking neurons”. In: *J. Comput. Neurosci.* 8 (2000), p. 183.

[174] T. Schwalger and L. Schimansky-Geier. “Interspike interval statistics of a leaky integrate-and-fire neuron driven by Gaussian noise with large correlation times”. In: *Phys. Rev. E.* 77 (2008), p. 031914.

[175] L. Shiau, T. Schwalger, and B. Lindner. “Interspike interval correlation in a stochastic exponential integrate-and-fire model with subthreshold and spike-triggered adaptation”. In: *J. Comput. Neurosci.* 38 (2015), p. 589.

[176] E. Urdapilleta. “Noise-induced interspike interval correlations and spike train regularization in spike-triggered adapting neurons”. In: *Europhys. Lett.* 115.6 (2016), p. 68002.

[177] Lauralee Sherwood. *Human physiology: from cells to systems*. Cengage learning, 2015.

[178] D. K. Vassilatis, J. G. Hohmann, H. Zeng, F. Li, J. E. Ranchalis, M. T. Mortrud, A. Brown, S. S. Rodriguez, J. R. Weller, A. C. Wright, et al. "The G protein-coupled receptor repertoires of human and mouse". In: *Proc. Natl. Acad. Sci.* 100.8 (2003), pp. 4903–4908.

[179] G. W. De Young and J. Keizer. "A single-pool inositol 1,4,5-trisphosphate-receptor-based model for agonist-stimulated oscillations in Ca^{2+} concentration." In: *PNAS* 89.20 (1992), pp. 9895–9899.

[180] Y. Li and J. Rinzel. "Equations for $InsP_3$ receptor-mediated $[Ca^{2+}]_i$ oscillations derived from a detailed kinetic model: a Hodgkin-Huxley like formalism". In: *J. Theor. Biol.* 166.4 (1994), pp. 461–473.

[181] T. Höfer, L. Venance, and C. Giaume. "Control and plasticity of intercellular calcium waves in astrocytes: a modeling approach". In: *J. Neurosci.* 22.12 (2002), pp. 4850–4859.

[182] S. Schuster, M. Marhl, and T. Höfer. "Modelling of simple and complex calcium oscillations: From single-cell responses to intercellular signalling". In: *Eur. J. Biochem.* 269.5 (2002), pp. 1333–1355.

[183] A. Politi, L. D. Gaspers, A. P. Thomas, and T. Höfer. "Models of IP3 and Ca^{2+} oscillations: frequency encoding and identification of underlying feedbacks". In: *Biophys. J.* 90.9 (2006), pp. 3120–3133.

[184] Martin Falcke. "On the role of stochastic channel behavior in intracellular Ca^{2+} dynamics". In: *Biophys. J.* 84.1 (2003), pp. 42–56.

[185] A. Skupin, H. Kettenmann, and M. Falcke. "Calcium Signals Driven by Single Channel Noise". In: *PLoS Comput. Biol.* 6 (2010), e1000870.

[186] A. Calabrese, D. Fraiman, D. Zysman, and S. Ponce Dawson. "Stochastic fire-diffuse-fire model with realistic cluster dynamics". In: *Phys. Rev. E* 82 (3 2010), p. 031910.

[187] K. Thurley and M. Falcke. "Derivation of Ca^{2+} signals from puff properties reveals that pathway function is robust against cell variability but sensitive for control". In: *P. Natl. Acad. Sci. USA* 108 (2011), p. 427.

[188] J.K. Foskett, C. White, K. Cheung, and D.D. Mak. "Inositol Trisphosphate Receptor Ca^{2+} Release Channels". In: *Physiol. Rev.* 87.2 (2007), pp. 593–658.

[189] M. Bootman, E. Niggli, M. Berridge, and P. Lipp. "Imaging the hierarchical Ca^{2+} signalling system in HeLa cells." In: *J. Physiol.* 499.2 (1997), pp. 307–314.

[190] G. Fan, M. L. Baker, Z. Wang, M. R. Baker, P. A. Sinyagovskiy, W. Chiu, S. J. Ludtke, and I.I. Serysheva. "Gating machinery of InsP3R channels revealed by electron cryomicroscopy". In: *Nature* 527.7578 (2015), pp. 336–341.

[191] D. L. Prole and C. W. Taylor. "Structure and function of IP_3 receptors". In: *Cold Spring Harb. Perspect. Biol.* 11.4 (2019), a035063.

[192] M. Bootman, M. Berridge, and P. Lipp. "Cooking with calcium: the recipes for composing global signals from elementary events". In: *Cell* 91.3 (1997), pp. 367–373.

[193] Y. Yao, J. Choi, and I. Parker. "Quantal puffs of intracellular Ca^{2+} evoked by inositol trisphosphate in Xenopus oocytes". In: *J Physiol* 482.3 (1995), pp. 533–553.

[194] S. C. Tovey, S. G. Dedos, E. J. A. Taylor, J. E. Church, and C. W. Taylor. "Selective coupling of type 6 adenylyl cyclase with type 2 IP_3 receptors mediates direct sensitization of IP_3 receptors by cAMP". In: *J. Cell Biol.* 183.2 (2008), pp. 297–311.

[195] M. V. Keebler and C. W. Taylor. "Endogenous signalling pathways and caged IP_3 evoke Ca^{2+} puffs at the same abundant immobile intracellular sites". In: *J. Cell Sci.* 130.21 (2017), pp. 3728–3739.

[196] K. Bentele and M. Falcke. "Quasi-Steady Approximation for Ion Channel Currents". In: *Biophys. J.* 93.8 (20200716), pp. 2597 –2608.

[197] G. D. Dickinson, D. Swaminathan, and I. Parker. "The probability of triggering calcium puffs is linearly related to the number of inositol trisphosphate receptors in a cluster". In: *Biophys. J.* 102.8 (2012), pp. 1826–1836.

[198] M Iino. “Biphasic Ca^{2+} dependence of inositol 1,4,5-trisphosphate-induced Ca release in smooth muscle cells of the guinea pig taenia caeci.” In: *J. Gen. Physiol.* 95.6 (1990), pp. 1103–1122.

[199] I. Bezprozvanny, J. Watras, and B. E. Ehrlich. “Bell-shaped calcium-response curves of Ins(1,4,5)P_3-and calcium-gated channels from endoplasmic reticulum of cerebellum”. In: *Nature* 351.6329 (1991), pp. 751–754.

[200] D. D. Mak, S. McBride, and J. K. Foskett. “Inositol 1,4,5-tris-phosphate activation of inositol tris-phosphate receptor Ca^{2+} channel by ligand tuning of Ca^{2+} inhibition”. In: *PNAS* 95.26 (1998), pp. 15821–15825.

[201] S. M. Wiltgen, G. D. Dickinson, D. Swaminathan, and I. Parker. “Termination of calcium puffs and coupled closings of inositol trisphosphate receptor channels”. In: *Cell Calcium* 56.3 (2014), pp. 157–168.

[202] M. Prakriya and R. S. Lewis. “Store-operated calcium channels”. In: *Physiol. Rev.* (2015).

[203] A. B. Parekh and J.W. Putney. “Store-operated calcium channels”. In: *Physiol. Rev.* 85.2 (2005), pp. 757–810.

[204] J. Suzuki, K. Kanemaru, K. Ishii, M. Ohkura, Y. Okubo, and M. Iino. “Imaging intraorganellar Ca^{2+} at subcellular resolution using CEPIA”. In: *Nat. Commun.* 5.1 (2014), p. 4153.

[205] I. Siekmann, L. E. Wagner II, D. Yule, E. J. Crampin, and J. Sneyd. “A kinetic model for type I and II IP_3R accounting for mode changes”. In: *Biophys. J.* 103.4 (2012), pp. 658–668.

[206] K. Thurley, I. F. Smith, S. C. Tovey, C. W. Taylor, I. Parker, and M. Falcke. “Timescales of IP_3-evoked Ca^{2+} spikes emerge from Ca^{2+} puffs only at the cellular level”. In: *Biophys. J.* 101.11 (2011), pp. 2638–2644.

[207] E. Gin, M. Falcke, L. E. Wagner, D. I. Yule, and J. Sneyd. “A Kinetic Model of the Inositol Trisphosphate Receptor Based on Single-Channel Data”. In: *Biophys.J.* 96.10 (2009), pp. 4053–4062.

[208] L. Ionescu, C. White, K. H. Cheung, J. Shuai, I. Parker, J. E. Pearson, J. K. Foskett, and D. O. D. Mak. “Mode switching is the major mechanism of ligand regulation of $InsP_3$ receptor calcium release channels”. In: *J. Gen. Physiol.* 130.6 (2007), pp. 631–645.

[209] P. Cao, G. Donovan, M. Falcke, and J. Sneyd. “A stochastic model of calcium puffs based on single-channel data”. In: *Biophys. J.* 105.5 (2013), pp. 1133–1142.

[210] P. Cao, X. Tan, G. Donovan, M. J. Sanderson, and J. Sneyd. “A deterministic model predicts the properties of stochastic calcium oscillations in airway smooth muscle cells”. In: *PLoS Comput. Biol.* 10.8 (2014), e1003783.

[211] L. E. Wagner II and D. I. Yule. “Differential regulation of the $InsP_3$ receptor type-1 and-2 single channel properties by $InsP_3$, Ca^{2+} and ATP”. In: *J. Physiol.* 590.14 (2012), pp. 3245–3259.

[212] D. D. Mak, J. E. Pearson, K. P. Loong Campion, S. Datta, M. Fernández-Mongil, and J. K. Foskett. “Rapid ligand-regulated gating kinetics of single inositol 1,4,5-trisphosphate receptor Ca^{2+} release channels”. In: *EMBO reports* 8.11 (2007), pp. 1044–1051.

[213] A. Atri, J. Amundson, D. Clapham, and J. Sneyd. “A single-pool model for intracellular calcium oscillations and waves in the Xenopus laevis oocyte”. In: *Biophys. J.* 65.4 (1993), pp. 1727–1739.

[214] M. Domijan, R. Murray, and J. Sneyd. “Dynamical probing of the mechanisms underlying calcium oscillations”. In: *J. Nonlinear Sci.* 16 (2006), pp. 483–506.

[215] E. Harvey, V. Kirk, M. Wechselberger, and J. Sneyd. “Multiple timescales, mixed mode oscillations and canards in models of intracellular calcium dynamics”. In: *J. Nonlinear Sci.* 21 (2011), pp. 639–683.

[216] T. Pawelczyk and A. Matecki. “Structural requirements of phospholipase C $\delta1$ for regulation by spermine, sphingosine and sphingomyelin”. In: *European journal of biochemistry* 248.2 (1997), pp. 459–465.

[217] K. Kuba and S. Takeshita. “Simulation of intracellular Ca^{2+} oscillation in a sympathetic neurone”. In: *J. Theor. Biol.* 93.4 (1981), pp. 1009–1031.

[218] A. Goldbeter, G. Dupont, and M. J. Berridge. “Minimal model for signal-induced Ca^{2+} oscillations and for their frequency encoding through protein phosphorylation.” In: *Proc. Natl. Acad. Sci.* 87.4 (1990), pp. 1461–1465.

[219] G. Dupont and A. Goldbeter. “One-pool model for Ca^{2+} oscillations involving Ca^{2+} and inositol 1, 4, 5-trisphosphate as co-agonists for Ca^{2+} release”. In: *Cell calcium* 14.4 (1993), pp. 311–322.

[220] J. Shuai, J. E. Pearson, J. K. Foskett, D. D. Mak, and I. Parker. “A kinetic model of single and clustered IP_3 receptors in the absence of Ca^{2+} feedback”. In: *Biophys. J.* 93.4 (2007), pp. 1151–1162.

[221] E. R. Higgins, H. Schmidle, and M. Falcke. “Waiting time distributions for clusters of IP_3 receptors”. In: *J. Theor. Biol.* 259.2 (2009), pp. 338 –349.

[222] J. T. Lock, I. F. Smith, and I. Parker. “Comparison of Ca^{2+} puffs evoked by extracellular agonists and photoreleased IP_3”. In: *Cell Calcium* 63 (2017), pp. 43–47. ISSN: 0143-4160.

[223] J. T. Lock, K. J. Alzayady, D. I. Yule, and I. Parker. “All three IP_3 receptor isoforms generate Ca^{2+} puffs that display similar characteristics”. In: *Sci. Signal.* 11.561 (2018), eaau0344.

[224] I. F. Smith and I. Parker. “Imaging the quantal substructure of single IP_3R channel activity during Ca^{2+} puffs in intact mammalian cells”. In: *PNAS* 106.15 (2009), pp. 6404–6409.

[225] G. D. Dickinson and I. Parker. “Factors determining the recruitment of inositol trisphosphate receptor channels during calcium puffs”. In: *Biophys. J.* 105.11 (2013), pp. 2474–2484.

[226] C. E. Adkins and C. W. Taylor. “Lateral inhibition of inositol 1, 4, 5-trisphosphate receptors by cytosolic Ca^{2+}”. In: *Curr. Biol.* 9.19 (1999), pp. 1115–1118.

[227] I. Bosanac, T. Michikawa, K. Mikoshiba, and M. Ikura. “Structural insights into the regulatory mechanism of IP3 receptor”. In: *Biochim Biophys Acta Mol Cell Res* 1742.1-3 (2004), pp. 89–102.

[228] A. M. Rossi, S. C. Tovey, T. Rahman, D. L. Prole, and C. W. Taylor. “Analysis of IP_3 receptors in and out of cells”. In: *Biochimica et Biophysica Acta (BBA) - General Subjects* 1820.8 (2012), pp. 1214–1227.

[229] P. Cao, M. Falcke, and J. Sneyd. “Mapping interpuff interval distribution to the properties of inositol trisphosphate receptors”. In: *Biophys. J.* 112.10 (2017), pp. 2138–2146.

[230] J. K. Foskett and D.O.D. Mak. “Regulation of IP_3R channel gating by Ca^{2+} and Ca^{2+} binding proteins”. In: *Curr. Top. Membr.* Vol. 66. Elsevier, 2010, pp. 235–272.

[231] S. Ross. *A first course in probability*. Pearson, 2010.

[232] V. K. Rohatgi and A. K. M. E. Saleh. *An introduction to probability and statistics*. John Wiley & Sons, 2015.

[233] B. Lindner. “The diffusion coefficient of nonlinear Brownian motion”. In: *New J. Phys.* 9 (2007), p. 136.

[234] B. Lindner. “Diffusion Coefficient of a Brownian Particle with a Friction Function Given by a Power Law”. In: *J. Stat. Phys.* 130 (2008), p. 523.

[235] F. L. Bygrave and A. Benedetti. “What is the concentration of calcium ions in the endoplasmic reticulum?” In: *Cell Calcium* 19.6 (1996), pp. 547–551.

[236] J. T. Lock and I. Parker. “IP_3 mediated global Ca^{2+} signals arise through two temporally and spatially distinct modes of Ca^{2+} release”. In: *Elife* 9 (2020), e55008.

[237] I. Vorontsova, J. T. Lock, and I. Parker. “KRAP is required for diffuse and punctate IP_3-mediated Ca^{2+} liberation and determines the number of functional IP_3R channels within clusters”. In: *Cell Calcium* 107 (2022), p. 102638.

[238] G. L. Gerstein and B. Mandelbrot. “Random walk models for the spike activity of a single neuron”. In: *Biophys. J.* 4 (1964), p. 41.

[239] D. T. Gillespie. “The chemical Langevin equation”. In: *J. Chem. Phys.* 113 (2000), p. 297.

[240] X. Wang, Y. Hao, S. H. Weinberg, and G. D. Smith. “Ca^{2+}-activation kinetics modulate successive puff/spark amplitude, duration and inter-event-interval correlations in a Langevin model of stochastic Ca^{2+} release”. In: *Mathematical Biosciences* 264 (2015), pp. 101–107.

[241] E. Wong and M. Zakai. “On the convergence of ordinary integrals to stochastic integrals”. In: *Ann. Mat.h Stat.* 36 (1965), p. 1560.

[242] I. M. Sokolov. “Itô, Stratonovich, Hänggi and all the rest: The thermodynamics of interpretation”. In: *Chem. Phys.* 375.2-3 (2010), pp. 359–363.

[243] G. Blankenship and G. C. Papanicolaou. “Stability and control of stochastic systems with wide-band noise disturbances. I”. In: *SIAM J Appl Math* 34.3 (1978), pp. 437–476.

[244] L. Abbott and C. van Vreeswijk. “Asynchronous states in networks of pulse-coupled oscillators”. In: *Phys. Rev. E.* 48 (1993), p. 1483.

[245] N. Fourcaud and N. Brunel. “Dynamics of the firing probability of noisy integrate-and-fire neurons”. In: *Neural Comput.* 14 (2002), p. 2057.

[246] B. Lindner. *Coherence and Stochastic Resonance in Nonlinear Dynamical Systems*. Berlin: Logos-Verlag, 2002.

[247] M. J. E. Richardson. “Effects of synaptic conductance on the voltage distribution and firing rate of spiking neurons”. In: *Phys. Rev. E.* 69 (2004), p. 051918.

[248] B. Lindner. “Moments of the first passage time under external driving”. In: *J. Stat. Phys.* 117 (2004), p. 703.

[249] T. Schwalger, D. Miklody, and B. Lindner. “When the leak is weak - how the first-passage statistics of a biased random walk can approximate the ISI statistics of an adapting neuron”. In: *Eur. Phys. J. Spec. Topics* 222 (2013), p. 2655.

[250] A. Skupin and M. Falcke. “From puffs to global Ca^{2+} signals: How molecular properties shape global signals”. In: *Chaos* 19.3 (2009), p. 037111.

[251] F. Gao and L. Han. “Implementing the Nelder-Mead simplex algorithm with adaptive parameters”. In: *Comput. Optim. Appl.* 51.1 (2012), pp. 259–277.

[252] A. Skupin and M. Falcke. “Statistical analysis of calcium oscillations”. In: *Eur. Phys. J-Spec. Top.* 187 (2010), p. 231.

[253] N.L. Allbritton, T. Meyer, and L. Stryer. “Range of messenger action of Calcium ion and inositol 1,4,5 trisphosphate”. In: *Science* 258 (1992), pp. 1812–1815.

[254] R.E. Milner, K.S. Famulski, and M. Michalak. “Calcium binding proteins in the sarco / endoplasmatic reticulum of muscle and nonmuscle cells”. In: *Mol. Cell. Biochem.* 112 (1992), pp. 1–13.

[255] J. Wagner and J. Keizer. “Effects of rapid buffers on Ca^{2+} diffusion and Ca^{2+} oscillations”. In: *Biophys. J.* 67.1 (1994), pp. 447–456.

[256] B. Lindner, A. Longtin, and A. Bulsara. “Analytic expressions for rate and CV of a type I neuron driven by white Gaussian noise”. In: *Neural. Comp.* 15 (2003), p. 1761.

[257] F. T. Arecchi and A. Politi. “Transient Fluctuations in the Decay of an Unstable State”. In: *Phys. Rev. Lett.* 45 (1980), p. 1219.

[258] M. J. Chacron, B. Lindner, L. Maler, A. Longtin, and J. Bastian. “Experimental and theoretical demonstration of noise shaping by interspike interval correlations”. In: *Fluctuations and Noise in Biological, Biophysical and Biomedical Systems III*. Proc. SPIE. Ed. by N. G. Stocks, D. Abbott, and R. P. Morse. Vol. 5841. SPIE, 2005, p. 150.

[259] Pauli Virtanen, Ralf Gommers, Travis E. Oliphant, Matt Haberland, Tyler Reddy, David Cournapeau, Evgeni Burovski, Pearu Peterson, Warren Weckesser, Jonathan Bright, Stéfan J. van der Walt, Matthew Brett, Joshua Wilson, K. Jarrod Millman, Nikolay Mayorov, Andrew R. J. Nelson, Eric Jones, Robert Kern, Eric Larson, C J Carey, İlhan Polat, Yu Feng, Eric W. Moore, Jake VanderPlas, Denis Laxalde, Josef Perktold, Robert Cimrman, Ian Henriksen, E. A. Quintero, Charles R. Harris, Anne M. Archibald, Antônio H. Ribeiro, Fabian Pedregosa, Paul van Mulbregt, and SciPy 1.0 Contributors. “SciPy 1.0: Fundamental Algorithms for Scientific Computing in Python”. In: *Nature Methods* 17 (2020), pp. 261–272.

[260] N. B. Thillaiappan, A. P. Chavda, S. C. Tovey, D. L. Prole, and C. W. Taylor. “Ca^{2+} signals initiate at immobile IP3 receptors adjacent to ER-plasma membrane junctions”. In: *Nat. Commun.* 8.1 (2017), p. 1505.

[261] T. Schwalger, J. Tiana-Alsina, M. C. Torrent, J. Garcia-Ojalvo, and B. Lindner. "Interspike-interval correlations induced by two-state switching in an excitable system". In: *Epl-Europhys. Lett.* 99 (2012), p. 10004.

[262] D. Hansel, G. Mato, and C. Meunier. "Synchrony in excitatory neural networks". In: *Neural Comput.* 7 (1995), p. 307.

[263] A. M. Thomson, J. Deuchars, and D. C. West. "Large, deep layer pyramid-pyramid single axon EPSPs in slices of rat motor cortex display paired pulse and frequency-dependent depression, mediated presynaptically and self-facilitation, mediated postsynaptically". In: *J. Neurophysiol.* 70.6 (1993), pp. 2354–2369.

[264] S. Lefort, C. Tomm, J.C.F. Sarria, and C.C.H. Petersen. "The Excitatory Neuronal Network of the C2 Barrel Column in Mouse Primary Somatosensory Cortex". In: *Neuron* 61 (2009), p. 301.

[265] A. Loebel, G. Silberberg, D. Helbig, H. Markram, M. Tsodyks, and M. J. E. Richardson. "Multiquantal release underlies the distribution of synaptic efficacies in the neocortex". In: *Front Comput. Neurosci.* 3 (2009), p. 27.

[266] H. Barlow. "Single units and sensation: a neuron doctrine for perceptual psychology". In: *Perception* 1 (1972), p. 371.

[267] T. W. Margrie, M. Brecht, and B. Sakmann. "In vivo, low-resistance, whole-cell recordings from neurons in the anaesthetized and awake mammalian brain". In: *Pflug. Arch. Eur. J. Phy.* 444 (2002), p. 491.

[268] N. Hohn and A. N. Burkitt. "Shot noise in the leaky integrate-and-fire neuron". In: *Phys. Rev. E.* 63 (2001), p. 031902.

[269] F. Droste and B. Lindner. "Exact analytical results for integrate-and-fire neurons driven by excitatory shot noise". In: *J. Comp. Neurosci.* 43 (2017), p. 81.

[270] O. Á. Åkerberg and M. J. Chacron. "Noise shaping in neural populations". In: *Phys. Rev. E.* 79 (2009), p. 011914.

[271] M. J. Chacron, B. Lindner, and A. Longtin. "ISI correlations and information transfer". In: *Fluct. Noise Lett.* 4 (2004), p. L195.

[272] D. J. Mar, C. C. Chow, W. Gerstner, R. W. Adams, and J. J. Collins. "Noise shaping in populations of coupled model neurons". In: *Proc. Natl. Acad. Sci.* 96 (1999), p. 10450.

[273] J. Shin. "The noise shaping neural coding hypothesis: a brief history and physiological implications". In: *Neurocomp.* 44 (2002), p. 167.

[274] S. Blankenburg and B. Lindner. "The effect of positive interspike interval correlations on neuronal information transmission". In: *Math. Biosci. Eng.* 13 (2016), p. 461.

[275] D. Bernardi and B. Lindner. "A frequency-resolved mutual information rate and its application to neural systems". In: *J. Neurophysiol.* 113 (2015), p. 1342.

[276] S. Blankenburg, W. Wu, B. Lindner, and S. Schreiber. "Information filtering in resonant neurons". In: *J. Comput. Neurosci.* 39 (2015), p. 349.

[277] B. Lindner. "Mechanisms of Information Filtering in Neural Systems". In: *IEEE Trans. Mol. Biol. Multi-Scale Commun.* 2 (2016), p. 5.

[278] J. Schwabedal and A. Pikovsky. "Phase Description of Stochastic Oscillations". In: *Phys. Rev. Lett.* 110 (2013), p. 204102.

[279] P. J. Thomas and B. Lindner. "Asymptotic Phase of Stochastic oscillators". In: *Phys. Rev. Lett.* 113 (2014), p. 254101.

[280] A. Perez-Cervera, B. Gutkin, P. J. Thomas, and B. Lindner. "A Universal Description of Stochastic Oscillators." In: *preprint (PNAS, accepted)* (2023).

[281] J. Shuai and P. Jung. "Stochastic properties of Ca^{2+} release of inositol 1,4,5-trisphosphate receptor clusters". In: *Biophys. J.* 83.1 (2002), pp. 87–97.

[282] Alexander Skupin and Martin Falcke. "Statistical properties and information content of calcium oscillations". In: *Genome inform.* 18 (2007), pp. 44–53.

[283] M. Falcke and V. N. Friedhoff. "The stretch to stray on time: Resonant length of random walks in a transient". In: *Chaos* 28.5 (2018), p. 053117.

[284] V. N. Friedhoff, B. Lindner, and M. Falcke. "Modeling IP_3-induced Ca^{2+} signaling based on its interspike interval statistics". In: *Biophysical Journal* 122.13 (2023), pp. 2818–2831. ISSN: 0006-3495.

[285] A. Einstein. "Über die von der molekularkinetischen Theorie der Wärme geforderte Bewegung von in ruhenden Flüssigkeiten suspendierten Teilchen". In: *Ann. Phys. (Leipzig)* 17 (1905), p. 549.

[286] M von Smoluchowski. "Zur kinetischen Theorie der Brownschen Molekular Bewegung und der Suspensionen". In: *Ann. d. Phys.* 21 (1906), pp. 756–780.

[287] M. Von Smoluchowski. "Experimentell nachweisbare, der üblichen Thermodynamik widersprechende Molekularphänomene". In: *Phys. Z.* XIII (1912), p. 1069.

[288] X. Wang, Y. Hao, S. H. Weinberg, and G. D. Smith. "Ca^{2+}-activation kinetics modulate successive puff/spark amplitude, duration and inter-event-interval correlations in a Langevin model of stochastic Ca^{2+} release". In: *Math. Biosci.* 264 (2015), pp. 101–107.

[289] S. Dragoni, U. Laforenza, E. Bonetti, F. Lodola, C. Bottino, R. Berra-Romani, G. Carlo Bongio, M. P. Cinelli, G. Guerra, P. Pedrazzoli, et al. "Vascular endothelial growth factor stimulates endothelial colony forming cells proliferation and tubulogenesis by inducing oscillations in intracellular Ca^{2+} concentration". In: *Stem Cells* 29.11 (2011), pp. 1898–1907.

[290] J. S. Marchant and I. Parker. "Role of elementary Ca^{2+} puffs in generating repetitive Ca^{2+} oscillations". In: *EMBO J.* 20.1-2 (2001), pp. 65–76.

[291] S. P. Dawson, J. Keizer, and J. E. Pearson. "Fire-diffuse-fire model of dynamics of intracellular calcium waves". In: *Proc. Natl. Acad. Sci.* 96.11 (1999), pp. 6060–6063.

[292] S. Coombes and Y. Timofeeva. "Sparks and waves in a stochastic fire-diffuse-fire model of Ca^{2+} release". In: *Phys. Rev. E* 68.2 (2003), p. 021915.

[293] S. Coombes, R. Hinch, and Y. Timofeeva. "Receptors, sparks and waves in a fire-diffuse-fire framework for calcium release". In: *Prog. Biophys. Mol. Biol.* 85.2-3 (2004), pp. 197–216.

[294] T. J. Collins, P. Lipp, M. J. Berridge, and M. D. Bootman. "Mitochondrial Ca^{2+} uptake depends on the spatial and temporal profile of cytosolic Ca^{2+} signals". In: *J. Biol. Chem.* 276.28 (2001), pp. 26411–26420.

[295] G. Szabadkai, A. M. Simoni, K. Bianchi, D. De Stefani, S. Leo, M. R. Wieckowski, and R. Rizzuto. "Mitochondrial dynamics and Ca^{2+} signaling". In: *Biochim. Biophys. Acta, Mol. Cell Res.* 1763.5-6 (2006), pp. 442–449.

[296] R. Rizzuto, D. De Stefani, A. Raffaello, and C. Mammucari. "Mitochondria as sensors and regulators of calcium signalling". In: *Nat. Rev. Mol. Cell Biol.* 13.9 (2012), pp. 566–578.

[297] T. Pathak and M. Trebak. "Mitochondrial Ca^{2+} signaling". In: *Pharmacol. Ther.* 192 (2018), pp. 112–123.

[298] L. Modesti, A. Danese, V. A. M. Vitto, D. Ramaccini, G. Aguiari, R. Gafà, G. Lanza, C. Giorgi, and P. Pinton. "Mitochondrial Ca^{2+} signaling in health, disease and therapy". In: *Cells* 10.6 (2021), p. 1317.

Danksagung

Die Entstehung dieser Arbeit ist in erster Linie meinem wissenschaftlichen Betreuer und Lehrer Prof. Dr. Benjamin Lindner zu verdanken. Ich danke ihm für die viele Zeit, die er aufgewendet hat, um meine Fragen zu beantworten, meine Fehler zu korrigieren und neue Ideen zu entwickeln. Insbesondere die vielen anregenden wissenschaftlichen Diskussionen werden mir in guter Erinnerung bleiben.

Ein weiterer großer Dank gilt Prof. Dr. Martin Falcke, ohne dessen Zutun diese Arbeit ebenfalls nicht zustande gekommen wäre. Seine Expertise auf dem Gebiet der Kalzium-Signalübertragung hat in konstruktiver und freundlicher Weise immer wieder dazu beigetragen, die Schwachstellen dieser Arbeit zu erkennen und zu beheben. Außerdem möchte ich ihm für die Bereitstellung der experimentellen Daten danken.

Ich danke allen Mitgliedern der Arbeitsgruppe "Theorie komplexer Systeme und Neurophysikäm Bernstein Zentrum Berlin. Insbesondere Dr. Greg Knoll und Mascha Schlungbaum. Beide haben wesentlich zu einem offenen und freundlichen Arbeitsklima beigetragen. Darüber hinaus möchte ich mich bei Greg für sein immer offenes Ohr bedanken.

Abschließend möchte ich mich bei Leona Bauer bedanken. Zum einen hat sie große Teile dieser Arbeit Korrektur gelesen. Viel wichtiger war aber ihre kontinuierliche Unterstützung in den letzten viereinhalb Jahren. Vielen Dank.